

**Chronic stress: Tissue-specific impact on
energy metabolism and metabolic adaptation**

Chronischer Stress: Gewebespezifische Auswirkungen auf den
Energistoffwechsel und die metabolische Anpassung

Inaugural-Dissertation

zur Erlangung des Doktorgrades
der Mathematisch-Naturwissenschaftlichen Fakultät
der Heinrich-Heine-Universität Düsseldorf

vorgelegt von

Aleksandra Nikolić
aus Hilden

Düsseldorf, Oktober 2023

aus dem Institut für Klinische Biochemie und Pathobiochemie
des Deutschen Diabetes-Zentrums
Leibniz-Zentrum für Diabetes-Forschung
an der Heinrich-Heine-Universität Düsseldorf

Gedruckt mit der Genehmigung der
Mathematisch-Naturwissenschaftlichen Fakultät der
Heinrich-Heine-Universität Düsseldorf

Berichtersteller:

1. Prof. Dr. Hadi Al-Hasani
2. Prof. Dr. Michael Feldbrügge

Tag der mündlichen Prüfung: 11.04.2024

ZUSAMMENFASSUNG

Episoden chronischen Stresses können zu psychischen Störungen wie der posttraumatischen Belastungsstörung führen, aber auch langfristig die Entwicklung des metabolischen Syndroms und Typ-2-Diabetes fördern. Stress benötigt Energie und beeinflusst den molekularen Stoffwechsel nachhaltig. Mitochondrien liefern zelluläre Energie und kontrollieren gleichzeitig wesentliche Faktoren der Stresshormonsynthese und epigenetischen Regulation. In der vorliegenden Studie soll die Hypothese untersucht werden, ob die mitochondriale Funktion ein Schlüsselmechanismus in der Verknüpfung von Stoffwechseladaptation und epigenetischer Regulierung der Genexpression nach Stressexposition ist. Im Sinne eines *circulum vitiosus* könnte ein durch Stress induzierter veränderter Energiemetabolismus zu dauerhaft veränderten DNA-Methylierungsmustern führen, die sich auf das Transkriptom und Genregulationsnetzwerke auswirken und eine langfristige Anpassung des Stoffwechsels in Skelettmuskulatur (SM) und Leber zur Folge haben. Hierzu wurde die Auswirkung eines bereits etablierten Chronisch variablen Stress (Cvs) Protokolls bei männlichen C57BL/6-Mäusen untersucht. Trotz erhöhter Energiezufuhr weisen diese im Vergleich zu den Kontrollen einen geringeren Energieverbrauch (EE), eine geringere Körpermasse und einen verringerten Glukosestoffwechsel auf. Hingegen nimmt die β -Oxidation zu, die mit dem EE korreliert.

Die Untersuchungen zeigen erstmalig, dass in SM nach Cvs die Funktion der mitochondrialen Komplexe I und II beeinträchtigt sind und die thermodynamische Effizienz (η -opt) von Komplex II deutlich erhöht ist. Letzteres korreliert mit dem EE in der Ruhephase und dem bereits reduzierten EE in der aktiven Phase. Das Transkriptom und das Methylom im SM werden durch Cvs nur geringfügig beeinflusst, was auf die mitochondriale Anpassung als Haupteffekt hindeutet. In der Leber zeigen die Untersuchungen erstmalig eine erhöhte thermodynamische Effizienz (η -opt) des Komplex I, die positiv mit Blutzucker und NEFA und umgekehrt mit dem EE korreliert. In der Leber wurde außerdem ein verringertes Komplex I-gesteuertes NAD⁺/NADH-Verhältnis und verringerte Komponenten des methylierungsrelevanten One-Carbon -Zyklus nachgewiesen, was auf eine epigenetische Regulierung hindeutet. So konnte hier auch erstmalig gezeigt werden, dass durch Stressexposition Methylierungsmuster der mitochondrialen DNA (mtDNA) verändert werden, die sich auch auf die zugehörigen Transkriptionsnetzwerke auswirken.

ABSTRACT

Episodes of chronic stress can lead to psychological disorders such as post-traumatic stress disorder, but also promote the development of metabolic syndrome and type 2 diabetes in the long term. Stress requires energy and has a lasting effect on molecular metabolism. Mitochondria provide cellular energy while controlling essential factors of stress hormone synthesis and epigenetic regulation. The present study aims to investigate the hypothesis whether mitochondrial function is a key mechanism in linking metabolic adaptation and epigenetic regulation of gene expression after stress exposure. In terms of *circulum vitiosus*, stress-induced altered energy metabolism could lead to permanently altered DNA methylation patterns that affect the transcriptome and gene regulatory networks, resulting in long-term metabolic adaptation in skeletal muscle (SM) and liver.

For this purpose, the effect of a previously established chronic variable stress (Cvs) protocol was investigated in male C57BL/6- mice. Despite increased energy intake, these exhibits decreased energy expenditure (EE), body mass, and glucose metabolism compared to controls. In contrast, β -oxidation increases, which correlates with EE. These studies show for the first time that in SM after Cvs, the function of mitochondrial complexes I and II are impaired and the thermodynamic efficiency (η -opt) of complex II is significantly increased. The latter correlates with the EE in the resting phase and the already reduced EE in the active phase. The transcriptome and methylome in the SM are only slightly affected by Cvs, suggesting mitochondrial adaptation as the main effect. In liver, the studies show for the first time an increased thermodynamic efficiency (η -opt) of complex I, which correlates positively with blood glucose and NEFA and inversely with EE. In liver, a decreased complex I-driven NAD⁺/NADH ratio and decreased components of the methylation-related one-carbon cycle were also detected, suggesting epigenetic regulation. Thus, it was also shown here for the first time that stress exposure alters methylation patterns of mitochondrial DNA (mtDNA), which also affect the associated transcription networks. In summary, chronic stress exposure leads to direct adaptation of complex-specific thermodynamic efficiency. Tissue-specifically, complex II is altered in SM and complex I in liver, with both tissues associated with decreased whole-body EE to control energy balance. In liver, in particular, mtDNA gene regulation is additionally altered, which ultimately manifests itself in terms of stress memory also in epigenetic changes and in metabolic changes after a recovery phase.

TABLE OF CONTENT

| | |
|--|----|
| 1. Introduction..... | 1 |
| 1.1 Stress as an environmental risk factor for disease | 1 |
| 1.1.1 HPA axis and glucocorticoids..... | 1 |
| 1.1.2 Influence of glucocorticoids (GC) on glucose and lipid metabolism..... | 2 |
| 1.1.3 Animal models of stress | 3 |
| 1.1.4 Pathophysiology of the Cvs model | 3 |
| 1.2 Stress and its role in energy metabolism | 4 |
| 1.2.1 Whole-body energy metabolism | 4 |
| 1.2.2 Contribution of different tissues to energy metabolism | 5 |
| 1.2.3 The role of the skeletal muscle to energy metabolism | 5 |
| 1.2.4 The role of liver in energy metabolism..... | 6 |
| 1.2.5 Metabolic flexibility | 6 |
| 1.3 Mitochondria..... | 6 |
| 1.3.1 The mitochondria as energy producer | 7 |
| 1.3.2 The role of the substrate cycle of mitochondria..... | 8 |
| 1.3.3 Mitochondrial bioenergetics, thermodynamic efficiency and coupling in energy metabolism..... | 9 |
| 1.3.4 Stress response of mitochondria | 10 |
| 1.4 Epigenetics and transcriptional regulation | 10 |
| 1.4.1 Mechanism of DNA methylation | 11 |
| 1.4.2 Metabolic regulation of epigenetics..... | 13 |
| 1.4.3 Adaptation process in response to altered environment and metabolic memory | 16 |
| 1.5 Objectives..... | 21 |
| 2. Material & Methods | 22 |
| 2.1 Material | 22 |
| 2.1.1 Instruments and devices | 22 |
| 2.1.2 Disposals | 24 |
| 2.1.3 Chemicals..... | 25 |
| 2.1.4 Buffers and solutions | 28 |
| 2.1.5 Cell culture and assay medium..... | 30 |
| 2.1.6 Commercial kits | 31 |
| 2.1.7 Oligonucleotides..... | 33 |
| 2.1.8 Software..... | 33 |
| 2.2 Methods | 35 |
| 2.2.1 Animals | 35 |
| 2.2.2 Experimental design | 35 |

| | |
|--|-----|
| 2.2.3 Cvs protocol | 36 |
| 2.2.4 <i>In vivo</i> analyses | 37 |
| 2.2.5 <i>Ex vivo</i> analyses in plasma | 39 |
| 2.2.6 <i>Ex vivo</i> analyses in muscle and liver..... | 40 |
| 2.2.7 <i>Ex vivo</i> analyses of mitochondrial function in muscle and liver | 44 |
| 2.2.8 <i>Ex vivo</i> analyses in primary hepatocytes | 49 |
| 2.2.9 Omics Analyses..... | 52 |
| 2.2.10 Databases | 60 |
| 2.2.11 Statistics | 60 |
| 3. Results | 62 |
| 3.1 Immediate effects of chronic variable stress (Cvs) on the regulation of energy metabolism in muscle in the C57BL/6 mouse model..... | 62 |
| 3.1.1 Metabolic characteristics after Cvs..... | 62 |
| 3.1.2 Indirect calorimetry in Cvs mice..... | 63 |
| 3.1.3 Mitochondrial composition assessment..... | 65 |
| 3.1.4 Cvs interferes with mitochondrial function and EE in muscle..... | 70 |
| 3.1.5 Bioenergetic assessment of mitochondrial respiratory control ratio and calculation of thermodynamic coupling and efficiency..... | 73 |
| 3.1.6 Cvs impacts on muscle transcriptome and methylome..... | 75 |
| 3.2 Immediate effect of Cvs on energy balance leads to metabolic adaptation with longitudinal effect on liver gene regulation of C57BL/6 mouse..... | 78 |
| 3.2.1 Cvs interferes with hepatic metabolism | 78 |
| 3.2.2 Altered protein abundance in main pathways for glucose and lipid metabolism after Cvs | 81 |
| 3.2.3 Cvs increases mitochondrial thermodynamic efficiency of complex I in liver | 84 |
| 3.2.4 The molecular action of stress interferes with gene regulation in two phases | 91 |
| 4. Discussion | 97 |
| 4.1 Chronic stress targets mitochondrial respiratory efficiency in the skeletal muscle of C57BL/6 mice | 97 |
| 4.2 Chronic stress leads to sustained metabolic changes with increased thermodynamic efficiency of mitochondrial complex I in the liver that in sum alter the liver epigenome..... | 104 |
| 4.3 Chronic stress targets tissue specific mitochondrial respiratory efficiency and leads in liver to altered mitochondrial DNA methylation with loss of metabolic flexibility | 111 |
| 5. Conclusion..... | 116 |
| References | 117 |
| Appendix | 137 |
| Danksagung | 142 |
| Eidesstattliche Erklärung..... | 143 |

LIST OF FIGURES

| | |
|---|----|
| Figure 1: Mitochondrial electron transport chain (ETC) and oxidative phosphorylation (OXPHOS) complexes. | 7 |
| Figure 2: Illustration of different types of epigenetic modifications and drivers. | 11 |
| Figure 3: DNA Methylation and demethylation pathways for CpG methylation in mammals. | 13 |
| Figure 4: Compartmentalization of one-carbon metabolism and its related pathways. | 15 |
| Figure 5: TCA cycle regulation of chromatin modifications and DNA methylation. | 16 |
| Figure 6: Experimental design. | 35 |
| Figure 7: Time schedule of Cvs protocol. | 37 |
| Figure 8: Effect of 15 days of chronic stress intervention (Cvs) on weight change, body composition, and food uptake. | 63 |
| Figure 9: Effect of 15 days of Cvs intervention on physical activity, energy expenditure (EE), and substrate utilization. | 64 |
| Figure 10: Quality control of mitochondrial fractions in regard to content and membrane integrity. | 65 |
| Figure 11: Cvs intervention interferes with metabolic pathway component abundance in enriched muscle mitochondria. | 66 |
| Figure 12: Cvs intervention interferes with metabolic pathway component abundance in enriched muscle mitochondria. | 67 |
| Figure 13: Mitochondrial proteome. | 69 |
| Figure 14: Cvs does not affect proton leakage in mitochondrial fractions. | 70 |
| Figure 15: Electron flow capacity and coupling efficiency of mitochondrial ETC after Cvs, injection time-line diagrams. | 71 |
| Figure 16: Electron flow and coupling experiments of mitochondrial ETC after Cvs. | 73 |
| Figure 17: Respiratory control ratio, thermodynamic q value and calculated optimal thermodynamic efficiencies of mitochondrial complex I and II after Cvs. | 74 |
| Figure 18: Differential methylated areas after Cvs intervention in gastrocnemius muscle. | 75 |
| Figure 19: Cvs does not affect DNA modifying enzyme activity. | 76 |
| Figure 20: Transcriptome analyses of gastrocnemius muscle after Cvs. | 76 |
| Figure 21: Systemic effects of a 15-day chronic stress intervention (Cvs). | 80 |
| Figure 22: Intraperitoneal glucose (i.p. GTT), pyruvate (i.p. PTT) tolerance test of plasma after Cvs. | 81 |
| Figure 23: Cvs intervention impairs the proteome abundance and ex vivo activity of key metabolic pathways. | 83 |
| Figure 24: Cvs does not affect mitochondrial mass, membrane integrity, and ROS. | 85 |

| | |
|--|-----|
| Figure 25: Mitochondrial proteome and electron flow assessment. | 86 |
| Figure 26: Calculating of classical mitochondrial respiratory states after Cvs..... | 88 |
| Figure 27: Mitochondrial complex I efficiency is impaired after Cvs..... | 90 |
| Figure 28: Molecular action of stress on hepatic genetic and epigenetic processes..... | 92 |
| Figure 29: Stress interferes with hepatic mitochondrial gene regulation and function. | 96 |
| Figure 30: Graphical summary of mitochondrial compensatory mechanism in skeletal muscle after Cvs. | 103 |
| Figure 31: Graphical summary of metabolic and epigenetic adaptation after Cvs in liver mitochondria. | 110 |

LIST OF TABLES

| | |
|--|-----|
| Table 1: Instruments and devices..... | 22 |
| Table 2: Disposals..... | 24 |
| Table 3: Chemicals used in the study | 25 |
| Table 4: Buffers and solutions..... | 28 |
| Table 5: Used cell culture and assay media | 30 |
| Table 6: Used commercial kits | 31 |
| Table 7: Oligonucleotides for qPCR | 33 |
| Table 8: Software | 33 |
| Table 9: Overview of persons who contributed to experiments in publication Nikolic et al. 2023 (muscle). | 140 |
| Table 10: Overview of persons who contributed to experiments in unpublished manuscript (liver). | 141 |

LIST OF ABBREVIATIONS

| | |
|------------|---|
| 5-caC | 5-carboxylcytosine |
| 5-fC | 5-formylcytosine |
| 5-hmC | 5-hydroxymethylcytosine |
| 5-mC | 5-methylcytosine |
| ACC | Acetyl-CoA carboxylase |
| ADP | Adenosine diphosphate |
| ALT | Alanine aminotransferase |
| ATP | Adenosine triphosphate |
| AUC | Area under the curve |
| CHO | Carbohydrate oxidation |
| CHD | Coronary Heart Disease |
| CpG | Cytosine nucleotide is followed by a guanine nucleotide |
| CS | Citrate synthase |
| Ctrl | Control |
| Cvs | Chronic variable stress |
| DMRs | Differentially methylated regions |
| DNA | Deoxyribonucleic acid |
| DNMTs | DNA methyltransferases |
| DNL | De novo lipogenesis |
| DTNB | 5,5'-Dithiobis-(2-nitrobenzoic acid) (Ellman's Reagent) |
| ECAR | Extracellular acidification rate |
| EE | Energy expenditure |
| FAD | Flavin-Adenine-Dinucleotide |
| FAO | Fatty acid oxidation |
| FCCP | Carbonyl cyanide-4-(trifluoromethoxy)phenylhydrazone |
| FCS | Fetal calf serum |
| FFA | Free fatty acid |
| GC | Glucocorticoid |
| GLP-1 | Glucagon-like peptide-1 |
| GTT | Glucose tolerance test |
| HDAC | Histone deacetylase |
| HPA | Hypothalamic-pituitary-adrenal axis |
| IRS2 | Receptor substrate 2 |
| KOH | Potassium Hydroxide |
| KRH | Krebs-Ringer-HEPES buffer |
| lncRNA | Long non-coding RNA |
| MetS | Metabolic syndrome |
| MODY | Maturity-onset Diabetes of the Young |
| MTase | Methyltransferase |
| NAD / NADH | oxidized and reduced forms of nicotinamide adenine dinucleotide |
| NAFLD | Non-alcoholic fatty liver disease |
| NEFA | Non-esterified fatty acids |
| NMR | Nuclear magnetic resonance |
| OCR | Oxygen consumption rate |
| PTSD | Post-traumatic stress disorder |
| PTT | Pyruvate tolerance test |

| | |
|------------------------------------|---|
| RER | Respiratory exchange ratio |
| RNA | Ribonucleic acid |
| ROS | Reactive oxygen species |
| SAM | S-adenyl methionine |
| SIRT | Sirtuin |
| T1DM | Type 1 Diabetes Mellitus |
| T2DM | Type 2 Diabetes Mellitus |
| TAG | Triglyceride |
| TCA | Tricarboxylic acid cycle |
| TDG | Thymine DNA glycosylase |
| TET | Ten-eleven translocation |
| TMPD | N, N, N', N'-Tetramethyl-p-phenylenediamine |
| TNB | Trinitrobenzol (1,3,5-Trinitrobenzene) |
| UCP3 | Uncoupling protein 3 |
| VCO ₂ | CO ₂ production |
| VO ₂ | O ₂ consumption |
| VO ₂ / VCO ₂ | Volume of Oxygene / Carbon dioxide |

1. INTRODUCTION

1.1 Stress as an environmental risk factor for disease

Stress is the result of a living organism's inability to respond appropriately to actual or imagined emotional or physical threats (Chrousos and Gold, 1992). Several external environmental factors can induce stress, which is broadly defined as any threat to an organism's homeostasis (Arner and Kulyté, 2015; Chrousos, 2009). Chronic or intense stressors characterized by uncontrollability and unpredictability (e.g. Chronic variable stress (Cvs)) can elicit a stress response that damages cellular functions and triggers maladaptive processes (Selye, 1980). In prospective life course studies, exposure to various stressors, at both the individual and community level, has been shown to increase systemic inflammation, as well as poor glycemic characteristics, high blood pressure, and composite measures of an adverse metabolic profile (Belsky et al., 2020; Crick et al., 2022; Kivimäki and Steptoe, 2018; Winning et al., 2015). So, recent studies suggest that both chronic and (repeated) acute stress are involved in the development of the metabolic syndrome (Bouillon-Minois and Dutheil, 2022). In addition, both oxidative and psychosocial stress have been linked to heart disease and metabolic syndrome (Bizerea-Moga et al., 2022; Bouillon-Minois and Dutheil, 2022; Wijnant et al., 2021) and thus stress emerges as an additional risk factor for metabolic disorders.

1.1.1 HPA axis and glucocorticoids

The acute physiological stress response is well characterized and consists of activation of multiple neuroendocrine circuits, including the hypothalamic-pituitary-adrenal (HPA) axis, sympathomedullary axis and autonomic nervous system (Gunnar and Quevedo, 2007; Russell and Lightman, 2019; Ulrich-Lai and Herman, 2009). Activation of the HPA axis leads to secretion of the adrenal glucocorticoid (GC) cortisol (or in rodents the glucocorticoid corticosterone), which is one of the most commonly assessed stress effectors and is also used as a biomarker for stress (Kivimäki and Steptoe, 2018). Other stress responses include the catecholamine epinephrine released by the sympathomedullary axis or norepinephrine released by the sympathetic nervous system (Gunnar and Quevedo, 2007; Russell and Lightman, 2019; Ulrich-Lai and Herman, 2009). Activation of stress-induced neuroendocrine systems to maintain homeostasis is usually short-lived and adaptive, with no deleterious effects on cellular function (Koolhaas et al., 2011; McEwen, 1998). However, abnormal glucocorticoid levels are a risk factor for insulin resistance, chronic inflammation, high glucose levels and cardiometabolic disorders such as type 2 diabetes mellitus (T2DM) and cardiovascular disease (Hackett and Steptoe, 2016; Iyegha et al., 2019; Oster et al., 2017). Impaired metabolic functions after stress exposure, such as increased insulin resistance, impaired and uncontrolled hepatic gluconeogenesis, adipose lipogenesis, impaired glycogen

synthesis and glucose uptake in skeletal muscle have also been linked to aging and alterations in mitochondrial DNA (Barzilai et al., 2012). Several longitudinal studies also found that individuals who experienced childhood trauma and those with severe post-traumatic stress disorder exhibit accelerated aging, as indicated by site-specific changes in CpG DNA methylation (Wolf et al., 2018).

1.1.2 Influence of glucocorticoids (GC) on glucose and lipid metabolism

Chronic GC exposure leads to an increase in visceral adipose tissue, insulin resistance, an increase in lipolysis-associated release of free fatty acids into the bloodstream, and the accumulation of lipids in the liver, skeletal muscle, and pancreas (Beaupere et al., 2021; Rahimi et al., 2020).

For example, in stressed human patients who had sustained trauma, maximal glucose uptake in peripheral tissues was reduced by ~35% compared with controls (Black et al., 1982). Studies have shown that glucocorticoids acutely inhibit glucose uptake into skeletal muscle by preventing insulin-stimulated translocation of SLC2A4 (GLUT4) to the plasma membrane (Beaupere et al., 2021) and also promote muscle breakdown (proteolysis) by inducing ubiquitin ligases (Bodine and Furlow, 2015). In human adipocytes, glucocorticoids have been shown to stimulate lipogenesis in the non-fasting state in cooperation with insulin (Berdanier, 1989). Glucocorticoids stimulate lipogenic genes such as fatty acid synthase (FASN) and acetyl-CoA carboxylase (ACACB) (Gathercole et al., 2011) and also increase hepatic expression of the fatty acid receptor CD36 (D'Souza A et al., 2012). However, in the absence of insulin (i.e. fasting), glucocorticoids inhibit lipogenesis in adipocytes (Gathercole et al., 2011), and systemic lipid availability from adipose tissue and liver is increased (Koliwad et al., 2009). In adipose tissue, glucocorticoids inhibit the lipolysis inhibitory effects of insulin, albeit to a lesser extent than in other tissues such as skeletal muscle (Hazlehurst and Tomlinson, 2013; Radhakutty et al., 2016). The synthetic glucocorticoid dexamethasone was found to increase lipolysis in adipocytes through the expression of Plin1 (Zhou et al., 2016). Together with increased amounts of specific amino acids derived from muscle breakdown, the increased glycerol and NEFA from lipolysis provide the necessary precursors and energy to drive hepatic gluconeogenesis. Interestingly, glucocorticoid-induced increases in gluconeogenesis, proteolysis, and lipolysis may occur even in the absence of insulin, because these were maintained in animal models of insulin-deficient diabetes (Dallman et al., 1993). In the liver, glucocorticoids suppress insulin action both directly via the gluconeogenic enzymes phosphoenolpyruvate carboxykinase (PEPCK) (Sasaki et al., 1984) and glucose-6-phosphatase (G6PC) (Lin et al., 1998) as well as indirectly via sympathetic projections from the hypothalamic arcuate nucleus (ARC) to the liver (Yi et al., 2012), as demonstrated in rats.

1.1.3 Animal models of stress

Since increased levels of GCs under stress conditions have influence on multiple aspects of the glucose, lipid homeostasis and disease progression, there have been a number of different animal models for stress. For example, there is the predator exposure-based model (Arlington, 2000), stress induced by circadian rhythm changes (Rai et al., 2003), stress induced by a noise stimulus (File and Fernandes, 1994), low-temperature-induced stress (Jaggi et al., 2011), restriction and immobilization stress (Padovan and Guimarães, 2000), stress due to social defeat (Lagace et al., 2010) and the Chronic variable stress (Cvs) (Willner, 1997).

The advantage of this protocol is the repetition of novel and unpredictable stressors during intervention to avoid stress adaptation and to initiate long lasting dysregulation of the HPA axis. Based on its high validity and the similarity of the stressors to which people are exposed in everyday life the Cvs protocol was suitable for this study to analyse physical and psychological homeostasis followed by stress.

1.1.4 Pathophysiology of the Cvs model

The Chronic variable stress (Cvs) protocol consists of 5 different stressors per day in a randomized order for a period of 15 days to prevent adaptation. It was previously used to address the long-lasting dysregulation of the HPA axis a mouse model of PTSD with an already established Chronic variable stress protocol (Castañeda et al., 2011). It has been successful for metabolic investigations (Dille et al., 2022; Jelenik et al., 2018) Since acute stress triggers cascade of biological events mainly due to activation of two major pathways i.e. hypothalamic–pituitary– adrenal (HPA) axis and sympathetic adreno-medullary system. However, repeated exposure of a same stressor is generally associated with general adaptation syndrome (a phase of resistance to the homologous stressful condition). Nevertheless, during persistent exposure of stress, the initial “adaptive response” may change to “maladaptation” in which biological and behavioral responses are counter-productive to the organism. Furthermore, repeated exposure of same stressor (chronic stress) sensitizes the HPA axis and exposure to novel, unpredictable stressor may cause long lasting dysregulation of the HPA axis (Herman et al., 2016). Accordingly, over activation of these systems during persistent stress tends to produce the deleterious effects in the body. In fact, the lack of turning off the physiological response to a stressor (when it is not required) produces allostatic load/overload leading to the development of pathophysiological changes (Karatsoreos and McEwen, 2011; McEwen, 2007).

Moreover, the peculiarity of this animal protocol is that only the stress effect alone can be considered, since the animals were isolated from confounding effects. The animals had the same genetic background, were fed the same diet during the experiment, experienced the same circadian rhythm and had the same age (Castañeda et al., 2011).

1.2 Stress and its role in energy metabolism

The stress response is not synonymous with GC response, but is a bundle of coordinated factors and processes that act in an energy-dependent manner to adapt to the stress challenge. These processes interfere with energy homeostasis in energy provision, energy consumption, and/ or substrate utilization, bringing the focus to the close relation between whole-body energy metabolism, mitochondria and stress response (Bassi et al., 2021).

1.2.1 Whole-body energy metabolism

Whole-body energy metabolism is described as the chemical energy contained in nutrients obtained by a process that consumes oxygen and releases carbon dioxide and water (Frankenfield, 2010). This energy is converted into energy-rich molecules, mainly ATP and creatinine (Frankenfield, 2010). These are used in endergonic reactions such as thermogenesis, anabolism, and muscle work. In homeotherms, ~40% of energy is used to maintain body temperature of ~37-39°C (Even and Nadkarni, 2012). Whole-body energy metabolism changes under different conditions and can be determined by indirect calorimetry, a method which used respiratory gas exchange to estimate whole-body energy expenditure (EE) and whole-body respiratory exchange ratio (RER) (Weir, 1949). Due to its relatively low cost and high accuracy, non-invasive indirect calorimetry is an indispensable tool that provides insights into the mechanisms by which energy homeostasis is regulated (Lam and Ravussin, 2016). Indirect calorimetry is considered as the gold standard to determine EE by measuring oxygen consumption (VO_2) and carbon dioxide production (VCO_2) in a whole-room respiratory chamber. To obtain accurate EE data, data processing, the correction factor "metabolic weight" is used to scale the ratio between body mass and body surface area and is the weight raised to 0.75 (Rubner, (1883)). Respiratory exchange ratio (RER) can be used to validate conclusions about the metabolic state and current substrate utilization in the organism. Based on the energy intake, which can include carbohydrates, amino acids, and lipids, it serves to generate energy in the organism. The ratio of oxygen consumed (VO_2) to carbon dioxide produced (VCO_2) and the amount of energy released per gram differ depending on the substrate (carbohydrates, amino acids or lipids) (Ferrannini, 1988; Simonson and DeFronzo, 1990) and substrates can therefore be calculated specifically from indirect calorimetry measurements. From the difference in energy release, i.e. the ratio of VCO_2/VO_2 , the RER is different for carbohydrates, amino acids, and lipids. Carbohydrates, amino acids, and lipids are imported into the cell and delivered to the mitochondria, where biosynthetic reactions occur and ATP is generated using the respiratory chain in a process known as oxidative phosphorylation (OXPHOS). As a result, mechanisms of interplay between the mitochondria, the nucleus, the mitochondria and the cytosol have evolved to supply cells, tissues and organisms with the energy demanding conditions, but also to adapt to changing conditions

such as environmental factors or disease (Arner and Kulyté, 2015). Emerging evidence suggests that these two parameters (EE, RER) are controlled by a more complex model in which a perturbation in one of the components can lead to biological/behavioral compensatory changes in entirely different components in the body. Specifically, an increase in EE would lead to an increase in energy intake and *vice versa* (Basolo et al., 2022; Piaggi et al., 2018; Timper and Brüning, 2017).

1.2.2 Contribution of different tissues to energy metabolism

Energy consumption is essential for the maintenance of the physiological state of the organism but varies according to metabolic state and condition (Wieser et al., 1989). For example, during exercise, the metabolic rate of some organs (e.g., kidney and intestine) and protein synthesis in skeletal muscle may decrease, whereas gluconeogenesis in the liver increases. Thus, the processes underlying standard metabolic rate (SMR) cannot be considered fixed, but change with conditions. An initial assessment of the contribution of various organs to the rate of oxygen consumption in humans and rats was already made in 1984 by Schmidt-Nielsen (Schmidt-Nielsen, 1984). The study showed that each organ's contribution varied by species and body mass. No organ is responsible for most of the SMR, which represents the lowest measured EE, but rather represents an interaction of all organs together (Schmidt-Nielsen, 1984). However, they also showed that some organs such as the brain, kidney, heart, liver and gastrointestinal tract contribute for much larger proportion of the total SMR compared to the proportion measured by the proportion of body mass and body volume, while others such as bone, white adipose tissue, skin and muscle contribute less. It should be noted, that some tissues (e.g., skeletal muscle) contribute significantly to SMR only because of their size, although the metabolic rate of these tissues is often more relevant to the study of SMR than that of more metabolically active tissues (Pattaranit and van den Berg, 2008).

1.2.3 The role of the skeletal muscle to energy metabolism

In healthy individuals, the skeletal muscle (SM) represents about 40% of body mass, is a significant contributor to basal energy expenditure (Zurlo et al., 1990), and accounts for 70% – 90% of insulin-mediated glucose disposal (DeFronzo, 1981; Shulman et al., 1990). The skeletal muscle is a key organ of whole-body EE, which is coupled to its mitochondrial respiratory capacity (Lewis et al., 2022; Zumbaugh et al., 2022) and, as has been demonstrated in rats, accounts for 30% of whole-body oxygen consumption (Rolfe and Brown, 1997). In skeletal muscle, oxygen consumption and mitochondrial content are higher in red muscle than white muscle and decrease in the order type I > type IIa > type IIb muscle fiber (Rolfe and Brown, 1997). As a result, modulation of skeletal muscle metabolism and insulin sensitivity has proven to be an effective means of alleviating metabolic disorders in humans (Izumiya et al., 2008; Meng et al., 2013).

1.2.4 The role of liver in energy metabolism

The liver accounts for approximately 2% of body mass (Rolfe and Brown, 1997) and is a major metabolic organ. It is involved in energy metabolism, protein synthesis, fat synthesis, and blood glucose control (Ramos Figueira et al., 2015). It is composed of 60% parenchyma cells, i.e., hepatocytes, and 30 to 35% non-parenchymatous cells, i.e., Kupffer cells (KCs), hepatic stellate cells (HSCs), and liver sinusoidal endothelial cells (LSECs) (Williams and Iatropoulos, 2002). The hepatocytes have an extremely active intrinsic metabolic activity that can be adapted to physiological requirements (Alberti et al., 1981), so that the liver is responsible for 24% of energy consumption in the whole organism (Schneeweiss et al., 1993). The liver is quite homogeneous: 80% of hepatocytes show equal mitochondrial content (Loud, 1968).

1.2.5 Metabolic flexibility

The capacity to react or adjust to conditional variations in metabolic demand is known as metabolic flexibility. Every cell has the ability to adapt to different conditions, such as changes in substrate availability and can be determined by metabolic flexibility measurements. These measurements give insights into preferred energy pathway the cell utilizes (mitochondrial respiration or glycolysis), especially concerning how the cell cover energy- and biosynthesis needs at current metabolic state (Fahlbusch et al., 2022). The ability to distinguish or to combine the mentioned pathways to utilize energy gives an insight into the metabolic flexibility and adaptive power of a cell to overcome altered metabolic conditions as during stress intervention. A challenging aspect of mitochondrial functionality is studying their effect on overall cellular metabolism. Studies have identified dysfunctional mitochondria by assessing cell energy phenotypes (Ryu et al., 2022).

1.3 Mitochondria

The mitochondrion is a cellular organelle that generates ATP and metabolites for survival and growth. According to the endosymbiont theory of a prokaryotic predecessor, mitochondria have been a component of the eukaryotic cell for 2 billion years. Thus, they traded the protection of the larger cell for the mitochondria's ability to produce energy from carbohydrates or lipids with oxygen (Margulis, 1975, 1981; Margulis and Bermudes, 1985). Mitochondria have their own genome (Mansour and Nass, 1970) and two membranes. An outer membrane, which is of eukaryotic origin, and an inner membrane, of prokaryotic origin. The inner membrane is highly folded and forms so-called cristae, the density of which varies depending on the tissue type and activity level of the cell (Lea and Hollenberg, 1989; Mannella et al., 1994). The membranes give rise to two independent compartments, the intermembrane space and the mitochondrial matrix. The contribution of mitochondria to energy metabolism is strongly dependent on mitochondrial functionality and density (Islam et al., 2022).

1.3.1 The mitochondria as energy producer

Mitochondria convert energy from fuels into ATP through oxidative phosphorylation (OXPHOS). The first describer of the respiratory chain was Otto Warburg in 1931 (Warburg, 1931), whereas Keilin et al. discovered in 1925 (Keilin, 1925) that the respiratory chain consists of several components such as the redox mediator cytochrome, which serves as electron transport. The classical respiratory chain is composed of four enzyme complexes, ATP synthetase and two mobile electron transfer molecules ubiquinone and cytochrome C (Hatefi, 1985) (Figure 1). The enzyme complexes consist of NADH dehydrogenase, complex I (Hatefi and Bearden, 1976; Hatefi et al., 1962), succinate dehydrogenase, complex II (Kita et al., 1990), cytochrome C reductase, complex III (Keilin, 1939), and cytochrome C oxidase, complex IV (Kadenbach et al., 1983). In 2000, Schägger et al. discovered that the complexes do not occur in isolation in the mitochondrial membrane but form so-called supercomplexes or respirasomes (Schägger and Pfeiffer, 2000).

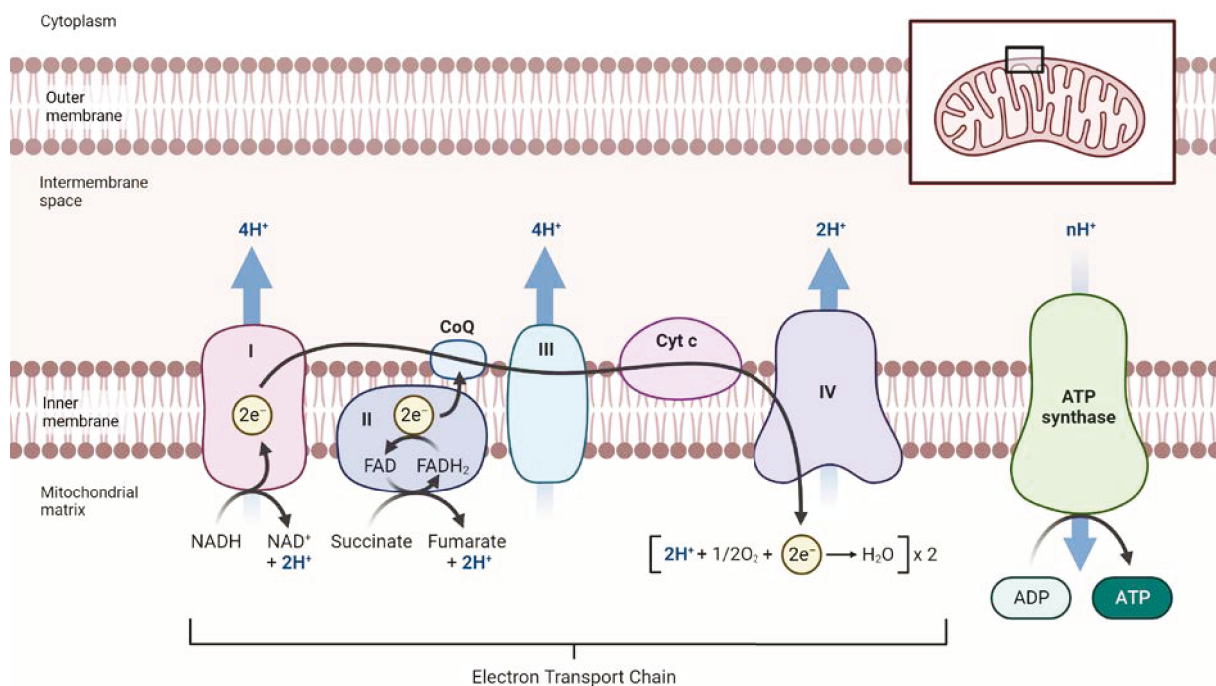


Figure 1: Mitochondrial electron transport chain (ETC) and oxidative phosphorylation (OXPHOS) complexes.

The mitochondrial ETC includes the proton-pumping enzymes complex I (NADH dehydrogenase), complex II (Succinate dehydrogenase), complex III (cytochrome c oxidoreductase) and complex IV (cytochrome c oxidase), which generate proton motive force that drives ATP synthase. Electron transport between complexes is mediated by membrane-embedded ubiquinone (Q) and soluble cytochrome c. Complex I or II are the entry point for electrons which are used to reduce Q to ubiquinol (QH₂). QH₂ is used by complex III to reduce cytochrome c in the intermembrane space and complex IV uses cytochrome c to reduce molecular oxygen as the ultimate electron acceptor.

The respiratory chain complexes receive their electrons from the electron donors NADH and FADH₂, which are generated by citrate cycle enzymatic activity and acetyl-CoA generating pathways, like fatty acid metabolism and amino acid metabolism. NADH specifically provides electrons to complex I mediated transfer, while FADH₂ provides electrons to complex II. The reduction of oxygen to water then occurs in complex IV. Complexes I, III, and IV use the energy from electron transport to establish a proton gradient. ATP synthetase uses the energy from the proton gradient to catalyze the addition of inorganic phosphate on ADP, to generate the energy currency of the cell ATP (Mitchell, 1961). Complex I, NADH dehydrogenase, transfers an electron from the donor NADH H⁺ to the electron acceptor ubiquinone (Q), causing the latter to react to form ubiquinol (QH₂). This electron transfer results in the translocation of two protons (H⁺) into the intermembrane space (Wikström, 1984). Complex I is composed of 46 subunits and 9 redox cofactors (Hirst et al., 2003). The cofactors are composed of a flavin mononucleotide (FMN) and 8 iron sulfur clusters (Ohnishi, 1998; Sazanov and Hinchliffe, 2006). The genes encoding the subunits are mostly located on the nuclear DNA. Only the genes of seven of the 46 subunits are located in the mitochondrial genome (Chomyn et al., 1986; Chomyn et al., 1985). An important mitochondrial gene relevant to complex I assembly is NADH-ubiquinone oxidoreductase chain 1 (*ND1*). Alternatively, electrons can enter the ETC via complex II, the succinate dehydrogenase. Complex II is composed of 4 subunits (Oyedotun and Lemire, 2001) and the genes encoding the subunits are located on nuclear DNA. The hydrophobic subunits SDHC/SDH3 and SDHD/SDH4 constitute the complex II membrane anchor, containing a haem b group and two CoQ binding sites (Oyedotun and Lemire, 2001; Yankovskaya et al., 2003). It oxidizes succinate and the reduced FADH₂ donates two electrons to ubiquinone. Then, the oxidation of ubiquinone to ubiquinol in a coupled reaction with the reduction of cytochrome c resulting in the extrusion of two protons across the inner mitochondrial membrane is catalyzed by complex III, the cytochrome c oxidoreductase (Crofts, 2004).

Finally, complex IV, the cytochrome c oxidase, oxidizes cytochrome c and reduces molecular oxygen to two water molecules. This process leads to the translocation of four protons, which leads to the build-up of a membrane potential (Liu et al., 2011). The reflux of protons back into the mitochondrial matrix drives energy production through ATP synthase by the conversion of adenosine diphosphate (ADP) to ATP (Chaaban et al., 2014). The complexes I, III, IV and V are under mitochondrial and nuclear control as subunits of these complexes are encoded on both genomes (Osellame et al., 2012; Wiedemann and Pfanner, 2017).

1.3.2 The role of the substrate cycle of mitochondria

The profile of substrate consumption has attracted considerable interest in medical research, as it has been associated with various health conditions such as metabolic disorders, diabetes, heart failure, and cancer that exhibit altered patterns of glucose and fat utilization. The interplay

between fat and glucose utilization has been extensively studied in the context of feeding fasts, caloric restriction, starvation, and insulin insensitivity in metabolic disorders (McGarry and Foster, 1980; Randle, 1998; Soeters et al., 2012). However, the exact molecular mechanisms are still not fully understood. In the context of cellular homeostasis, the substrate cycles serve to maintain an independent steady state cycle flow, that is highly adapted to changes in metabolite availability in the organism. This characteristic shows that cycle flow is a key feature of the cell's modularity (Stelling et al., 2004), in terms of maintaining energy balance. If a substrate cycle significantly affects the consumption or generation of a particular cofactor, the enzymes of the cycle could be manipulated to selectively adjust cofactor levels, while minimally perturbing other parts of metabolism. It has been shown that the type of cellular substrates (e.g., fatty acids versus carbohydrates) can influence the stoichiometry of oxidative phosphorylation by means of the ratio between NADH and FADH₂ (Tseng et al., 2010). NADH oxidation involves three consecutive coupling sites (complexes I, III, and IV), whereas FADH₂ oxidation involves only two coupling sites (complexes III and IV). Therefore, the yield of ATP synthesis in the oxidation of FADH₂ is about 40% lower compared to NADH. In contrast to carbohydrate metabolism, equimolar amounts of NADH and FADH₂ are formed during the oxidation of fatty acids. Therefore, the stoichiometry of ATP synthesis to oxygen consumption is lower when fats are oxidized instead of carbohydrates.

1.3.3 Mitochondrial bioenergetics, thermodynamic efficiency and coupling in energy metabolism

Mitochondria are the main cellular compartment involved in the control of energy transduction efficiency. Mitochondrial efficiency depends on the degree of coupling between oxygen consumption (O₂) and ATP synthesis. The degree of coupling can vary according to the metabolic needs of the cell (Stucki, 1980), and is regulated by the amount of cellular unbound fatty acids that can act as natural uncouplers of oxidative phosphorylation (Jezek et al., 1998; Skulachev, 1991). In addition, the mitochondria are the main producers of reactive oxygen species (ROS), and are also highly exposed to oxidative stress (Brand, 2010).

The cell respiration of mitochondria is catalyzed by a linear array of three energy-transducing membrane-bound proteins, via complexes I, III and IV. Each complex links the catalyzed redox reaction (reduction of ubiquinone by NADH, reduction of ferricytochrome c by ubiquinol and reduction of O₂ by ferrocycytochrome c, respectively) to net translocation of protons from the inside (mitochondrial matrix) to the outside (intermembrane space) of the inner mitochondrial membrane, thus creating an electrochemical proton gradient as the primary form of conserved energy. Research over the last 40 years has revealed, that the mechanisms of redox-linked proton translocation are fundamentally different for the three complexes (Verkhovskaya and Bloch, 2013; Wikström et al., 2018; Wikström et al., 2015). To assess these different redox-

linked mechanisms and their bioenergetics, the thermodynamic coupling (q) is used as a reference of the economic degree of energy production, which is needed in the current metabolic state of the mitochondria (Stucki, 1991). Dependent on the q -value, the thermodynamic efficiency (η -opt) of oxidative phosphorylation value is used to validate the efficiency of substrate conversion to energy in mitochondria (Stucki, 1991).

1.3.4 Stress response of mitochondria

Every aspect of the stress response requires energy. Mitochondria are the "first responders" for cells on altered energy demands. This includes energy-dependent enzymatic reactions, transcription and translation that affect gene expression and protein synthesis, neurotransmitter release and reuptake, hormone biosynthesis, sympathetic nervous system activation, behavioral adaptations, and long-term structural remodeling of organs and tissues for which ATP is needed (Chandel, 2015; Picard et al., 2016). Although, in fact, basic life-sustaining biological functions also require energy for their maintenance, the energy requirements for stress responses exceed the basic requirements of organisms, which is why there is a link between stress and energy metabolism (Yang et al., 2019).

Despite the accumulating evidence for mitochondrial involvement in stress responses, the individual mechanisms are yet not fully understood. However, it has recently been demonstrated in a new mouse model that in the brain the *Nduf* gene encoding the NDUFS4 protein (which forms a structural component of complex I of the mitochondrial electron transport chain) has a direct influence on the stress response and coping strategy via reprogramming of amino acid metabolism. These data suggest that impaired mitochondrial complex activity could be seen as a candidate target for altered stress response and stress-induced metabolic reprogramming of the brain (Emmerzaal et al., 2020).

1.4 Epigenetics and transcriptional regulation

Today it came clear, that understanding the energy metabolism, transcriptional dynamics, development and disease progression, also requires an understanding of the so-called epigenome. Epigenetics (from Greek *epi*, meaning in addition) refers to the field studying molecular mechanisms which layer on top of genetic variation. Epigenetics affect transcription, and result in changes to phenotype, which cannot be explained by genetics alone (Corella et al., 2017; Waddington, 1942). Epigenetic drivers are DNA methylation, histone modification and expression of regulatory RNA such as short and long non-coding RNA (miRNA and lncRNA, respectively) (Figure 2). These modalities can affect modulation of chromatin accessibility or organization, as well as interaction with DNA binding transcription factors, interfere with mRNA maturation and stability and finally modify the RNA expression. Similar to genomics, the entirety of the epigenetic profile is called the epigenome.

Although all cells in an organism have the same genetic material, gene expression is specific to cell type and differentiation stage (D'Urso and Brickner, 2014). Unlike the genome, the epigenome undergoes massive changes during development (John and Rougeulle, 2018), epigenetic mechanisms play an important role in tissue-specific gene regulation, genomic imprinting (Li et al., 1993), X chromosome inactivation (Mohandas et al., 1981) and aging (Horváth et al., 2009). Epigenetic modifications can also affect gene expression and the phenotype in response to environmental stimuli (Martínez et al., 2014). The epigenome can be inherited at mitosis and reestablished after meiosis, creating an "epigenetic memory" that enables for the inheritance of cellular identity and adapted modifications. As disruption of epigenetic processes can result in aberrant expression changes and cellular behavior, epigenetics is therefore of great importance in the study of disease (Berglund et al., 2021).

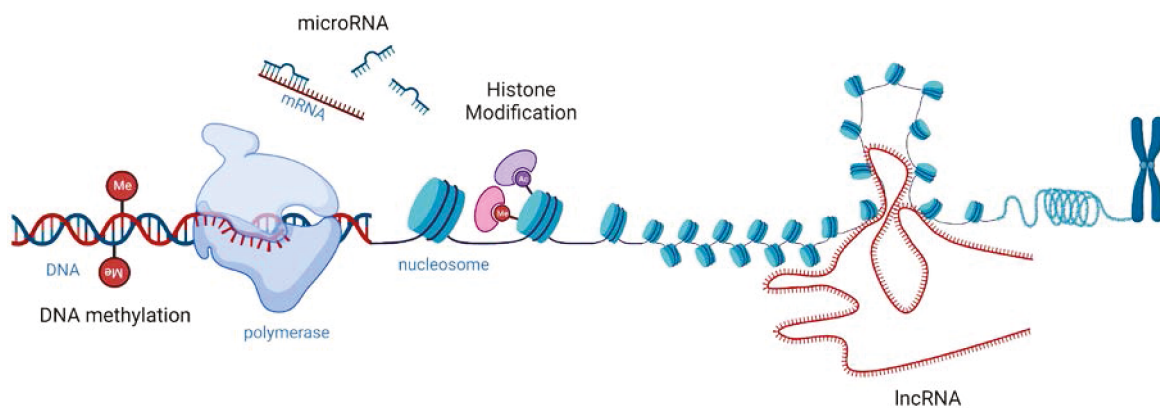


Figure 2: Illustration of different types of epigenetic modifications and drivers.

DNA methylation annotates DNA by binding of methyl-groups to nucleobases, affecting the binding of transcription factors which enhance or repress gene expression. Histone modifications, here illustrated as acetylation and methylation, modulate chromatin organization and accessibility. MicroRNA affects translation by modifying mRNA posttranscriptionally. LncRNA is illustrated here in one of its many functions, as an architect of chromatin organization.

1.4.1 Mechanism of DNA methylation

In mammalian organisms, including humans, cytosine methylation represents one of the most important epigenetic modifications. DNA methylation is an epigenetic mechanism involving the covalent transfer of a methyl group to the fifth carbon (C5) of the cytosine ring of DNA and with this, forming 5-methylcytosine (5-mC). This reaction is catalyzed by DNA methyltransferases (DNMTs) via transferring the methyl group from S-adenyl methionine (SAM) onto the C5 of a dinucleotide (Goll and Bestor, 2005; Greenberg and Bourc'his, 2019; Skvortsova et al., 2018). There are two types of methyltransferases responsible for CpG methylation (Figure 3). One type is de novo methyltransferase 3 alpha and beta (DNMT3a and DNMT3b), which bind to unmethylated sites. These are mainly active in early embryonic development as well as in pluripotent cells (Okano, 2000) and are important for imprinting and cell differentiation. The

second type is the methyltransferase 1 (DNMT1), which is responsible for maintaining methylation in a cell. Indeed, it has been reported that fully differentiated somatic cells are approximately 70-80% methylated at CpG sites (Li and Zhang, 2014). Sequential CpG motives, so called CpG islands notably within promoter regions are common targets for epigenetic DNA methylation. Cytosine methylation also drives the formation of heterochromatin, so the nucleosome tightening prevents transcriptional machinery from interacting with the DNA (Li et al., 2022). Further, methylated CpGs within a promoter region recruit gene suppressor proteins and reduce interaction between the DNA and transcription factors (Wang et al., 2022), as such, result in gene silencing. Unlike prokaryotic cells, mammalian cells also contain mechanisms for the demethylation of CpG sites. Passive demethylation describes the dilution of methylation by failure of methylation maintenance through DNMT1. Active demethylation is performed through oxidation followed by passive dilution or base repair mechanisms. The ten-eleven translocation (TET) enzyme is a DNA binding protein which interacts with 5-mC, successively oxidizing the methyl group (CH₃) to a hydroxymethyl group (CH₂OH), then a formyl group (CHO), and ultimately a carboxyl group (CO₂H). The respective oxidative derivatives of 5-mC, called 5-hydroxymethylcytosine (5-hmC), 5-formylcytosine (5-fC), and 5-carboxylcytosine (5-caC), have then shown to be more difficult to maintain by DNMT1 during mitosis, leading to passive dilution (Onodera et al., 2021). Alternatively, thymine DNA glycosylase (TDG), a DNA repair enzyme responsible for excising mismatched thymine from G/T pairs, has also been found to react to 5-fC and 5-caC, excising these nucleobases (Maiti and Drohat, 2011).

DNA Methylation

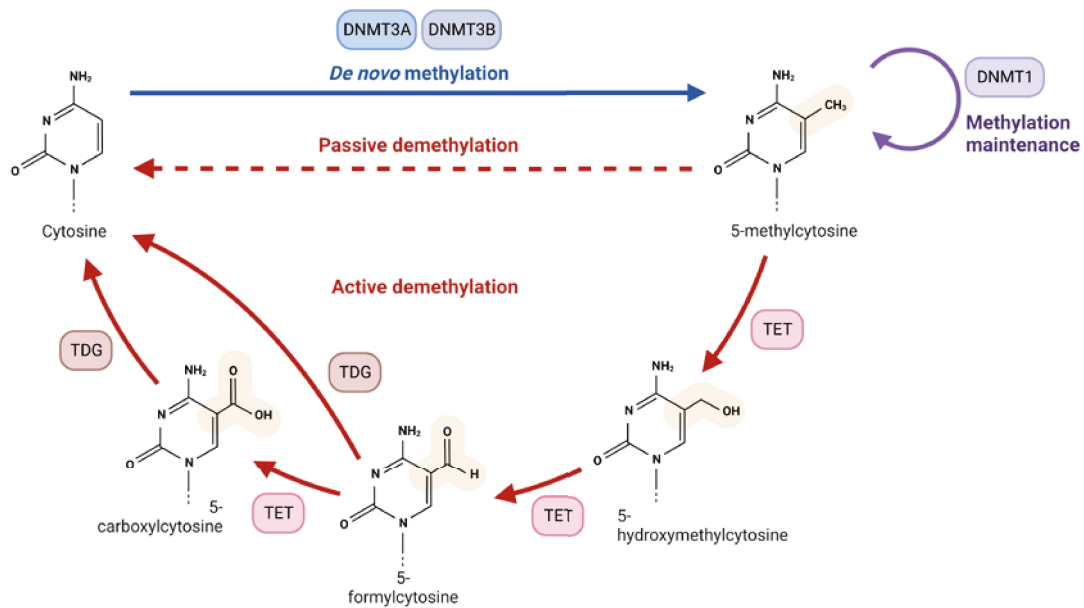


Figure 3: DNA Methylation and demethylation pathways for CpG methylation in mammals.

Chemical composition of cytosine nucleobases, from unmethylated cytosine to 5-mC, to its oxidative derivatives 5-hmC, 5-fC, and 5-caC. Methylation and passive demethylation on double stranded DNA. DNMT3a and b de novo methylate both strands. Maintenance methylase DNMT1. Passive demethylation occurs when DNMT1 fails to perform and the methylation state. Active demethylation pathways. TET successively oxidates methyl group, transforming it into a hydroxymethyl-, formyl and ultimately carboxyl group. All three can be demethylated passively. The latter two may have the entire modified nucleobase excised by TDG. 5-mC, 5-methylcytosine; 5-hmC, 5-hydroxymethylcytosine; 5-fC, 5-formylcytosine; DNMT, methyltransferase; TET, ten-eleven translocation enzyme.

1.4.2 Metabolic regulation of epigenetics

Some of the first data to indicate that both environmental exposures and age could have an effect on the epigenetic profile of our genome was obtained from a study of monozygotic twins. A study showed that despite sharing identical genomes, the patterns of DNA methylation and histone acetylation in several tissues were more diverse in twin pairs who were older, had different lifestyles, and had spent less of their lives together (Fraga et al., 2005).

1.4.2.1 TCA cycle metabolites affect transcription

Stress signals from the environment must be translated into both, short- and long-term biological alterations that alter cellular composition and functions for a complex system like the human body to respond. Transcriptional regulation of genomic elements, or modifications in gene expression, is a key mechanism at the heart of pervasive biological adaptations. First, they affect how certain genetic elements interact with transcription factors and coactivators, which in turn affects how transcripts (messenger RNA, or mRNA) are formed (Hao and O'Shea, 2011). For instance, in response to hypoxia, mitochondria move closer to the nucleus where

they produce ROS, which in turn activates the hypoxia-inducible factor 1 (HIF1) by creating an oxidized environment (Al-Mehdi et al., 2012). A lack of energy also activates certain cytoplasmic energy sensors (mTORC1, AMPK), as well as their downstream transcriptional coactivators PGC-1 and PPAR and have a broad impact on nuclear gene expression (Al-Mehdi et al., 2012).

1.4.2.2 Mitochondrial regulation of epigenetics

Remarkably, the metabolic pathways in mitochondria all provide metabolic intermediates that serve as substrates or cofactors for epigenetic changes (Gut and Verdin, 2013; Matilainen et al., 2017) (Figure 4, Figure 5). For instance, the one-carbon metabolism comprises a complex set of biochemical reactions in which methyl groups (CH₃) are generated or utilized (Hazra et al., 2009). Central to this is the methylation cycle that produces S-adenosyl-methionine (SAM) from methionine and ATP. SAM is converted to S-adenosylhomocysteine (SAH) by methyltransferase enzymes in a transmethylation reaction that generates a methyl group that is available for DNA methylation, protein lipid and carbohydrate synthesis. The S-adenosylhomocysteine produced from transmethylation is converted to homocysteine. Methionine can be regenerated from homocysteine in the presence of a methyl donor such as 5-methyltetrahydrofolate and the enzyme methionine synthase, which itself requires vitamin B12 (cobalamin) as a co-factor. 5-Methyltetrahydrofolate is generated, in part, from dietary folate. Folate species, when not utilized in the methylation cycle, can be redirected to thymidine and purines production for DNA/RNA synthesis, generation of high-energy molecules and cofactors including ATP, NAD and coenzyme A. Transmethylation reactions are also regulated by the availability of dietary micronutrients betaine, choline and the non-essential amino acid serine and glycine (Figure 4).

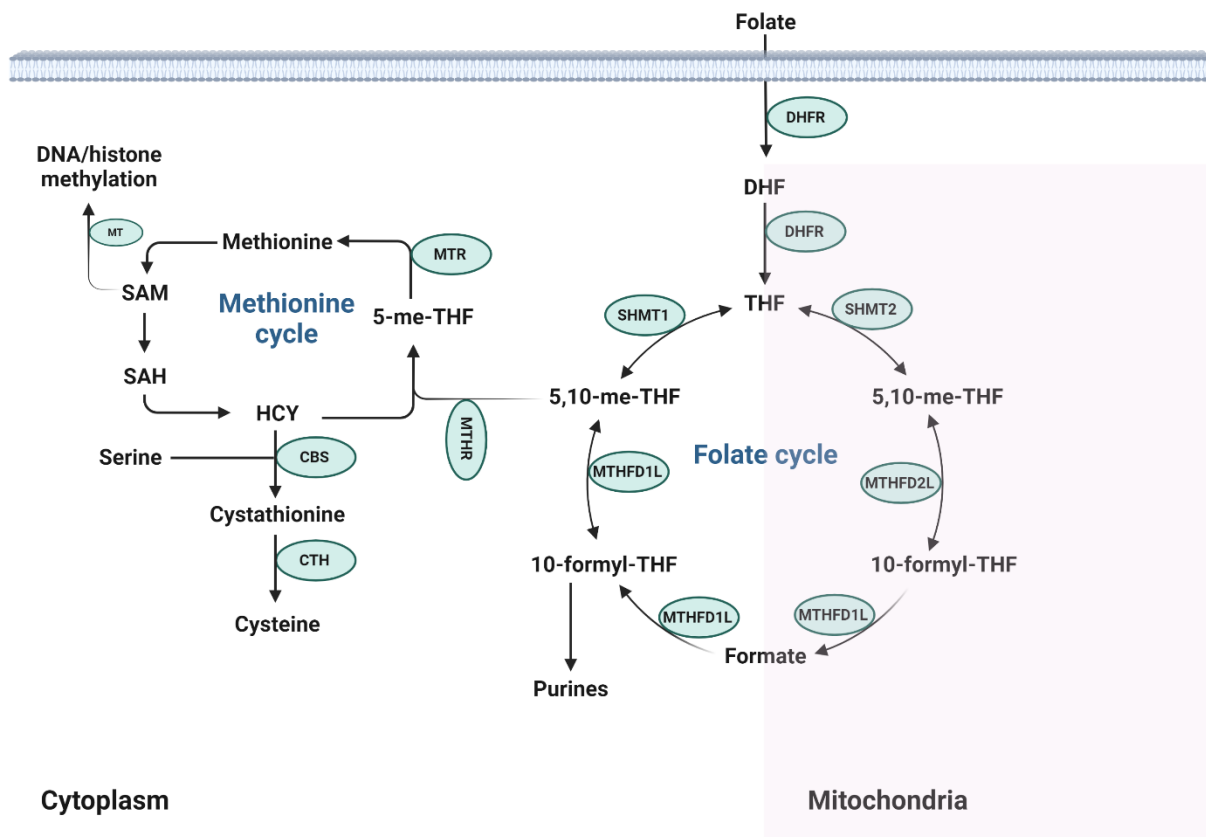


Figure 4: Compartmentalization of one-carbon metabolism and its related pathways.

One-carbon metabolism, which includes the methionine and folate cycles, are central to multiple cellular function. Dietary folate is reduced to THF, which accepts one-carbon unit upon the conversion of serine into glycine by SHMT. Alternatively, the glycine cleavage system (glycine dehydrogenase) converts glycine into ammonia, carbon dioxide, and one-carbon units for the methylation of THF. THF undergoes a series of oxidative/reductive transformations in both the cytoplasm and mitochondria. Through a closely linked set of mitochondrial and cytosolic reactions, folate metabolism supports the methionine cycle, purine synthesis, dTMP synthesis, and the trans-sulfuration pathway. DHF, dihydrofolate; DHFR, dihydrofolate reductase; THF, tetrahydrofolate; SHMT, serine hydroxymethyl transferase; MTHFD, methylenetetrahydrofolate dehydrogenase; TYMS, thymidylate synthetase; dTMP, deoxythymidine monophosphate; MTHFR, methylenetetrahydrofolate reductase; MTR, methionine synthase; SAM, S-adenosylmethionine; SAH, S-adenosylhomocysteine; HCY, homocysteine; CBS, cystathionine b-synthase; CTH, cystathionine glyase; MT, methyl transferase.

Regarding the TCA cycle, citrate is exported from mitochondria to the cytoplasm via the mitochondrial enzyme citrate synthase. Here, ATP citrate lyase converts citrate into acetyl-CoA, which is used as a substrate for histone acetylation (Wellen et al., 2009). Histone acetylation, HIF-1 function, and cell proliferation depend on physiological mitochondrial metabolism (Martínez-Reyes et al., 2016). On the other side, mitochondrial substrates are also needed for the removal of epigenetic markers. Histone and DNA demethylation activities require the presence of the cofactor α -ketoglutarate, a TCA cycle metabolic intermediate (Klose and Zhang, 2007) (Figure 5).

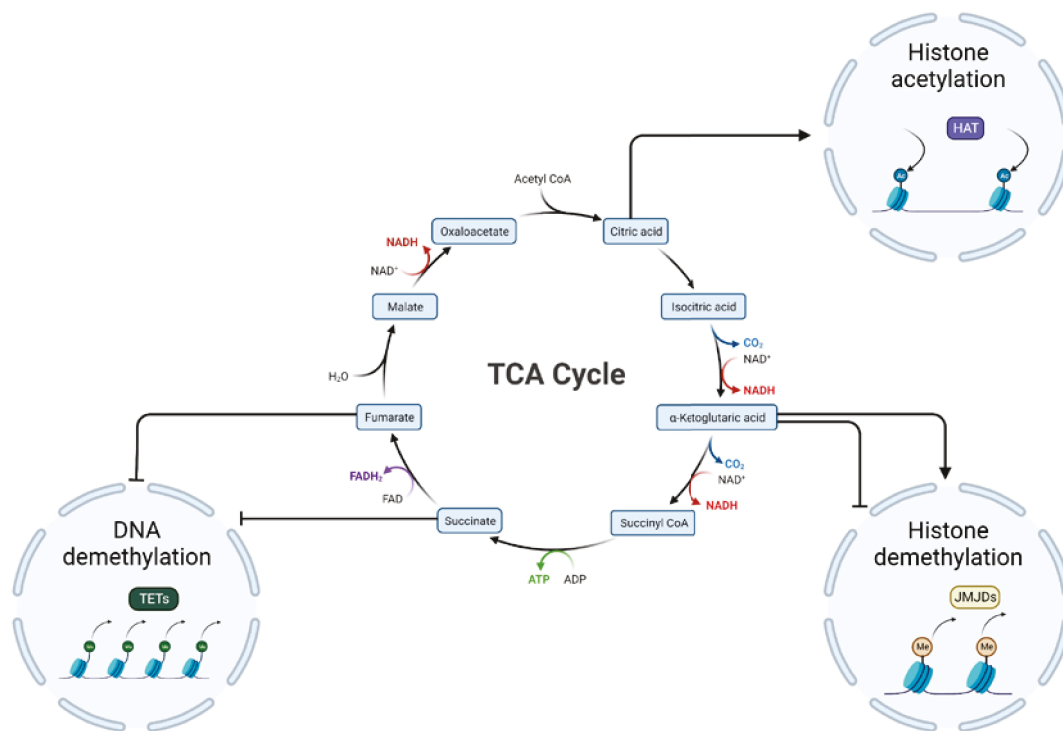


Figure 5: TCA cycle regulation of chromatin modifications and DNA methylation.

TCA cycle activity provides the metabolites essential for the regulation of DNA methylation and chromatin changes. The availability of acetyl-CoA, which provides the acetyl groups, is particularly important for the histone acetylation by histone acetyltransferases (HATs). Citrate exported from the mitochondrial TCA cycle is used by ACLY to synthesize acetyl-CoA in the cytosol. A crucial cofactor for the histone demethylases JMJDs and TET DNA demethylases is α -ketoglutarate (α -KG), succinate, and when they build up, they function as an inhibitor of the process. By blocking histone and DNA demethylases, fumarate can also alter the epigenetic makeup of cells. ACLY, ATP Citrate Lyase; HATs, histone acetyltransferases; JMJDs, Jumonji C domain-containing histone demethylases; TET, ten-eleven translocation enzyme.

1.4.3 Adaptation process in response to altered environment and metabolic memory

The epigenome is able to respond dynamically to environmental changes and there is evidence in both humans and rodents that environmental factors can lead to permanent epigenetic changes at different stages of life. Epigenetic changes can be triggered by various environmental factors such as diet (Mathers et al., 2010), pollution (Christensen and Marsit, 2011), and smoking (Talikka et al., 2012), which can commonly be referred to as "stressors", referring to the neutral, adaptive meaning of the term (Cabib and Puglisi-Allegra, 2012). The resulting aberrations in the epigenome are associated with many diseases, primarily cancer, but also cardiovascular, autoimmune, metabolic, and neurodegenerative diseases, often with particular reference to aging (Jung and Pfeifer, 2015; van Otterdijk et al., 2013). These resulting diseases are associated with permanent metabolic abnormalities (Fernandez-Twinn and Ozanne, 2010) and are referred to as "metabolic programming," and can even cause profound changes in offspring in utero (Rogers, 2019). Analysis of infants born during the

Dutch winter famine found an association between maternal diet and risk of metabolic disorders later in life (Lumey et al., 1993). Another more recent example shows that metabolic memory is recovered in patients with hyperglycemia. Hyperglycemia, characterized by elevated hemoglobin A1c (HbA1c), is a major risk factor for diabetic complications. Despite efforts to control blood glucose levels through diet, exercise, and medications such as insulin, many diabetic patients continue to experience various deleterious complications long after blood glucose levels have normalized, suggesting a "memory" of previous glucose exposure in target cells (Ling and Rönn, 2019; Ouni and Schürmann, 2020).

1.4.3.1 Contribution of epigenetics to metabolic diseases

Aberrations in DNA methylation are an important clinical factor in the understanding, identification, and treatment of a number of diseases. The methylome undergoes large-scale changes not only in the early embryonic development, but also during aging. Age related hypomethylation has been linked to a number of diseases, from autoimmune disease (Urban et al., 2021), cancers (Baylin and Jones, 2016) to endocrine (Kodama et al., 2020), and metabolic disorders, including diabetes mellitus and its complications, obesity, NAFLD, and osteoporosis (Wu et al., 2023).

1.4.3.1.1 *Diabetes mellitus*

Type 2 diabetes mellitus (T2DM) is a complex multifactorial, and chronic endocrine and metabolic disorder, influenced by genetic, epigenetic and environmental factors. It is characterised by several pathological conditions, including insulin resistance, β -cell dysfunction, and elevated hepatic glucose production. Globally, diabetes is one of the leading causes of death according to the World Health Organization (WHO, 2021b) and the estimated prevalence of T2DM is 463 million people in 2019 worldwide, and this figure is projected to rise to 700 million people by 2045 (Saeedi et al., 2019). Although significant advances have been made in the understanding of glucose homeostasis and the pathophysiology of T2DM (Kahn et al., 2014) elaborate molecular mechanisms remains far from clear. Classically, disease related genetics is divided into two categories: monogenic forms, which is inherited in a Mendelian pattern, is typically rare, early-onset and severe and involves either small or large chromosomal deletions or single-gene defects; and polygenic forms (also known as common disease), which is the result of hundreds of polymorphisms that each have a small effect. The most obvious etiological processes may be caused by single gene defects leading to monogenic diabetes, and these have been categorized into the pediatric forms: maturity-onset diabetes of the young (MODY) and neonatal diabetes mellitus (NDM). More than 40 loci have been associated with monogenic diabetes (MODY and NDM). 1-6% of patients with diabetes worldwide have monogenic diabetes (Hattersley et al., 2018) of which 0.4% belong to MODYs (Shields et al., 2017). However, the majority of diabetes cases attributed to type 2 (90–95%) or type 1 (5–10%) with increasing evidence that the interaction between several genetic and

environmental factors contributed to the risk of developing T2DM by causing certain degrees of insulin resistance and pancreatic β -cell dysfunction (Stumvoll et al., 2005). Pearson (Pearson, 2019) stated that individuals who predominantly carry a genetic variation affecting beta cell function will develop diabetes. Concerning polygenetic diabetes, today, there are approximately 400 genetic variants suspected to be associated with diabetes risk, but all share a low odds ratio to account to the overall risk. Therefore, Mahajan et al. (Mahajan et al., 2018) have partitioned 177 diabetes risk variants according to their association with metabolic traits, resulting in six groups of variants each characterized by particular pathophysiology. These different groups with their characteristics raised the potential that external factors, such as behavior and environment are also critical in T2D progression and that DNA sequence alone is not the only determinant of clinical phenotype (Tremblay and Yergeau, 2019). Another rising subclassification of diabetes is divided into 5 groups based on clinical parameters, including GADA, BMI, hemoglobin (HbA1c), age at diabetes onset, measures of beta cell function (HOMA2-B), and insulin resistance (HOMA2-IR) (Ahlqvist et al., 2018), and thus relies heavily on measures that describe the pathogenesis of diabetes, i.e., measures of insulin secretion and action. This type of classification targets the clinical differences between subtypes in order to select a treatment that targets the underlying metabolic defects (Zaharia et al., 2019), and there were already explored different epigenetic patterns associated with future diabetic complications (Ahlqvist et al., 2018; Schrader et al., 2022), which may predict complications in patients with newly diagnosed T2D. Furthermore, researchers have found changes in DNA methylation levels in organs and tissues related to T2D. An epigenetic study revealed increased DNA methylation levels in PGC-1 α promoter of T2D patients in skeletal muscle (Yang et al., 2011). Besides that, another study found decreased insulin receptor substrate 2 (IRS2) expression in the liver of patients with obesity and diabetes compared with participants with obesity but not diabetes. Decreased IRS2 expression is accompanied by DNA methylation at a CpG in IRS2 and increased miRNA hsa-let-7e-5p (let-7e-5p) in liver (Krause et al., 2020). Recently, a large meta-analysis of individual epigenome-wide association studies (EWAS) was performed and explored DNA methylation in blood cells, including leucocyte, lymphocytes, monocytes and granulocytes, in patients with T2D. The authors identified three novel CpGs related to T2D in Europeans. They also discovered 77 T2D-associated differentially methylated regions (DMRs), most of which were hypomethylated in patients with T2D compared with the control groups (Juvinao-Quintero et al., 2021). Taken together, DNA methylation levels occurs in several tissues and organs in diabetes development.

1.4.3.1.2 Metabolic syndrome

Metabolic syndrome (MetS) forms a cluster of metabolic dysregulations including insulin resistance, atherogenic dyslipidemia, central obesity, and hypertension (Nandipati et al., 2017). According to the National Heart, Lung, and Blood Institute (USA), MetS is common in

the United States and about 1 in 3 adults have MetS (NIH.gov, 18.05.2022). Fortunately, the National Health and Nutrition Examination Survey (NHANES) released recent data demonstrating declining numbers of the disease with 24% in men and 22% in women (Swarup et al., 2023), but still the pathophysiology of the MetS encompasses several complex mechanisms that are yet to be fully elucidated. MetS includes insulin resistance, which is associated with abdominal obesity, high blood pressure, glucose intolerance, and increased rates of morbidity and mortality (Nandipati et al., 2017), by themselves distinct pathologies or fall under a common, broader pathogenic process. The underlying mechanisms of MetS are multifaceted, and both genetic and non-genetic factors are critically responsible for the initiation and development of metabolic diseases (Fan and Pedersen, 2021; Hoffman et al., 2021). Emerging evidence indicates that epigenetic regulation plays a crucial role in the occurrence and progression of diverse metabolic diseases (Chiou et al., 2021; Eslam et al., 2018; Hoffman et al., 2021; Ling and Rönn, 2019; Muraca and Cappariello, 2020; Rohde et al., 2019). A causative role can be attributed to high caloric intake, as visceral obesity has been shown to be an important trigger that activates most of the pathways of the MetS (Fathi Dizaji, 2018; Pekgor et al., 2019). Even if glycemia, triglycerides, and HDL are mandatory for the assessment of MetS, other biomarkers have recently been proposed to be linked. In addition to lifestyle and environmental factors such as overeating and physical inactivity, which have been identified as major factors in the development of MetS (Fathi Dizaji, 2018), there were recognised various candidate genes as well, however a common genetic basis could not be identified.

1.4.3.1.3 Obesity

According to the World Health Organization's (WHO) (WHO, 2021a) most recent report, worldwide obesity has nearly tripled since 1975. Overweight people account for more than 1.9 billion (39%) of the adult population, with over 650 million (13%) obese. This enormous increase in obesity rates over the last few decades cannot be explained entirely by genetics. So, obesity is in general reported as a multifactorial disorder with various accelerating genetic and environmental factors. Associated with monogenic obesity, researchers reported mutations in genes encoding multiple components of the melanocortin pathway, including PCSK1 (Jackson et al., 1997), MC4R (Huszar et al., 1997; Vaisse et al., 1998) and POMC (Challis et al., 2004; Krude et al., 1998), all of which were found to result in severe early-onset obesity. More recent studies showed, that defects in single genes of leptin, LEPR, and MC4R are generally responsible for nearly 50% of obesity (Saeed et al., 2020). The influence of polygenic obesity is more common in the general population. In the context of polygenic obesity, the first obesity-prone gene discovered by GWAS in European patients with T2D was Fat Mass and Obesity Associated Gene (FTO) (Frayling et al., 2007; Kalantari et al., 2018). Studies revealed the associations between FTO SNPs and increased intake of dietary fat,

protein, energy, increased appetite, but decreased satiety (den Hoed et al., 2009) and were not associated with physical activity (Loos and Yeo, 2022). Even FTO gene methylation have been associated with childhood obesity and the FTO expression affected waist circumference and body fat in kilogram (Czogala et al., 2021). The importance of other influencing factors and their impact on the epigenome has increasingly shifted the focus of obesity studies towards epigenetic studies. Researchers found higher methylation levels in children with obesity, e.g. in the HIF-3 α gene, which were positively related to the alanine aminotransferase (ALT) levels, which is associated with the development of NAFLD (Wang et al., 2015). More recent, a clinical trial indicated that a specific DNA methylation signature in blood could reflect individual responsiveness to lifestyle intervention and methylation changes in the specific genes could predict to successful weight loss (Krieg et al., 2022). Overall, DNA methylation is associated with the initiation and progression of obesity.

1.4.3.1.4 NAFLD

Nonalcoholic fatty liver disease (NAFLD) is one of the most common causes of liver diseases, and its prevalence continues to increase worldwide (Younossi et al., 2020). The disease is linked to various extrahepatic disorders such as obesity and T2D (Younossi et al., 2016), and cardiovascular complications (Adams et al., 2017). NAFLD affects ~24% of the general population (Younossi et al., 2016) and up to 70% of overweight and more than 90% of morbidly obese people (Younossi et al., 2019) so it became an epidemic in parallel with the obesity epidemic. Although studied intensively, the molecular mechanism of NAFLD development is currently still unknown. At present, a multifactorial theory acquires an increased importance, where the progression of NAFLD and NASH is developed by several hepatic and systemic metabolic alterations as well as genetic susceptibility and environmental factors (Buzzetti et al., 2016; Tilg and Moschen, 2010). Metabolic alterations in adipose tissue and liver play the main role in developing NAFLD (Lee et al., 2023). Interestingly, there are also correlation between DNA methylation and NAFLD. For example, Chen et al. revealed that maternal consumption of a high-fat or high-cholesterol western diet can induce the pathogenesis of NAFLD in male offspring by modulating the expression of the apolipoprotein B (ApoB) gene due to methylation (Chen et al., 2020; Pan et al., 2022), which illustrates the influence of nutrition on epigenetic level. Furthermore, Pan et al reported that hypomethylation of PRKCE and SEC14L3 promoter influence the development of NAFLD (Pan et al., 2022). In this context, our group has shown, that hypomethylation of IGF2BP2 promoter is linked to the degree of hepatic lipid accumulation in mice and humans (Fahlbusch et al., 2022).

1.5 Objectives

Stress increases the risk to develop metabolic diseases, even after stress free recovery. Stress-induced changes and overall energy balance are closely related to mitochondrial function and its regulation of the epigenome (Matilainen et al., 2017). In addition to their established role in bioenergetics and biosynthesis, mitochondria are signaling organelles that communicate fitness to the nucleus and trigger transcriptional programs to adjust homeostasis, which are critical for health and maintenance of energy metabolism in organisms. Recent studies have shown that communication between mitochondria and the epigenome occurs via changes in the concentration of mitochondrial metabolites (Martínez-Reyes et al., 2016).

The present study aimed to investigate the hypothesis whether Cvs alters energy metabolism by affecting mitochondrial function in a tissue-specific manner in skeletal muscle (SM) and/or liver. As mitochondrial efficiency changes can further interfere with epigenetic patterns of DNA methylation and gene regulation, stress-induced metabolic changes could permanently manifest and aggravate in the sense of a *circulum vitiosus*.

Since SM and the liver are important in regulation of energy metabolism homeostasis of the whole organism (Jing et al., 2021), the study is separated into two parts.

The first part aims the identification of immediate effects of chronic variable stress (Cvs) on the regulation of energy metabolism in muscle in the C57BL/6 mouse model and the second part aims to investigate the immediate effect of Cvs on energy balance, which is leading to metabolic adaptations with longitudinal effect on liver gene regulation of C57BL/6 mouse.

The focus of this work is on:

- (a) identifying immediate metabolic changes after chronic stress such as regulation of physical activity, whole-body energy expenditure (EE), respiratory exchange ratio (RER), and glucose and lipid metabolism,
- (b) analysing tissue-specific metabolic adaptations in SM and liver through proteome and *ex-vivo* analyses of physiological pathways and detailed mitochondrial function analyses, to identify relevant modulators of metabolic and energy regulation after stress,
- (c) analyses of differences in methylation and gene regulation, as well as potential mechanisms of metabolic adaptation after stress.

2. MATERIAL & METHODS

2.1 Material

2.1.1 Instruments and devices

Conventional instruments belonging to the standard laboratory equipment are not listed in the Table below.

Table 1: Instruments and devices

| Instruments | Manufacturer (name, location) |
|--|---|
| 4150 TapeStation System | Agilent Technologies, Santa Clara, CA, USA |
| AE31 Trinocular inverted microscope | Motic, Wetzlar, Germany |
| AC 210 Analytical Balance | Sartorius Lab Instruments GmbH & Co. KG, Göttingen, Germany |
| AT261 DeltaRange [®] Analytical Balance | Mettler-Toledo, Columbus, OH, USA |
| Applied Biosystems [®] StepOnePlus Real-Time PCR System | Applied Biosystems [™] by Thermo Fischer Scientific Inc., Darmstadt, Germany |
| Bioplex 200 suspension array system | Bio-Rad Laboratories Inc. Hercules, CA, USA |
| Bioruptor [®] Pico sonication device | Diagenode SA, Seraing, Belgium |
| Centrifuge 5427 R | Eppendorf AG, Hamburg, Germany |
| Centrifuge 5471 R | Eppendorf AG, Hamburg, Germany |
| EchoMRI [®] Body Composition Analyser | EchoMRI [®] , Houston, TX, USA |
| Gas chromatograph 6890N Network GC System | Agilent Technologies, Santa Clara, CA, USA |
| GeneChip [™] Fluidics Station 450 | Applied Biosystems [™] by Thermo Fischer Scientific Inc., Darmstadt, Germany |
| GFL 1083 Shaking Water Bath | GFL Gesellschaft für Labortechnik mbH, Burgwedel, Germany |
| Glucometer and glucose test stripes | Bayer AG, Leverkusen, Germany |
| Heracell [™] 240i CO ₂ incubator | Thermo Fisher Scientific Inc., Darmstadt, Germany |
| Heraeus LaminAir HB 2448 S GS | Thermo Fisher Scientific Inc., Darmstadt, Germany |
| Heraeus [™] Fresco [™] 21 Centrifuge | Thermo Fisher Scientific Inc., Darmstadt, Germany |

| Instruments | Manufacturer (name, location) |
|--|---|
| Heraeus™ Multifuge™ X3 Zentrifuge | Thermo Fisher Scientific Inc., Darmstadt, Germany |
| iMark™ Microplate Reader | Bio-Rad Laboratories Inc. Hercules, CA, USA |
| Infinite® M200 plate reader | Tecan Group Ltd., Männedorf, Switzerland |
| MS 3 basic Vortexer | IKA-Werke GmbH & Co. KG, Staufen, Germany |
| NanoDrop™ 2000/2000c spectrophotometer | Thermo Fisher Scientific Inc., Darmstadt, Germany |
| Neubauer counting chamber | BRAND®, Wertheim, Germany |
| NextSeq550™ | Illumina, San Diego, CA, USA |
| Orbital shaker | Assistent GmbH, Altnau, Switzerland |
| Peristaltic pump | Gilson's MINIPULS® 3, Middleton, USA |
| Phenomaster | TSE systems, Bad Homburg, Germany |
| Power Pac 200 Electrophoresis Power Supply | Bio-Rad Laboratories Inc. Hercules, CA, USA |
| Seahorse XFe24 Analyser | Agilent Technologies Inc., Santa Clara, CA, USA |
| Seahorse XF Prep Station | Agilent Technologies Inc., Santa Clara, CA, USA |
| T100™ thermal cycler | Bio-Rad Laboratories Inc. Hercules, CA, USA |
| Thermomixer compact | Eppendorf AG, Hamburg, Germany |
| TissueLyser | QIAGEN GmbH, Hilden, Germany |
| TissueRuptor II Homogenizer | QIAGEN GmbH, Hilden, Germany |
| Titramax 100 Shaker | Heidolph Instruments GmbH & CO. KG, Schwabach, Germany |
| Universal U 4100 Balance | Sartorius Lab Instruments GmbH & Co. KG, Göttingen, Germany |
| WTW InoLab Serie pH 720 pH meter | Xylem Analytics Germany Sales GmbH & Co. KG, WTW, Weilheim, Germany |
| Qubit™ 4 Fluorometer | Invitrogen™ by Thermo Fisher Scientific Inc., Darmstadt, Germany |

2.1.2 Disposals

Table 2: Disposals

| Disposables | Manufacturer (name, location) |
|---|---|
| Cell culture plates, sterile (6-, 12-, 96-well) | Greiner Bio-One, Frickenhausen, Germany |
| Cell scraper | Sarstedt, Nümbrecht, Germany |
| Clariom™ D Array, mouse Array | Affymetrix™ by Thermo Fischer Scientific Inc., Darmstadt, Germany |
| D1000 ScreenTape | Agilent Technologies Inc., Santa Clara, CA, USA; 5067-5582 |
| Chromatography column FS-FFAP-CB-0.25; Cat. No: 23208330 | CS- Chromatographie Service GmbH, Langerwehe, Germany |
| ClearLine® cell strainers, 70 µm | Kisker Biotech, Steinfurt, Germany |
| Falcon® cell culture dishes, sterile | VWR, Darmstadt, Germany |
| Filter papers | Oehmen, Essen, Germany |
| Filtration unit Stericup® With MILLIPORE | Carl Roth GmbH + Co. KG, Karlsruhe, Germany; X340.1 |
| Greiner centrifuge tubes, 15 ml | Merck KgaA, Darmstadt, Germany; T1943-1000EA |
| Greiner centrifuge tubes, 50 ml | Merck KgaA, Darmstadt, Germany; T2318-500EA |
| High Sensitivity D1000 ScreenTape | Agilent Technologies Inc., Santa Clara, CA, USA; 5067-5584 |
| Injekt®-F syringe, 1 ml | B. Braun Melsungen AG, Melsungen, Germany; 9166017V |
| Injekt® Luer Solo syringe, 20 ml | B. Braun Melsungen AG, Melsungen, Germany; 4606205V |
| Mesh, 125 µm | VWR International GmbH, Darmstadt, Germany; 510-9529 |
| MicroAmp™ Fast Optical 96-Well Reaction Plate, 0.1 ml | Thermo Fischer Scientific Inc., Darmstadt, Germany; 4346907 |
| MicroAmp™ Optical Adhesive Film | Thermo Fischer Scientific Inc., Darmstadt, Germany; 4311971 |
| Micro test plate, 96 well, base shape: conical, PS, transparent | SARSTEDT AG & Co. KG, Nümbrecht, Germany; 82.1583 |

| Disposables | Manufacturer (name, location) |
|--|---|
| MILLEX®AA Syringe Filter Unit, 0.80 µm | Merck KgaA, Darmstadt, Germany; SLAAR33SB |
| PCR SoftTubes, 0.2 ml | Biozym Scientific GmbH, Oldendorf, Germany; 711087X |
| Petri Dish | SARSTEDT AG & Co. KG, Nümbrecht, Germany/83.3902.500 |
| Qubit™ Assay Tubes | Invitrogen™ by Thermo Fisher Scientific Inc., Darmstadt, Germany; Q32856 |
| Seahorse XFe24 FluxPaks | Agilent Technologies Inc., Santa Clara, CA, USA; 102340-100 |
| Seahorse XFe96 FluxPaks | Agilent Technologies Inc., Santa Clara, CA, USA; 102601-100 |
| Semi-micro cuvettes | SARSTEDT AG & Co. KG, Nümbrecht, Germany/67.742 |
| Serological Pipettes 10 ml, wide mouth | JET BIOFIL®, Guangzhou, China; GSP010110 |
| Serological Pipettes 25 ml | JET BIOFIL®, Guangzhou, China; GSP010025 |
| Standard laboratory, normal-caloric chow | Ssniff, Soest, Germany |
| Sterican® cannula G 26 / ø 0,45 x 25 mm | B. Braun Melsungen AG, Melsungen, Germany; 4657683 |
| Surgical blades | VWR, Darmstadt, Germany |
| TissueRuptor Disposable Probes | QIAGEN GmbH, Hilden, Germany; 990890 |
| Whatman Nitrocellulose membrane | Oehmen, Essen, Germany |

2.1.3 Chemicals

Table 3: Chemicals used in the study

| Chemicals | Manufacturer (name, location) |
|---|---|
| 0,5 % Trypsin-EDTA (10x) | Gibco® by Thermo Fisher Scientific Inc., Darmstadt, Germany; 1540054 |
| 1 Kb Plus DNA Ladder | Invitrogen™ by Thermo Fisher Scientific Inc., Darmstadt, Germany; 10787018 |
| 2-[4-(2-Hydroxyethyl)piperazin-1-yl]ethanesulfonic acid (HEPES) | AppliChem GmbH, Darmstadt, Germany; A1069 |

| Chemicals | Manufacturer (name, location) |
|---|--|
| 3-(N-Morpholino)propanesulfonic acid (MOPS) | Merck KGaA, Darmstadt, Germany; M1254 |
| (+)-Etomoxir, sodium salt hydrate, $\geq 98\%$, (HPLC), powder | Merck KGaA, Darmstadt, Germany |
| [^{14}C]-acetate | PerkinElmer Cellular Technologies GmbH, Hamburg, Germany |
| [^{14}C]-palmitic acid | PerkinElmer Cellular Technologies GmbH, Hamburg, Germany |
| Adenosine 5'-diphosphate monopotassium salt dihydrate (ADP) | Merck KGaA, Darmstadt, Germany; A5285 |
| Agarose | peqLab Biotechnologie GmbH, Erlangen, Germany; 35-1020 |
| Albumin Fraction V (BSA), fatty acid-free | Carl Roth GmbH + Co. KG, Karlsruhe, Germany; 0052.3 |
| Albumin Standard (BSA) | Thermo Fischer Scientific Inc., Darmstadt, Germany; 23209 |
| Ambion® Nuclease-Free Water, not DEPC treated, autoclaved, 0.2 μm filtered | Thermo Fischer Scientific Inc., Darmstadt, Germany; AM9930 |
| Antimycin A from Streptomyces sp. | Merck KGaA, Darmstadt, Germany; A8674 |
| Bromphenol Blue | AppliChem GmbH, Darmstadt, Germany |
| Carbonyl cyanide 4-(trifluoromethoxy) phenylhydrazone (FCCP, $\geq 98\%$ (TLC), powder) | Merck KGaA, Darmstadt, Germany |
| Chloroform | Carl Roth, Karlsruhe, Germany |
| Collagen I, rat tail | Advanced BioMatrix, Inc., California, USA |
| Collagenase type IV | Worthington Biochemical Corp., Lakewood, NJ, USA |
| D-Glucose | AppliChem GmbH, Darmstadt, Germany |
| Disodium hydrogen phosphate dihydrate ($\text{Na}_2\text{HPO}_4 \cdot 2\text{H}_2\text{O}$) | Sigma-Aldrich, Darmstadt, Germany |
| Dithiothreitol (DTT) | Sigma-Aldrich, Steinheim, Germany |
| D-Mannitol | AppliChem GmbH, Darmstadt, Germany; A1903 |
| D(+)-Sucrose | AppliChem GmbH, Darmstadt, Germany; A2211 |

| Chemicals | Manufacturer (name, location) |
|---|---|
| Dimethyl sulfoxide (DMSO) | Merck KGaA, Darmstadt, Germany; D8418 |
| Ethylene diamine tetraacetic acid (EDTA) | Serva, Heidelberg, Germany |
| Ethylene glycol-bis(β -aminoethyl ether)-N,N,N',N'-tetraacetic acid (EGTA) | AppliChem GmbH, Darmstadt, Germany; A0878 |
| Ethanol absolute (EtOH _{abs.}) | AppliChem GmbH, Darmstadt, Germany; A1613 |
| Fetal calf serum (FCS) | Biochrom GmbH, Berlin, Germany |
| GlutaMAX™ (100x) | Gibco®, Thermo Fisher Scientific Inc., Darmstadt, Germany |
| Hydrochloric acid (HCl) | Carl Roth, Karlsruhe, Germany |
| Insulin from porcine pancreas | Sigma-Aldrich, Darmstadt, Germany |
| L-Ascorbic acid | Merck KGaA, Darmstadt, Germany; 1831 |
| L-Glutamine | Sigma-Aldrich, Darmstadt, Germany |
| L-(-)-Malic acid | Merck KGaA, Darmstadt, Germany; 02288 |
| Malonic acid | Merck KGaA, Darmstadt, Germany; M1296 |
| Magnesium chloride hexahydrate (MgCl ₂ 6H ₂ O) | AppliChem GmbH, Darmstadt, Germany/A1036 |
| Magnesium sulfate (MgSO ₄) | Serva Electrophoresis GmbH, Heidelberg, Germany; 28311 |
| Oligomycin from <i>Streptomyces diastatochromogenes</i> | Merck KGaA, Darmstadt, Germany |
| Percoll gradient (Easycoll) | Biochrom GmbH, Berlin, Germany |
| Potassium chloride (KCl) | Merck, Darmstadt, Germany |
| Potassium dihydrogen phosphate (KH ₂ PO ₄) | Merck KGaA, Darmstadt, Germany; 104873 |
| Potassium hydroxide (KOH) | AppliChem GmbH, Darmstadt, Germany; A1575 |
| Pyruvic acid | Merck KGaA, Darmstadt, Germany; 107360 |
| Rat tail type-I collagen stock (4 mg/ml) | CellSystems®, Troisdorf, Germany |
| Rotenone, $\geq 95\%$ | Merck KGaA, Darmstadt, Germany |
| Rotiszint® eco plus | Carl Roth, Karlsruhe, Germany |
| Sodium acetate | AppliChem GmbH, Darmstadt, Germany |
| Sodium bicarbonate (NaHCO ₃) | Merck KGaA GmbH, Darmstadt, Germany |
| Sodium chloride (NaCl) | Carl Roth, Karlsruhe, Germany |
| Sodium deoxycholate | AppliChem GmbH, Darmstadt, Germany |

| Chemicals | Manufacturer (name, location) |
|---|---|
| Sodium dihydrogen phosphate monohydrate (NaH ₂ PO ₄ H ₂ O) | Sigma-Aldrich, Darmstadt, Germany |
| Sodium dodecyl sulfate (SDS) | AppliChem GmbH, Darmstadt, Germany |
| Sodium pyruvate (100 mM) | Gibco®, Thermo Fisher Scientific Inc., Darmstadt, Germany |
| Succinic acid | Merck KgaA, Darmstadt, Germany; S3674 |
| N, N, N', N'-Tetramethyl-p-phenylenediamine (TMPD) | Merck KgaA, Darmstadt, Germany; 100-22-1 |
| Tris-Borat-EDTA (TBE), 10x | Thermo Fisher Scientific Inc., Darmstadt, Germany |
| Tris(hydroxymethyl)aminomethane (TRIS) | Carl Roth, Karlsruhe Germany |
| Tris-HCl | AppliChem GmbH, Darmstadt, Germany |
| Triton X-100 | Roche Diagnostics, Mannheim, Germany |
| Trypan blue solution (0.4%) | Sigma Aldrich, St Louis, MO, USA |
| Tween® 20 | AppliChem GmbH, Darmstadt, Germany |

2.1.4 Buffers and solutions

Table 4: Buffers and solutions

| Name | Composition | Final concentration/volume |
|--|----------------------------------|----------------------------|
| 2x Mitochondrial Assay Solution (MAS) pH adjusted to 7.4 with KOH | Sucrose | 140 mM |
| | Mannitol | 440 mM |
| | KH ₂ PO ₄ | 20 mM |
| | MgCl ₂ | 10 mM |
| | HEPES | 4 mM |
| | EGTA | 2 mM |
| | Fatty-acid free BSA | 0.4% |
| 5x DNA loading dye | Sucrose (w/v) | 50% |
| | 0.5x TBE buffer | 50% |
| | Bromophenol blue | 0.25% |
| 1X Phosphate-Buffered Saline (PBS) | NaCl | 137 mM |
| | KCl | 2.7 mM |
| | Na ₂ HPO ₄ | 8 mM |
| | KH ₂ PO ₄ | 2 mM |
| Chappel-Perry buffer I (CPI) | KCl | 100 mM |

| Name | Composition | Final concentration/volume |
|---|--|----------------------------|
| (Muscle mitochondria isolation buffer I) pH adjusted to 7.4 with NaOH | MOPS | 50 mM |
| | EDTA | 1 mM |
| | MgSO ₄ | 5 mM |
| Chappel-Perry buffer I (CPII) | KCl | 100 mM |
| (Muscle mitochondria isolation buffer II) pH adjusted to 7.4 with NaOH | MOPS | 50 mM |
| | EDTA | 1 mM |
| | MgSO ₄ | 5 mM |
| | Fatty-acid free BSA | 0.5% |
| Hanks balanced salt solution (HBSS) pH adjusted to 7.4 with NaOH | KCl | 5.33 mM |
| | KH ₂ PO ₄ | 0.44 mM |
| | Na ₂ HPO ₄ | 0.34 mM |
| | NaCl | 138 mM |
| | NaHCO ₃ | 4.17 mM |
| | Glucose | 5.56 mM |
| | EGTA | 0.5 mM |
| | HEPES | 25 mM |
| Liver mitochondrial isolation buffer pH adjusted to 7.2 with KOH | Sucrose | 70 mM |
| | Mannitol | 210 mM |
| | HEPES | 5 mM |
| | EGTA | 1 mM |
| Low TE pH adjusted to 7.5 with HCl | Tris/HCl | 10 mM |
| | EDTA | 0.1 mM |
| Percoll gradient 90% | Percoll | 90% |
| | 10x PBS | 10% |
| Seahorse lysis buffer pH adjusted to 7.5 with NaOH | Tris/HCl | 10 mM |
| | Na ₂ HPO ₄ 2H ₂ O | 10 mM |
| | NaH ₂ PO ₄ H ₂ O | 10 mM |
| | NaCl | 130 mM |
| | Na ₄ P ₂ O ₇ 10H ₂ O | 10 mM |
| | Triton X-100 | 1% (v/v) |

2.1.5 Cell culture and assay medium

Table 5: Used cell culture and assay media

| Name | Base | Composition | Final concentration |
|---|--|--|---|
| Collagenase medium | DMEM, glucose | low 1x Antimycotic mix Collagenase IV | Antibiotic- 2% (v/v) 100 U/ml |
| Dulbecco's modified Eagle's (DMEM) | DMEM, glucose, glutamine, phenol red, sodium pyruvate and sodium bicarbonate, powder | w/o L- | 1x |
| Dulbecco's modified Eagle's (DMEM) | DMEM | Glucose Pyruvate HEPES | 5.5 mM 1 mM 25 mM |
| DMEM/F-12, GlutaMAX™ Supplement | DMEM | w/o HEPES | 1x |
| DMEM/F-12 | DMEM | w/o phenol red | 15 mM |
| Dulbecco's Phosphate Buffered Saline (DPBS) | DMEM, CaCl ₂ , MgCl ₂ | w/o and | 10x |
| FAO assay medium | DMEM/F-12, GlutaMAX™ Supplement | 1x Antimycotic mix BSA Fraction V fatty acid free Sodium pyruvate L-Carnitine ¹⁴ C-palmitate | Antibiotic- 2% (v/v) 10 μM 1 mM 1 μM 2.6 μM |
| Glucose production medium | | 1x Antimycotic mix | Antibiotic- 2% (v/v) |

| | | | | |
|---|--|-----------------|----------------------------|--|
| Isolation medium | DMEM, low glucose | FCS 1x | Antibiotic-Antimycotic mix | 10% (v/v) 2% (v/v) |
| | | | Sodium pyruvate | 1 mM |
| | | | Porcine insulin | 1.1 μ M |
| | | | Dexamethasone | 1 μ M |
| Mito stress assay medium (Seahorse), pH adjusted to 7.4 with NaOH | DMEM, w/o glucose, L-glutamine, phenol red, sodium pyruvate and sodium bicarbonate, powder | L-Glutamine | | 2 mM |
| | | Sodium pyruvate | | 1 mM |
| | | Glucose | | 10 mM |
| Plating medium | DMEM/F-12, GlutaMAX™ Supplement | FCS 1x | Antibiotic-Antimycotic mix | 10 % (v/v) 1.5 mM 0.1 μ M 1 μ M |
| | | | | 2% (v/v) |
| Serum-free medium | DMEM/F-12, GlutaMAX™ Supplement | 1x | Antibiotic-Antimycotic mix | 2% (v/v) |
| | | | Sodium pyruvate | 1 mM |

2.1.6 Commercial kits

Table 6: Used commercial kits

| Kits | Manufacturer (name, location) |
|---|--|
| Bio-Plex Pro™ Mouse Diabetes 8-plex | Bio-Rad Laboratories Inc. Hercules, CA, USA; 171F7001M |
| Citrate Synthase Assay Kit | Merck KGaA, Darmstadt, Germany; CS0720 |
| Corticosterone Double Antibody I ¹²⁵ RIA kit | MP Biomedicals, Orangeburg, NY, USA; 0712010-CF |
| Cytochrome c Oxidase Assay Kit | Merck KGaA, Darmstadt, Germany; CYTOCOX1 |

| Kits | Manufacturer (name, location) |
|---|---|
| DNeasy® Blood & Tissue Kit | QIAGEN GmbH, Hilden, Germany; 69504 or 69506 |
| EpiXplore™ Methylated DNA Enrichment Kit | Takara Bio Europe, Saint-Germain-en-Lage, France; 631962 |
| GeneChip™ Hybridization Control Kit | Thermo Fisher Scientific Inc., Darmstadt, Germany; 900454 |
| GeneChip™ Poly-A RNA Control Kit | Thermo Fisher Scientific Inc., Darmstadt, Germany; 900433 |
| GeneChip™ WT Amplification Kit | Thermo Fisher Scientific Inc., Darmstadt, Germany; 902224 |
| GeneChip™ WT Terminal Labeling Kit | Thermo Fisher Scientific Inc., Darmstadt, Germany; 900671 |
| GeneChip™ WT PLUS Reagent Kit | Thermo Fisher Scientific Inc., Darmstadt, Germany; 902281 |
| Glucose Assay Kit | Sigma-Aldrich, Darmstadt, Germany; MAK263 |
| Glutamate Assay Kit | Sigma-Aldrich, Darmstadt, Germany; MAK330 |
| GoTaq® qPCR Master Mix | Promega, Heidelberg, Germany; A6101 |
| OxiSelect TBARS Assay Kit (MDA Quantification) | Cell Biolabs, Inc., USA, STA-330 |
| Lactate Assay Kit | Sigma-Aldrich, Darmstadt, Germany; MAK064 |
| miRNeasy RNA mini kit | QIAGEN, Hilden, Germany; 217084 |
| MTase-Glo™ Methyltransferase Assay | Promega, Heidelberg, Germany; V7601 |
| NAD ⁺ /NADH-Glo™ Assays | Promega, Heidelberg, Germany; G9071 |
| NEBNext® Enzymatic Methyl-seq Kit | New England BioLabs® Inc., Frankfurt a. M., Germany; E7120 |
| NEBNext® Ultra™ II DNA Library Prep Kit for Illumina® | New England BioLabs® Inc., Frankfurt a. M., Germany; E7645S/L or E7103S/L |
| NextSeq 500/550™ High Output Reagent Kit (300-cycles) | Illumina, San Diego, CA, USA; FC-420-1003 |
| Pierce™ BCA Protein Assay Kit | Thermo Fisher Scientific Inc., Darmstadt, Germany; 23227 |
| SIRT-Glo™ Assay | Promega, Heidelberg, Germany; G6450 |

| Kits | Manufacturer (name, location) |
|---|--|
| Triglyceride Quantification Kit | Sigma-Aldrich, Darmstadt, Germany; MAK044 |
| qPCR Mastermix | Kaneka Eurogentec S.A., Seraing, Belgium |
| Qubit™ dsDNA BR (broad range) Assay Kit | Invitrogen™ by Thermo Fisher Scientific Inc., Darmstadt, Germany; Q32850 or Q32853 |
| Qubit™ 1x dsDNA HS (high sensitivity) Assay Kit | Invitrogen™ by Thermo Fisher Scientific Inc., Darmstadt, Germany; Q33230 or Q33231 |
| Randox Triglycerides | RANDOX Laboratories, Antrim, United Kingdom; TR1697 |
| β-hydroxybutyrate Assay Kit | Sigma-Aldrich, Darmstadt, Germany; MAK041 |

2.1.7 Oligonucleotides

Table 7: Oligonucleotides for qPCR

| Target | Probe | Forward 5'->3' | Reverse 5'->3' |
|----------------|-------------------------|--------------------------|--------------------------|
| MT-ND 1 | CCAATACGCCCTTTAACAACCTC | CTACAACCATTTGCAGACGC | GGAAGTCATAGACTTAATGCT |
| LPL | CTTTGAGTATGCAGAAGCCC | GGTTTGGATCCAGCTGGGCC | GATCCAATACTTCGACCAGG |

2.1.8 Software

Table 8: Software

| Software | Version | Distributor |
|--|----------------|------------------------------|
| BaseSpace Sequence Hub | | Illumina, San Diego, CA, USA |
| BioRender | | © 2023 BioRender |
| bcl2fastq2 | 2.20 | Illumina, San Diego, CA, USA |
| Conversion Software | | |
| DRAGEN Germline pipeline | 3.2.8 | Illumina, San Diego, CA, USA |
| DRAGEN Methylation pipeline | 3.9.5 | Illumina, San Diego, CA, USA |
| DRAGEN Reference builder | 3.10.4 | Illumina, San Diego, CA, USA |
| FastQ toolkit pipeline | 1.0.0 | Illumina, San Diego, CA, USA |
| FastQ raw data analyses | | Illumina, San Diego, CA, USA |
| Galaxy (http://galaxyproject.org) | | Taylor et al., 2007 |
| Galaxy SamTools | | Li, H. et al., 2009 |

| Software | Version | Distributor |
|---|----------|--|
| GO enrichment analyses (http://www.pantherdb.org) | | Paul, D et al., 2022 and Huaiyu, Mi et al., 2019 |
| GraphPad Prism | 9.4.0 | GraphPad software Inc, San Diego, CA, USA |
| Illumina Dragen® Bio-IT platform | 3.9.5 | Dico Genome, Illumina, San Diego, CA, USA |
| Integrated Genome Browser | 9.1.6 | Freese et al., 2016 |
| Integrative Genome Viewer | 2.8.13 | Broad Institute and the Regents of the University of California, USA |
| Ingenuity® Pathway Analysis (IPA®) | | Krämer, A et al., 2014 |
| NanoDrop 2000/2000c | 1.6.198 | Thermo Fisher Scientific Inc., Darmstadt, Germany |
| Proteome Discoverer™ | 2.5 | Thermo Fisher Scientific Inc., Darmstadt, Germany |
| R/Bioconductor package CHIPseeker | 1.18.0 | Yu, G et al., 2015 |
| R package MeDIP | | Lienhard M et al., 2014 |
| R package MethylKit | | BaseSpaceLabs, Illumina San Diego, CA, USA (Akalin et al., 2012) |
| Spectronaut™ Pulsar software | 17 | Biognosys AG, Zuerich, Switzerland |
| TapeStation Software Analysis | 3.2 | Agilent Technologies Inc., Santa Clara, CA, USA |
| TapeStation Controller Software | 3.2 | Agilent Technologies Inc., Santa Clara, CA, USA |
| Transcriptome Analysis Console™ | 4.01 | Thermo Fisher Scientific Inc., Darmstadt, Germany |
| Tecan i-control | 1.6.19.0 | Tecan Group Ltd., Männedorf, Switzerland |
| Wave | 2.6.0 | Agilent Technologies, Santa Clara, CA, USA |

2.2 Methods

2.2.1 Animals

In this work, we studied male twelve-week-old C57BL/6 mice housed (5-6 animals per cage) under standard laboratory conditions (12h light/12h dark, 22-24°C, ad libitum access to tap water and standard chow (rat/mouse extrudate; 58% carbohydrate, 9% fat, 33% protein (ssniff Spezialdiäten GmbH, Soest, Germany)). All experiments were approved (LANUV, NRW, Germany (81-02.04.2017.A421)) and performed in accordance with the German Animal Welfare Act and the 'Principle of Laboratory (NIH Publication No. 85-23, revised 1996).

2.2.2 Experimental design

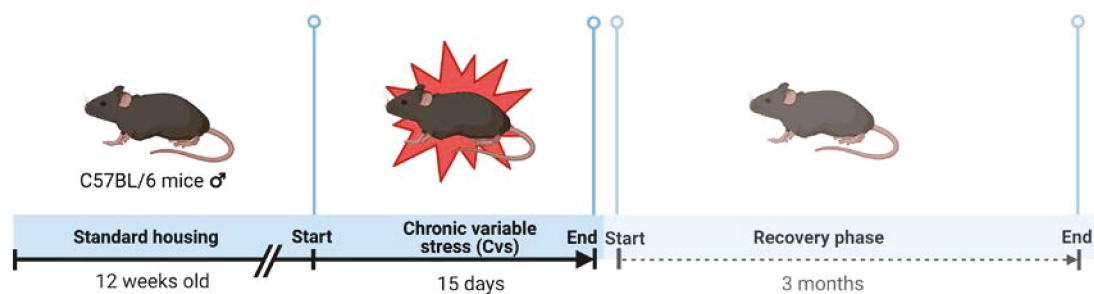


Figure 6: Experimental design.

C57BL/6 mice at age of 12 weeks underwent our Chronic variable stress (Cvs) protocol for 15 days. An additional cohort of mice experienced after Cvs intervention a 3-month recovery phase.

At age of 15 weeks (acute) or 27 weeks (recovery), mice were sacrificed by CO₂ asphyxiation, blood was collected by cardiac puncture. Muscle (*M. gastrocnemius*) and liver biopsies were immediately used for cell fractioning (600xg, 10,000xg, 11,000xg fraction) according to our established protocol (2.2.6.1, 2.2.6.2). Remaining biopsy material and EDTA-plasma was snap frozen at -80°C for nucleotide analyses.

In order to generate and analyse the amount of data per tissue, multiple cohorts were used and analysed for this work. The multiple cohorts with the same background of the Cvs protocol were also used to verify the reproducibility of the experimental setting, as well as to validate whether the experimental setting is identical.

2.2.2.1 Muscle analysis

For muscle analyses two experimental cohorts were used: 1. for body composition (n=6 animals per group); 2. for indirect calorimetry, plasma analyses, tissue analyses and nucleotide analyses (n=6 animals per group).

2.2.2.2 Liver analysis

For liver analyses, four experimental cohorts were used: 1. for indirect calorimetry and acute analyses in primary hepatocytes (n=5 animals per group); 2. for body composition and liver tissue data including acute methylome and transcriptome (acuteCvs; acuteCtrl) (n=6 animals per group); 3. for methylation and transcriptional analyses after a 3-month recovery phase (recoveryCvs; recoveryCtrl) (n=3-5 animals per group); 4. for analyses in primary hepatocytes after the recovery phase (n=5 animals per group). Dr. M. Dille, (Institute of Clinical Biochemistry at the German Diabetes Center) applied the Cvs protocol to the recovery cohorts 3 and 4. Dr. M. Dille collected liver biopsies stored at -80°C of cohort 3, and performed mitochondrial respiration and glycolysis analysis in the Seahorse XF assay (2.2.8.5) on primary hepatocytes (2.2.8.1) of cohort 4.

In this thesis, stored biopsies of cohort 3 were used for transcriptome and methylation analyses. The data interpretation on energetic flexibility of hepatocytes, i.e. energy map (2.2.8.5) (unpublished data) was performed as part of this thesis based on data collected from cohort 4 as part of a previous project (Dille, Nikolic et al. 2022).

2.2.3 Cvs protocol

Animals were subjected to our established chronic variable stress (Cvs) protocol (Castañeda et al., 2015; Dille et al., 2022). Briefly, animals were exposed to 2 stressors per day over a 15-day period in alternating order. The protocol provides a varied stress exposure to avoid adaptations. Following, the list of stressors:

- Warm swim 20 min swimming in 30°C warm water
- Cold exposure 1 h cold exposure at 4°C in individual cages without bedding
- Shaking 1 h shaking at 100 rpm
- Restraint 30 min restrain in a 50 ml tube with a hole to enable breathing
- Overnight isolation individual o/n isolation in large cages with ad libitum access to food and water

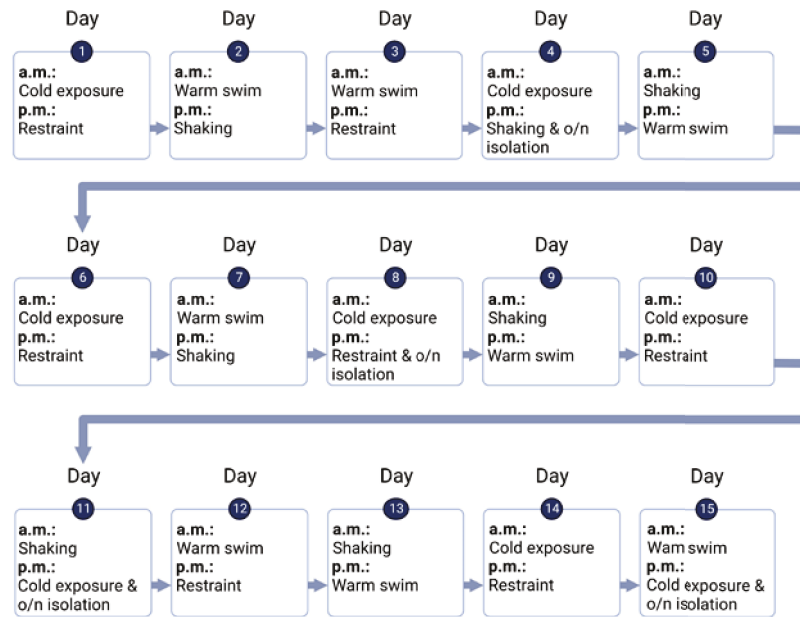


Figure 7: Time schedule of Cvs protocol.

Time course of the individual stress interventions per day and time of the day.

2.2.4 *In vivo* analyses

2.2.4.1 Indirect calorimetry

The energy expenditure (EE), respiratory exchange ratio (RER), spontaneous physical activity (SPA) and the food intake of the animals were measured using customized metabolic cages (PhenoMaster, TSE Systems, Bad Homburg, Germany). After a 24 h acclimation period of the mice, every 30 min for 72 h for two complete circadian cycles (48 h) the SPA measurements were taken with a non-invasive infra-red based light beam system, the O_2 consumption (VO_2) and CO_2 production (VCO_2) were measured starting with the light phase (n=5 animals per group). Animals had unrestricted access to food and water at a temperature of 22°C. Feed intake was determined with weighing sensors. The RER were automatic calculated by the system with the following formula:

$$RER = VCO_2 / VO_2 \text{ (Weir, 1949).}$$

Energy expenditure (EE) were calculated from the VO_2 normalized by body surface:

$$EE = VO_2 / kg^{0.75} \text{ (Rubner, (1883)).}$$

The carbohydrate oxidation rate (CHO) was calculated with the following formula:

$$CHO \text{ [g/min]} = 4.585 \times VCO_2 \text{ (L/min)} - 3.226 \times VO_2 \text{ (L/min)} \text{ (Péronnet and Massicotte, 1991).}$$

The fatty acid oxidation rate (FAO) was calculated with the following formula:

$$FAO \text{ [g/min]} = 4.585 \times VCO_2 \text{ (L/min)} - 3.226 \times VO_2 \text{ (L/min)} \text{ (Péronnet and Massicotte, 1991).}$$

2.2.4.2 Nuclear magnetic resonance (NMR)

Body composition was assessed with nuclear magnetic resonance (NMR) using an EchoMRI® Body Composition Analyser (EchoMRI®, Houston, TX, USA). Mice were analysed for determining lean mass and fat mass. The essence of quantitative magnetic resonance is the production of a sequence of radio pulses and subsequent recording of nuclear magnetic resonance responses (NMR echoes) by a scan. The transmitted sequence is composed of certain periodic Carr-Purcell-Meiboom-Gill parts (CPMG segments), which are separated by pauses varying in duration. The characteristic NMR echoes are specific for lean mass, fat mass or free water. The mentioned body's basic substances differ in relaxation rate which is then utilized for the calculation of the amount of fat mass, lean mass and free water via linear regression (Kovner et al., 2010). The used EchoMRI® Body Composition Analyser was calibrated by canola oil and used as recommended by the manufacturer.

2.2.4.3 Intraperitoneal glucose tolerance test (i.p. GTT)

To analyse an impaired glucose metabolism an i.p. GTT was performed. 6 h fasted Ctrl and Cvs mice were injected intraperitoneally with glucose solution (2 g glucose/kg body weight). During the experiment, the animals were single housed in fresh cages with *ad libitum* access to water. The blood glucose was monitored before and after 15, 30, 60, and 120 min after glucose injection. The individual blood glucose was determined with a commercially available glucometer (Contour, Bayer AG, Leverkusen, Germany). The area under the curve (AUC) was calculated by the sum of all trapezoid areas. Each trapezoid between each time point were calculated by the formula for calculating area of a trapezoid = (Sum of 2 vertical sides) / 2 x (Base of trapezoid).

Accordingly, calculation of the AUC of an i.p. GTT was done by

$$\text{AUC} = \sum (\text{Sum of 2 blood glucose values}) / 2 \times (\text{timespan between these measuring points}).$$

2.2.4.4 Intraperitoneal pyruvate tolerance test (i.p. PTT)

The i.p. PTT is a variant of the i.p. GTT to assess gluconeogenesis. Ctrl and Cvs mice were fasted for 16 h to clear all glucose and glycogen storage. After fasting a pyruvate solution (1.5 g pyruvate/kg body weight) was injected and at the time point 0, 15, 30, 60, and 120 min the blood glucose was measured from the tail tip with a commercially available glucometer (Contour, Bayer AG, Leverkusen, Germany). During the experiment the animals were single housed with *ad libitum* access to water. Calculation of AUC for i.p. PTT is described in i.p. GTT (2.2.4.3).

2.2.5 *Ex vivo* analyses in plasma

At age of 15 weeks (acute) or 27 weeks (recovery), Ctrl and Cvs mice were sacrificed by CO₂ asphyxiation. Thereafter, mice were doused with 70 % ethanol and subjected to laparotomy. Severing the diaphragm enabled access to the thorax for cardiopuncture. The blood was aspirated with needles, syringes and transferred to tubes, which were previously rinsed with 0.5 M EDTA in order to prevent coagulation. Whole-blood was inverted several times and centrifuged at 2,600xg for 10 min at 4°C. Plasma was then removed, transferred to fresh tubes and plasma as well as blood clot were stored at -80°C.

2.2.5.1 Determination of corticosterone

Corticosterone levels in plasma were determined by a radioimmunoassay according to manufacturer's instructions (Corticosterone Double Antibody I¹²⁵ RIA kit; MP Biomedicals, Orangeburg, NY, USA).

2.2.5.2 Determination of glucose

Glucose levels in plasma were determined by kit-colorimetric based assay according to the manufacturer's instructions (Glucose Assay Kit with a range of 2-10 nmole, Sigma-Aldrich, Darmstadt, Germany).

2.2.5.3 Determination of lactate

Lactate levels in plasma were determined by kit-colorimetric based assay according to the manufacturer's instructions (Lactate Assay Kit with a range of 0.2–10 nmole, Sigma-Aldrich, Darmstadt, Germany).

2.2.5.4 Determination of glutamate

Glutamate levels in plasma were determined by kit-colorimetric based assay according to the manufacturer's instructions (Glutamate Assay Kit, Sigma-Aldrich, Darmstadt, Germany).

2.2.5.5 Determination of triglyceride (TAG)

TAG levels in plasma were determined by kit-colorimetric based assay according to the manufacturer's instructions (Triglyceride Quantification Kit with a range of 2 pmole – 10 nmole, Sigma-Aldrich, Darmstadt, Germany).

2.2.5.6 Measurement of metabolic hormones

A commercially available multiplex bead-based immunoassay (Bio-Plex Pro™ Mouse Diabetes 8-plex; Bio-Rad Laboratories Inc. Hercules, CA, USA) was used to determine plasma levels of leptin, glucagon and insulin.

2.2.5.7 Analyses of fatty acid composition

For determination of fatty acid composition, an experimental approach involving gas chromatography was conducted. The analysis in this work was conducted in house with plasma samples of Ctrl and Cvs mice. Plasma samples were handed to the Proteomics Core Facility (Head: Dr. S. Lehr) of the Institute of Clinical Biochemistry at the Germany Diabetes Center and analyses of fatty acid composition were conducted by Martina Schiller. Analyses raw data were returned for analyses.

0.2 ml plasma was incubated with 50 μ l pentadecanoic acid ([1 μ g/ μ l] in n-hexane) in 1 ml 1M methanolic NaOH (4 g NaOH pellets dissolved in 100 ml methanol (MeOH)) for 60 min at 90°C in a water bath to saponify the fatty acids in the sample. After the samples had reached room temperature they were transferred to glass reaction tubes and supplemented with 4 ml n-hexane. Samples were vortexed for 30 sec and subsequently centrifuged for 5 min at 1,400xg. The upper hexane phase was discarded. The lower phase was neutralized with 1 M HCl. 4 ml n-hexane were added and the samples were vortexed. After centrifugation for 5 min at 1,400xg, 3 ml of the upper organic phase were transferred to a reaction tube. The total volume was evaporated with N₂ at 40°C. Next, 110 μ l derivatization solution of MeOH (100%) with 0.9 M acetyl chloride were added to each sample and tubes were incubated for 30 min at 90°C. After cooling, the samples were evaporated completely with N₂ at 50-60°C. Thereafter, samples were reconstituted in 500 μ l n-hexane by vortexing. 1 μ l of derivatized fatty acid was injected into the gas-liquid chromatography system (Agilent Technologies 6890N) equipped with fused silica capillary column (FS-FFAB-CB-0.25; CS - Chromatographie Service GmbH, Langerwehe, Germany) and a flame ionization detector (FID). Nitrogen was used as the carrier gas at a flow rate of 4 ml/min. The injector block and detector were maintained at 250°C. The column temperature was initially set at 100°C and then increased to 220°C at a rate of 2°C/min.

2.2.6 *Ex vivo* analyses in muscle and liver

Muscle and liver biopsies were immediately used for cell fractioning (600xg, 10,000xg or 11,000xg fraction) according to our established protocol (2.2.6.1, 2.2.6.2). All *ex vivo* experiments were conducted in muscle and liver tissue from Ctrl and Cvs mice directly after the Cvs intervention.

2.2.6.1 Preparation of cellular fractions (600xg and 10,000xg) of muscle tissue

After CO₂ asphyxiation, both *Musculi gastrocnemius* (*M. gastrocnemius*) were dissected from the hind limb after skin removal. At the *Achilles tendon*, sharp scissors were inserted to separate the tendon from the bone and further separation of the hind limb muscle from the tibia and fibula bones up to the knee joint. After the *gastrocnemius* muscle was cut loose, it was isolated from the internal *soleus muscle*. Finally, tendon remnants were removed. Weight

of isolated gastrocnemius muscle from the left hind limb was measured and (partially) used for mitochondrial cellular fractioning. The *M. gastrocnemius* was used as a representative tissue for skeletal muscles.

10,000xg cellular fractions were isolated from gastrocnemius muscle of Ctrl and Cvs mice. The main target was to achieve functional and intact mitochondria from both tissues for maximum analyses and minimum use of laboratory animals. A protocol for muscle mitochondria isolation was established within this study based on the mitochondrial isolation protocol by Bharadwaj et al. (Bharadwaj et al., 2015). Fresh 100 mg muscle tissue was immersed in ice-cold 1x PBS and then minced into >10 mg pieces, washed and immersed again in ice-cold 1x PBS. The minced muscle pieces were incubated with 1 ml CPI buffer and 0.05% trypsin for 7.5 min at room temperature and then transferred on ice. The minced muscle pieces were homogenized with TissueRuptor II Homogenizer (QIAGEN, Hilden, Germany) with a pulse of 2 sec and of 8-times stroke at lowest stage. The homogenized muscle was then washed with equal volume of CPI buffer (1 ml) and 2x volumes of CPII buffer. The content was collected and centrifuged at 600xg for 10 min at 4°C. Pellet was frozen away at -20°C and the supernatant was passed through a fine gauze. Then the filtrate was centrifuged at 10,000xg for 10 min at 4°C. Pellets were suspended in 1 ml of CPII buffer and again centrifuged at 10,000xg for 10 min at 4°C. Pellet was suspended in 200 µl CPI buffer.

2.2.6.2 Preparation of cellular fractions (600xg and 11,000xg) of liver tissue

The liver located in the upper right abdominal cavity was dissected under special diligence to not injure the gallbladder. Subsequent to determination of total weight, the liver was divided into pieces, whereby one was immediately used for mitochondrial cellular fractioning.

11,000xg cellular fractions were isolated from liver tissue of Ctrl and Cvs mice. The main target was to achieve functional and intact mitochondria from both tissues for maximum analyses and minimum use of laboratory animals. Based on the established muscle mitochondria enriched cellular fraction isolation protocol, the liver protocol was established. Fresh 200 mg of liver tissue was used and immersed in ice-cold isolation buffer. Then liver tissue was minced in to <10 mg pieces and washed in fresh and ice-cold isolation buffer. Minced liver tissue was transferred to 1 ml isolation buffer and homogenized with TissueRuptor II Homogenizer (QIAGEN GmbH, Hilden, Germany) with a pulse of 2 sec and a stroke of 2-times at lowest stage. Then the homogenate was centrifuged at 600xg for 20 min at 4°C. Pellet was discarded. Supernatant was again centrifuged at 11,000xg for 20 min at 4°C. Supernatant was discarded and pellet was suspended in 200 µl isolation buffer.

2.2.6.3 Determination of beta-hydroxybutyrate from liver tissue

Beta-Hydroxybutyrate levels from liver tissue were determined by kit-colorimetric based assay according to the manufacturer's instructions (Beta-Hydroxybutyrate Assay Kit, Sigma-Aldrich, Darmstadt, Germany).

2.2.6.4 Determination of glucose from liver tissue

Glucose levels from liver tissue were determined by kit-colorimetric based assay according to the manufacturer's instructions (Glucose Assay Kit with a range of 2-10 nmole, Sigma-Aldrich, Darmstadt, Germany).

2.2.6.5 Determination of triglyceride (TAG) from liver tissue

Triglyceride (TAG) levels from liver tissue were determined by kit-colorimetric based assay according to the manufacturer's instructions (Triglyceride Quantification Kit with a range of 2 pmole - 10 nmole, Sigma-Aldrich, Darmstadt, Germany).

2.2.6.6 Analysis of flavin adenine dinucleotide (FAD) content in 11,000xg cellular fractions of liver

Flavin Adenine Dinucleotide (FAD) was determined as the cofactor of an oxidase which catalyze the formation of a product that reacts with OxiRed probe and generates fluorescence by the Flavin Adenine Dinucleotide (FAD) assay kit (FAD Assay Kit, Abcam, Germany) in 11,000xg cellular fractions of liver. 10 µg of 11,000xg were utilized and pre-processed by deproteinization. FAD detection was performed according to manufacturer's instructions and fluorescence by using Tecan Infinite 200 reader (Tecan Group Ltd., Männedorf, Switzerland).

2.2.6.7 Analysis of nicotinamide dinucleotide (NAD) content in 11,000xg cellular fractions of liver

The ratio of oxidized NAD⁺ and reduced NADH were determined by NAD⁺/NADH-Glo™ Assay (Promega, Heidelberg, Germany) by separated measurements of each molecule in 11,000xg cellular fractions of liver tissue. The assay benefits from the heat stability of NAD⁺ in acid solutions and NADH in basic solutions. In both measurements 200 µg of 11,000xg lysate were utilized and either pre-treated with 0.4 M HCl for NAD⁺ or with a 1:1 HCl/Tris (v/v) solution for NADH examination. NAD⁺/NADH detection was performed according to manufacturer's instructions and luminescence were measured by using Tecan Infinite 200 reader (Tecan Group Ltd., Männedorf, Switzerland).

2.2.6.8 Analysis of methyltransferase (MTase) activity in 600xg fraction of muscle and 11,000xg cellular fractions of liver

Methyltransferase activity was measured in cell lysates from 600xg muscle fraction and 11,000xg liver cellular fractions by MTase-Glo™ Methyltransferase assay (Promega,

Heidelberg, Germany) according to manufacturer's instructions. For the luminescence-based assay 100 ng of 600xg muscle fraction and 1 µg of 11,000xg liver fraction from each sample were used and luminescence were measured by using Tecan Infinite 200 reader (Tecan Group Ltd., Männedorf, Switzerland). The luminescence is directly proportional to methyltransferase activity. Briefly, the cellular fractions were incubated with 2.5 mM SAM for 30 min at RT, succeeded by 30 min incubation with MTase-Glo™ Reagent. Next, MTase-Glo™ Detection Solution was added, followed by 30 min incubation at RT before luminescence was read.

2.2.6.9 Analysis of sirtuin (SIRT) activity in 600xg fraction of muscle and 11,000xg cellular fractions of liver

Sirtuins belong to the NAD⁺-dependent histone deacetylases class III. After lysis 1 µg of the 600xg muscle cellular fraction and 5 µg of the 11,000xg liver cellular fraction, the SIRT activity via the commercially luminescence-based SIRT-Glo™ assay system (Promega, Heidelberg, Germany) was measured. Cellular fractions were incubated with SIRT substrate for 15 minutes and then luminescence was measured using the Tecan Infinite 200 Reader (Tecan Group Ltd., Männedorf, Switzerland). The luminescence is directly proportional to deacetylase activity.

2.2.6.10 Determination of reactive oxygen species (ROS) in 600xg fraction of muscle and whole-tissue biopsy of liver

Reactive oxygen species (ROS) was determined by MDA quantification from 600xg cellular fraction of muscle and whole-tissue biopsy of liver by kit-colorimetric based assay according to the manufacturer's instructions (OxiSelect™ TBARS Assay (MDA Quantification); Cell Biolabs, Inc., USA). In brief, 30 mg of the muscle cellular fraction and 10 mg liver tissue were homogenized in 100x BHT solution within the TissueLyser (QIAGEN GmbH, Hilden, Germany) (10,000xg, 5 min). 100 µl of the supernatant was added to 100 µl SDS Lysis Solution and incubated for 5min at room temperature. 250 µl of TBA Reagent was added to each standard and incubated at 95°C for 50 min. After the samples were cooled down to room temperature, all samples were centrifuged at 956xg for 15 min and supernatant was removed for further analysis. To prevent interference with hemoglobin and its derivatives, an extra Butanol extraction was done by manufacturer's instructions. MDA colorimetric detection was performed according to manufacturer's instructions by using Tecan Infinite 200 reader (Tecan Group Ltd., Männedorf, Switzerland).

2.2.6.11 Analysis of mitochondrial copy number

Real-time quantitative polymerase chain reaction (qPCR) targeting mitochondrially and nuclear encoded genes

Using total DNA extracted from the *gastrocnemius* muscle and liver of Ctrl and Cvs mice, real-time quantitative polymerase chain reaction (qPCR; Applied Biosystems® StepOnePlus Real-

Time PCR System) was used to calculate the ratio of mtDNA to nDNA molecules. Two genes were chosen to assess the relative copy number of mtDNA. These were the nuclear-encoded single copy lipoprotein lipase (LPL) and the mitochondrial encoded NADH dehydrogenase subunit 1 (MT-ND1) gene. Sequences for primers and probes are provided in 2.1.7. Final concentrations for the MT-ND1 and LPL-targeting primers and probes were 0.5 nM and 0.3 nM, respectively. Each sample containing 5 ng of DNA underwent triplicate qPCR runs. Preincubation at 95°C for 20 sec for enzyme activation was followed by 40 cycles of denaturation at 95°C for 1 sec and annealing and elongation at 60°C for 20 sec.

Calculating the ratio of mtDNA to nDNA molecules involved counting the number of mtDNA molecules relative to nDNA molecules (Quiros et al., 2017). The relative mtDNA/nDNA ratio was calculated by comparing the amount of MT-ND1 DNA to that of LPL threshold cycle (Ct) values derived from qPCR software (StepOnePlus™ Software 3.2, Thermo Fisher Scientific Inc., Darmstadt, Germany). Relative mtDNA content was calculated as follows:

$$\Delta Ct = Ct(nDNA\ gene) - Ct(mtDNA\ gene)$$

$$mtDNA\ copies = 2 * 2^{\Delta Ct}$$

$$Relative\ mtDNA\ content = \frac{mtDNA\ copies\ (C57Bl6_Ctrl)}{mtDNA\ copies\ (C57Bl6_Cvs)}$$

2.2.7 Ex vivo analyses of mitochondrial function in muscle and liver

2.2.7.1 Cytochrome c oxidase activity

Cytochrome c oxidase activity and outer membrane integrity of mitochondrial cellular fraction (2.2.6.1, 2.2.6.2) were determined by using a Cytochrome c Oxidase Assay Kit (2.1.6). The manufacturer's procedure was followed and 1 µg of the 10,000xg muscle fraction and 1 µg of the 11,000xg liver fraction protein in a volume of 10 µl isolation buffer was used for analysis. The principle of this assay is that cytochrome c oxidase catalyzes the oxidation from ferrocytochrome c to ferricytochrome c. Within this, the absorption at 550 nm decreases and indicates cytochrome c activity. The enzyme activity was determined in presence of the detergent n-dodecyl β-D-maltoside, allowing the maintenance of cytochrome c oxidase dimer in solution at low detergent concentrations. Additionally, enzyme activity in absence of the detergent was measured, whereby the outer mitochondrial membrane presents a barrier for entrance of cytochrome c into the organelle. The ratio of enzyme activity between assays performed with and without detergent was used to assess the mitochondrial outer membrane integrity. Data were analysed following the decrease in absorption at 550 nm using a kinetic program measuring at 10 sec intervals for 6 readings (Tecan Group Ltd., Männedorf, Switzerland) For calculation, the OD₅₅₀ values were plotted versus the time in sec and the

slope was computed. The following formula was used to calculate the cytochrome c oxidase activity, expressed in Units (U)/ml:

$$U/ml = \frac{\Delta\Delta A/min * dil * 1.1 ml}{0.01 ml * 21.84}$$

$$\begin{aligned} \Delta\Delta A/min &= \Delta A/min_{sample} - \Delta A/min_{blank}; \text{ dil} = \text{dilution factor of sample}; 21.84 \\ &= \Delta\epsilon^{mM} \text{ between ferrocytochrome c and ferricytochrome c at } 550 \text{ nm} \end{aligned}$$

The ratio of enzyme activity in presence (total activity) and absence (intact activity) of the detergent n-dodecyl β -D-maltoside corresponds to outer membrane integrity of mitochondria and was calculated with the following formula, expressed in percentage of mitochondria with intact outer membranes:

$$\% = \frac{(\Delta A_{total} - \Delta A_{intact}) * 100}{\Delta A_{total}}$$

2.2.7.2 Citrate synthase activity

Enzyme activity was measured in 10,000xg muscle and 11,000xg liver cellular fraction (2.2.6.1, 2.2.6.2) using a Citrate Synthase Assay Kit. Total citrate synthase activity was determined after lysis of mitochondrial cellular fraction according to the provided protocol by inserting 20 μ g muscle protein and 100 μ g liver protein in a volume of 10 μ l isolation buffer. The principle of the analyses is that citrate synthase catalyzes the reaction between acetyl CoA and oxaloacetic acid to form citric acid. The hydrolysis of the thioester of acetyl CoA results in the formation of CoA with a thiol group. In a further colorimetric reaction, the thiol group reacts with the added DTNB to TNB, which can be detected spectrophotometrically by the absorbance at 412 nm. Citrate Synthase activity was colorimetric detected according to manufacturer's instructions by using Infinite[®] M200 Plate Reader (Tecan Group Ltd., Männedorf, Switzerland).

2.2.7.3 Analysis of mitochondrial coupling efficiency in Seahorse XF Analyser

Reagents and solutions

Stocks of 0.5 M succinate, 0.5 M malate, 0.5 M malonate, 0.5 M pyruvate, 0.5 mM ADP and 1 M ascorbate were dissolved in ultrapure H₂O_{bidest.} and adjusted to pH 7.2 with KOH. A stock of 10 mM TMPD was made in 10 mM ascorbate, pH 7.2. Stocks of 2 mM rotenone, 10 mM FCCP, 40 mM antimycin A and 5 mg/ml oligomycin were dissolved in ethanol absolute (EtOH_{abs.}). All reagents and solutions were stored at -20 °C, except pyruvate, which was always freshly prepared.

Mitochondrial respiratory states

The respiratory states of mitochondria can be defined in terms of the state of coupling control as well as the state of the electron transfer pathway (Chance and Williams, 1955a):

State 1 describes the state of isolated mitochondria in the respiratory medium with oxygen and inorganic phosphate, but without ADP or other respiratory substrates. Thus, *state 1* describes the mitochondria as such.

State 2 describes isolated mitochondria in the medium in the absence of ADP and respiratory substrates. It describes the basal respiration of isolated mitochondria.

State 3 describes ADP-stimulated respiration of isolated mitochondria in the presence of high ADP and Pi concentrations and is controlled by the membrane potential for phosphorylation of ADP to ATP and substrate oxidation including substrate uptake, processing enzymes, relevant electron-transport-chain complexes, pool sizes of UQ (ubiquinone) and cytochrome c, and O₂. It describes the oxidative phosphorylation state of isolated mitochondria.

State 3u is *state 3* in an uncoupled environment of electron transfer capacity by addition of an uncoupler to the isolated mitochondria. This state is controlled exclusively by the oxidation of substrates, so that dysfunctions in components of the respiratory chain, substrate translocases or dehydrogenases can be detected. It describes the uncoupled respiration of isolated mitochondria.

State 4 is the state after *state 3* of isolated mitochondria when supplied ADP has been maximally phosphorylated to ATP and is controlled by the proton leak.

State 4o represents leak respiration while ATP synthase is inhibited by oligomycin. In the leak state of non-phosphorylating resting respiration, the oxygen flux is reduced to a minimum.

State 5 is reached when the O₂ concentration is depleted and no respiration occurs.

Respiratory coupling experiment

Mitochondrial coupling between the mitochondrial ETC and OXPHOS is the essential mechanism for ATP generation utilizing oxygen. For the coupling experiment, the 10,000xg muscle and 11,000xg liver cellular fractions were incubated with pyruvate/malate, pyruvate/malate plus malonate, succinate and succinate plus rotenone as substrates. The compounds ADP, oligomycin, FCCP and antimycin A were then successively injected, whereby the oxygen consumption rate (OCR) was measured after each injection. Rates of basal complex I and II respiration in a coupled state (*state 2*, in presence of substrate(s), respectively), phosphorylating respiration in the presence of ADP (*state 3*), non-phosphorylating respiration after the addition of oligomycin, an ATP synthase inhibitor, (*state 4o*) and maximal uncoupled respiration induced by FCCP, a proton ionophore and uncoupler of OXPHOS, (*state 3u*) were analysed. As the last step, in response to the addition of the complex III inhibitor antimycin A, the total mitochondrial respiration was blocked.

Substrates and injections had final concentrations as follows: 10 mM succinate, 2 μM rotenone, 10 mM pyruvate, 5 mM malate, 10 mM malonate, 2 mM (muscle 10,000xg)/4 mM (liver

11,000xg) ADP, 2 μ M (muscle 10,000xg)/2.5 μ g/ml (liver 11,000xg) oligomycin, 6 μ M (muscle 10,000xg)/4 μ M (liver 11,000xg) FCCP, 2 μ M (muscle 10,000xg)/4 μ M (liver 11,000xg) antimycin A, 10 mM ascorbate, 100 μ M TMPD. All substrates and injected solutions were adjusted to pH 7.4 (KOH/hydrochloric acid (HCl)).

Seahorse XF data treatment

Seahorse XF results were evaluated with the Wave software version 2.6.0 (Agilent Technologies Inc., Santa Clara, CA, USA). The obtained data were normalised to citrate synthase activity (2.2.7.2).

Acceptor control ratio (ACR)

For the assessment of the quality of mitochondrial activity, the acceptor control ratio (ACR) as a quantity value for the ADP-dependent mitochondrial respiration was calculated (*state 3/state 2*) (Feo et al., 1973) based on the data of the coupling experiment. The ACRs were calculated specifically for complex I- and complex II-driven respiration from Ctrl and Cvs mice. Calculation of ACR required addition of an arbitrary factor to all readings of *state 3* and *state 2*, to raise negative values of individual samples to a positive numeric range, so that they could be used for the calculation.

$$ACR = \frac{state\ 3}{state\ 2}$$

Respiratory control ratio (RCR)

For the assessment of the quality of mitochondrial activity, the respiratory control ratio (RCR), a reference value for proton leak was calculated (*state 3/state 4o*) (Chance and Williams, 1955b), based on the data of the coupling experiment. The RCRs were calculated specifically for complex I- and complex II-driven respiration from Ctrl and Cvs mice. Calculation of RCR required addition of an arbitrary factor to all readings of *state 3* and *state 4o*, to raise negative *state 4o* values of individual samples to a positive numeric range, so that they could be used for the calculation.

$$RCR = \frac{state\ 3}{state\ 4o}$$

2.2.7.3.1 Bioenergetic assessment of mitochondria

Degree of mitochondrial thermodynamic coupling (q)

To assess the economic degree of mitochondria in muscle tissue after Cvs, the degree of thermodynamic coupling was calculated based on the data of the coupling experiment (Cairns et al., 1998). To delineate the efficiency of mitochondrial respiration for the integrated cellular substrate response through NADH (complex I), and through the TCA cycle (complex II), the calculation of Stucki et al. (Stucki, 1991) was applied as followed:

$$q\ value = \sqrt{(1 - (state\ 4o / state3))}$$

The q-value is associated to different thermodynamic set points which express the overall degree of thermodynamic coupling within the mitochondria. The four set points are defined as: maximal net output flow (ATP) at optimal efficiency ($q_r=0.786$), maximal net output power ($q_e=0.910$), economic net output flow ($q_r^{ec}=0.953$), and economic net output power at optimal efficiency ($q_e^{ec}=0.972$).

Analysis of mitochondrial thermodynamic efficiency of oxidative phosphorylation (η -opt)

The determination of the thermodynamic efficiency of oxidative phosphorylation of mitochondrial enriched cellular fractions (10,000xg) from muscle and (11,000xg) from liver after Cvs, based on Stucki et al. (Stucki, 1991) was used dependent on the coupling experiment data. The thermodynamic efficiency of oxidative phosphorylation is defined as the efficiency of substrate to energy conversion in mitochondria and was calculated specifically for complex I- and complex II-driven respiration as followed:

$$\eta_{opt} = \frac{q^2}{(1 + \sqrt{1 - q^2})^2}$$

2.2.7.4 Analysis of mitochondrial electron flow in Seahorse XF Analyser

In the electron flow assays, the transport of electrons was followed and interrogated from each complex, I to IV, of the ETC. The electron flow was monitored in presence of the uncoupling agent FCCP, disrupting ATP production by carrying protons through the inner mitochondrial membrane and therefore, lacking a proton gradient formation (Das, 2013; Stauch et al., 2014). Herefore, the 10,000xg muscle and 11,000xg liver cellular fractions were used for mitochondrial analysis. First, mitochondria complex I and II respiration was analysed in an uncoupled state (pyruvate/malate, succinate plus FCCP). Next, electron flow at complex I or II was inhibited by supplementary adding rotenone or malonate, respectively. As controls, the assay was conducted applying only substrates mediating complex I (pyruvate/malate plus FCCP) or complex II respiration (succinate plus FCCP). For the first injection strategy, rotenone, succinate, antimycin A and TMPD/ascorbate were added sequentially, latter, as an electron donor for complex IV (Rogers et al., 2011). The second injection strategy was comprised of malonate, pyruvate/malate and again antimycin A and TMPD/ascorbate.

Substrates and injections had final concentrations as follows: 10 mM succinate, 2 μ M rotenone, 10 mM pyruvate, 5 mM malate, 10 mM malonate, 2 mM (muscle 10,000xg)/4 mM (liver 11,000xg) ADP, 2 μ M (muscle 10,000xg)/2.5 μ g/ml (liver 11,000xg) oligomycin, 6 μ M (muscle 10,000xg)/4 μ M (liver 11,000xg) FCCP, 2 μ M (muscle 10,000xg)/4 μ M (liver 11,000xg) antimycin A, 10 mM ascorbate, 100 μ M TMPD. All substrates and injected solutions were adjusted to pH 7.4 (KOH/hydrochloric acid (HCl)).

Seahorse XF results were evaluated with the Wave software version 2.6.0 (Agilent Technologies Inc., Santa Clara, CA, USA). The obtained data were normalized to citrate synthase activity (2.2.7.2).

2.2.8 *Ex vivo* analyses in primary hepatocytes

The *ex vivo* analyses in section 2.2.8 were performed on primary hepatocytes from Ctrl and Cvs mice immediately after the Cvs intervention and after a three-month recovery period (cohort 4) (2.2.2). Dr. M. Dille (Institute of Clinical Biochemistry at the German Diabetes Center) applied Cvs protocol to recovery cohort 4 (2.2.2) and performed analysis of mitochondrial respiration and glycolysis using the Seahorse XF assay on primary hepatocytes (2.2.8.1). Data interpretation on the energetic flexibility of hepatocytes, i.e., the energy map (2.2.8.5) (unpublished data), was performed as part of this work based on data collected on cohort 4 as part of a previous project (Dille, Nikolic et al. 2022).

2.2.8.1 Primary hepatocyte isolation, purification and cultivation

Primary hepatocytes in each experimental group were isolated from mouse livers by two-step perfusion. The isolation procedure was originally described (Jelenik et al., 2018). After killing the mouse by CO₂ asphyxiation, the superior vena cava was clamped to prevent chest decompression and perfusion. Then, the needle was inserted into the inferior *vena cava* and the liver was perfused with 5 ml/min HBSS perfusion buffer (2.1.4) for approximately 3-4 min. The *portal vein* was cut to release the perfusion buffer. After complete hemorrhage, the color of the liver tissue changed from red to beige, and the liver was digested by perfusing it with collagenase medium (0) containing 100 U/ml collagenase for about 4 to 5 min.

After that, the liver appeared swollen and pink. The livers of the mice were then excised and the gallbladders removed. The dissected livers were covered with isolation medium (0) and scraped with a razor blade until the entire liver was converted into a cell suspension. The liver cell suspension was filtered through a 70- μ m cell strainer and centrifuged at 4°C for 5 min at 50xg. The liver cell suspension was then removed. The pellet was washed by centrifugation with plating medium (0). To separate viable hepatocytes from non-viable cells, density separation was performed using a 90% Percoll gradient (2.1.3) (50xg, 10 min, 4°C) with low acceleration and delay. After a final washing step cell number and viability was evaluated through trypan blue staining and using a Neubauer chamber for cell counting. Isolated hepatocytes were seeded in assay specific densities on rat tail type-I collagen coated plates and cultured in serum-free medium (0) over night at 37°C and 5% CO₂.

2.2.8.2 *De novo* lipogenesis (DNL) assay

The lipogenesis assessment after Cvs was done by examining the DNL after Cvs in primary hepatocytes from both groups. According to Jelenik et al. 2017, cells were seeded in a 24-well plate at a density of 9×10^4 cells/well. Cells were treated overnight with or without 100 nM insulin in serum-free media (37°C, 5% CO₂). After that, the medium received an addition of 0.5 ¹⁴Ci of ¹⁴C-acetate in a 10 μ M acetate solution. After 4 h of treatment (37°C, 5% CO₂), cells were washed two times with 1x PBS and lysed in 120 μ l 0.1 M HCl by scraping. To extract lipids from the lysates a 2:1 chloroform/methanol solution were used for 5 min. After adding 250 μ l H₂O the mixture was centrifuged (3,000xg, RT, 10 min). The lower lipid containing phase were taken with a syringe and transferred to 3 ml liquid scintillation fluid (Rotiszint®, Roth) to analyzing the incorporated ¹⁴C into lipids of hepatocytes.

2.2.8.3 Fatty acid oxidation (FAO) assay

By examining the emission of radioactive ¹⁴CO₂, the effect of Cvs on the FAO in primary hepatocytes from Ctrl and Cvs mice was determined. In a 48-well plate, 3×10^4 cells/well of cells were planted, and following an overnight serum starvation period, the cells were treated

with or without 40 μM etomoxir to inhibit the mitochondrial FAO. Next, to each cell well was a filter paper with a surface area of 4 cm^2 that had been soaked in 50 μl of 1 M NaOH. For gas exchange, a tube connects the cell wells and the associated filter wells. Following that, cells were subjected to an FAO working solution made up of 9 μM L-carnitin, 57 μM fatty acid-free BSA, and 0.3 μCi ^{14}C -palmitic acid in the proper volume of serum-starvation medium. The cell culture plate was then secured in an oxidation chamber with 5% CO_2 at 37°C. After 4 h of incubation, HCl was added to the cell wells at a final concentration of 0.5 M to completely dissolve the CO_2 in the supernatant. The oxidation chamber was then incubated for an additional night at 37°C with 5% CO_2 . Sodium carbonate, which is bonded in the filter paper, is created when the liberated CO_2 combines with the NaOH in the soaked filter. The radioactive counts were determined the next day after each filter was transferred to 3 ml of liquid scintillation fluid (Rotiszint®, Roth).

2.2.8.4 Glucose production assay

Glucose concentration in culture supernatant was measured using the Glucose Assay Kit according to the manufacturers' manual. Volumes were down-scaled to measure the colorimetric reaction in 96-well plates. In brief, 100 μl of each blank (glucose production medium), sample or standard were mixed with 200 μl assay reagent (kit component). The reaction took place at 37°C for 30 min. Directly at the end of incubation the reaction was stopped with the addition of 200 μl 12 N H_2SO_4 to each sample. After the samples were carefully mixed all samples were measured in quadruplicates by pipetting 100 μl /well in a clear 96-well plate and absorbance was measured at 540 nm against blank reaction. Glucose concentration was quantified from glucose standard curve which ranged from 10 to 100 $\mu\text{g}/\text{ml}$ glucose.

2.2.8.5 Assessment of Cell Energy Phenotype of primary hepatocytes

To assess the energetic flexibility of mitochondrial hepatocytes in both groups immediately after the stress intervention and after a 3-month recovery period, the Agilent Seahorse XF Cell Energy Phenotype was calculated.

Phenotype was calculated based on Baseline Phenotype, Stressed Phenotype, and Metabolic Potential. All data are calculated and displayed as absolute oxygen consumption rate (OCR) in $\text{pmol O}_2/\text{min}$, and absolute extracellular acidification rate (ECAR) in mpH/min based from the data generated from the mitochondrial respiration analysis. The calculated parameters were conducted according to the manufacturer's specifications (Agilent Seahorse XF Cell Energy Phenotype Test, Report Generator User Guide, © Agilent Technologies, Inc. 2017, Manual Part Number: S7888-10002).

| Parameter name | Parameter equation |
|-----------------------|--|
| Baseline OCR | Last OCR measurement before first injection |
| Baseline ECAR | Last ECAR measurement before first injection |
| Stressed OCR | Maximum OCR measurement after the first injection |
| Stressed ECAR | Maximum ECAR measurement after the first injection |

2.2.9 Omics Analyses

2.2.9.1 Proteome analysis

For a tissue-specific proteomic analysis, a label-free proteomic approach was chosen using the LC-MS/MS analysis method. For the muscle tissue specific analysis 15 µg of the 10,000xg fraction and for the liver tissue specific analysis 15 µg of the 11,000xg fraction was used of 5 animals per group. Sample preparation and mass spectrometry running both data dependent acquisition (DDA) and data-independent acquisition (DIA) strategies were performed by Dr. S. Hartwig and U. Kettel at the Proteomics Core Facility (Head: Dr. S. Lehr) of the Institute of Clinical Biochemistry at the German Diabetes Center. DDA run data files were analysed using Proteome Discoverer™ 2.5 software (ThermoFisher Scientific) and Sequest HT search was performed against the FASTA database (SwissProt *mus musculus* (TaxID=10900, version 2022-01)). In the processing workflow, Sequest HT parameters were set to trypsin as digestion enzyme with maximum tolerance of 2 miscleavages, a peptide length of 5-144 and maximum 10 peptides per spectrum. Allowed modifications were cysteine carbamidomethylation static and N-terminal acetylation and methionine oxidation as dynamic modifications. In the *percolator node* Peptide-spectrum match (PSM) analysis was performed setting q-values to 0.01 (strict) and 0.05 (relaxed) false discovery rate (FDR). Q-values are a statistical means, giving the percentage of significant tests that will statistically result in false positives and thus representing FDR adjusted p-values.

Resulting matched spectra file (MSF) was subjected to the consensus workflow, where PSMs were grouped, validated and identified peptides filtered before protein confidence scores were calculated. In the protein grouping node parsimony was applied excluding all protein groups not strictly explaining identified peptides. Furthermore, scored proteins were filtered according to a FDRs 0.01/0.05 (strict/relaxed) and annotated using the standard Gene Ontology term annotations. For label-free protein quantification, peptides linked to proteins were quantified using the Precursor Ions Quantifier (PiQ). Importantly, Imputation Mode parameter in the PiQ node was selected to Low Abundance Resampling, which replaces missing values with

random values sampled between the minimum and the lower 5 percent of all detected values. This step allows for low abundant proteins to be tagged as identified providing a more complete picture of present and non-present proteins in the cellular fraction.

For a more reliable quantification of label-free probe sets LC/MS runs were performed also in DIA scan mode and spectral data was analysed using Spectronaut™ Pulsar software (Biognosys, Zürich, Switzerland). DIA runs are evaluated using the self-performed spectral library based on DDA runs analysed with the Proteome Discoverer™ in Sequest HT mode (2.1.8). Additionally, normalization and quantification of the cellular fractions was granted by spiking the samples with indexed Retention Time (iRT) standard, containing eleven non-naturally occurring synthetic peptides, which allows for calibration of the chromatographic system. Based on the standard parameter settings, the software identified the proteins and calculated the folds between set numerator and denominator groups including p-value and FDR.

Z-Score analysis

Z-score significance was assessed for estimation plot analysis using the over and under-representation of proteins in each condition with respect to the overall experimental mean were used. For mitochondrial proteome, five animals per group were analysed, and the mass spectrometry data are available at the ProteomeXchange Consortium via the PRIDE partner repository with the dataset identifiers PXD035798 for muscle and PXD042472 for liver.

2.2.9.2 Transcriptome analysis

Affymetrix Microarray Analysis

Transcriptome analysis was performed using the Affymetrix microarray technology. Basically, mRNA is first transcribed into cDNA using fluorescence labeling, before the native strand is removed and the fluorescent strand is hybridized with complementary probes spotted on a microarray chip. In this study the Clariom™ D Array, mouse Array (Applied Biosystems™) was employed, which covers >214,000 transcripts sourced from the largest number of public databases, the most comprehensive coverage of the mouse transcriptome.

RNA Extraction

RNA from 60 mg muscle and 40 mg liver tissue was isolated extraction using the miRNeasy-Mini Kit (Qiagen, Hilden, Germany) (2.1.6) to avoid size restriction of isolated RNAs. Frozen tissue was lysed in 700 µl of QIAzol lysis Reagent for 5 min using the TissueLyser. After incubating the samples for 5 min at room temperature, 700 µl of lysate were centrifuged in spin columns (QIAshredder, Qiagen, Hilden, Germany) at 18,407xg for 2 min at 4°C. The flow-through was collected and the RNA was subsequently extracted with 140 µl of chloroform using MAXtract High Density tubes (Qiagen, Hilden, Germany) and centrifugation at 12,000xg for 15 min at 4°C. The resulting aqueous RNA solution was transferred to 1.5 ml tubes and mixed

with 1.5 volume of EtOH_{abs.}. Subsequently, the RNA was purified using miRNeasy-Mini columns. DNase digest was performed using the RNase-free DNase Set according to the manufacturer's instructions. Concentration of the RNA was measured photometrically at 260 nm using the NanoDrop™ 2000/2000c spectrometer (Thermo Fisher Scientific Inc., Darmstadt, Germany).

cDNA synthesis and Chip Loading preparation (Affymetrix)

The synthesis of complementary DNA (cDNA) from the isolated RNA was performed by using GeneChip™ WT PLUS Reagent Kit (Thermo Fisher Scientific Inc., Darmstadt, Germany) according to manufacturer's instructions. All incubations were performed in a T100 thermal cycler (Bio-Rad Laboratories Inc. Hercules, CA, USA) using the heated lid function if temperature was greater than 35°C and no heated lid function for incubation at lower incubation temperatures. WT PLUS Kit uses a reverse transcription priming method that primes the entire length of each RNA transcript independent of poly-A tails to provide complete and unbiased coverage of the transcriptome. The kit efficiently generates amplified and biotinylated sense-stranded DNA targets, avoiding loss of specificity due to antisense strand interference. In brief, 100 ng of total RNA samples of Ctrl and Cvs groups were used for complementary DNA (cDNA) synthesis. 100 ng RNA were supplemented with 2 µl diluted Poly-A RNA Controls in a final volume of 5 µl. Subsequently, the first-strand cDNA was synthesized by adding premixed 4 µl of the first-strand buffer and 1 µl First-Strand Enzyme per sample. The mix was incubated for 60 min at 25°C, then for 60 min at 42°C and chilled on 4°C for at least 2 min. The second-strand cDNA synthesis was immediately proceeded by adding premixed 18 µl of the second-strand buffer with 2 µl Second-strand enzyme to each 10 µl first-strand cDNA sample and 60 min incubation at 16°C, then for 10 min at 65°C. Subsequently, the in vitro transcription (IVT) for cRNA synthesis was proceeded by transferring the first-strand cDNA sample with 30µl IVT Master Mix (24 µl IVT buffer and 6 µl IVZ enzyme) to each 30 µl second-strand cDNA sample and incubated for 16 h at 40°C. The cRNA was purified according to manufacturer's instructions with magnetic purification beads, and the cRNA yield was assessed by measuring 260 nm absorbance using a NanoDrop™ 2000/2000c spectrometer (Thermo Fisher Scientific Inc., Darmstadt, Germany). 15 µg of cRNA in a total volume of 24 µl nuclease-free water were used for 2nd-Cycle ss-cDNA synthesis. 4 µl of 2nd-Cycle primers were added to each cRNA sample and denatured for 5 min at 70°C, then incubated 5 min at 25°C and for 2 min at 4°C. On ice, the Master Mix of the 2nd-Cycle ss-cDNA was prepared according to manufacturer's instructions (8 µl of the 2nd-Cycle ss-cDNA buffer, 4 µl 2nd-Cycle ss-cDNA Enzyme). 12 µl of the 2nd-Cycle ss-cDNA Master Mix were transferred to each cRNA/2nd-Cycle Primer sample and incubated for 10 min at 25°C, 90 min at 42°C and for 10 min at 70°C. Finally, RNA was hydrolyzed by adding 4 µl RNase H for each 2nd-Cycle ss-cDNA sample, mixed, and incubated for 45 min at 37°C. Reactions were stopped on ice,

and diluted with 11 µl nuclease-free water. After purification of the 2nd-Cycle ss-cDNA magnetic beads according to manufacturer's protocol and then the ss-cDNA yield was assessed using NanoDrop™ 2000/2000c spectrometer (Thermo Fisher Scientific Inc., Darmstadt, Germany). After that, the ss-cDNA was fragmented and labelled according to manufacturer's protocol. Therefore 5.5 µg of ss-cDNA in 31.2 µl nuclease-free water were supplemented with 16.8 µl fragmentation Master Mix (10 µl nuclease-free water, 4.8 µl 10x dDNA Fragmentation Buffer, 1 µl UDG (10U/µl), and 1 µl APE 1 (1000U/µl)) and incubated for 60 min at 37°C, then for 2 min at 93°C. 45 µl fragmented ss-cDNA were transferred to individual tubes and 15 µl of the preprocessed labeling Master Mix (12 µl 5x TdT Buffer, 1 µl DNA Labeling Reagent (5 mM) and 1 µl TdT (30 U/µl)) were added and incubated for 60 min at 37°C, then for 10 min at 70°C. Hybridization Master Mix was prepared by adding 5.5 µg of the fragmented and labeled ss-cDNA to 3.7 µl Control Oligonucleotide B2, 11 µl 20x Hybridization Controls, 110 µl 2x Hybridization Mix, 15.4 µl DMSO and 19.9 µl nuclease-free water.

Hybridization Master Mix was added to individual tube containing the biotin-labeled ss-cDNA sample to prepare Hybridization Cocktail. The Hybridization Cocktail consists of 160 µl Hybridization Master Mix and 60 µl fragmented and labeled ss-cDNA. The Hybridization Cocktail was denatured for 5 min at 99°C, and brought to hybridization temperature for 5 min at 45°C and immediately injected into an MTA mouse 1.0 Array. Hybridization was performed at 45°C for 16h at 60 rpm in a hybridization oven. This was followed by probe array washing and staining. Washing and staining was performed on a Fluidics Station according to manufacturer's instructions. The Scanning was performed in a 7.0 G laser.

Experimental groups were analysed using the Transcriptome Analysis Console (TAC) software version 4.0 to determine differential expression using the restrictions: 1.3-fold differences and p-value 0.05. Further bioinformatic analysis was performed using the knowledge-based Ingenuity® Pathway Analysis (IPA®) (Qiagen, Hilden, Germany).

2.2.9.3 Methylome analysis

Methylome analysis

For methylation analysis, two sets of experiments with different experimental setups and analysis pipeline were used: 1. Muscle tissue (acuteCvs, acuteCtrl) (n=6 animals per group); 2. Liver tissue (acuteCvs, acuteCvs, recoveryCvs, recoveryCtrl) (n=3-6 animals per group).

Basically, genomic DNA was extracted and sheared by ultrasound to an average length of 200 nt. Subsequently, DNA was processed in two steps and analysed by Next-Generation Sequencing. First, sample complexity was reduced by enrichment of DNA fragments with methylated cytosines by using the methyl-binding domain proteins (MBDs) which bind specific to methylated sites at regions to higher CpG density such as CpG islands. Next, to facilitate

the direct identification of methylated Cs enriched methylated DNA fragments were subjected to TET mediated enzymatic conversion of unmethylated cytosines. Enzymatic Methyl-conversion is a two-step process to detect modified cytosines. The first step uses TET2 and an oxidation enhancer to protect modified cytosines from downstream deamination. TET2 enzymatically oxidizes 5-mC and 5-hmC through a cascade reaction into 5-carboxycytosine [5-methylcytosine (5-mC), 5-hydroxymethylcytosine (5-hmC), 5-formylcytosine (5-fC), 5-carboxycytosine (5-caC)]. This protects 5-mC and 5-hmC from deamination. 5-hmC can also be protected from deamination by glycosylation to form 5-ghmc using the oxidation enhancer. The second enzymatic step uses APOBEC to deaminate C but does not convert 5-caC and 5-ghmC. This TET mediated enzymatic conversion step was only applied to muscle samples. The resulting converted sequence can be analysed like bisulfite-treated DNA and were subsequently processed for library preparation.

DNA isolation

Isolation of DNA from 20 mg muscle and 10 mg liver tissue from Ctrl and Cvs group was conducted using the DNeasy® Blood & Tissue Kit (Qiagen, Hilden, Germany). Isolation procedure was carried out according to the manufacturer' protocol. Purified DNA was eluted in 200 µl 10 mM Tris-HCl, pH 7.8. DNA concentration was measured using the NanoDrop™ 2000/2000c spectrometer (Thermo Fisher Scientific Inc., Darmstadt, Germany) via OD₂₆₀ measurement and quality was visually assessed after separation by 1.5% agarose gel electrophoresis.

DNA fragmentation

500 ng of the DNA was sheared to fragments of an average length of 270 nt via ultra-sonic energy (Bioruptor® Pico sonication device, Diagenode SA, Seraing, Belgium). The parameters for sonication were set to 30 sec *Time ON*, 30 sec *Time OFF* and 10 sonication cycles at 4°C. 1 µl of fragmented DNA was analysed with an automated gel electrophoresis (4150 TapeStation System, Agilent) for quality control and size distribution using a D1000 ScreenTape assay following the provided manufacturer's instructions.

Methylated DNA enrichment

For methylome analysis a first enrichment step of methylated regions from muscle and liver tissue of Ctrl and Cvs group was done by using the EpiXplore Methylated DNA Enrichment Kit ((EpiXplore™ Methylated DNA Enrichment Kit (Takara Bio Europe, Saint-Germain-en-Lage, France)). In brief, the provided TALON Magnetic Beads were pre-washed and then the Methyl-CpG-binding domain (MBD2 Proteins) (10 µl) were coupled to the TALON Magnetic Beads (100 µl) and 90 µl WB by mixing and incubation for 1 h, RT, on a rocking shaker (1400 rpm), and purified from uncoupled MBD2 proteins with two washing/magnetic enrichment cycles. The fragmented DNA (500 ng in 100 µl 1xWB) was bound to the MBD2 Protein/TALON

Magnetic Bead complex by an incubation for 1 h at room temperature on a rocking shaker. Then magnetic beads with the enriched methylated DNA were collected, subjected to one washing/enrichment cycle and methylated DNA was eluted in 200 μ l Elution Buffer. The enriched methylated DNA was purified by precipitation (1:10 Vol 3M NaAc pH5.2, 4 μ l TLE carrier and 1000 μ l EtOH_{abs.} and overnight incubation at -80°C followed centrifugation (20 min. 14000 rpm, 4°C) according to the manufacturer's instructions. The pellet was washed twice in 70% EtOH_{abs.} dried for 5 min at RT and resuspended in 20 μ l low TE pH 7.5.

Library preparation I

Following the manufacturer's instructions to the latter, a sequencing library was created using the NEBNext® Ultra™ II DNA Library Prep Kit for Illumina®. All incubations were performed in a T100 thermal cycler (Bio-Rad Laboratories Inc. Hercules, CA, USA) using the heated lid function if temperature was greater than 35°C and no heated lid function for incubation at lower incubation temperatures. The kit's provided adapter and indexing sequences are compatible with Illumina® sequencing and correspond to the TruSeq DNA library preparation technique. The steps involved in preparing a library using kit components as suggested by the manufacturer were, in brief, as follows: The input fragmented methyl enriched DNA (100 ng from 2.1.6 EpiXplore Methylated DNA Enrichment Kit) was end repaired, phosphorylated, and adenine tailed to the 3'-end (30 min., 20°C; 30 min., 65°C). Then, partly double-stranded adapters with a single thymine overhang were ligated and directed by the dA-tail (15 min., 20°C). Libraries of the adapter-ligated fragments were size selected utilizing predetermined amounts of magnetic beads as per the manufacturer's instructions. Following this cleanup, 17 μ l of 10 mM Tris/HCl, pH 7.0, was added to elute the DNA from the beads.

2.2.9.3.1 Enzymatic Conversion of muscle

Enzymatic Conversion

Enriched methylated DNA fragments derived from muscle biopsies, were further proceeded by TET-mediated enzymatic conversion of unmethylated cytosines using NEBNext® Enzymatic Methyl-seq conversion module (NewEngland BioLabs® Frankfurt, Germany) according to manufacturer's instructions prior to continuing library preparation. Here, fragmented methylation pre-enriched DNA with ligated adapters (Library I) was added to 10 μ l TET2 Reaction Buffer, 1 μ l Oxidation Supplement, 1 μ l DTT, 1 μ l Oxidation Enhancer, 4 μ l TET and 5 μ l FE(II) Solution in 50 μ l reaction volume and incubated at 37°C for 1h. TET converted DNA was cleaned up using magnetic purification beads provided with the kit and 2 washing cycles with 80% EtOH_{abs.} Finally, the pellet was 2 min air dried and eluted with 17 μ l elution buffer. 16 μ l were denatured by adding 4 μ l NaOH (0.1N) mixed and incubated at 50°C 10 min and placed on ice. Cytosines were deaminated by added to 68 μ l nuclease-free water, 10 μ l APOBEC Reaction Buffer, 1 μ l BSA and 1 μ l APOBEC to the denatured DNA and incubated at 37°C for

3h followed by magnetic bead cleanup and elution in 20 µl elution buffer were used to continue library preparation.

Library preparation II indexing

Distinct index sequences were introduced to each size selected library that represented a particular sample to enable a multiplex analysis in the sequencing runs. Three PCR cycles were run to add the indices without significantly increasing the amount of the library under the specified conditions as per the manufacturer's procedure. Another cleanup of the indexed library was performed using magnetic beads, and the library was then eluted from the beads by adding 33 µl of 10 mM Tris/HCl, pH 7.0. For quality assurance, 1 µl of library DNA was examined using a High Sensitivity D1000 ScreenTape assay (4150 TapeStation System Agilent).

Library quantification and normalization

Libraries were quantified in ng/µl using the Qubit™ 1x dsDNA HS Assay Kit. The concentration was converted in nM by using the following formula:

$$conc [nM] = \left(\frac{conc \text{ ng}/\mu\text{l}}{660 \text{ g/mol} * n} \right) * 10^6$$

conc = concentration, *n* = fragment size in bp

Each library was normalized to 10 nM, as suggested in the “NextSeq550™ System Denature and Dilute Libraries Guide” (Illumina, San Diego, CA, USA).

NGS run

Libraries normalized to 10 nM to be multiplexed in one sequencing run were pooled to create a 10 nM library pool and diluted to 1 nM with RSB buffer. 5 µl of the library pool was denatured with 5 µl 0.1 N NaOH (5 min, RT) and neutralized by adding 5 µl 200 mM TrisHCl, pH 7.0. Libraries were diluted to a loading concentration of 1.4 pM in prechilled buffer hybridization buffer (HF) provided with the kit in a total volume of 500 µl and sequenced with the NextSeq550™ sequencing system (Illumina, San Diego, CA, USA), using 300 paired end high-output sequencing kit (NextSeq™ 500/550 High Output Reagent Kit (300-cycles). Raw data were automatically subjected to the Illumina “Generate FASTQ” routine for initial run quality control and demultiplexing into 8 separate FASTQ files per individual samples.

Data analysis

For methylome analyses, raw Illumina paired-end reads were converted into FastQ format by executing bcl2fastq2 Conversion Software version 2.20 (Illumina, San Diego, USA). FastQ files of methylation analyses were analysed using the Illumina Dragen® (Dynamic Read Analysis for Genomics) Bio-IT platform v 3.9.5 (Edico Genome, Illumina San Diego) on the

Illumina cloud providing predesigned analysis pipelines. Runs were prepared and quality checked using Fast Q toolkit pipeline (v1.0.0.) with a minimum length of 32 bp adapter trimming using the TRUESEQ HT/LT adapters sequence (Illumina San Diego, USA). Settings were: trimming strength: 4 and a quality score <10 to trim bases at 5' and 3' sites before mapping.

Analyses of muscle samples

Paired read FastQ files generated from the MeDIP enriched and TET converted libraries (muscle samples) were mapped using a Hash table generated by DRAGEN Reference builder (v.3.10.4) based on the mouse genome (GRCm38.p6.genome.fa, including methylation information). Mapping was performed using the DRAGEN Methylation pipeline (version v3.9.5) based on (Krueger and Andrews, 2011) for read conversion (C-to-T and G-to-A), deduplication, sorting, and alignment of bisulfite converted reference genome, genome-wide methyl calling and the calculation of alignment and methylation metrics. The outputs of sequence alignment/map files were further analysed using the R package MethylKit (Akalin et al., 2012) (BaseSpaceLabs, Illumina San Diego, USA). CpG sites with a minimum read quality of at least 20 and a minimum read coverage of at least 5, as well as a maximum coverage of 99.9%, were considered for differential methylation analysis with >2% difference in conditions. In the single-base CpG resolution analysis, methylation calls were optimized by combining methylated sites from both the forward and reverse reads. Settings were as: 5×CpG Coverage, 2% methylation difference, and q value of 0.05).

Analyses of liver samples

Paired read FastQ files generated of the MeDIP enriched libraries from liver samples were mapped using a hash table generated by DRAGEN Reference builder (v.3.10.4) based on the mouse genome (GRCm38.p6.genome.fa). Fragments with a minimum read quality of at least 20 and a minimum read coverage of at least 5, as well as a maximum coverage of 99.9%, were considered for analysis. Deduplication, sorting, and alignment mapping to reference genome was performed using the DRAGEN Germline pipeline (version v3.2.8). Further Bioinformatics analyses tools were used on Galaxy.Org <https://usegalaxy.org/> (2022). Outputs of sequence alignment/mapped Bam files were merged per condition using SamTools (Samtools (Li et al., 2009) Galaxy) and analysed using the R package MeDIP (Settings were: extend: 300; paired: TRUE; shift: 0; uniq: 0.001, window size: 100) (Lienhard et al., 2014). Annotations of MeDIP results based on edgeR log fold change and edgeR p-value were performed using R/Bioconductor package ChIPseeker (version 1.18.0) (Yu et al., 2015) and gencode.vM10.chr_patch_hapl_scaff.annotation.gtf to enable comparability to the transcriptome data generated in this study. Enrichment analyses were performed with GO enrichment analyses using <http://www.pantherdb.org/> (Mi et al., 2019; Thomas et al., 2022) and knowledge-based with the use of QIAGEN IPA (QIAGEN Inc.,

<https://digitalinsights.qiagen.com/IPA>, Spring release 2023) (Krämer et al., 2014). Data visualization of omics data was conducted using R packages Circos plot (version 0.69.8) (Hussain et al., 2018; Krzywinski et al., 2009; Rasche and Hiltmann, 2020).

All omics data analyses and bioinformatic interpretations were performed under the supervision of Dr. B. Knebel and Dr. J. Kotzka.

2.2.10 Databases

Data availability of transcriptome and methylome datasets in public databases

Mass spectrometry muscle data are available from the ProteomeXchange Consortium via the PRIDE partner repository dataset identifier PXD035798. Superserial transcriptome and or methylome data of the muscle samples are accessible at NCBI GEO (<https://www.ncbi.nlm.nih.gov/geo/query/acc.cgi?acc=GSE210510> or transcriptome dataset accession number GSE210365). Methylome data at NCBI GEO (<https://www.ncbi.nlm.nih.gov/geo/dataset> accession GSE210509).

Mass spectrometry liver data are available from the ProteomeXchange Consortium via the PRIDE partner repository dataset identifier PXD042472. Superserial transcriptome and or methylome data of the liver samples are accessible at NCBI GEO (<https://www.ncbi.nlm.nih.gov/geo/query/acc.cgi?acc=GSE235424> or transcriptome dataset accession number GSE23494.). Methylome data at NCBI GEO (<https://www.ncbi.nlm.nih.gov/geo/dataset> accession GSE235423).

Liver data are embargoed until publication.

2.2.11 Statistics

Analysis of data was performed using the GraphPad Prism 9.4.0 software and all data were represented as mean with 95% confidence interval (CI) unless otherwise stated for the specified number of animals. For two variables the Mann-Whitney test and for more than two groups a two-way analysis of variance (ANOVA) with Tukey was performed. P-values are corrected for multiple testing using the Benjamini–Hochberg (FDR) method. Values less than 0.05 were considered as statistically significant.

Transcriptome analysis was conducted using the Transcriptome Analysis Console™ 4.0.1 to identify statistically significant gene regulation in pairwise analysis of the investigated groups. Bioinformatic analysis was performed using Ingenuity® Pathway Analysis.

Data dependent as well as independent analysis of proteomics was performed using the Proteome Discoverer™ version 2.5 and Spectronaut™ pulsar software (version 17). Bioinformatic analysis was performed using Ingenuity® Pathway Analysis (IPA).

Correlation analyses were performed using linear regression calculations and verified by Pearson Correlation ($p < 0.05$). Estimation plots were calculated based on the Z-Score data by unpaired t-test and 95% CI ($p < 0.05$).

3. RESULTS

3.1 Immediate effects of chronic variable stress (Cvs) on the regulation of energy metabolism in muscle in the C57BL/6 mouse model

The described results of this work for muscle tissue from 3.1 to 3.1.6 have been adopted word by word from the results section of Nikolic et al. (Nikolic et al., 2023) DOI: 10.1007/s00018-023-04761-4. All analyses and calculations of the data sets shown in the result section and the manuscript were performed as part of this thesis. Numbering of figures from the manuscript were adjusted to numbering of the thesis.

3.1.1 Metabolic characteristics after Cvs

12-week-old male C57BL/6 mice were subjected to our 15-day stress protocol, whereas control mice were kept untreated. The comparison of body weight before and after the stress intervention showed a significant decrease of up to 2 g in the stressed animals, whereas the control animals showed an increase of 4 g in body weight (Fig. 8A). Quantification by NMR revealed a significant change in body composition. In detail, in this short phase stress decreased not only the fat mass up to 10% (approx. 0.4 g) but also the lean mass up to 7.5% (approx. 2 g) (Fig. 8A). In contrast, the control animals showed a significant increase in fat mass of up to 10% (approx. 0.3 g) (Fig. 8A) and lean mass of 7.5% (approx. 2 g) (Fig. 8A). The weight change of the animals during the Cvs protocol was not due to food intake. During the stress intervention, the Cvs animals had a 20% higher average energy intake per gram of body weight compared to the control animals (Fig. 8B). Consistent with this, body weight changes per convertible energy (mg/kJ) were significantly different and showed a decrease in the Cvs group compared to controls (Fig. 8B).

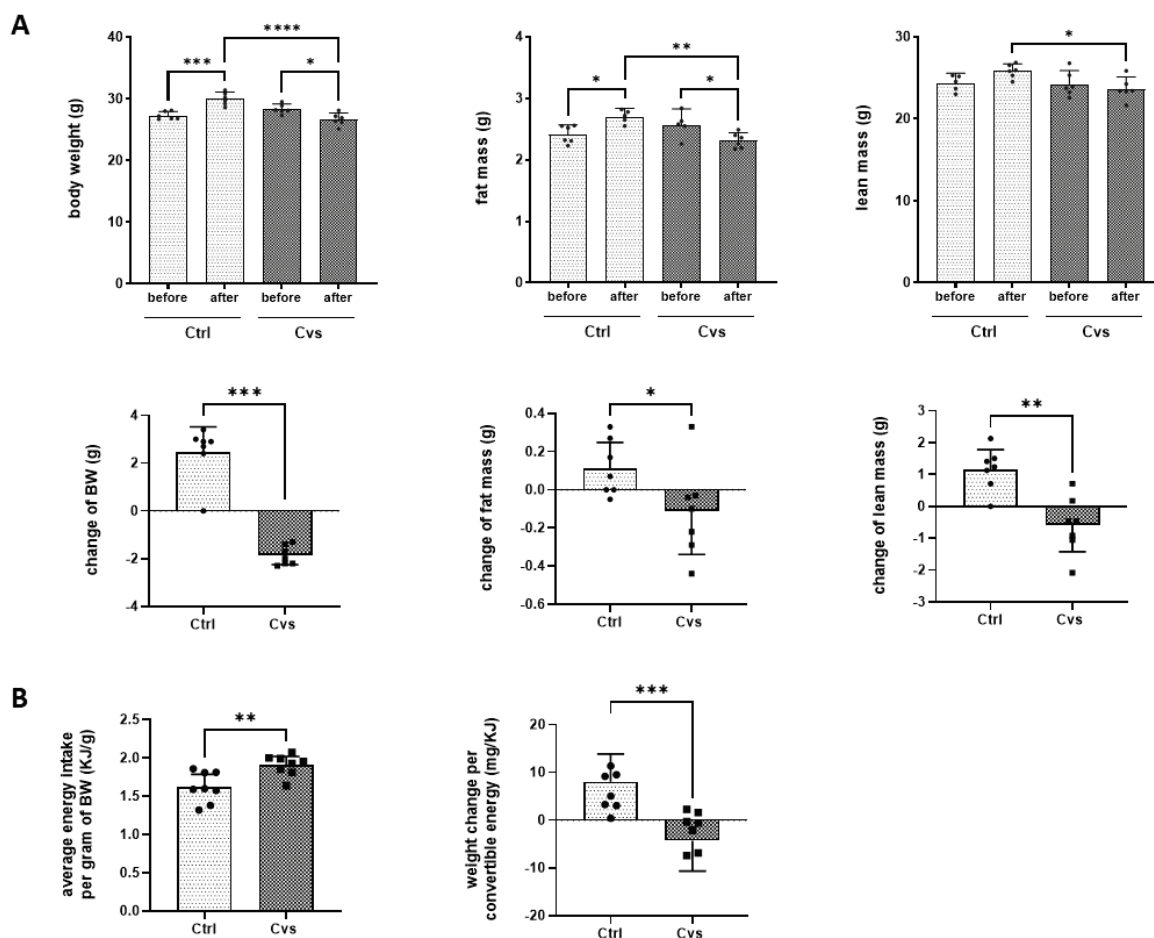


Figure 8: Effect of 15 days of chronic stress intervention (Cvs) on weight change, body composition, and food uptake.

(A) NMR-determined analysis of body composition, consisting of body weight (BW), lean mass, and fat mass, before and after chronic variable stress in control (Ctrl) and Cvs mice ($n=6/\text{group}$). **(B)** Differences in mean energy intake per gram of body weight (BW) and weight change per convertible energy are presented as mean of 8 measurements taken during the intervention period per group ($n=6/\text{group}$). Statistics: two-tailed paired t test or one-way ANOVA with Tukey test for multiple comparisons, $*p<0.05$, $**p<0.01$, $***p<0.001$, $****p<0.0001$, Ctrl: C57BL/6, Cvs: C57BL/6 after stress intervention, CHO carbohydrate oxidation, FAO fatty acid oxidation. (according to Fig. 1, Nikolic et al. 2023)

3.1.2 Indirect calorimetry in Cvs mice

To investigate the differences observed, the metabolic activity was measured by indirect calorimetry immediately after Cvs. Data were analysed for light and dark phases to distinguish metabolic phenomena, depending on low (light) and high (dark) activity levels. Compared with control mice, the stressed mice showed an increase in total physical activity over the observation period, which is especially due to increased dark phase activity (light: Cvs=389; Ctrl=288; dark: Cvs = 1245; Ctrl = 794) (Fig. 9A). Total energy expenditure (EE) during the entire observation period was significantly lower after Cvs compared to control animals (Cvs=6.3 ml/min/g*0.75; Ctrl=7.2 ml/min/g*0.75) (Fig. 9A). Consistent with higher dark phase physical activity the circadian EE indicated in all animals that the EE rates of the dark were significantly higher (7.9–8.3 ml/min/g*0.75) than light period (5.9–6.3 ml/min/g*0.75). The

overall decrease in EE in stressed mice was solely due to the reduced dark EE (Fig. 9A). Over the observation period, respiratory exchange ratio (RER) indicated a shift in whole body substrate utilization from preferential carbohydrate utilization towards fat oxidation in Cvs mice (Ctrl=0.95; Cvs=0.89). In stressed animals, the RER was significantly decreased compared to control mice in both, the light and dark phases, (Fig. 9B), with the greatest decrease in the light phase. Detailed analyses showed that carbohydrate oxidation (CHO) was reduced after Cvs (Fig. 9C). In both groups, CHO was mainly driven in the dark phase (Ctrl: 2.2 mg/min; Cvs: 1.4 mg/min) in contrast to the light phase (Ctrl: 1.4 mg/min; Cvs: 0.6 mg/min) and the Cvs group exhibited a significantly decreased circadian CHO compared to controls (Fig. 9C). In contrast, the average fat oxidation (FAO) increased after Cvs. In both groups, FAO was higher in the light phase than in the dark phase. The observed difference comes from a significantly increased FAO during light phase in Cvs mice (Fig. 9C). So, the Cvs group showed an overall decrease in whole body substrate utilization, except for resting FAO during light phase.

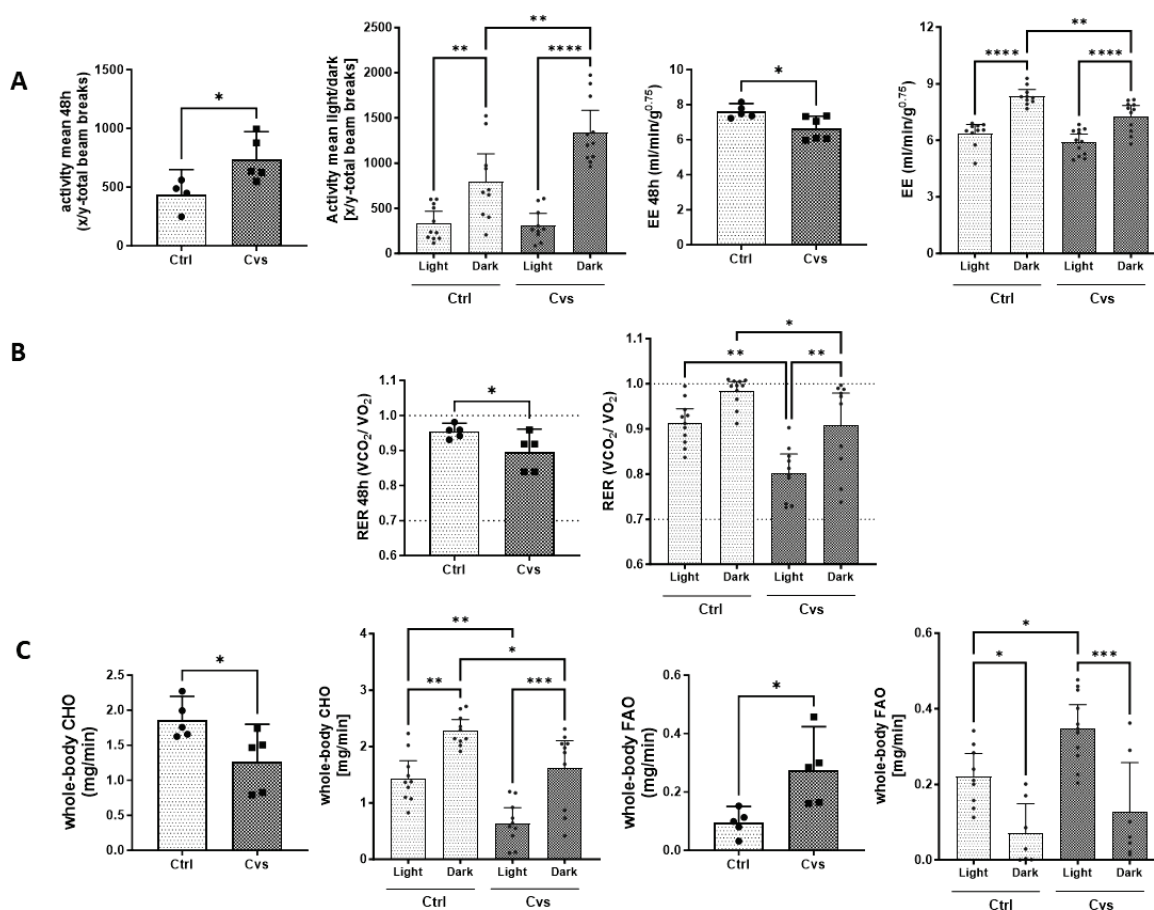


Figure 9: Effect of 15 days of Cvs intervention on physical activity, energy expenditure (EE), and substrate utilization.

(A) Detailed differences in activity and energy expenditure (EE) of Cvs mice in comparison to the Ctrl group during light and dark phases, **(B)** Respiratory exchange ratio (RER). The dotted lines mark the thresholds for preferential whole-body carbohydrate oxidation (CHO) ($VCO_2/VO_2=1.0$) or whole-body fatty acid oxidation (FAO) ($VCO_2/VO_2=0.7$) substrate utilization, **(C)** CHO and FAO. The pairwise bar graphs represent the mean \pm 95% CI over 48 h measurement, dots indicate single animals ($n=6$ /group). Graphs separated for light and dark phases depict each light or dark phase measurement for the respective animal ($n=6$ /group, with two measurements per phase). Statistics: two-tailed paired t test or one-way ANOVA with Tukey test for multiple comparisons, * $p<0.05$, ** $p<0.01$;

*** $p < 0.001$, **** $p < 0.0001$, Ctrl: C57BL/6, Cvs: C57BL/6 after stress intervention, CHO carbohydrate oxidation, FAO fatty acid oxidation. (according to Fig. 2, Nikolic et al. 2023)

3.1.3 Mitochondrial composition assessment

To follow this, we analysed how stress interferes with the status quo of cellular energy metabolism in a label-free proteomic analysis of 10,000×g fractions. Following stress, mitochondrial DNA copy number determined by mtDNA/nDNA ratio showed a small but significant increase in the muscles of the stressed mice (Fig. 10A). In the enriched mitochondrial fractions, mitochondrial content, as determined by the commonly used valid biomarker citrate synthase activity (Larsen et al., 2012), was not significantly altered within the groups (Fig. 10B). Mitochondrial membrane integrity analysis, based on cytochrome-c-oxidase activity, showed an average integrity of above 90% with no differences between both groups (Fig. 10C).

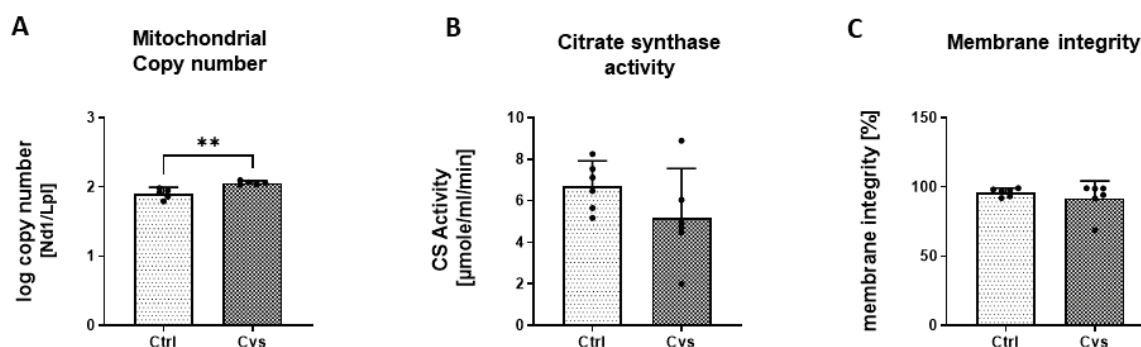


Figure 10: Quality control of mitochondrial fractions in regard to content and membrane integrity.

Mitochondrial mass and integrity after Cvs. **(A)** Relative mtDNA/nDNA ratio was analysed in muscle tissue from Cvs and Ctrl groups (n = 5 animals/ group). **(B)** Citrate synthase activity was measured from fractions of enriched mitochondria (10,000 xg) (n = 6 animals/ per group). **(C)** The percentage of membrane integrity derived from cytochrome-c-oxidase activity of mitochondrial fractions (10,000 xg) from Cvs vs Ctrl muscle tissue (n = 6 animals/ group). Values are displayed as means \pm 95 % CI. Single measurements of each animal are shown as dots. Statistics: Mann–Whitney test, ** $p < 0.01$, Ctrl: C57BL/6, Cvs: C57BL/6 after stress intervention. (according to Supplement Fig. 2, Nikolic et al. 2023)

In the label-free proteomic analysis, 1090 proteins were identified. Of these, 86 proteins were significantly altered in abundance in Cvs mice (Up-regulated: 73/ Down-regulated: 13; ratio: >1.5 ; p-value: < 0.05) (Fig. 12A) (Supplement table 1, DOI: 10.1007/s00018-023-04761-4). Gene ontology analysis of biological processes indicated changes in catabolic processes. In the more detailed analysis of the proteome, the metabolic pathways and the ETC were examined separately and revealed 34 up-regulated and 6 down-regulated proteins followed Cvs (Fig. 12B). The most prominent change with significantly increased protein abundance was the glycolysis pathway (Fig. 12C). In contrast, key catabolic pathways, like ketolysis, glutaminolysis, and branched-chain amino acids metabolism were unaltered by Cvs (Fig. 11).

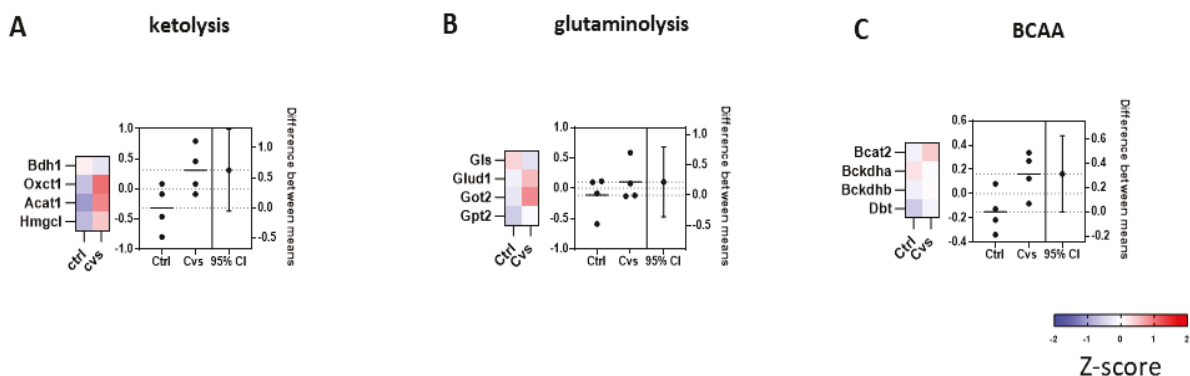


Figure 11: Cvs intervention interferes with metabolic pathway component abundance in enriched muscle mitochondria.

Proteome analyses comparing Ctrl and Cvs group ($n = 5$ animals/ group). **(A-C)** Z-score plots show the over and under-represented proteins of the indicated pathways. Red identifies upregulation, blue identifies downregulation, and white indicates no change of protein abundance to the mean of each condition with respect to the overall experimental mean. The corresponding estimation plots show on the left axis scatter dot plots with mean z-scores, while dots represent each pathway protein as mean of $n=5$ / group. On the right axis the mean $\pm 95\%$ CI alteration in pathway protein abundance of the Cvs and Ctrl comparison is shown. Dotted lines represent the mean of each group centered on 0. **(A)** ketolysis, and **(B)** glutaminolysis, **(C)** Branched chain amino acids (BCAA), Ctrl: C57BL/6, Cvs: C57BL/6 after stress intervention. (according to Supplement Fig. 3, Nikolic et al. 2023)

The proteome data pointed to increased mitochondrial activity, as tricarboxylic acid (TCA) cycle and the ana/cataplerosis pathway proteins showed higher abundances after Cvs (Fig. 12C, D). In addition, fatty acid import into mitochondria, β -oxidation, and pyruvate import into mitochondria was elevated after stress intervention (Fig. 12E–H).

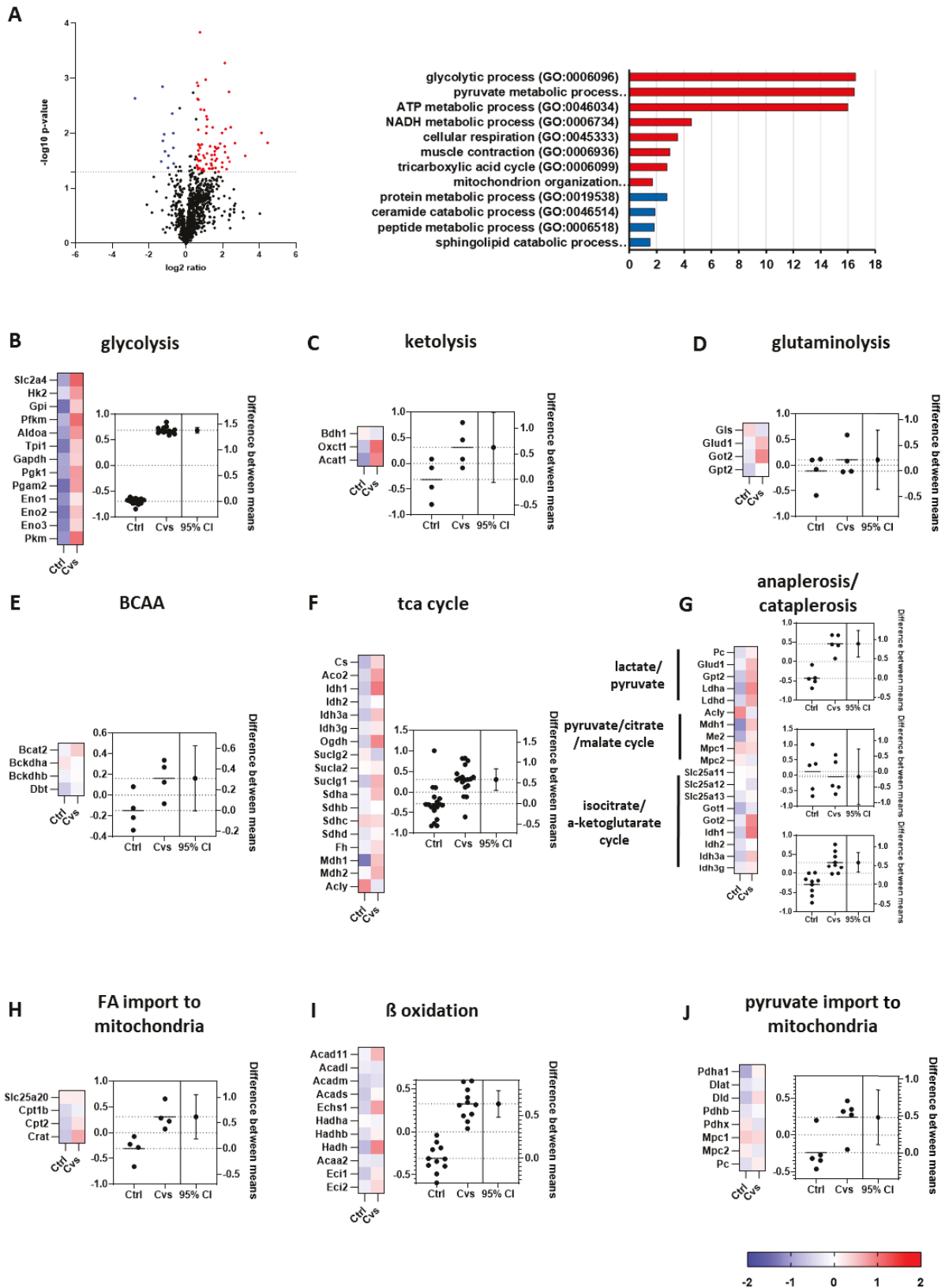


Figure 12: Cvs intervention interferes with metabolic pathway component abundance in enriched muscle mitochondria.

(A) Volcano plot analyses and Gene Ontology classification of proteome analyses. Upregulated (red; n = 73) or downregulated proteins (blue; n = 13) were determined by Student's t-test ($p < 0.05$) with at least 1.5-fold regulation. Significantly, enriched pathways (FDR < 0.1) are shown for GO biological process ontology. A modified Fisher's exact test was used for the functional enrichment analyses (B-J) Heat maps resulting from z-score analyses and

estimation plots: **(B)** glycolysis, **(C)** ketolysis, **(D)** glutaminolysis, **(E)** BCAA, **(F)** TCA cycle, **(G)** ana/cataplerosis, **(H)** fatty acid import to mitochondria, **(I)** β -oxidation (mitochondria), **(J)** pyruvate import to mitochondria. Estimation plots show differences between means of Cvs vs Ctrl ($\pm 95\%$ CI) (mean z-score: left axis, effect size: right axis). BCAA: branched-chain amino acids; TCA: tricarboxylic acid cycle, Ctrl: C57BL/6, Cvs: C57BL/6 after stress intervention. (according to Fig. 3, (Nikolic et al., 2023))

The proteome data after the Cvs period pointed towards an increase in mitochondrial key metabolic protein components to maintain energy supply. Next, we assessed mitochondrial component compositions about protein abundance differences in sum indicated by estimation plots. There were no significant changes in proteins involved in cristae formation following Cvs (Fig. 13A), and the Coenzyme Q (CoQ) biosynthesis modules (Fig. 13B). The CoQ e donors, i.e. the additional respiratory membrane-bound complexes, showed increased abundances after Cvs (Fig. 13C). A total of 109 of identified proteins could be assigned to the electron transport chain (ETC) (Fig. 13D–H). Complex I and III were unaltered (Fig. 13D, F) in muscle mitochondria derived from Cvs animals. Complex II showed increased abundance between the Cvs and Ctrl groups (Fig. 13E). Complex IV showed differences in subunit abundance of the Mt-Co2 and the Mt-Co3- modules, while Mt-Co1 remained unchanged after stress intervention (Fig. 13G). Although single proteins of complex V F(0) complex and F1 particle were altered, there was no significant overall change (Fig. 13H). In total, the analysis of protein composition of the ETC complexes I to V showed only few changes in single subunit abundances, suggesting that Cvs intervention did not induce substantial changes in ETC composition.

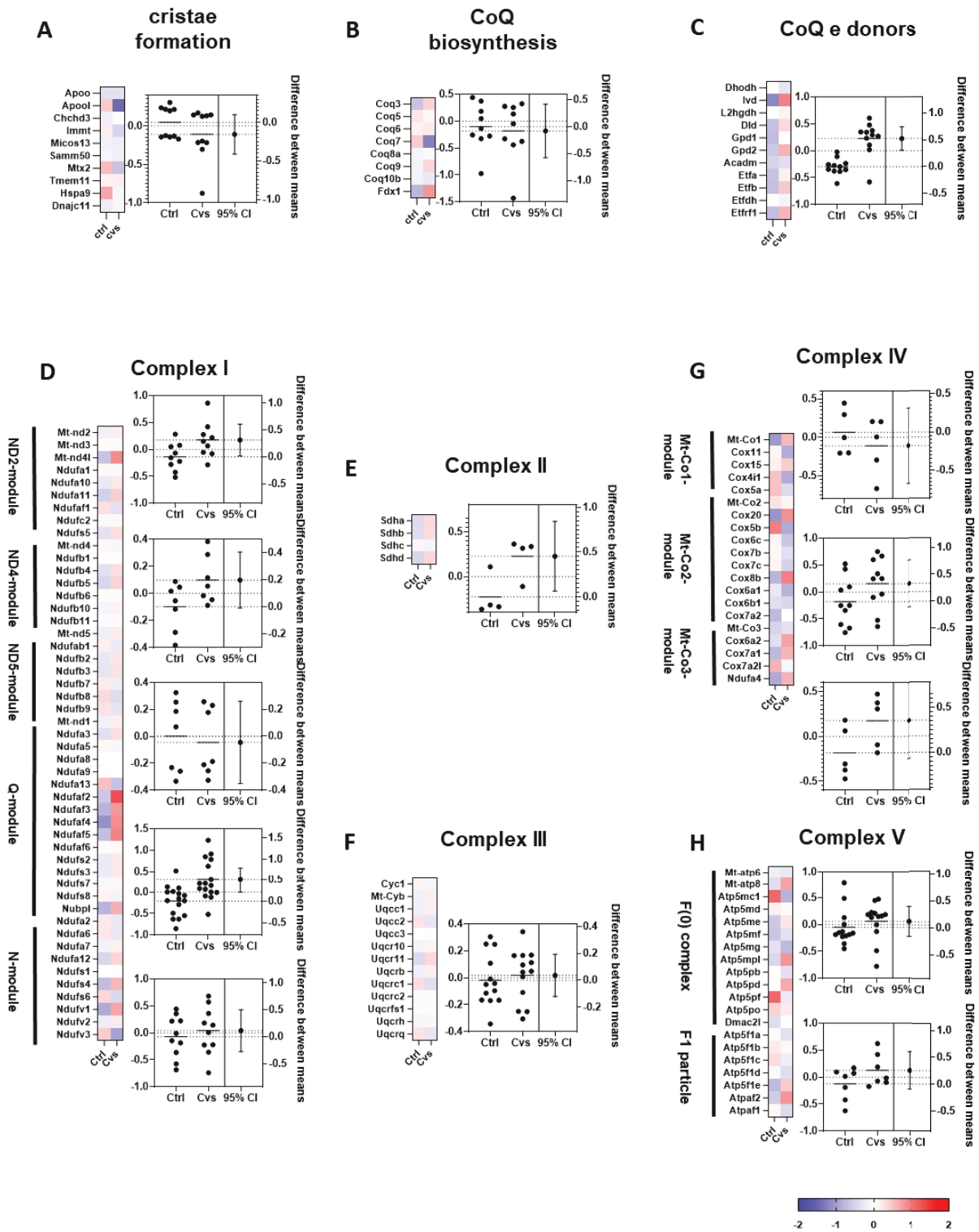


Figure 13: Mitochondrial proteome.

(A-C) Heat maps resulting from z-score analyses and estimation plots: (A) cristae formation, (B) CoenzymeQ (CoQ) biosynthesis, and (C) CoQ e donors, (D-H) Z-score analyses of protein abundance for individual complex I, II, III, IV, and V subunits of electron transport chain. Red identifies upregulation, and blue identifies downregulation of proteins. White indicates no change. Ctrl: C57BL/6, Cvs: C57BL/6 after stress intervention. (according to Fig. 4, (Nikolic et al., 2023))

3.1.4 Cvs interferes with mitochondrial function and EE in muscle

Alterations in fuel preferences and the composition of major mitochondrial metabolic pathways, without evidence of modulation of ETC complex proteins or changes of mitochondrial structural components for cristae formation, may indicate altered mitochondrial activity after Cvs. In addition, the abundance of UCP3 at the transcriptional and protein levels was not altered between the two groups (Fig. 14 A, B). The status of oxidative stress was assessed by proteome analyses of redox-regulating proteins and by measuring the reaction of malondialdehyde with thiobarbituric acid. Here, the proteome and enzyme analysis indicated no changes in redox balance between Cvs and Ctrl groups (Fig. 14C).

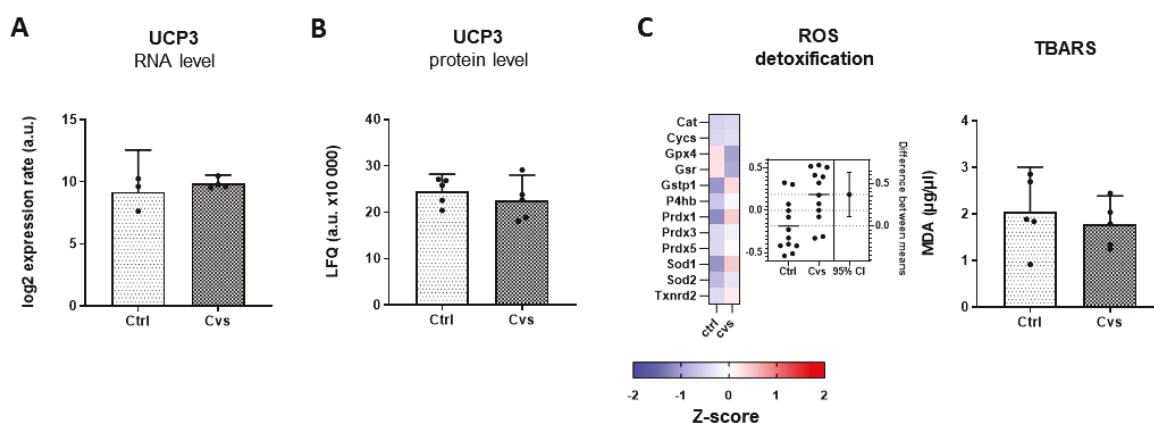


Figure 14: Cvs does not affect proton leakage in mitochondrial fractions.

(A) Log₂-fold changes of UCP3 transcript abundance in Cvs and Ctrl muscle (n = 5 animals/ group). (B) Label-free quantitation (LFQ) x10 000 of UCP3 protein abundance in Cvs and Ctrl muscle (n = 5 animals/ group). (C) Plotted z-score analyses and estimation plot of proteins involved in ROS detoxification. Malondialdehyde (MDA) concentration was measured fluorometrically after reaction with TBARS of 600 xg muscle fraction (n = 5 animals/ group). Data (bar graphs) are expressed as means \pm 95 % CI. Statistics: Mann–Whitney test, not significant. Single measurements of each animal are shown as dots. The z-score plot shows the over and under-represented proteins of the indicated pathway. Red identifies upregulation, blue identifies downregulation, and white indicates no change of protein abundance to the mean of each condition with respect to the overall experimental mean. The corresponding estimation plot shows on the left axis scatter dot plots with mean z-scores, while dots represent each pathway protein as mean of n = 5/ group. On the right axis the mean \pm 95 % CI alteration in pathway protein abundance of the Cvs and Ctrl comparison is shown. Dotted lines represent the mean of each group centered on 0. Ctrl: C57BL/6, Cvs: C57BL/6 after stress intervention. TBARS: Thiobarbituric Acid Reactive Substances; ROS: reactive oxygen species. (according to Supplement Fig. 4, (Nikolic et al., 2023))

First, to determine potential differences in substrate entry to the ETC, and eventual differences in the capacity of such entry on electron transport, basal oxygen consumption rate (OCR) was measured without substrate limitation in uncoupled mitochondria. This was followed by subsequent inhibition of complex I or II using malonate or rotenone in two different experimental setups, respectively, with subsequent complex-specific stimulation of the respective other either by pyruvate/ malate or succinate (Fig. 15).

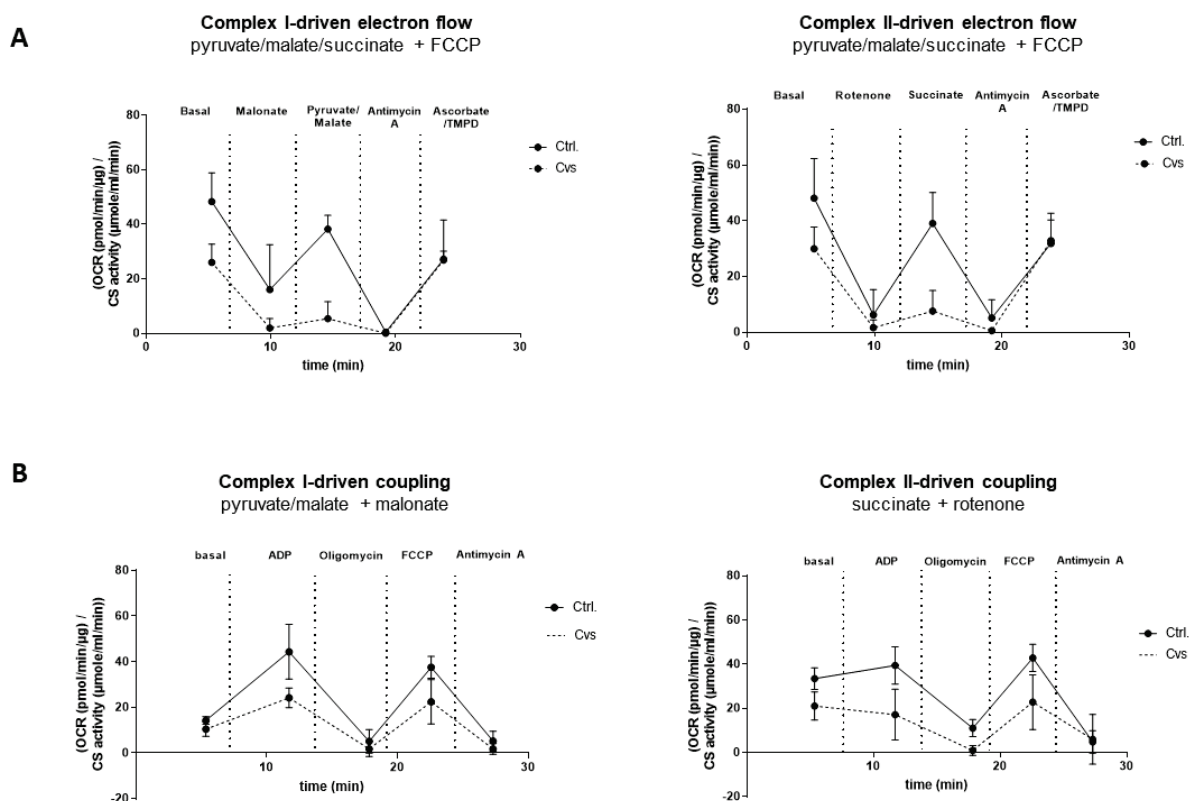


Figure 15: Electron flow capacity and coupling efficiency of mitochondrial ETC after Cvs, injection time-line diagrams.

Electron flow capacity and coupling efficiency of mitochondrial ETC after Cvs. Respiratory capacity was measured in the enriched mitochondrial fractions of isolated muscle mitochondria from Cvs compared to Ctrl muscles in response to ETC manipulation. The dotted vertical lines refer to the time point at which the listed compound was injected. Shown is the oxygen consumption rate (OCR) recorded during the time course of the experiment. **(A)** Electron transport was measured in the uncoupled state (induced by FCCP) specific for complex I (left) and complex II (right) –driven electron transport. OCR at basal level was measured in the presence of unlimited substrate condition (pyruvate/malate/succinate), then OCR was measured after serial injection of complex-specific inhibitor malonate or rotenone, complex-specific substrate stimulation by injection pyruvate/ malate or succinate, this was followed by Antimycin A and Ascorbate/TMPD injections. **(B)** Coupling experiments were performed by measuring OCR individually for complex I (left) and complex II (right). Complex I-specific OCR was measured using complex I-specific substrate pyruvate and malate, with inhibition of complex II activity by malonate. Complex II-specific OCR was measured using complex II-specific substrate succinate with inhibition of complex I activity by rotenone. Mitochondrial respiration was measured at basal experimental condition and in response to serial injection of ADP, oligomycin, FCCP and Antimycin A. Data points represent the mean of $n = 6$ animals/ group shown as mean $\pm 95\%$ CI. All data evaluation and interpretations are given in Figure 5, main document. Ctrl: C57BL/6, Cvs: C57BL/6 after stress intervention. (according to Supplement Fig. 5, (Nikolic et al., 2023))

In both settings, the Cvs group showed significantly decreased OCR values over the time course of the assay (Fig. 15). Already the basal level in the presence of all substrates to drive complex I as well as complex II in the uncoupled condition, showed lower OCR values (46% for complex I; 38% for complex II-driven respiration) after Cvs compared with the control group (Fig. 16A/B). Inhibition of complex II under these conditions decreased respiration rate by half in both groups and the complex I-specific electron transport showed a fourfold decrease in OCR in mitochondria following Cvs compared with control animals (Fig. 16A). Inhibition of complex I by rotenone showed a strong reduction in OCR in both groups (Fig. 16B). Forced electron flow either through complex I or II by additional pyruvate/malate or succinate addition in uncoupled Cvs mitochondria resulted in significant fourfold reduction of OCR compared to

controls (Fig. 16A/B). To follow the complex I and complex II-independent reduction in electron flows after Cvs, the coupling efficiency of ETC complexes I to IV to ATP synthase (complex V) were measured. Complex I-driven respiration was forced with the specific complex I substrates pyruvate/malate with simultaneous inhibition of complex II by malonate and was significantly lower after Cvs (Fig. 16C; Fig. 15B). Detailed examination of complex I-driven mitochondrial function revealed a 40% lower OCR in *state 2* in Cvs animals compared to controls (Fig. 16C). The initiation of oxidative phosphorylation (*state 3*) with ADP showed a significant 55% decrease in OCR in the Cvs animals (Fig. 16C). Here, *state 3* via complex I, significantly correlated with interindividual light phase EE rates ($R^2=0.405$; $p\text{-value}=0.0261$), but not with the dark phase EE. Maximal uncoupled respiration (*state 3u*) after FCCP injection was significantly decreased by 42% in mitochondria from Cvs mice (Fig. 16C) but showed no correlations to circadian EE rates. Complex II-specific coupling forced by the specific substrate succinate and simultaneous inhibition of complex I by rotenone revealed a consistently lower OCR over time in Cvs mitochondria compared to control (Fig. 16D). Complex II-driven function showed a 36% lower respiration in *state 2* and 56% lower respiration in *state 3* in the Cvs group (Fig. 16D), both without correlations to circadian EE rates. The *state 3u* via complex II (*state 3u*) showed a 47% reduction following Cvs, and there was a significant intraindividual correlation to both, light and dark EE (light: $R^2=0.549$; $p\text{-value}=0.0091$ / dark: $R^2=0.432$; $p\text{-value}=0.0278$). Overall, *states 3* and *3u* were reduced for both complex I- and complex II-driven coupling after chronic stress.

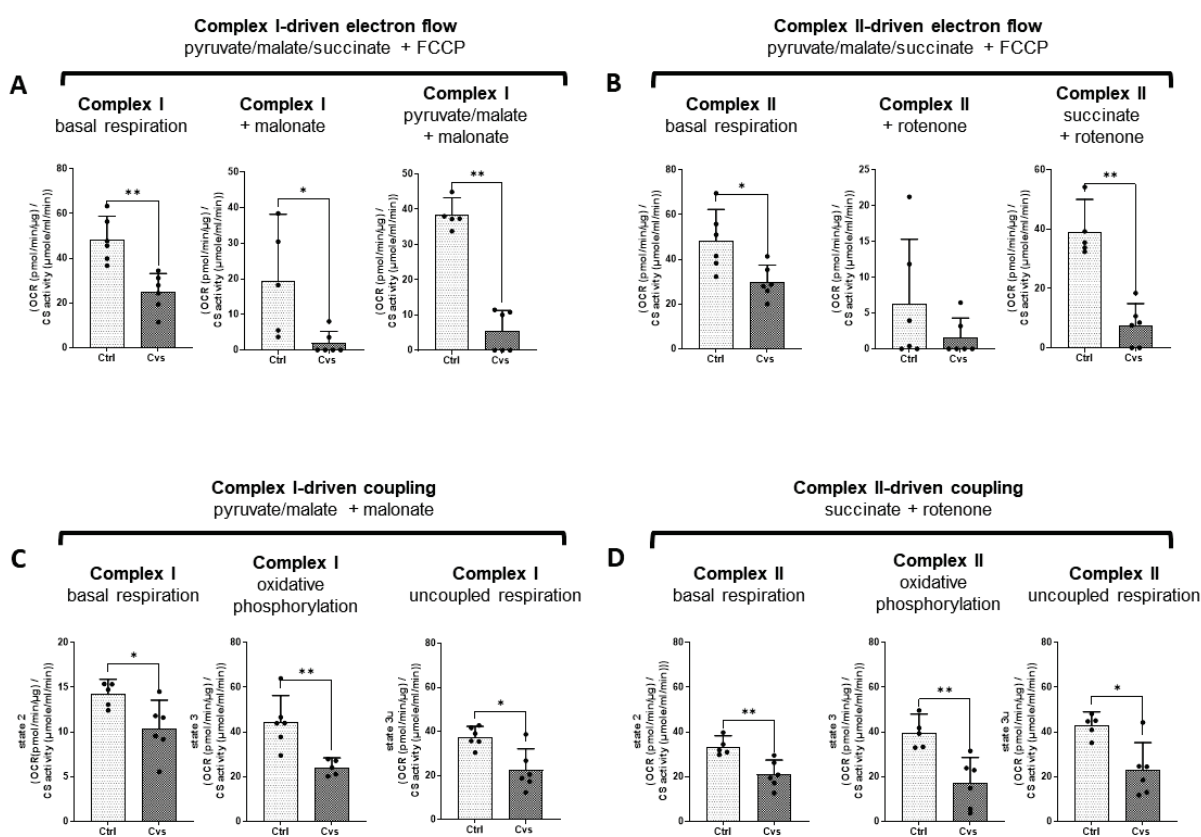


Figure 16: Electron flow and coupling experiments of mitochondrial ETC after Cvs.

Oxidative capacity was measured in the enriched mitochondrial fraction of Cvs vs Ctrl muscles in response to ETC manipulation. **(A)** Electron flow was measured in the uncoupled state of the mitochondrial membrane using a combination of pyruvate, malate, and succinate as substrates with two different injection strategies. The oxygen consumption rate (OCR) recorded during the time course of the experiment is shown. **(B)** Complex I-specific OCR was measured by stimulation of complex I with pyruvate and malate after inhibition of complex II with malonate; complex II-specific OCR was measured by stimulation of complex II with succinate after inhibition of complex I with rotenone. **(C)** Coupling experiments were conducted by measurement of OCR individually for complex I- and complex II-driven mitochondrial coupling in fractions of isolated muscle mitochondria. **(D)** Basal respiration (*state 2*), oxidative phosphorylation (*state 3*), maximal respiratory capacity (*state 3u*) are shown individually for complex I- and complex II-specific assay. Data are expressed as means ($\pm 95\%$ CI, $n=6$ per group). Statistics: Student's t-test, * $p<0.05$, ** $p<0.01$, *** $p<0.001$, **** $p<0.0001$, Ctrl: C57BL/6, Cvs: C57BL/6 after stress intervention. (according to Fig. 5, (Nikolic et al., 2023))

3.1.5 Bioenergetic assessment of mitochondrial respiratory control ratio and calculation of thermodynamic coupling and efficiency

For the assessment of the quality of mitochondrial activity, the respiratory control ratio (RCR), a reference value for proton leak was calculated (*state 3/state 4o*). The Cvs RCRs for neither complex I- nor complex II-driven respiration differ from the controls (Fig. 17A). To determine the thermodynamic coupling of oxidative phosphorylation capacity the q-value was calculated (Fig. 17B). This approached the thermodynamic set point of economic net output power at optimal efficiency. These analyses define the maximal net output flow (ATP) at optimal efficiency ($q_f=0.786$), maximal net output power ($q_e=0.910$), economic net output flow ($q_f^{ec}=0.953$), and economic net output power at optimal efficiency ($q_e^{ec}=0.972$) (Cairns et al., 1998). The oxidative phosphorylation capacity of complex I was unaltered by Cvs. For control

animals, the coupling of complex I ($> \text{stage } q_p (=0.910)$) is greater than that for complex II-driven respiration ($\text{stage } q_p^{ec} (=0.972)$) than that for complex I-driven respiration ($< \text{stage } q_f^{ec} (=0.953)$). In accordance with that, the efficiency of substrate to energy conversion ($\eta\text{-opt}$) related to the thermodynamic coupling shows significantly higher levels in Cvs mitochondria with an increase of up to 38.6% compared to the Ctrl group (Fig. 17C).

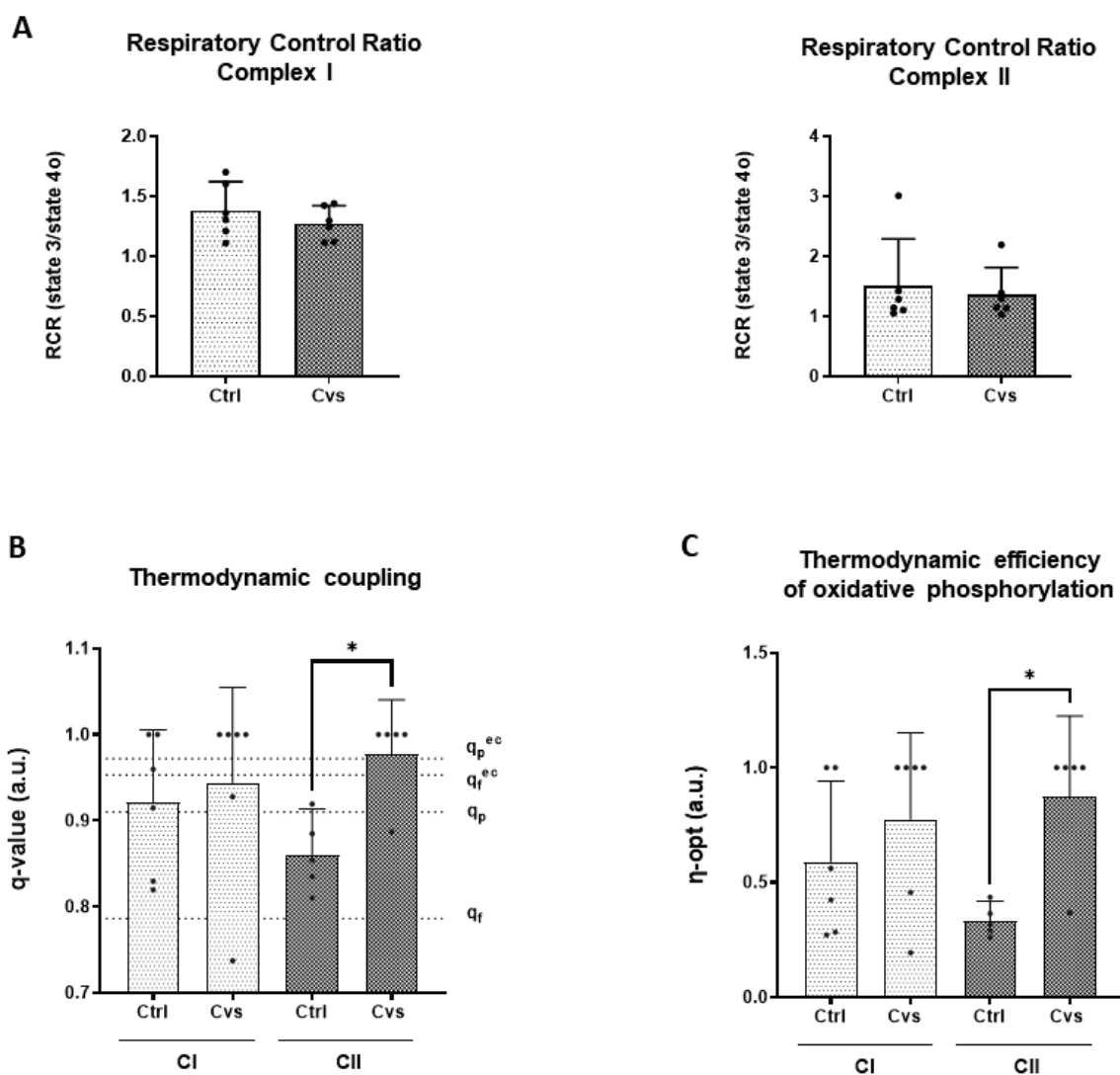


Figure 17: Respiratory control ratio, thermodynamic q value and calculated optimal thermodynamic efficiencies of mitochondrial complex I and II after Cvs.

Control values of mitochondria were measured in the enriched mitochondrial fraction of Cvs vs Ctrl muscles. **(A)** RCR ($\text{state } 3/\text{state } 4o$) was calculated from complex I- and complex II-specific respiration ($n=6$ animals per condition). **(B)** Calculated thermodynamic coupling q values are shown for complex I- and complex II-dependent respiration. hashed lines indicate the maximal coupling values of the thermodynamic set points corresponding to maximal net output flow (ATP) at optimal efficiency ($q_f=0.786$), maximal net output power ($q_e=0.910$), economic net output flow ($q_f^{ec}=0.953$), and economic net output power at optimal efficiency ($q_e^{ec}=0.972$), ($n=6$ animals per condition). **(C)** Calculated optimal thermodynamic efficiencies ($\eta\text{-opt}$) of oxidative phosphorylation are shown for complex I- and complex II-dependent respiration. Data are expressed as means ($\pm 95\%$ CI, $n=6$ per group). Statistics: Student's t-test, $*p<0.05$, Ctrl: C57BL/6, Cvs: C57BL/6 after stress intervention. (according to Fig. 6, (Nikolic et al., 2023))

3.1.6 Cvs impacts on muscle transcriptome and methylome

According to our hypothesis, Cvs interferes directly with metabolism but also initiates a memory effect for metabolic adaptation. The genome-wide DNA methylation patterns in *M. gastrocnemius* showed a tight correlation between the conditions and thereof no gross alteration directly after chronic stress in muscle (Supplementary Table 2, DOI: 10.1007/s00018-023-04761-4; Fig. 17).

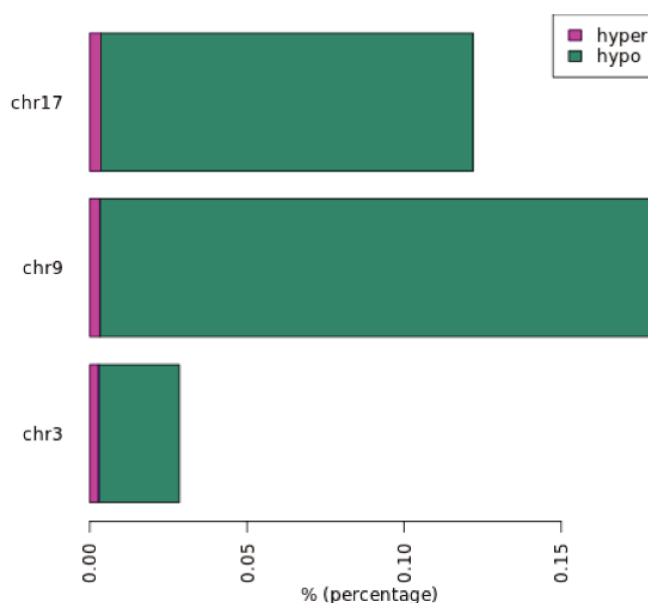


Figure 18: Differential methylated areas after Cvs intervention in gastrocnemius muscle.

Hyper and hypomethylated regions per chromosome as identified in differential methylation analyses (q-value <0.01, methylation difference >2 %; MethylKit, (BaseSpaceLabs, Illumina San Diego, USA); (n = 5 animals/ group)). Corresponding data are given in Supplement Table 2, DOI: 10.1007/s00018-023-04761-4, Datasheet “Differential Methylation”. (according to Supplement Fig. 6, (Nikolic et al., 2023))

The only significant variations found on methylation level were the hypomethylation of three intergenic areas including some coding genes like neuroactive *Gphn*, *DDscaml*, cell cycle active *Sdk1*, *Mid1*, and the nuclear-encoded mitochondrial leucyl-tRNA synthetase *Lars2*, but methylation differences were low (Supplementary Table 2, DOI: 10.1007/s00018-023-04761-4). Consistently, there were no changes in Sirt and MTase activity (Fig. 19).

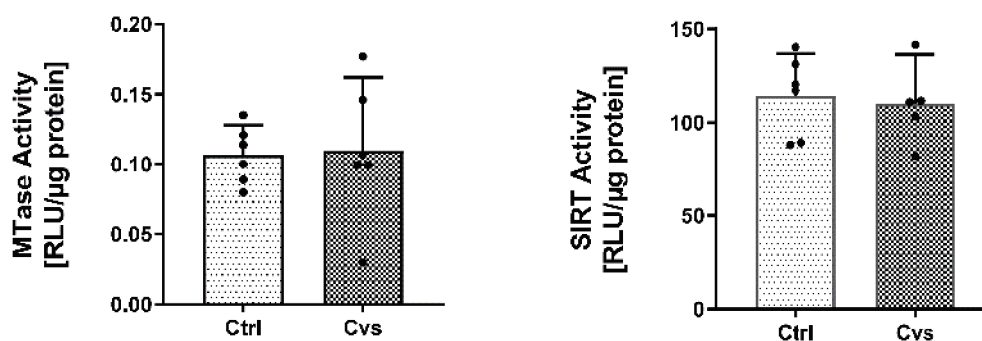


Figure 19: Cvs does not affect DNA modifying enzyme activity.

Enzyme activity of methyltransferases (MTase) and sirtuins (histone deacetylases class III: SIRT1 to SIRT7), in muscle from Cvs compared to Ctrl mice ($n = 6$ animals/ group). Data are presented as mean \pm 95 % CI. Single measurements of each animal are shown as dots. Statistics: Mann–Whitney test, not significant. Ctrl: C57BL/6, Cvs: C57BL/6 after stress intervention. (according to Supplement Fig. 7, (Nikolic et al., 2023))

In concordance, there was no gross significant alteration in transcriptome level maintained after the stress phase within Cvs and Ctrl mice even for 1.2-fold expression differences (p -value <0.05) (Supplementary Table 3, DOI: 10.1007/s00018-023-04761-4; Fig. 19).

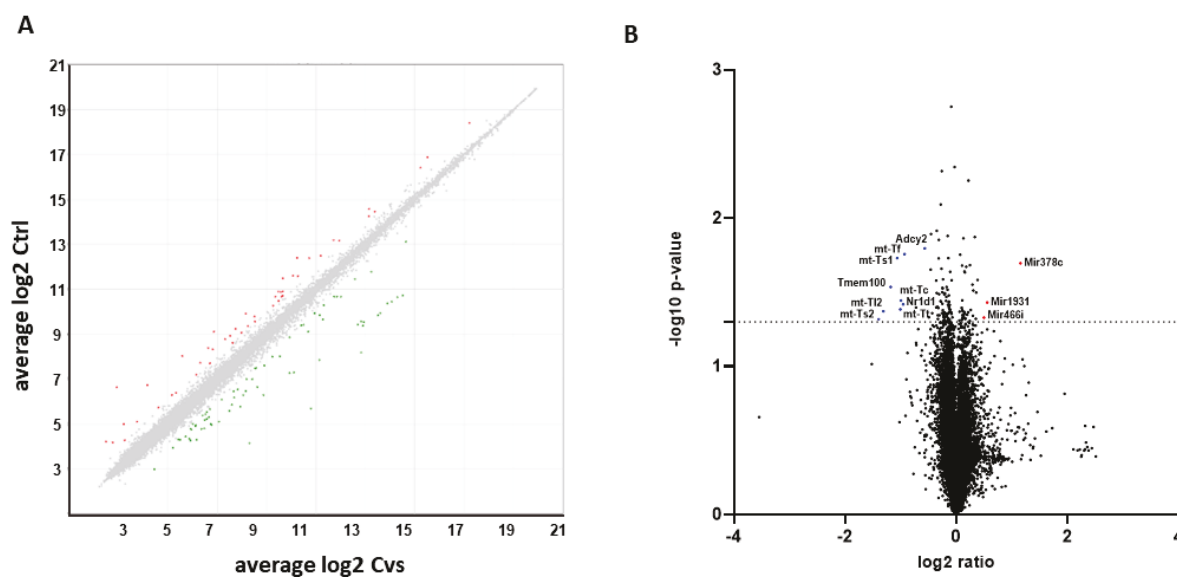


Figure 20: Transcriptome analyses of gastrocnemius muscle after Cvs.

(A) Scatter plot with 1.2-fold difference (y-axis: Avg Log2 condition Ctrl; x-axis Avg Log2 condition CVS). (B) The log2 fold changes of transcriptome data abundance in Cvs compared to Ctrl mice ($n = 5$ animals/ group). 14084 RNA transcripts were detected. Upregulated (Red; $n = 3$) or downregulated (blue; $n = 10$) were determined by Student's t-test ($p < 0.05$) with 1.2- fold regulation. Corresponding data are given in Supplement Table 3, DOI: 10.1007/s00018-023-04761-4. (according to Supplement Fig. 8, (Nikolic et al., 2023))

Nevertheless, ND1R1 and 6 mitochondrial tRNAs (mt-Tc, mt-Tt, mt-Tf, mt-TI2 and the mitochondria-specific iso-acceptors mt-Ts1, mt-Ts2) were in the 10 most suppressed transcripts after Cvs (Fig. 20). Mitochondrial tRNAs differ from nuclear tRNAs in sequence, stability, and folding, and are essential for mitochondrial protein synthesis. This may indicate

alterations in the translation of mitochondrial-coded transcripts, and may additionally point to the central role of mitochondrial function after Cvs also in the long-term alterations.

3.2 Immediate effect of Cvs on energy balance leads to metabolic adaptation with longitudinal effect on liver gene regulation of C57BL/6 mouse.

The second part of this work focuses on the study of liver tissue and whether the altered energy balance after chronic stress (Cvs) has altered metabolism and thus has an impact at a longitudinal level such as gene regulation, with direct influence on the maintenance of a healthy energy balance.

For this study, four additional experimental cohorts were used to provide the amount of data and analysis from liver tissue: 1. for indirect calorimetry and acute analyses in primary hepatocytes (n=5 animals per group); 2. for body composition and liver tissue data including acute methylome and transcriptome (acuteCvs; acuteCtrl) (n=6 animals per group); 3. for methylation and transcriptional analyses after a 3-month recovery phase (recoveryCvs) (n = 3-5 animals per group) (recoveryCvs; recoveryCtrl); 4. for analyses in primary hepatocytes after the recovery phase (n=5 animals per group). Additionally, with the further cohort of stress animals the correctness and variability of the stress protocol (Cvs) was examined and proven. Dr. M. Dille, (Institute of Clinical Biochemistry at the German Diabetes Center) applied the Cvs protocol to the recovery cohorts 3 and 4. Dr. M. Dille collected liver biopsies stored at -80°C of cohort 3, and performed mitochondrial respiration and glycolysis analysis in the Seahorse XF assay (2.2.8.5) on primary hepatocytes (2.2.8.1) of cohort 4. In this thesis, stored biopsies of cohort 3 were used for transcriptome and methylation analyses. The data interpretation on energetic flexibility of hepatocytes, i.e. energy map (2.2.8.5) (unpublished data) was performed as part of this thesis based on data collected from cohort 4 as part of a previous project (Dille, Nikolic et al. 2022). The described results of this work for liver tissue are prepared as results section of a manuscript yet under revision. All analyses and calculations of the data sets shown in the result section and the manuscript were performed as part of this thesis.

3.2.1 Cvs interferes with hepatic metabolism

Immediately after undergoing our stress protocol, stressed C57BL/6 mice (Cvs) or untreated littermates (Ctrl) were tested for acute metabolic effects. Cvs mice exhibited a decrease in body weight (6.2%), fat mass (21%), and lean mass (8.1%) (Fig. 21 A – C) compared to the Ctrl mice, despite unchanged food intake (Fig. 21D). Levels of non-fasted plasma blood glucose, insulin, glucagon, and leptin were unchanged in Cvs mice (Fig. 21E – H). Insulin resistance and dysfunctional gluconeogenesis could also be excluded via glucose- and pyruvate tolerance test (GTT, PTT) (Fig. 22A, B). Plasma lactate, glutamate, and triglyceride levels showed no significant changes (Fig. 21I – K), while the non-esterified fatty acids (NEFA) levels were three times higher in Cvs mice than in Ctrl mice (Fig. 21L).

Detailed analyses revealed increased linoleic acid (cC18:2) (14.6%) and decreased arachidonic acid (cC20:4) (27.7%) levels after Cvs compared to Ctrl (Fig. 21M).

Diurnal metabolic capacity assessed by indirect calorimetry to distinguish between low (light) and high (dark) activity levels. Total energy expenditure (EE) throughout the observation period was significantly lower after Cvs compared to Ctrl (Cvs: 6.7 ml/min/g^{*0.75}; Ctrl: 7.3 ml/min/g^{*0.75}), especially during the dark phase (Ctrl: 8.0 ml/min/g^{*0.75}; Cvs: 7.3 ml/min/g^{*0.75}) (Fig. 21N). Furthermore, the correlation analysis between plasma parameters and light and dark EE showed a significant relationship between dark EE and plasma NEFA (dark: R² = 0.5491; p = 0.0354) and especially cC18:2 (dark: R² = 0.6574; p = 0.0146) after Cvs. The respiratory exchange ratio (RER) remained unchanged throughout the observation period after Cvs (Fig. 21O). Diurnally, RER was higher in the dark phase (Ctrl: + 7.7%; Cvs: + 13%) in both groups compared to the light phase. In stressed animals, RER was significantly decreased by 6.5% in the light phase (Ctrl: 0.91 mg/min; Cvs: 0.85 mg/min) compared with control mice (Fig. 21O). Again, only NEFAs correlated with RER, particular light phase RER (light: R² = 0.5083; p = 0.0471), and cC18:2 (light: R² = 0.5136; p = 0.0455) after Cvs.

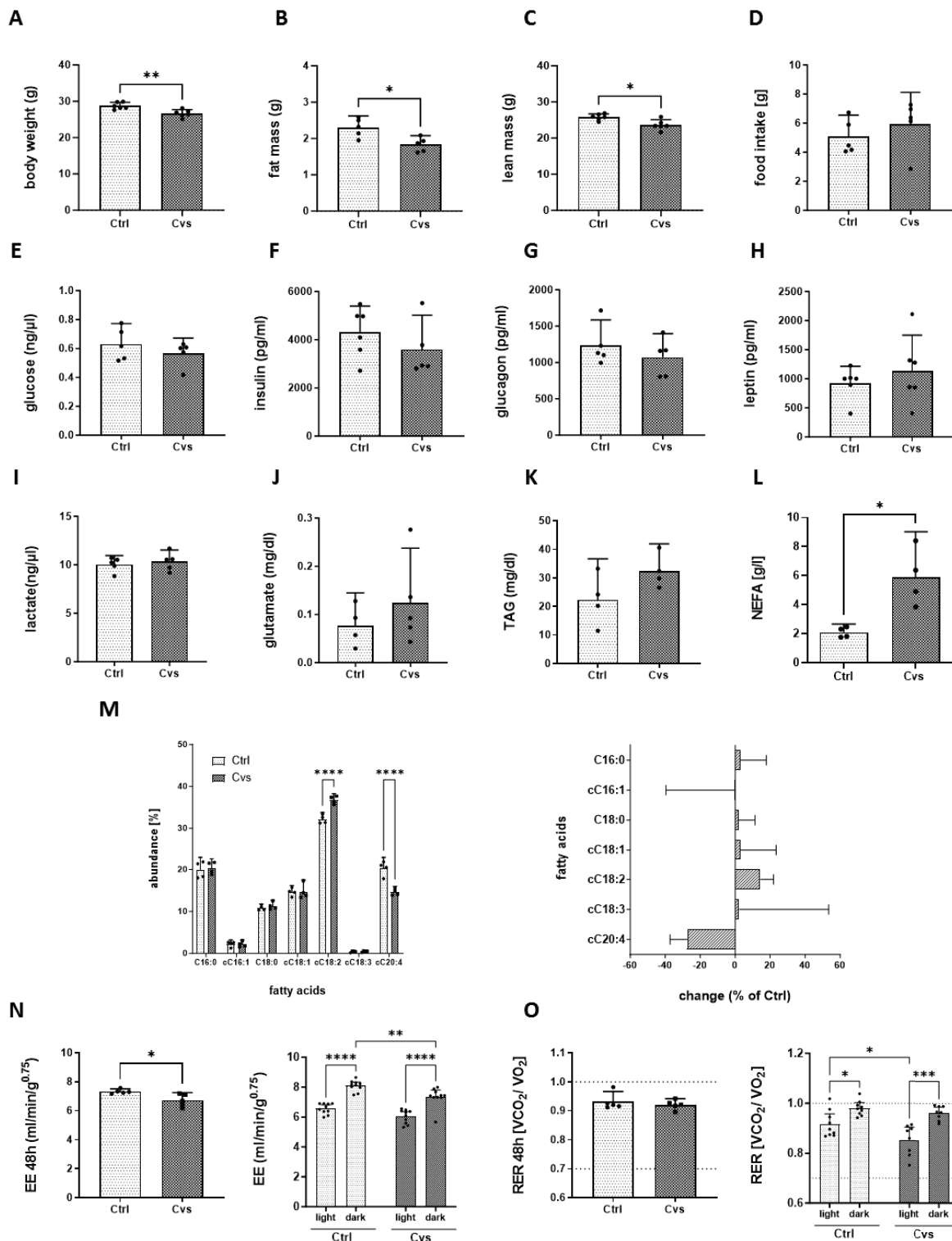


Figure 21: Systemic effects of a 15-day chronic stress intervention (Cvs).

NMR-determined analyses of (A) body weight, (B) fat mass, and (C) lean mass, after chronic variable stress in control (Ctrl) and Cvs mice ($n=6/\text{group}$). (D) Differences in food intake during Cvs intervention are shown per group ($n=6/\text{group}$). Intermediate substrate levels of (E) glucose, (F) insulin, (G) glucagon, (H) leptin, (I) lactate, (J) glutamate, (K) TAG, (L) NEFA in plasma after Cvs compared to Ctrl group. (M) Plasma NEFA composition of Ctrl and Cvs animals. Mean values for the percentage distribution are shown. The sum of measured fatty acids was set to 100%. Asterisks indicate significant changes in fatty acid content ($p<0.01$). (N) Indirect calorimetry with total energy expenditure (EE) and (O) respiratory exchange ratio (RER) and their differences during light and dark phases. For all analyses, bar graphs represent the mean $\pm 95\%$ CI ($n=5-6/\text{group}$). Individual measurements are shown as dots. Statistics: Mann-Whitney test or one-way ANOVA with Tukey test for multiple comparisons, * $p<0.05$, ** $p<0.01$, *** $p<0.001$, **** $p<0.0001$, Ctrl: C57BL/6, Cvs: C57BL/6 after stress intervention. Indirect calorimetry data

are given over 48h or the combined results of light and dark phases are reported individually. The dashed lines in the RER plot (O) mark the thresholds for preferential carbohydrate oxidation ($VCO_2/VO_2 = 1.0$) or lipid oxidation ($VCO_2/VO_2 = 0.7$).

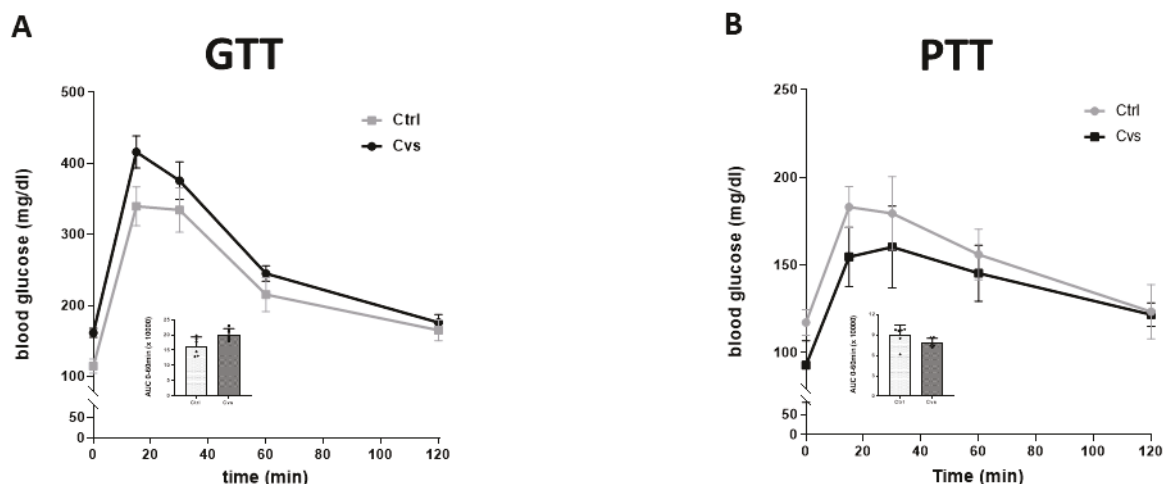


Figure 22: Intraperitoneal glucose (i.p. GTT), pyruvate (i.p. PTT) tolerance test of plasma after Cvs. *In vivo* analysis of glucose homeostasis in Ctrl and Cvs mice. (A) Glucose tolerance test (i.p.GTT) after 6h, and (B) Pyruvate tolerance test (i.p.PTT) as surrogate for liver functionality after 16h of fasting via intraperitoneal injection of glucose or pyruvate, respectively. AUC: Area under the curve, Ctrl: C57BL/6, Cvs: C57BL/6 after stress intervention. *In vivo* analyses (n=6 animals per condition).

3.2.2 Altered protein abundance in main pathways for glucose and lipid metabolism after Cvs

To investigate the immediate impact of the stress intervention on metabolic pathways, a label-free proteomic analysis was performed on the hepatic 11,000xg protein fraction to assess the status quo immediately the intervention. In addition, enzyme activity assays were conducted *ex vivo* on isolated hepatocytes, as the major metabolic cell type in the liver, to study key pathways related to glucose and lipid metabolism. Proteomic analyses revealed 3222 differentially abundant proteins. Of these, 29 proteins were significantly up-regulated and 91 down-regulated in Cvs mice (ratio:>1.5; p-value: < 0.05). Gene ontology (GO) analysis of biological processes revealed up-regulation of catabolic processes and a down-regulation of anabolic processes immediately after stress intervention (Supplement Table Proteome).

In terms of glucose homeostasis, the abundance of detected proteins involved in the glycolysis pathway was significantly reduced ($p < 0.0001$). Consistent with this observation, the glucose-stimulated rate of glycolysis in primary hepatocytes was 39% lower immediately after the stress intervention (Fig. 23A). Although proteins involved in ketone metabolism were enriched in the Cvs group ($p < 0.05$), the intra-individual variation was large and there were no significant changes in β -hydroxybutyrate concentrations immediately after the intervention (Fig. 23B). Proteins involved in gluconeogenesis were less abundant after the stress intervention ($p < 0.0001$). Although basal rates of hepatocyte gluconeogenesis were 2-fold higher, the ability to achieve substrate-stimulated glucose secretion was reduced in the Cvs group compared to

the Ctrl group. The suppression of gluconeogenesis by insulin administration was also reduced in hepatocyte culture (Fig. 23C). Interestingly, the glucose abundance in liver, which reflects glucose homeostasis in the liver, was not significantly altered immediately after the stress intervention (Fig. 23D).

Regarding the immediate effect of the stress intervention on lipid metabolism, exposure to Cvs resulted in decreased abundance of proteins associated with *de-novo* lipogenesis (DNL) ($p < 0.0001$). However, the DNL activity in hepatocytes was not significantly different between the two groups (Fig. 23E). The abundance of proteins involved in triglyceride synthesis/lipid droplet formation, and hepatic triglyceride (TG) levels did not change significantly following Cvs (Fig. 23F). In contrast, protein abundance of the mitochondrial β -oxidation pathway was significantly increased ($p < 0.0001$), which was accompanied by a 6-fold increase in mitochondrial β -oxidation activity after Cvs in hepatocytes (Fig. 23G). Furthermore, a significant correlation between the β -oxidation rate in hepatocytes and dark EE (dark: $R^2 = 0.5996$; $p = 0.0410$) was observed, highlighting the immediate effect of the stress intervention on mitochondrial function.

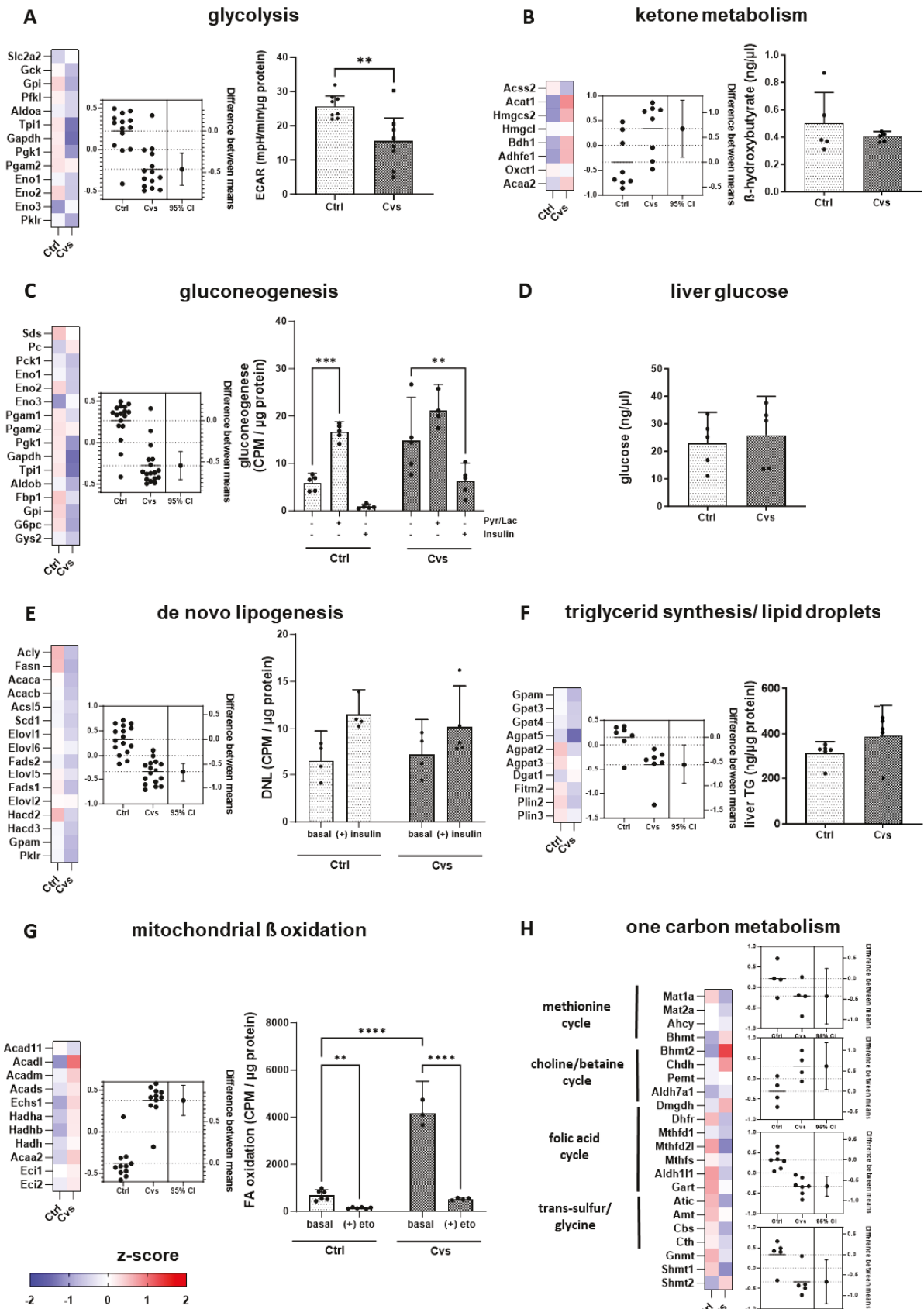


Figure 23: Cvs intervention impairs the proteome abundance and ex vivo activity of key metabolic pathways.

Proteomic data and the respective ex vivo metabolic activities in primary hepatocytes isolated from Ctrl and Cvs livers are shown as bar graphs. (A) Glycolysis, (B) ketone metabolism, (C) gluconeogenesis, (D) glucose

abundance in liver tissue determined by glucose assay kit (Sigma-Aldrich, Darmstadt, Germany, MAK263), **(E)** de novo lipogenesis **(F)** TG synthesis/lipid droplet formation and hepatic TG content, **(G)** mitochondrial β -oxidation, and **(H)** protein abundance of one-carbon metabolism, Z-score plots show the over- and underrepresentation of proteins associated with the indicated signaling pathways from a label-free proteome analysis of the liver 11,000 xg protein fraction. Red represents up-regulation, blue represents down-regulation, and white represents no change in protein abundance of the mean of each condition relative to the overall mean of the experiment. The corresponding estimation plots show the mean values for each protein (dots) and the mean change in the pathway of the Cvs and Ctrl group $\pm 95\%$ CI. The left axis shows the mean z-score and the right axis shows the effect size (n=5/group). Statistics: Mann-Whitney test or one-way ANOVA with Tukey test for multiple comparisons, **p<0.01, ***p<0.001, ****p<0.0001, Ctrl: C57BL/6, Cvs: C57BL/6 after stress intervention. Proteome analysis (n=5/group), activity assays in hepatocytes (n=6/group). TG: triglyceride, FA: fatty acid, Pyr/Lac: pyruvate/lactate, eto: etoxomir.

3.2.3 Cvs increases mitochondrial thermodynamic efficiency of complex I in liver

In liver, mitochondrial DNA amount, membrane integrity based on cytochrome-c-oxidase activity, or content determined by the commonly used validated biomarker citrate synthase activity (McLaughlin et al., 2020) was not altered by Cvs (Fig. 24A). Apart from energy metabolism, maintenance of the cellular redox balance by mitochondria is an important mediator of signal transduction, genetic and epigenetic processes. The status of oxidative stress was assessed by proteome analyses of redox-regulating proteins and the measurement of the reaction of malondialdehyde with thiobarbituric acid. The results showed a decreased abundance of redox-regulating proteins in the Cvs group (p < 0.0001), with enzyme analysis indicating unchanged redox balance in Cvs compared to Ctrl (Fig. 24B).

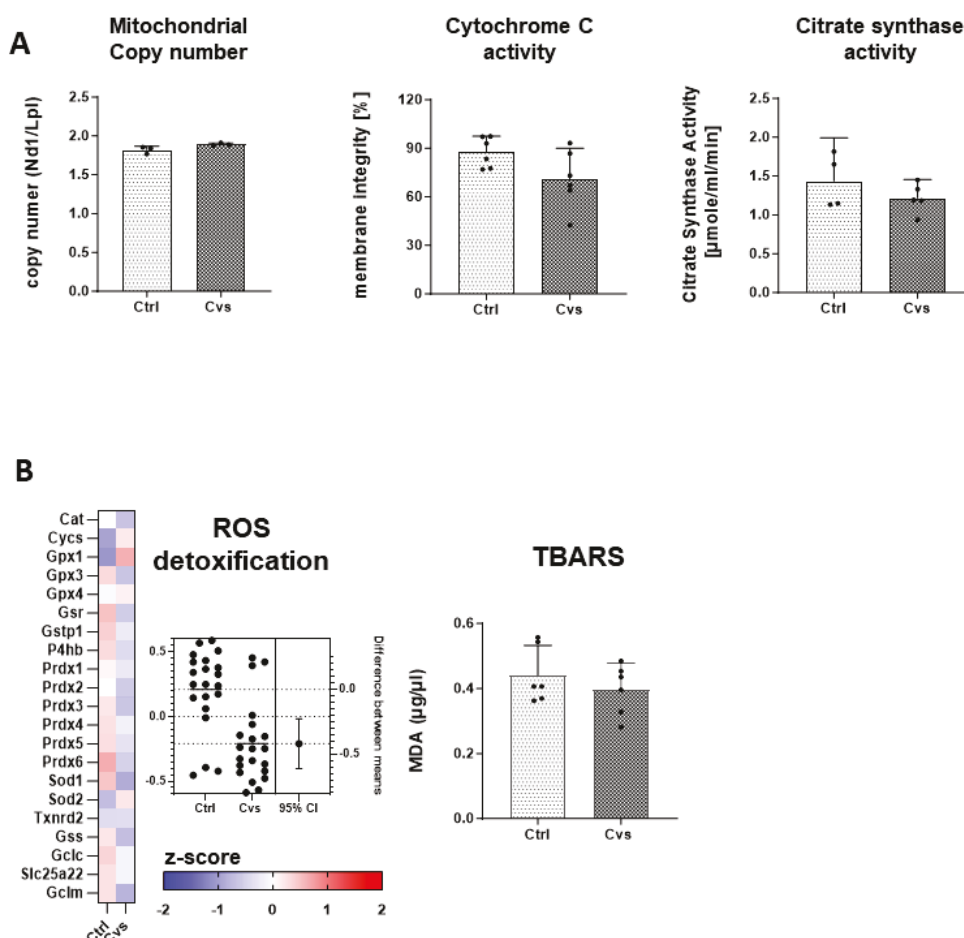


Figure 24: Cvs does not affect mitochondrial mass, membrane integrity, and ROS.

(A) Relative mtDNA/nuclear DNA ratio was analysed in liver tissue from Cvs and Ctrl groups. The percentage of membrane integrity derived from cytochrome-c-oxidase activity and citrate synthase activity from fractions of enriched mitochondria (n=6/group). (B) Plotted z-score analyses and estimation plot of proteins involved in ROS detoxification. The z-score plot shows the over and under-represented proteins of the indicated pathway. Red identifies upregulation, blue identifies downregulation, and white indicates no change of protein abundance to the mean of each condition with respect to the overall experimental mean. The corresponding estimation plot shows on the left axis scatter dot plots with mean z-scores, while dots represent each pathway protein as mean of n=5/ group. On the right axis the mean \pm 95 % CI alteration in pathway protein abundance of the Cvs and Ctrl comparison is shown. Malondialdehyde (MDA) concentration was measured fluorometrically after reaction with TBARS of 600 μ g liver fraction (n=5 animals/ group). Data (bar graphs) are expressed as means \pm 95 % CI. Statistics: Mann-Whitney test, not significant. Single measurements of each animal are shown as dots. Ctrl: C57BL/6, Cvs: C57BL/6 after stress intervention. TBARS: Thiobarbituric Acid Reactive Substances; ROS: reactive oxygen species.

However, the mitochondrial protein composition derived from the proteome analyses showed that the differential abundance of the electron transport chain (ETC) proteins in total resulted in a significant increase in the components of complexes (C)I (p<0.0001), CII (p=0.0279), CIII (p<0.0001), CIV (p=0.0474) and CV (p<0.0001) after Cvs compared to Ctrl (Fig. 25A). In addition, the electron transport capacity in the uncoupled state, without substrate limitation in enriched mitochondria indicated that the electron flow capacity via complex I remains unaltered, but increased via complex II after Cvs compared to Ctrl. Complex IV activity also showed enhanced function after Cvs compared to Ctrl when directly targeted by the electron donor TMPD (Fig. 25B).

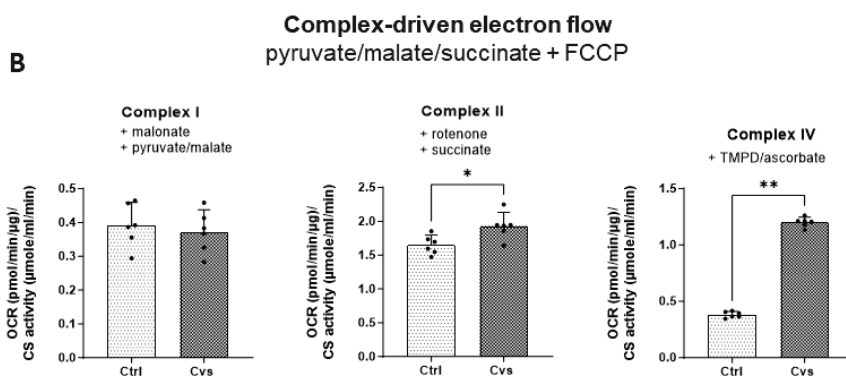
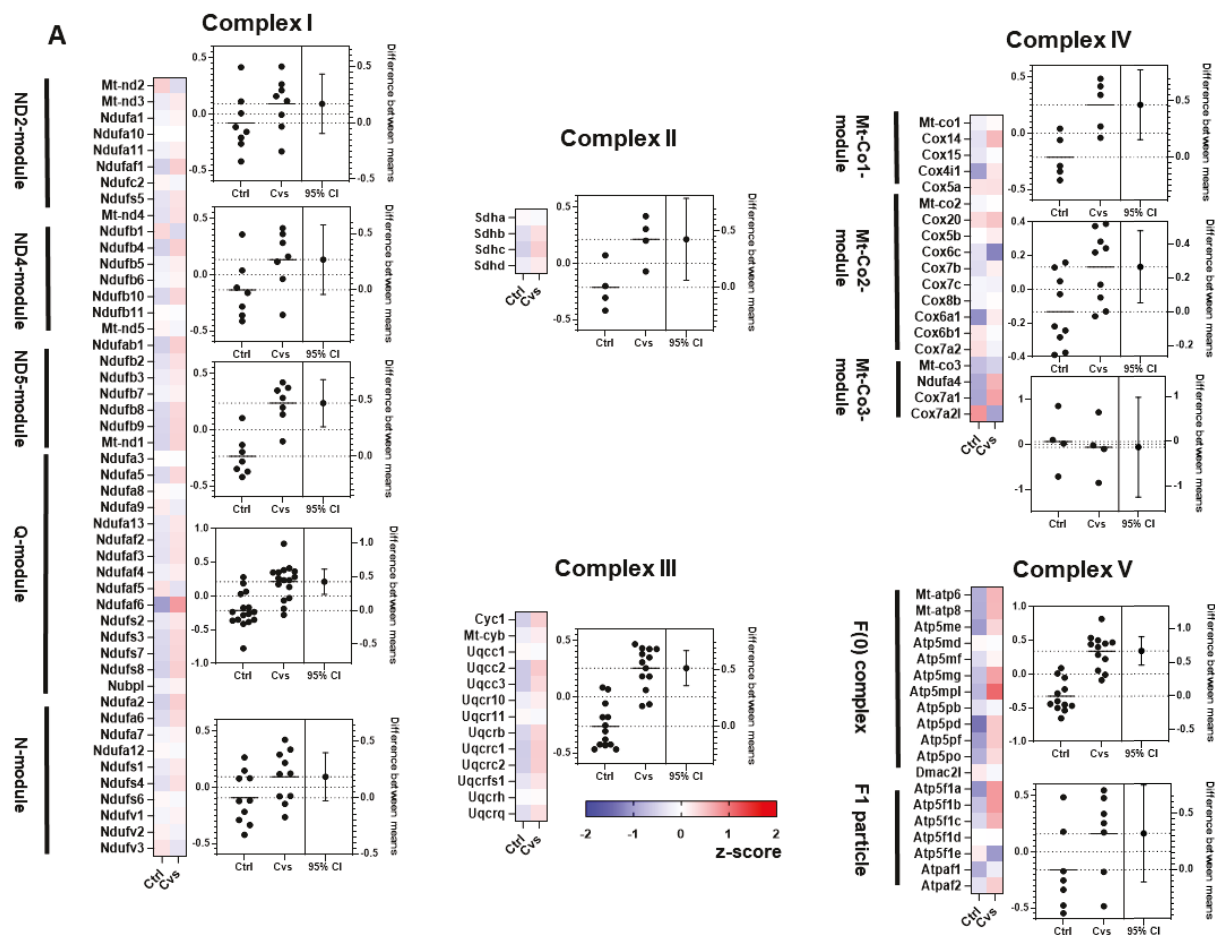


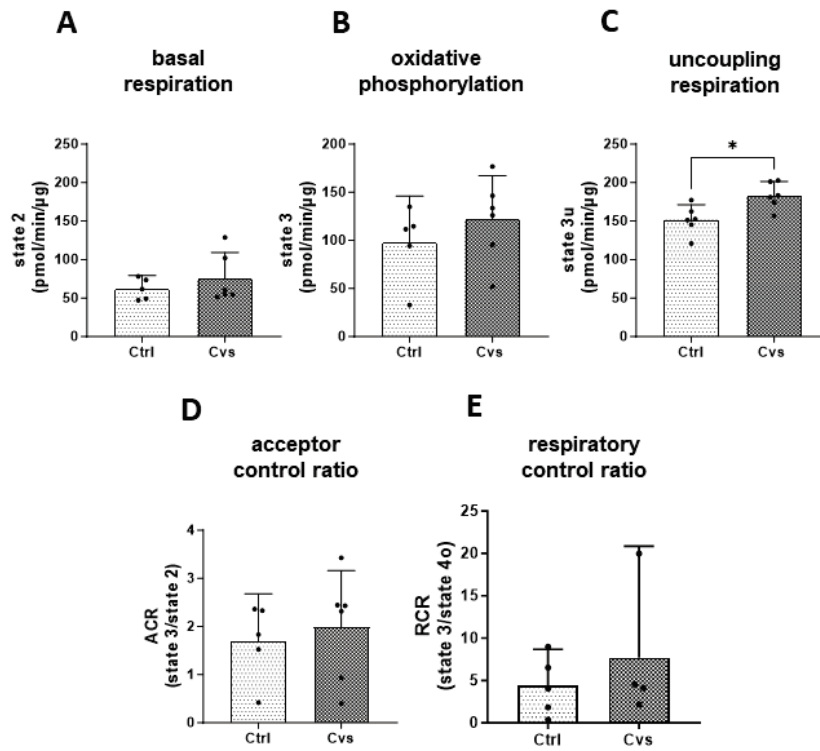
Figure 25: Mitochondrial proteome and electron flow assessment.

(A) Heat maps resulting from z-score analyses and estimation plots of protein abundance for individual complex I, II, III, IV, and V subunits of the electron transport chain. Red indicates up-regulation, and blue indicates down-regulation of proteins. White indicates no change. (B) Electron flow was measured in the 11,000xg fraction at uncoupled state of the mitochondrial membrane using a combination of pyruvate, malate, succinate, and FCCP present in the assay solution with injection strategies specific to the respective complex. The oxygen consumption rate (OCR) in relation to citrate synthase activity (CS) is shown. Injection strategies: Complex I was stimulated with pyruvate and malate after inhibition of complex II using malonate; complex II was stimulated with succinate after inhibition of complex I with rotenone; complex IV was stimulated by TMPD/ascorbate after inhibition of complex III using Antimycin A. Ctrl: C57BL/6, Cvs: C57BL/6 after stress intervention. Ctrl: C57BL/6, Cvs: C57BL/6 after stress intervention. Data are expressed as mean \pm 95% CI (n=6/group). Individual measurements are shown as dots. Statistics: Mann-Whitney test or one-way ANOVA with Tukey test for multiple comparisons, *p<0.05.

Therefore, further analysis of mitochondrial function focused on the coupling efficiencies of specifically complex I- and complex II-driven coupling efficiencies of complexes I to IV of the electron transport chain (ETC) and ATP synthase (complex V). Here we measured, basal oxygen consumption rate (OCR) and the electron transport capacity with complex-specific substrate limitation in enriched liver mitochondria, with simultaneous inhibition of the respective other complex using either malonate or rotenone in two different experimental setups Fig. 27A, B). Complex I-driven respiration was forced by the substrates pyruvate/malate and concomitant inhibition of complex II by malonate (Fig. 27A).

Detailed examination of complex I-driven oxygen consumption of mitochondria (states 2, 3, 3u, 4o) and calculated measures of oxidative phosphorylation coupling, i.e. ACR and RCR (Fig 26 A-E), revealed significantly increased OCR in state3u by 21% in Cvs compared to Ctrl (Fig. 26C), whereas complex II-specific coupling was not affected by Cvs (Fig. 26F- J).

Complex I-driven coupling:



Complex II-driven coupling:

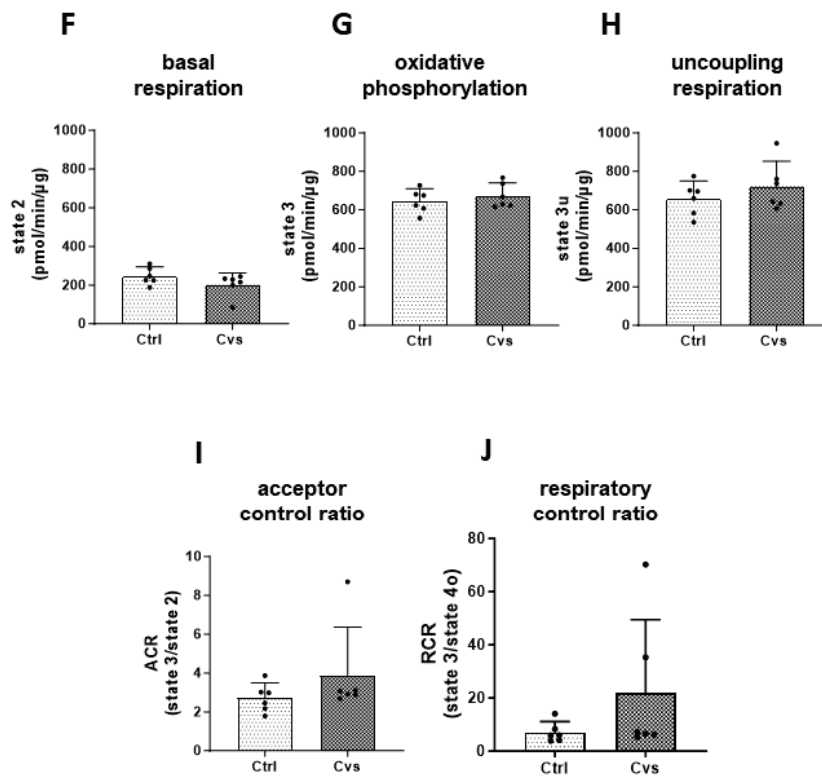


Figure 26: Calculating of classical mitochondrial respiratory states after Cvs.

Experiments were performed specifically for complex I- and complex II-driven mitochondrial coupling by measurement of the oxygen consumption rate (OCR). Complex I-specific OCR was measured by stimulation of

complex I with pyruvate and malate and simultaneous inhibition of complex II using malonate. Complex II-specific OCR was measured by stimulation of complex II with succinate and simultaneous inhibition of complex I using rotenone. **(A, F)** Basal respiration (*state 2*), **(B, G)** oxidative phosphorylation (*state 3*), **(C, H)** uncoupled respiration (*state 3u*), **(D, I)** the acceptor control ratio (ACR) (*state 3/state 2*), and **(E, J)** the respiratory control ratio (RCR) (*state 3/state 4o*) are shown for the complex I- and complex II-specific assays. Ctrl: C57BL/6, Cvs: C57BL/6 after stress intervention. Data are expressed as mean \pm 95% CI (n=6/group). Statistics: Mann-Whitney test or one-way ANOVA with Tukey test for multiple comparisons, * $p < 0.05$.

For detailed bioenergetic evaluation we calculated the degrees of thermodynamic coupling, i.e. q-values, applying thresholds for maximum net output current (ATP) at optimal efficiency ($q_f = 0.786$), maximum net output power ($q_e = 0.910$), net economic output current ($q_f^{ec} = 0.953$), and net economic output power at optimal efficiency ($q_e^{ec} = 0.972$) (Peronnet and Massicote, 1991). Bioenergetic assessment of enriched mitochondria with controlled substrate delivery showed that the maximal net ATP output was at optimal efficiency ($> q_f (= 0.786)$) in Ctrl animals, whereas the q-value was increased to a maximal net output ($> q_e (= 0.910)$) in the stress animals (Fig. 27C). For complex II thermodynamic coupling, Ctrl mice just reached the maximum net output ($< q_e (= 0.910)$), and Cvs mice were near the net economic output current ($< q_f^{ec} (= 0.953)$) (Fig. 27C). In accordance with that, the thermodynamic efficiency of substrate to energy conversion ($\eta-opt$) related to the thermodynamic coupling shows a significant 2-fold increase in Cvs mitochondria specific to complex I compared to the Ctrl group but remained unchanged to complex II between the groups (Fig 27D). The $\eta-opt$ of complex I was significantly negatively correlated with dark EE (dark: $R^2 = 0.6852$; $p < 0.01$) and positively correlated with plasma NEFA ($R^2 = 0.7978$; $p < 0.01$) after Cvs in contrast to Ctrl. The $NAD^+/NADH$ ratio closely associated with complex I activity was significantly increased by 3-fold ($p = 0.0079$) compared to Ctrl (Fig. 27E), and the FAD^+ content closely related with complex II remained unchanged (Fig. 27F). The activity of NAD^+ -dependent sirtuins (Sirt) was decreased following Cvs, whereas methyltransferase (MTase) activity remained unchanged (Fig. 27G, H). To account for a metabolic memory of Cvs, the energetic phenotype was assessed acutely after Cvs and after a recovery phase by plotting mitochondrial oxygen consumption rate (OCR) versus extracellular acidification rate (ECAR) in primary hepatocytes (Fig. 27I). Comparison of hepatocytes from acuteCvs and acuteCtrl showed no differences in basal and uncoupled energy phenotype. However, after recovery, the uncoupling of hepatocytes derived from *recoveryCvs* shifts towards the basal energy status of the cells, while hepatocytes from the *recoveryCtrl* still show a more energetic phenotype. These results indicate a long-term loss of metabolic flexibility in cells derived from stressed animals.

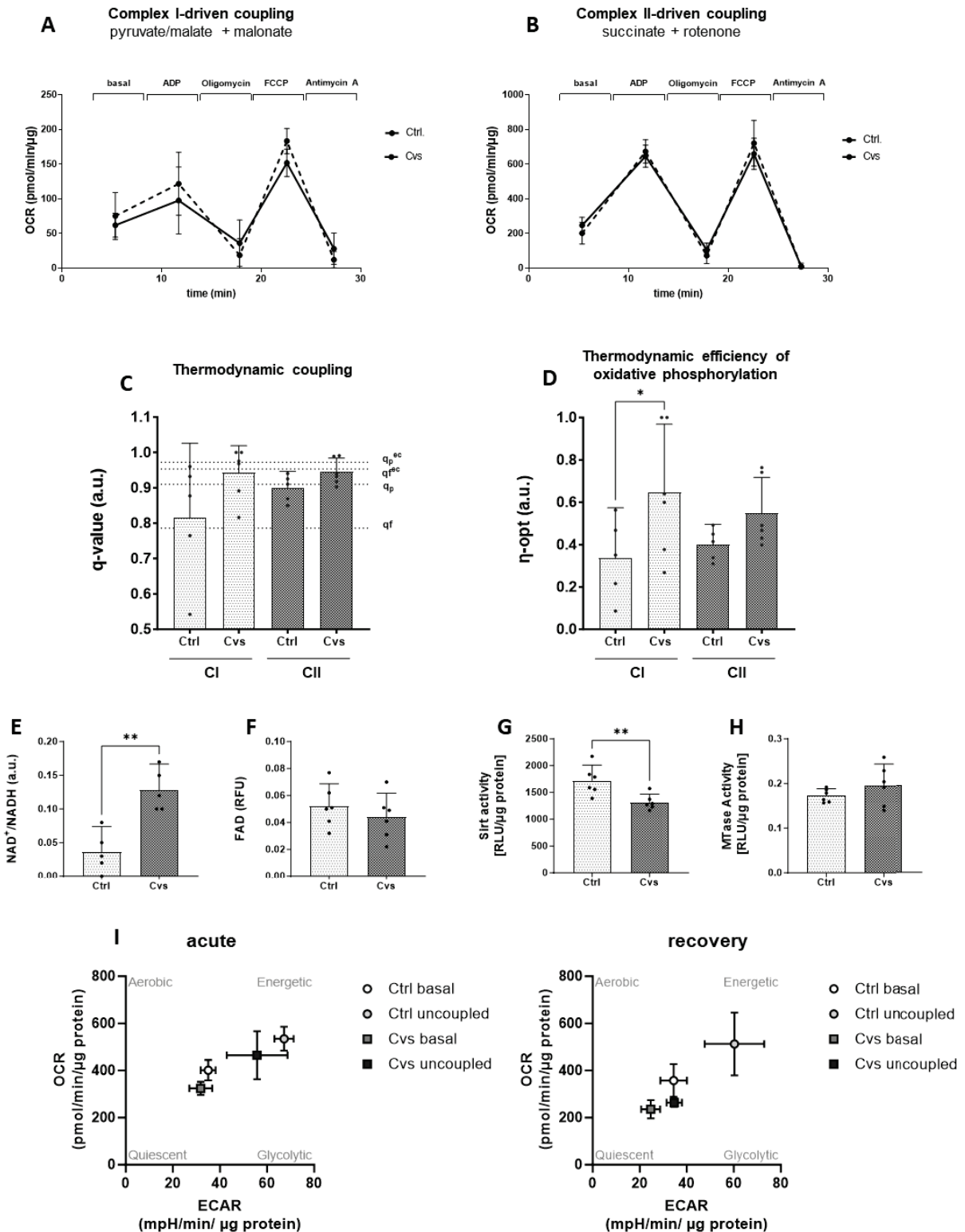


Figure 27: Mitochondrial complex I efficiency is impaired after Cvs.

Mitochondrial coupling efficiency, thermodynamic coupling and thermodynamic efficiency of oxidative phosphorylation specific for complex I and complex II of the ETC were studied in enriched mitochondrial fractions (11.000 xg) from Ctrl vs Cvs livers. Experiments were performed specifically for complex I- and complex II-driven mitochondrial coupling by measurement of the oxygen consumption rate (OCR). **(A)** Complex I-specific OCR was measured by stimulation of complex I with pyruvate and malate and simultaneous inhibition of complex II using malonate. Complex II-specific OCR was measured by stimulation of complex II with succinate and simultaneous inhibition of complex I using rotenone **(B)**. Mitochondrial respiration was measured under basal experimental conditions and in response to serial injection of ADP, oligomycin, FCCP, and Antimycin A. Data points represent the mean of n=6 animals/group shown as mean \pm 95% CI. **(C)** Thermodynamic coupling q-values, and the **(D)**

thermodynamic efficiency (η -opt) of oxidative phosphorylation calculated for both the complex I- and complex II-specific respiration for the overall assessment of mitochondrial function are shown. Dotted lines indicate the maximal coupling values of the thermodynamic thresholds corresponding to maximal net output flow (ATP) at optimal efficiency ($q_r = 0.786$), maximal net output power ($q_e = 0.910$), economic net output flow ($q_e^{ec} = 0.953$), and economic net output power at optimal efficiency ($q_e^{ec} = 0.972$). OCR values for all experiments were normalized by citrate synthase activity to adjust for possible changes in mitochondrial content. **(E)** NAD⁺/NADH ratio, **(F)** FAD⁺ abundance, **(G)** sirtuin (SIRT) activity, **(H)** methyltransferase (MT) activity was assessed in enriched hepatic mitochondria to monitor energy equivalent homeostasis. **(I)** Mitochondrial energy phenotype immediately after Cvs (acute) and after 3-month recovery (recovery) compared to age-matched controls in primary hepatocytes culture at basal and uncoupled conditions. Energetic phenotype was assessed by plotting OCR vs ECAR (n=6/group). All OCR values were normalized by citrate synthase activity to adjust for mitochondrial content. Ctrl: C57BL/6, Cvs: C57BL/6 after stress intervention. Data are expressed as mean \pm 95% CI (n=6/group). Individual measurements are shown as dots. Statistics: Mann-Whitney test or one-way ANOVA with Tukey test for multiple comparisons, *p<0.05. Raw data for energy map **(I)** was conducted by Dr. M. Dille, analyses and interpretation were made by Aleksandra Nikolic within the scope of this work.

3.2.4 The molecular action of stress interferes with gene regulation in two phases

To explore the potential association between acute stress exposure and long-term metabolic effects, we performed a holistic analysis of hepatic methylation and transcription patterns at two time-points. First, we compared the methylation and transcription patterns immediately after the stress phase between the acute control group and the acute stress intervention group (direct comparison: *acuteCtrl* vs *acuteCvs*). Second, we evaluated the individual progression in a separate group of mice who received a three-month recovery period after the chronic stress intervention (longitudinal comparison: *acuteCtrl* vs *recoveryCtrl* and *acuteCvs* vs *recoveryCvs*, respectively) (Fig. 28). The methylation and transcriptional analyses revealed that the variability after facing Cvs was reduced over time compared to the longitudinal progression of the unstressed littermates (Fig. 28A, B). There was no accumulation in any specific genomic region (Fig. 28C). Since the central intention of the work is to identify candidates that may be translatable to human disease, we further focused our analyses on the evaluation of genes with methylation in the core promoters (maximum = 3kb to transcription start site) (Fig. 28D). This indicated an accumulation of differential methylation especially on mitochondrial DNA in the longitudinal observation after Cvs (Fig. 28D).

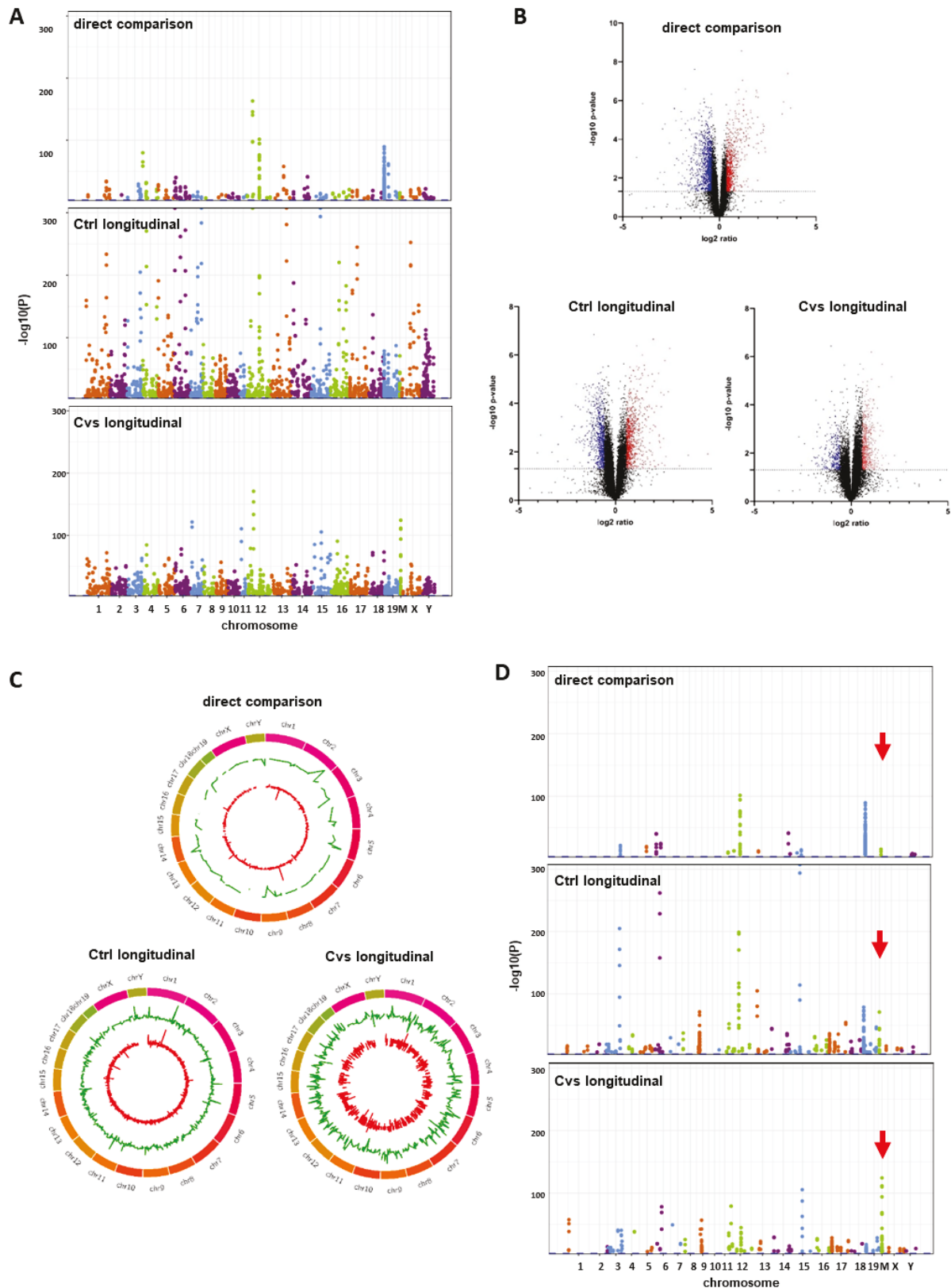


Figure 28: Molecular action of stress on hepatic genetic and epigenetic processes.

Methylation and transcriptional differences in the liver were analysed immediately after Cvs (direct comparison: *acuteCtrl* vs *acuteCvs*) or after a 3-month recovery phase (longitudinal of either Ctrl or Cvs: *acute* vs *recovery*). **(A)** Manhattan plots showing the chromosomal localization of differential methylation (y-axis: $-\log_{10}$ P-value; x-axis: chromosomal localization) of all differentially methylated fragments derived from methylome analyses based on the edgeR.p.value (Supplement Methylation; n=3-5/condition). **(B)** Volcano plot analyses showing the proportion of significantly differential regulated transcripts (y-axis: $-\log_{10}$ P-value; x-axis: \log_2 fold ratio) of all transcribed genes.

Color code: blue; enriched in condition 1 (acute Ctrl; acute Ctrl; acute Cvs) red enriched in condition 2 (*acuteCvs*; *recovery Ctrl*; *recovery Cvs*) (Supplement Transcription; n=5/condition) **(C)** Circos plot analyses visualizing the chromosomal localization of the differential methylation and transcription based on fold change derived from methylation and transcription analyses. Inner circle (red stacked histogram): transcriptome data (*acuteCtrl* vs *acuteCvs*; *acuteCtrl* vs *recoveryCtrl*; *acuteCvs* vs *recoveryCvs*), outer circle (green line) methylome data (*acuteCtrl* vs *acuteCvs*; *acuteCtrl* vs *recoveryCtrl*; *acuteCvs* vs *recoveryCvs*) (fold-change values, Supplement Table Methylation; n=3-5/condition in analyses, fold-change values, Supplement Table Transcription; n=5/condition). **(D)** Manhattan plot (y-axis: $-\log_{10}$ P-value; x-axis: chromosomal localization) of differentially methylated fragments solely in core promoter regions (maximum -3 kb to transcription start site) derived from methylome analyses based on the edgeR.p.value. The red arrow highlights variation in the mitochondrial DNA (Supplement Methylation; n=3-5/condition).

3.2.4.1 Effects of stress on the methylome

Differential methylated sites may provide hint on the underlying mechanisms of changes in energy metabolism, especially in the longitudinal loss of metabolic flexibility after Cvs. To go into detail on the genome-wide DNA methylation differences between acute stress exposure and long-term metabolic effects, methylation analysis with potential correlations of all methylation datasets (*acuteCtrl*, *acuteCvs*, *recoveryCtrl*, or *recoveryCvs*), were examined.

The methylation data showed a tight correlation for all conditions, which suggests a limited overall effect of stress (Supplement Table 9). Comparing acute conditions (*acute Ctrl* vs *acuteCvs*), the differences showed overrepresentation of methylation in *acuteCvs* in 98.2% of the enriched methylated fragments and in 99.1% restricted to the fragments located in primary promoters. Here, 170 chromosomal areas showed significant overrepresented methylation in *acuteCvs*, including 5 regions located in promoter regions of known genes, e.g. of inflammation gene *Trav23* or the distal promoter of *Cdc14b*. In addition, 4 significant chromosomal areas showed overrepresented methylation in *acuteCtrl* compared to *acuteCvs*, including the promoter region (<1kb) of *mt-Nd6* with a change of 0.4 – 0.57 (edgRp-value 2.69E-07 – 4.28E-16). Gene ontology (GO) analyses revealed no significant pathway enrichments based on these findings (Supplement Table 10). In the longitudinal observation of Ctrl animals, 99.7% of all enriched methylated DNA fragments and 99.3% if restricted to methylated DNA fragments located in a primary promoter, showed methylation overrepresentation after recovery. Combining these fragments according to chromosomal localization, 9 chromosomal regions were more methylated in *acuteCtrl* than in *recoveryCtrl*, including the promoter region of *serpinf-1* and various unknown genes. Vice versa, 796 significant frames including frames covering promoters of 50 annotated genes with overrepresented methylation in *recoveryCtrl*. These areas include fragments including *Trav23* and eight mitochondrial-coded genes i.e: *mt-Tt*, *mt-Ts*, *mt-Tw*, *mt-Atp6*, *mt-Nd5*, *mt-Nd3*, *mt-Nd6*, and *mt-Rn2* (Supplement Table 10). Focusing on genes with methylation events in the core promoters, GO analyses did not reach FDR significance levels (Supplement Table 10). In contrast, in the longitudinal comparison of Cvs animals 90% of all enriched methylated DNA fragments showed methylation overrepresentation after recovery. In regard to fragments located in a primary promoter, methylation is even less with 84% after recovery. These fragments can be combined to 82

chromosomal regions that were more methylated in the acuteCvs stage. When a promoter region was targeted, these were mainly uncharacterized genes. 593 chromosomal frames showed overrepresented methylation in recoveryCvs. Focusing on genes with promoter methylation, further mitochondrial DNA regions within a 1 kb distance to the start of 16 mitochondrial-coded genes i.e: mt-Atp6, mt-Co1, mt-Nd1, mt-Nd2, mt-Nd4, mt-Nd5, mt-Nd6, mt-Rnr2, mt-Th, mt-Tl1, mt-Tp, mt-Tr, mt-Ts1, mt-Tt, mt-Tv, and mt-Tw, were differentially affected. Notably, only three of the significant methylated DNA frames cover the identical mitochondrial regions in the Ctrl and Cvs analyses, all others are specific to either longitudinal analysis. Among all the conditions analysed, the GO analyses of the longitudinal Cvs analyses of primary promoter methylated genes are the only ones that reached significant pathway enrichment. As expected from the individual genes, various aspects of mitochondrial ATP synthesis related to electron transport were significantly enriched (enrichment p-value 3.71E-09, FDR 9.74E-06) (Supplement Table 10).

3.2.4.2 Effects of stress on the transcriptome

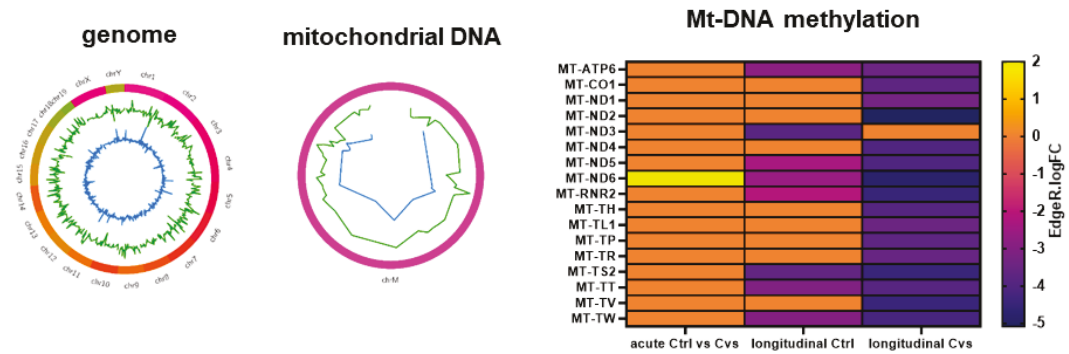
Based on the hypothesis, Cvs not only directly affects metabolism but also triggers a memory effect that leads to metabolic adaptation. As methylome data indicate a loss of methylation in the longitudinal development if mice faced Cvs. To determine whether this affects the transcription or holistic transcriptome also genome-wide DNA transcription differences between acute stress exposure and long-term metabolic effects, methylation analysis with potential (acuteCtrl, acuteCvs, recoveryCtrl, or recoveryCvs), were examined.

The analysis revealed that 859 functionally annotated molecules are differentially regulated (>1.5-fold; p-value <0.05), 553 up in Ctrl and 305 up in Cvs (Figure 27B, Supplement Table 11). These molecules could be assigned to activation of lipid metabolic pathways, e.g. cholesterol biosynthesis, mevalonate pathway I or a reduction in triacylglycerol biosynthesis (Supplement Table 11). In addition, central hepatic signaling pathways, e.g. regarding nuclear receptor RXR function, or RXR activation mediated by heterodimerization with LXR, PXR, FXR or TR, type II diabetes mellitus, and hepatic fibrosis-related signaling were enriched (Supplement Table 11). In line, also inflammation, e.g. cytokines of Th1 pathway, diabetes related IL-8, IL-9, IL-10, IL-12, IL-15, IL-23 signaling were enriched (Supplement Table 11). Of particular interest here, was the enrichment in the differential expression data of pathways related to mitochondrial function and redox systems, e.g. NRF2-mediated oxidative stress response, sirtuin signaling, glutathione-mediated detoxification, HIF1 α signaling, mitochondrial L-carnitine shuttle pathway or NAD⁺ signaling pathway at the time point of investigation (Supplement Table 11). In the longitudinal analyses in unstressed Ctrl animals, 1401 genes showed differential abundance with 716 up in *acuteCtrl*, and 738 in the longitudinal condition *recoveryCtrl* (Supplement Table 11). Here, e.g., various signaling pathways including PPAR α /RXR α activation, mTOR, PI3K/AKT, or glucocorticoid signaling are affected.

Metabolically, cholesterol-, and triacylglycerol biosynthesis and apoptosis processes such as unfolded protein response, protein ubiquitination, and inflammatory signaling *via* IL-6 or IL-10, and even DNA methylation and transcriptional repression signaling, were enriched. Moreover, mitochondrial action, sirtuin signaling, EIF2 signaling, oxidative phosphorylation, mitochondrial dysfunction, and NAD⁺-signaling, showed different abundance in the longitudinal setting (Supplement Table 11). Consistent with the reduced variability in the dataset after Cvs also at the transcriptional level, 210 genes are less abundant in *acuteCvs*, and 710 were more abundant in *recoveryCvs*. Enrichment of glucocorticoid receptor signaling molecules was higher than in the longitudinal Ctrl observation and affects different molecules. Other gene expression differences include e.g. metabolic pathways such as cholesterol biosynthesis, and the activation of pathways regulated by nuclear receptor complexes (PXR/RXR, LXR/RXR, FXR/RXR, PPAR α /RXR α) (Supplement Table 11). Regarding mitochondrial function, transcripts involved in mitochondrial dysfunction, oxidative phosphorylation, NAD⁺-signaling, reactive oxygen-related glutathione-mediated detoxification, EIF2, sirtuin signaling, or NRF2 (also known as Nfe2l2)-mediated oxidative stress response predicted differential activity. Any enrichment in lipid biosynthetic pathways was absent in the longitudinal development after previous Cvs.

So, the longitudinal observation indicated that mitochondrial DNA methylation showed different patterns depending on whether animals were exposed to acute stress (Fig. 29A). From the methylation and transcription data, it can be inferred that Cvs had a longitudinal effect on mitochondrial methylation and thus on transcriptional regulation, which was not directly caused by the Cvs intervention, but induced a *vicious cycle* on the one hand influenced by the Cvs-induced metabolic development and on the other hand altering the gene expression regulation (Fig. 29B).

A



B

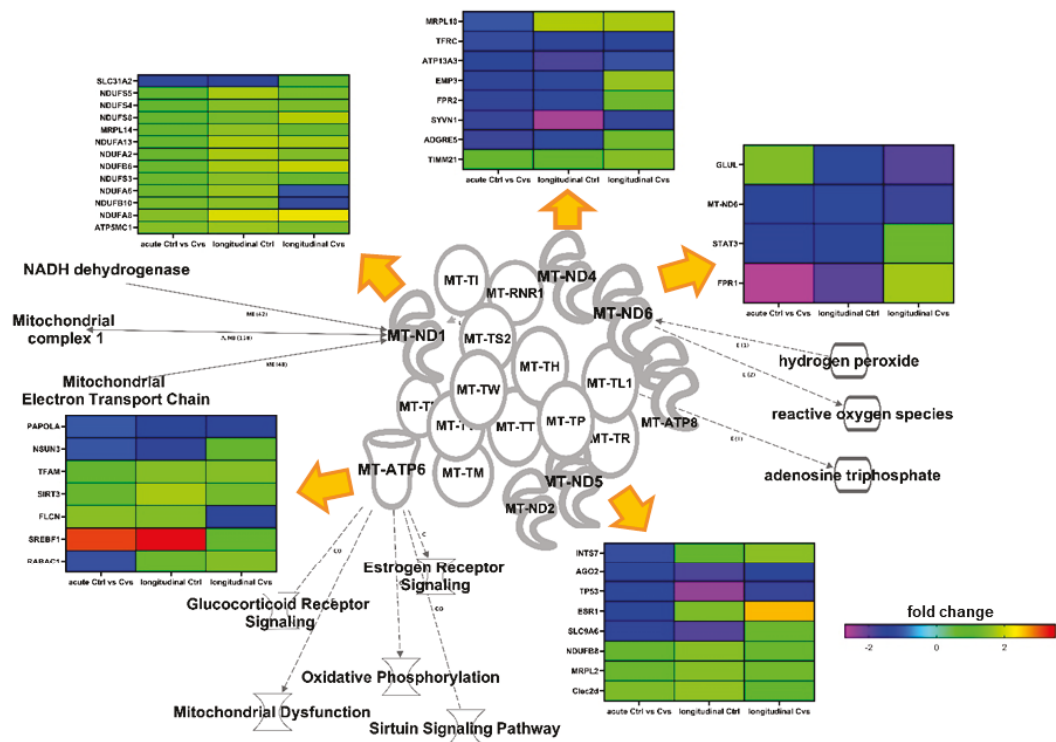


Figure 29: Stress interferes with hepatic mitochondrial gene regulation and function.

(A) Circus Plot analyses visualizing the chromosomal localization of longitudinal hepatic methylation differences after acute Cvs and with 3-month recovery period after Cvs (longitudinal of either Ctrl or Cvs: acute vs recovery) at the genomic level (genome) and on mitochondrial DNA. Color code: green: longitudinal Cvs, blue: longitudinal Ctrl (Supplement Methylation; n=3-5/condition). Heatmap of the differential methylation (edgeR.logFC) of all conditions (Supplement Table 10; n=3-5/condition). **(B)** Knowledge-based analyses of combined methylation and transcription data centered on the differential methylation of mt-DNA. Heatmaps of transcriptional differences (at least one condition fold change >1.5, p-value < 0.05 (Supplement Table 11)) interfering with main differentially methylated targets in mitochondria and transcription of knowledge-based interacting molecules. Knowledge-based analyses were performed using IPA (Krämer et al., 2014).

4. DISCUSSION

This thesis focuses on the acute and adaptive effects of chronic variable stress (Cvs) on energy metabolism in skeletal muscle as the main determinant of whole-body energy expenditure and in liver as the main organ with a role in many nutrition-related functions. From the literature, chronic high stress hormone levels leading to metabolic diseases like as obesity or T2DM and the metabolic function of GCs are well established. Prolonged GC exposure, like in the Cushing's syndrome or in psychological disease, is linked to metabolic disorders, such as insulin resistance, NAFLD and T2DM. However, only few studies investigated influences of chronic stress exposure on the energy metabolism and the onset of metabolic complications in the long-term (Faulenbach et al., 2012; Packard et al., 2014; Pibernik-Okanović et al., 1993; Reynolds et al., 2010). This study examined the influence of chronic stress load on energy metabolism in relation to mitochondrial efficiency and its effects on the transcriptome and methylome in skeletal muscle and liver. Our preclinical mouse model with chronic variable stress intervention to trigger chronic elevated stress hormone levels helps to investigate complicated relationships of cellular and hormonal metabolic adaptations isolated from interaction with exogenous confounding factors. Tissue specific analyses helped to investigate immediate metabolic changes and the mitochondrial function after Cvs. These investigations revealed adaptations of tissue-specific mitochondrial efficiency to control energy balance and identified epigenetic changes as a stress memory effect in metabolic regulation.

4.1 Chronic stress targets mitochondrial respiratory efficiency in the skeletal muscle of C57BL/6 mice

Like in the results section, parts of the discussion from page 94 to 100 have been taken over from the manuscript (Nikolic et al., 2023).

In the present study, we investigated the acute and adaptive effects of chronic variable stress (Cvs) on energy metabolism in skeletal muscle as the main determinant of whole-body energy expenditure. Analyses of the transcriptome, methylome, and proteome, as well as mitochondrial function in Cvs mice, were compared to controls. We show, that immediately following Cvs (i) body weight, fat- and lean mass decreased despite higher food intake, (ii) nocturnal energy expenditure (EE) is lower despite higher activity, (iii) respiratory exchange ratio (RER) shifted from carbohydrate (CHO) to fatty acid oxidation (FAO), (iv) mitochondrial metabolic capacity was altered with changes in the mitochondrial proteome, and (v) mitochondrial coupling capacity was reduced, but the thermodynamic efficiency increased. The advantage of preclinical animal models over human studies is the tight control of the environment by a standardized laboratory and the uniform genetic background of used mice. Thus, the Cvs effect can be isolated from interaction with exogenous confounding factors. With this, analyses of Cvs in a standardized preclinical model may help to unravel even metabolic

fine-tuning effects of cellular adaptation to maintain energy balance, which may be superimposed by confounding effects in more complex and externally influenced systems as clinical studies. Consistent with previous studies, Cvs exposure resulted in immediate activation of the hypothalamic–pituitary–adrenal (HPA) axis, with high corticosterone levels, and increased metabolic risk factors such as higher fasting blood glucose, triglycerides, and NEFA levels in plasma. These complex stress-induced alterations are consistent with the well-known pleiotropic effects of corticosterone on glucoregulatory insulin-responsive tissues (van Bodegom et al., 2017). So, the system used here mirrors human stress and chronic glucocorticoid (GC) exposure as risk of metabolic syndrome (Beaupere et al., 2021; Dille et al., 2022; Jelenik et al., 2018; Mellon et al., 2018; van den Berk-Clark et al., 2018; Yaribeygi et al., 2022).

Stress can interfere with food-seeking behavior, including high fat and sugar intake inducing obesity or alcohol-intake interfering with neuropsychiatric function and regulation of satiety hormone action as a futile cycle that may result in a dysfunctional HPA axis (Blessing et al., 2017; Pagoto et al., 2012). As a result of these complex and integrative processes, GC excess, either endogenous (e.g. Cushing's syndrome) or exogenous, remodels body composition with central obesity and muscle atrophy (Barbot et al., 2020). In a mouse model of Cushing syndrome insulin sensitivity and metabolic parameters negatively correlated to the loss of *M. gastrocnemius*, not *M. soleus*, mass (Uehara et al., 2020). Here, we observed a decreased lean and fat mass with a reduction in circadian EE despite increased food intake.

Furthermore, Cvs shifts energy utilization towards a greater proportion of FAO in whole-body substrate oxidation, despite relatively carb-heavy standard feed. The Cvs effect is mainly based on increased FAO during the light phase, while CHO is reduced during rest phase, as well as CHO and FAO during the active dark phase. The data may suggest that energy is restored after Cvs intervention by whole-body FAO during periods of low activity to compensate for reduced EE during the active phase. Lipid storage in white adipose tissue (WAT), remodeling or browning of WAT, and uncoupled mitochondrial respiration to thermogenesis in brown adipose tissue (BAT) also mediate systemic influence on FA metabolism and EE. Stress can trigger norepinephrine-mediated β -adrenergic receptor activation in BAT and WAT, promoting cAMP-mediated lipolysis, browning of WAT, and thermogenesis in BAT (Cheng et al., 2021; Ikeda et al., 2019; Vitali et al., 2012). Thus, increased lipolysis can provide the FA requirement after Cvs, which is reflected in the decreased fat mass. Also, cold exposure is one major driver for thermogenesis in BAT and repetitive periods of even short-term exposure increases total EE coupled to the expression of *Pgc1* and *Ucp1* in BAT (Ravussin et al., 2014). Even though cold exposure is a component of our Cvs protocol, EE was decrease in our mice after Cvs, so thermogenesis of BAT may not be the primary process, here. In addition, BAT is an endocrine organ and intraorgan crosstalk

e.g. with muscle has been shown (Gavaldà-Navarro et al., 2022; Kong et al., 2018). Batokines such as FGF21, regulating the expression of thermogenic genes, or IL-6 can be secreted in response to stress (Cheng et al., 2021; Gavaldà-Navarro et al., 2022; Hondares et al., 2011; Qing et al., 2020). Of note, consistent with observations after acute cold stress (Hondares et al., 2011), previous studies using our stress protocol showed that in the experimental timeframe immediately after Cvs, serum levels of FGF21 and IL-6 were not significantly altered (Dille et al., 2022; Jelenik et al., 2018). However, from our previous work, we saw no differences in glucose- and lipid uptake and insulin signaling in muscle tissues in our Cvs model (Jelenik et al., 2018). Although muscle FAO alone may not account for the changes in whole-body EE, there were signs of increased mitochondrial capacity that might affect muscle mitochondrial function. In addition, in the present analyses, proteins of the ana-/ catabolic pathways are increased following stress, which implicates an increased metabolic turnover after Cvs. The enrichment analysis of the differentially expressed proteins revealed that next to strictly mitochondrial proteins also others including metabolic-relevant proteins were enriched, which is consistent with previous reports (Granata et al., 2021). Here, the proteome analyses revealed changes in metabolic key enzymes in muscle tissue after Cvs. The rate-limiting enzymes of the glycolysis pathway hexokinase, phosphofruktokinase, and pyruvate kinase significantly increased in abundance after Cvs. Also the abundance of 3-oxoacid CoA-transferase 1 of the ketolysis pathway, isocitrate dehydrogenase of the TCA cycle pathway and the glutamic-oxaloacetic transaminase of the glutaminolysis pathway were significantly increased in Cvs muscle. These changes in protein data suggests upregulation of catabolic processes in the *M. gastrocnemius* after chronic stress intervention.

Mitochondrial dynamics including movement, tethering, fusion, and fission events are important for cell viability, senescence, intracellular signaling, mitochondria health, and bioenergetics function (Roca-Portoles and Tait, 2021). It still remains open if changed ATP demand or supply due to the balance of environmental influences and mitochondrial capacity are cause or consequence of the dynamic processes. However, Cvs may influence this process. Based on our proteomic data central proteins for fusion (Mfn1, Mfn2, as well as the Opa1 protein (Liesa et al., 2009; Roca-Portoles and Tait, 2021)) or fission (Fis1, Mf, Drp1) and associated recruiting factors (MiD49 and MiD51 (Losón et al., 2013; Palmer et al., 2011)), if present in the dataset were unaltered by Cvs. Depending on the circadian rhythm, Cvs causes a greater fluctuation in substrate utilization shown by decreased EE and CHO to save substrates in the activity phase, and recovery of energy demands in resting times by unaltered EE, accompanied by preferential FAO. In addition, we observed a correlation between energy expenditure and mitochondrial capacity. However, there was no evidence for oxidative stress, as ROS production even tended to be lower after Cvs. Taken together, this suggests an

imbalance of biogenesis to degradation, which is attempted to be compensated by the mitochondria as well as fuel utilization.

The gradual decline of mitochondrial functionality from reversible to irreversible physiological defects is a key event in metabolic diseases. This is due to the fact that mitochondria orchestrate energy homeostasis up to all levels of gene regulation. Mitochondria are the first responders to changing conditions and are an important organelle in triggering catabolic processes that affect cellular homeostasis, as seen here after Cvs. The gradual process in mitochondrial adaptation to altered metabolism follows a sequence from functional alteration, functional impairments with compensatory mitochondrial and genomic gene expression, and mitogenesis, up to organelle exhaustion and mitophagy (Kokkinopoulou and Moutsatsou, 2021; Weber et al., 2002; Yu and Feigelson, 1970).

GC administration can improve skeletal muscle mitochondria respiration even in a mouse model for Duchenne Muscular Dystrophy (Dubinin et al., 2020). Therefore, the differences in EE and RER seen after Cvs were most likely due to mitochondrial function itself. Defects in mitochondrial oxidative phosphorylation and lower mtDNA copy number are defined risks in diabetes type 2 patients (Sangwung et al., 2020). Clinically, it has been shown that primary mitochondrial dysfunction due to mutations in genes encoding mitochondrial proteins can cause defects in energy metabolism and this may account for GC action directly (Fisher-Wellman et al., 2015; Kokkinopoulou et al., 2021; Kokkinopoulou and Moutsatsou, 2021; Larsen et al., 2012). As mtDNA is not directly correlated to mitochondrial content (Larsen et al., 2012), an increased mtDNA content in Cvs skeletal muscle compared to Ctrl suggests that compensatory processes have already begun at this stage. Our observation is consistent with previously reported stress and corticosteroids regulation of mitochondrial DNA content and gene expression (Kokkinopoulou and Moutsatsou, 2021; Picard and McEwen, 2018a). In enriched mitochondrial fractions with comparable mitochondrial content, the mitochondrial proteome composition of *M. gastrocnemius* shows only a few changes in the electron transfer chain (ETC) components after Cvs. There were no hints to structural alterations, key proteins involved in mitochondrial dynamics fission or fusion in the mitochondrial proteome data, although the system used is able to detect such alterations (Knebel et al., 2019). However, this interpretation is implicative, as morphological alterations of the mitochondria were not determined in the present study. So, the shift in fuel preferences and altered EE could not be explained by reduced lean mass or changes in relevant mitochondrial structural proteins, which may indicate modifications in mitochondrial activity after Cvs.

The respiratory profile of muscle mitochondria after and the ability of the ETC to transfer electrons were analysed in isolated mitochondria of muscle tissue after Cvs. Since the assessment of mitochondrial morphology is implicit based on only proteome analyses, respiration data were normalized by defined protein input and by the accepted marker of

mitochondrial content citrate synthase activity (Larsen et al., 2012; Reichmann et al., 1985). Since both normalization strategies have limitations (Franko et al., 2013; Groennebaek et al., 2020), both approaches were used in combination for our purposes to avoid possible normalization-related misinterpretations. So, the presented results show Cvs effect that is independent of potential alterations in total protein content of enriched fractions or mitochondrial quantity based on citrate synthase activity.

The respiratory profile of isolated muscle mitochondria is reduced via both, complex I or II after Cvs. Our results agree with significantly decreased mitochondrial complex I enzyme activity data obtained in patients after corticosterone treatment (Mitsui et al., 2002a; Mitsui et al., 2002b). Moreover, we found that maximal uncoupled respiration (state 3u) of complex II correlates with whole-body EE. Since skeletal muscle is a major contributor to total EE in vivo, this suggests that total EE is dependent on mitochondrial function and coupling. Therefore, it appears that there is a specific mitochondrial impairment involved in GC-induced muscle atrophy (Romanello et al., 2010). In addition, we observe a reduced electron flow accompanied by significantly decreased mitochondrial coupling independent of NADH (complex I)-linked or FADH₂ (complex II)-linked OXPHOS after Cvs. Another limiting factor of ETC capacity could be the electron flux from glycerol via the glycerophosphate dehydrogenase complex (CGpDH) or from fatty acid β -oxidation via the electron-transferring flavoprotein complex (ETF) to Coenzyme Q as superordinated factors, as upstream bottleneck of electron flux to complex I and complex II (Gnaiger, 2009). A similar observation with reduced mitochondrial respiration in regard to complex I, II, and ETC was made following diet-induced vitamin D deficiency in *M. gastrocnemius* of C57BL/6 J mice. Alterations in ETC protein content or citrate synthase activity were excluded and the authors suggested alterations in mitochondrial respiration independent of ETC protein content (Ashcroft et al., 2021).

The decreased mitochondrial respiration could be explained by decreased basal proton conductance or can also be explained by a change in intrinsic coupling of the respiratory chain activity (Roussel et al., 2003). It is controversial whether the uncoupling mechanisms of UCP3, the major uncoupling protein expressed in skeletal muscle, affect total EE (Hirschenson et al., 2022). Here, there are no differences in UCP3 protein or transcription levels between the Cvs and the control groups. Surprisingly the thermodynamic coupling of mitochondrial phosphorylation is significantly increased in complex II after Cvs, indicating that the rate of energy production is at economic net output power at optimal efficiency. Additionally, the efficiency of both complexes was increased after Cvs. The optimal thermodynamic efficiency (η -opt) has been applied to assess biological processes and has been proposed as a measure of mitochondrial function (Wikstrom and Springett, 2020). According to Stucki (Stucki, 1980), the values observed suggest that muscle mitochondria adapt their function to maximize ATP production and to maintain cellular phosphate potential at the expense of the energy

conversion efficiency after Cvs. The complex II pathway is set toward maximizing the cellular energy state and cellular integrity. In the Cvs group, the complex II mitochondrial set point is associated with a high degree of coupling and high thermodynamic efficiency. The RCR in both complexes was unaltered after Cvs thus does not interfere with a higher degree of mitochondrial coupling. As a result, in vivo mitochondrial ATP synthesis might be more efficient through FADH₂ (complex II)-linked OXPHOS in Cvs mice. The observation that thermodynamic coupling is increased after Cvs, whereas a correlation of complex II-specific maximal uncoupled respiration with decreased EE, has led to the hypothesis that mitochondria demonstrate functional adaptation with increased efficiency to manage energy balance. This results in a significant increase in economic coupling with the goal of achieving the optimal efficiency of net ATP production rate at the economic benefit to maintain cellular homeostasis processes.

According to our hypothesis, Cvs interferes directly with metabolism but also initiates a memory effect for metabolic adaptation. We show that the direct effects on transcriptome and methylome solely initiated by Cvs are limited in muscle. Here, we specifically looked at the status quo after the stress intervention to evaluate any changes present in the transcriptome or even methylome and classify them as persisting after chronic stress. This snapshot of data should provide an indication of molecular changes that are prerequisites for cellular adaptation. Remarkable is the downregulated clock gene *Nr1d1* (*Rev-erb-α*), a transcription factor that is generally involved in energy metabolism featuring maximal oxidative capacity and circadian regulation (Amador et al., 2018). Interestingly, most of the significantly repressed transcripts by Cvs are of mitochondrial tRNAs. Specific mitochondrial tRNA mutations have long been linked to type 2 diabetes or metabolic syndrome and diabetes-associated genetic defects (Wilson et al., 2004; Yang et al., 2022). One may speculate that mitochondrial tRNAs are an early target in the decline cascade of mitochondrial function, following stress. Methylome analyses reveal that one of the hypo-methylated genes is the nuclear-encoded mitochondrial tRNA synthase *Lars2*. *Lars2* is expressed in skeletal muscle and controls the translation of mitochondrial-encoded genes via leucyl-tRNA synthetase, the mitochondrial genome stability, and its additional activation improves mitochondrial respiration (Feng et al., 2022).

In conclusion, our data showed that following Cvs mitochondrial mass is not changed and a correlation occurred of complex II in state 3u with decreased EE. Furthermore, the thermodynamic coupling was increased. This may indicate an early stage of mitochondrial adaptation to Cvs as a compensatory mechanism to manage the energy balance despite advancing atrophy.

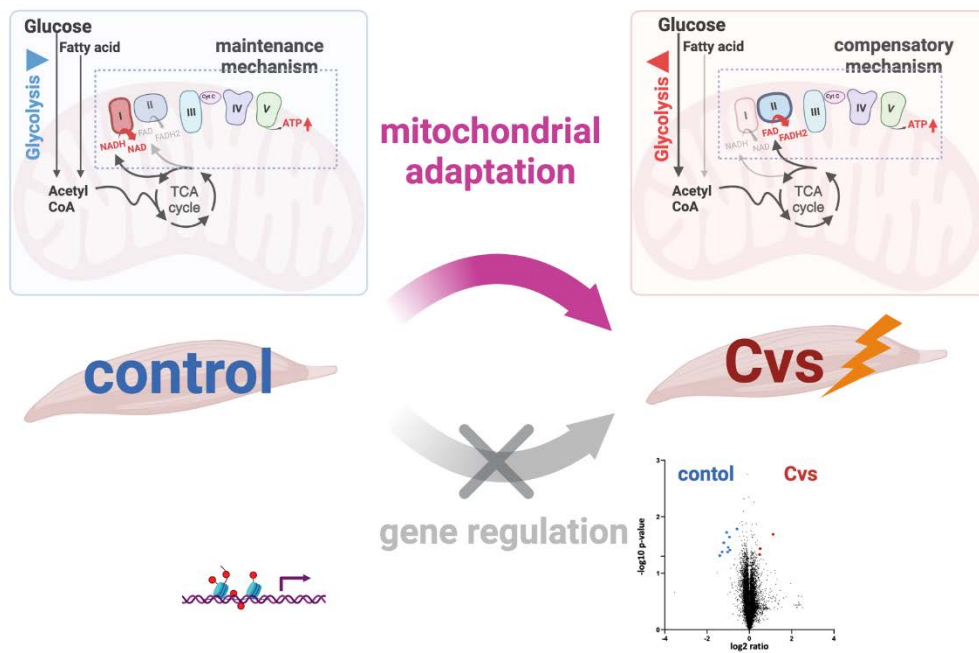


Figure 30: Graphical summary of mitochondrial compensatory mechanism in skeletal muscle after Cvs.

The muscle shows a shift in substrate utilization for the OXPHOS machinery and ATP production for the cell triggered by Cvs. A previously complex I driven respiratory chain as seen in the control changes after Cvs influence to a complex II driven respiratory chain without major effects on the epigenetic level in the mitochondrion. This compensation mechanism is solely based on the function and substrate availability of the mitochondria and serves to maintain the overall EE and to counteract an advancing atrophy.

4.2 Chronic stress leads to sustained metabolic changes with increased thermodynamic efficiency of mitochondrial complex I in the liver that in sum alter the liver epigenome

Chronic stress has been linked to the development of diabetes, metabolic disorders, and fatty liver disease, affecting energy metabolism and mitochondrial function. Cross-sectional studies in humans showed that persistent stress and PTSD can lead to fatty liver development in individuals with metabolic diseases (Kang et al., 2020; Pagoto et al., 2012). However, these effects' specific molecular mechanisms are still not fully understood. In previous studies in our Cvs mouse model, we have shown immediate tissue-specific effects of chronic stress, with subsequent metabolic adaptations leading to increased hepatic lipid accumulation even after a stress-free recovery phase (Dille et al., 2022; Jelenik et al., 2018). In this study, we hypothesized that the molecular basis of the increased metabolic risk is implemented immediately after Cvs in the liver to adapt metabolism even after stress-free recovery. Our findings revealed that immediately following chronic stress: (i) reduced metabolic capacity, evident through decreased EE and RER correlated with circulating NEFAs, especially linoleic acid (cC18:2); (ii) changes in the hepatic proteome indicating reduced glucose metabolism and increased lipid catabolism, confirmed by metabolic activity analyses; (iii) altered abundance of oxidative phosphorylation (OXPHOS) components, with unchanged electron flow capacity but increased mitochondrial thermodynamic efficiency, particularly in complex CI. Additionally, we observed differences in epigenetic modifications, especially in mtDNA, immediately after chronic stress compared to controls, which were not sufficient to explain the observed variations in gene expression. However, in the longitudinal observation from acute to recovery, distinct epigenetic patterns were observed in stressed mice, differing from those of unstressed mice. Here hypomethylation, particularly in mtDNA methylation, aggravated with corresponding effects on transcriptional networks.

Analysing chronic stress in a standardized preclinical model allows us to study the effects of cellular adaptations on maintaining energy balance, minimizing confounding factors present in more complex clinical studies. Our model accurately reflects the effects of corticosterone on insulin-responsive tissues, mimicking the risk of metabolic syndrome associated with stress and glucocorticoid exposure in humans (Beaupere et al., 2021; Dille et al., 2022; Jelenik et al., 2018; Mellon et al., 2019; van Bodegom et al., 2017; van den Berk-Clark et al., 2018; Yaribeygi et al., 2022). After acute Cvs, our previous analyses showed a shift to FAO for whole-body energy generation, accompanied by increased lipolysis to compensate for EE under identical feeding conditions (Nikolic et al., 2023). Next to increased serum NEFAs, as previously observed after stress intervention, we also noted changes in serum fatty acid patterns with increased levels of linoleic acid (cC18:2) and decreased levels of arachidonic acid (cC20:4)

following chronic stress. In conditions of increased energy demand, such as liver cancer, linoleic acid localizes to the mitochondria, and influences expression of lipid metabolism genes, including carnitine acyltransferases (CPTs) that control mitochondrial fatty acid uptake (Brown et al., 2018). The expression of CPT2, associated with the inner mitochondrial membrane, was slightly regulated in control mice but not in stressed mice, while CPT1A, associated with the outer mitochondrial membrane, was increased in stressed mice, suggesting enhanced mitochondrial fatty acid uptake. Linoleic acid serves as a precursor to arachidonic acid, suggesting a diminished elongation and desaturation cycle in our model. Arachidonic acid plays various roles, including induction of oxidative stress, modulation of membrane flexibility, vasodilation, and inflammation (Tallima and El Ridi, 2018). In human models of severe stress, inflammation increases, accompanied by decreased essential and long-chain fatty acids and enhanced beta-oxidation (Lindqvist et al., 2017; Mellon et al., 2019; Mellon et al., 2018). However, the reduced arachidonic acid in our study is consistent with the yet absence of inflammation in our model (Dille et al., 2022). We also observed increased expression of Ppara, a regulator of fatty acid oxidation, during the longitudinal comparison after stress. Activity phase EE correlated with NEFA and linoleic acid levels, suggesting that linoleic acid may undergo direct β -oxidation immediately after Cvs for energy supply.

The elevated cC18:2 levels observed in our study are in line with those in NAFLD conditions (Rasche and Hiltemann, 2020). We found an increase in liver fat after the recovery phase in our model of Cvs, but not during the acute stages following stress (Dille et al., 2022). The gene expression data indicate suppressed lipid synthesis during the longitudinal observation of Cvs. The DNL activity immediately after stress is consistent with previous chronic, intermittent, or social defeat stress in animal studies and human PTSD (Chuang et al., 2010; Lindqvist et al., 2017; Mellon et al., 2019; Mellon et al., 2018). However, in contrast to those studies, we observed increased fatty acid oxidation in our model in liver. Based on our data, one possible explanation for this discrepancy could be the attempt to supply necessary energy with a more efficient OXPHOS in our model after acute stress.

Immediately after Cvs, the liver undergoes a molecular shift characterized by increased catabolism and reduced anabolic processes, as supported by proteomic and functional data. After Cvs, stressed mice show decreased hepatic glucose metabolism, with suppressed hepatic glycolysis and gluconeogenesis pathways and the key enzyme G6P being repressed at transcription and protein levels. So, Cvs differs from glucocorticoid (GC) action, as GC excess in Cushing syndrome patients increases hepatic glucose production by directly inducing G6P for gluconeogenesis (Mazziotti et al., 2011). NEFAs transported to the liver following Cvs further reduce glucose metabolism. In liver, DNL decreased, ketogenesis remained unaffected, and mitochondrial β -oxidation increased immediately after Cvs. However, hepatic glucose levels, and the main DNL product cC16:1 still remain stable. This suggests that β -oxidation is

primarily activated for energy generation. The glucose-fatty acid cycle plays a crucial role in fuel metabolism (Hue and Taegtmeyer, 2009). In healthy stages, acetyl-CoA derived from FAO usually enters the TCA cycle and promotes ketogenesis to some extent. However, in human steatosis, it mainly goes to the TCA cycle rather than ketogenesis (Fletcher et al., 2019). We previously observed that increased glycolytic activity fuels DNL in a mouse model of metabolic-associated fatty liver disease (MAFLD) providing necessary carbon sources (Fahlbusch et al., 2022). Pyruvate derived from glycolysis may be less available after Cvs. Here, DNL does not serve as a sink for acetyl-CoA and acetyl-CoA may be redirected toward the TCA cycle to generate substrates for the electron transport chain (ETC), driving hepatic mitochondrial activity after Cvs. So, our findings align with this observation reflecting features observed in NAFLD and indicate that the observed shift points directly to mitochondrial function also in our Cvs model.

Mitochondrial dynamics play a crucial role in metabolic adaptation and various biological processes such as viability, aging, and bioenergetics (Roca-Portoles and Tait, 2021). Mitochondrial function adapts to conditions such as diabetes and NAFLD (Wang et al., 2023). Mitochondrial biology responds to stressors in a cell type-specific manner, resulting in quantitative changes in ATP synthesis, net energy equivalents, and ROS production, as well as qualitative changes in mitochondrial dynamics and substrate preferences for fat or carbohydrate metabolism (Picard and McEwen, 2018b). Previous studies have shown age and stress-related responses in mitochondrial function and copy number in various tissues, including peripheral blood mononuclear cells, or neurological cells, and reduced mtDNA copy number in veterans with post-traumatic stress disorder (PTSD) (Emmerzaal et al., 2020; Picard and McEwen, 2018b). However, information regarding the liver especially after stress intervention is rare (Rabasa et al., 2019). Consistent with our previous findings in muscle (Nikolic et al., 2023), the overall quality assessment of mitochondria showed no changes in mitochondrial content or integrity immediately following stress in liver. Additionally, key proteins of mitochondrial dynamics involved in fission and fusion (Roca-Portoles and Tait, 2021), did not indicate stress-induced alterations in the liver.

Following Cvs, no evidence for detoxifying reactive oxygen species (ROS) or increased lipid oxidation in the liver was observed, in line with decreased expression of nuclear factor erythroid-derived 2 like 2 (Nfe2l2) immediately after Cvs, a transcription factor that typically initiates gene expression to enhance cellular defense against oxidative stress (Vomhof-Dekrey and Picklo, 2012). MtDNA transcription and replication are tightly regulated and involve e.g. Tfam acting as a histone-like protein on mtDNA, and Pgc-1 α , controlling mitochondrial turnover, replication, transcription and fatty acid oxidation pathways (Chew and Zhao, 2021; Morris et al., 2012). From the gene expression data, Tfam showed age-dependent but stress-independent regulation, while Pgc-1 α exhibited changes only in the longitudinal analysis of

Cvs transcription. This might indicate a potential ongoing process of lipid metabolic adaptation, which might serve as link to the longitudinal metabolic adaptation.

Changes in the abundance of hepatic mitochondrial complex proteins of stressed animals were identified, and associated with changes in respiratory profile and electrons transfer capability. Respiratory chain complexes I and II serve as entry points for electrons derived from cellular substrate breakdown, linking mitochondrial activity to cellular metabolism. NAD⁺-derived from pyruvate enters the ETC specifically through CI. Immediately after Cvs, we observed an increase in the efficiency of ATP production specifically in NAD⁺-fueled CI, accompanied by a shift in the NAD⁺/NADH ratio. The turnover of substrates in the liver was impacted by Cvs, as evidenced by changes in mitochondrial thermodynamic coupling of complex I (CI) indicating an ongoing adaptation process to maximize ATP production. This is further supported by the fact that the increase in liver η -opt correlate with EE patterns during the activity phase and plasma NEFA levels. However, the resulting increase in CI thermodynamic efficiency to maintain cellular phosphorylation potential after Cvs is at the expense of the energy conversion efficiency (Stucki, 1980). CI activity was positively correlated with corticosteroid response and mortality rates in liver diseases (Solís-Muñoz et al., 2023), and dysfunctions in CI have been associated with oxidative phosphorylation disorders (Antonicka et al., 2003; Loeffen et al., 2000). In chronic stress-induced metabolic reprogramming in the brain also unaltered maximal ATP production rate despite altered CI was observed, similar to our model (Emmerzaal et al., 2020). Notably, in muscle, such tissue-specific fine-tuning correlated with EE and plasma NEFA levels was observed for complex II (CII)-linked η -opt, further indicating tissue specificity of metabolic fine-tuning (Nikolic et al., 2023).

The intriguing observation with stress is that the risk to develop a metabolic related diseases still persists after stress-free recovery phases. A key mechanism for metabolic control is the dynamic interaction between metabolism and transcription-modifying epigenetics. Altered acetyl-CoA concentrations, such as those that occur during hepatic lipid accumulation, can also directly affect epigenetic processes. Consistent with human stress studies (Kang et al., 2020; Pagoto et al., 2012), we have previously shown a significant increase in hepatic fat in response to Cvs intervention after the recovery phase (Dille et al., 2022). In addition, plasma NEFA levels remain elevated, accompanied by increased fatty acid uptake, decreased FAO, and key hepatic steatosis-relegated genes that were differentially expressed after the recovery period. Although NAD⁺/NADH ratios were restored after recovery, Sirt activity and methyltransferase activity remained reduced even three months after stress intervention, indicating ongoing epigenetic changes linked to energy balance (Dille et al., 2022). So, the long-term development of metabolic changes as seen in the altered energetic flexibility, here, may be influenced by the immediate stress-induced reduction of NAD⁺/NADH ratio, sirtuin activity and, OCM components. SIRT1 is a sensor and regulator of metabolism and their

interactions are associated with the development of fatty liver disease (Ding et al., 2017). The sirtuin family are NAD⁺-dependent modulators of liver energy and glucose metabolism (Wu et al., 2022) which regulate methyltransferase activity through rate-limiting enzymes of NAD⁺ metabolism and on transcriptional level (Peng et al., 2011). OCM encompasses interconnected pathways in cytosol and mitochondria including the folate cycle, methionine re-methylation, and trans-sulfuration. It aims to transfer one-carbon units (C1) to nucleotide synthesis and S-adenosylmethionine (SAM) generation, the latter being a methyl donor for epigenetic processes. The liver predominantly maintains the whole-body C1 pools (Clare et al., 2019; Ducker and Rabinowitz, 2017). Immediately after Cvs, an increased abundance of proteins of the choline module suggests glycerophospholipid synthesis (Wright et al., 2004) for lipid transport, as observed in stages of increased hepatic fatty acid influx (Shahsavari et al., 2016). However, proteins associated with the folate, trans-sulfur, and methionine cycles for SAM generation were less abundant immediately after Cvs, suggesting SAM depletion. In line, the overall proportion of methylation was lower in the longitudinal observation of mice previously facing Cvs than in unstressed mice. Additionally, components of the reduced folate cycle, particularly Mttfhd 1, which modulates the overall NAD⁺/NADH ratio (García-Martínez and Appling, 1993) were also less abundant after Cvs. Re-methylation of homocysteine to methionine plays a key role in regenerating of the reactive methyl carrier SAM. Elevated homocysteine levels observed in metabolic diseases like NAFLD (Dai et al., 2016), indicate the importance of the impaired methionine cycle as seen after Cvs in disease development. Interestingly, the antidiabetic drug metformin has been shown to target CI (Griss et al., 2015) of the mitochondrial respiratory chain, reducing the NAD⁺/NADH ratio. This action of metformin also negatively affects the folate cycle in OCM (Corominas-Faja et al., 2012), indicating the observed action of Cvs is related to diabetes development.

The immediate response of mitochondrial function to Cvs is in line with the role of dynamic epigenetic modifications in adapting to environmental changes. DNA methylation, catalyzed by DNA methyltransferases using methyl groups from SAM, affects chromatin remodeling, DNA stability, and gene regulation. While mtDNA methylation initially sparked controversy, increasing evidence now links it to age, health, and environmental responses (Liu et al., 2020; Sharma et al., 2021; Sharma et al., 2019; Zhang et al., 2023). MtDNA methylation potentially impacts mitochondrial gene expression regulation, and has been associated with metabolic diseases such as diabetic retinopathy, cardiovascular disease, and hepatic steatosis (Zhang et al., 2023). In addition, in response to harsh environmental factors like intoxication hypomethylation of mt-TF, mt-RMR1, mt-ND6, and the regulatory D-loop, have been observed. Changes in methylation patterns immediately after Cvs were not indicative of the observed transcriptional and metabolic alterations compared to unstressed mice. This is not unexpected, as a response to altered environmental conditions will first rely on immediate effects for

transcriptional regulation, like transcription factor modification or different homo-, and hetero-dimerization processes as suggested by the expression data. Nevertheless, target genes methylated in aggravated metabolic conditions like hepatic steatosis (Zhang et al., 2023) e.g. genes of lipid metabolism are differentially expressed in the liver after Cvs. Immediately after Cvs, altered methylation compared to Ctrl was observed near the mt-ND6 gene on the light inner mtDNA strand, which has previously been observed in diabetes or hepatic steatosis where expression negatively correlated to severity (Lapp et al., 2019; Pirola et al., 2013). No significant methylation differences were observed after Cvs in the regulatory D-loop region which is consistent with the observed unchanged mtDNA copy number and previous reports (Gao et al., 2015; Stocco et al., 2018).

The most pronounced variation in methylation levels was observed in the longitudinal analysis of Cvs mice, accompanied by changes in mitochondrial network transcription patterns. Although the overall proportion of methylation was lower in the longitudinal observation of mice previously facing Cvs than in Ctrl, the proportion of methylation especially in mt-DNA methylation was higher after recovery from Cvs. Overrepresented methylation of certain mtDNA regions was observed in unstressed mice during the longitudinal comparison but to a lesser extent than in Cvs mice. Mt-ND6 showed moderate methylation in aging in controls, but aggravated methylation after Cvs recovery. In addition, mt-ND6 transcription followed the methylation pattern, suggesting its involvement in Cvs-induced cellular adaptation. These findings demonstrate that Cvs initiates altered mtDNA methylation levels in the liver during the recovery phase. The differences in mtDNA methylation levels are accompanied by differential transcriptional patterns and support the observation that finally the energetic power of hepatocytes is lost after the recovery phase only after a previous Cvs experience.

In summary, our findings indicate that immediately after Cvs oxidative phosphorylation in liver mitochondria is affected by increased thermodynamic efficiency of CI. This effect is associated with reduced EE and increased NEFAs, especially cC18:2 levels. While the stress period alone only slightly alters methylation patterns, the metabolic changes manifest as an adaptation of the methylome in the stressed cohort, with decreased overall methylation, altered mtDNA methylation and related transcriptional networks. As depicted by the energy map, the energy metabolism of the liver shows a loss of metabolic flexibility as a sustainable consequence of former chronic stress exposure.

The role of methylation, particularly mtDNA methylation, in disease-prone metabolic maladaptation is still under debate, and further research is needed. To this point, our study has to remain speculative about how hypomethylation observed after Cvs affects mtDNA transcription or stability and whether it is an active mt-methyltransferases-driven process or a result of diminished mitochondrial renewal. Our study clearly indicates that methylation is a consequence of immediate Cvs-induced hepatic energy metabolism fine-tuning, to maintain

the environmental information for adaptation to altered life conditions, rather than a primary driving force. So, even short periods of chronic stress join the list of factors leading to the loss of epigenetic information as postulated key mechanism in disease and aging.

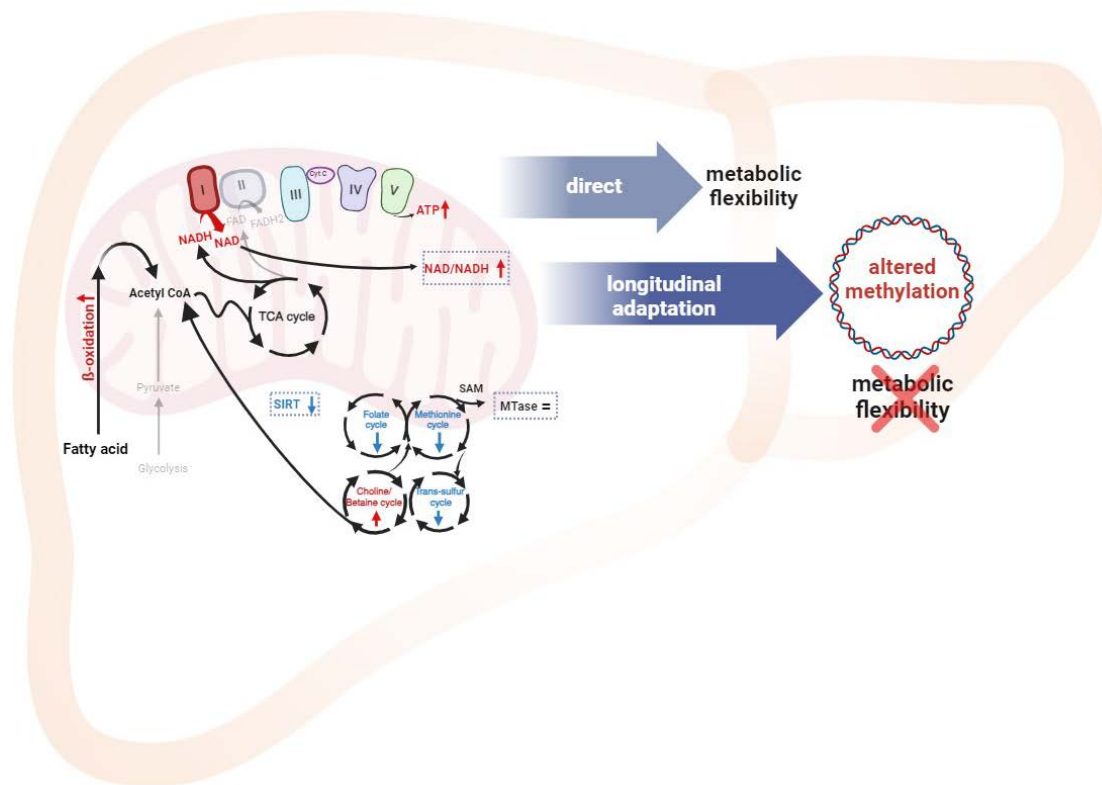


Figure 31: Graphical summary of metabolic and epigenetic adaptation after Cvs in liver mitochondria.

Cvs exposure resulted in metabolic adaptation manifested by increased thermodynamic turnover via complex II and NADH supply. The increased β -oxidation is likely one of the causes of the altered mitochondrial function and complex supply. Acute epigenetic changes were only marginally, whereas the 3-month recovery data showed a drastic epigenetic change in mtDNA with the decrease in metabolic flexibility measured by hepatocyte energy map.

4.3 Chronic stress targets tissue specific mitochondrial respiratory efficiency and leads in liver to altered mitochondrial DNA methylation with loss of metabolic flexibility

Overall, this study shows that immediately after a stressful event an imbalance in energy metabolism occurs with tissue-specific adjustments in mitochondrial efficiency. Furthermore, the mechanisms of metabolic adaptation lead to tissue-specific epigenetic changes. Essentially, this study shows that mitochondrial functionality was directly affected by metabolic derailment induced by Cvs of liver and muscle, whereas in a longitudinal analysis, the epigenetic pattern of liver mtDNA was altered by the previously induced aberrant metabolism despite recovery phase. Thus, the Cvs intervention not only affected overall metabolism, as the increased GC release observed during this period led to a shift in RER and EE, resulting in metabolic imbalance, but was manifested in tissue-specific cellular changes to maintain energy balance and cope with stress. Of particular interest were the novel findings of the study that the Cvs intervention significantly increased CII thermodynamic efficiency of oxidative phosphorylation in muscle tissue. Whereas liver tissue demonstrated significantly increased CI thermodynamic efficiency, although control animals showed slightly increased CII preference. It is known from previous studies that muscle tissue preferentially uses CI for substrate sparing for energy production and liver tissue the other way around uses CII (Kappler et al., 2019). Thus, interestingly, here, after Cvs intervention, a switch occurred from the previously preferred feeding of the ETC to the more underrepresented feeding pathway. The altered substrate utilization in both tissues could indicate that the preferred pathways for ETC delivery under normal physiological conditions for the tissues were exhausted to their maximum by the stress effect and the cell consequently tried to find another way of energy production. This mechanism could be interpreted as a rescue mechanism of the cell and the mitochondria, since mechanisms are activated here that are not directly considered under normal conditions. In general, the essential function of GC release during a period of stress is to provide the bloodstream with sufficient glucose to supply the brain with energy and to ensure the survival of the organism under conditions of acute stress or reduced food intake. To ensure metabolic balance, the interaction of different organs is necessary, and thus it is known that the insulin-sensitive organs such as the muscles contribute 30% and the liver 20% to the total body EE (Rolfe and Brown, 1997), and thus each organ has its influence on it. If this balance of the individual EE participants is disturbed, for example by various environmental factors, diseases or even Cvs, this can lead to metabolic derailments and a negative energy balance and, in the long term, to severe diseases such as T2D or NAFLD. Chronic GC release results in stimulation of hepatic glucose production (Vegiopoulos and Herzig, 2007), but this could not be confirmed in this study with Cvs. In agreement with previous data, GC release provides

increased peripheral glucose uptake in muscles (Jelenik et al., 2018), and in addition, fatty acid oxidation is increased, which provides additional substrates for glucose production in the liver (Bodine and Furlow, 2015). Thus, each organ functions and acts in its own way in coping with stress. Therefore, it can be hypothesized that skeletal muscle cells after Cvs result in lower mitochondrial content due to increased catabolic metabolism and a consequent decrease in fat-free mass and thus atrophy that consumes less oxygen. The data here show an immediate mitochondrial adaptation after Cvs in the muscle by a significant increase of glycolysis and feeding of FADH₂ by complex II for energy production. Thus, total ATP turnover is lower after Cvs in muscle cells and contributes to lower EE. This is supported by the correlation of plasma glucose level and total EE, which showed that an increased glucose level and thus the supply in the muscle cells is directly related to a lower EE. However, since the degree of coupling also depends on cellular fatty acid concentrations, it is probably dependent on the corresponding concentrations in plasma (Soboll and Stucki, 1985) and the finding of higher plasma NEFA levels in Cvs mice suggests that the degree of coupling of the liver is higher via β -oxidation and thus via CI feeding. Higher mitochondrial coupling means more substrate is oxidized to meet cellular energy demands, thus conserving energy. The correlation of NEFA plasma data to EE values confirms this relationship and the consequent justified contribution to altered EE. Whole-body EE analyses showed a shift to FAO for whole-body energy production accompanied by increased lipolysis to compensate for EE. The correlation of NEFA and linoleic acid levels with EE suggests that linoleic acid is the driving fatty acid that shifts directly to β -oxidation for energy production after Cvs. The shift in EE and the consequent shifted substrate fluxes in plasma have a direct impact on mitochondrial function and energy production. It seems that the individual tissues try to overcome the stress by seeking a metabolic adaptation induced by the shift of metabolite fluxes through Cvs, which have direct but also indirect influence on the overall EE. The consequence is that further organs with their individual mechanisms and contribution to the overall EE make up, but have not been further addressed here and would require further investigation.

In the past, defects in mitochondrial functions have been associated with mutations of the mtND1 - mtND5 subunits, which are important for supercomplex formation (Ramírez-Camacho et al., 2020). In this work, the compositions of the supercomplexes were not considered, but there is a necessary speculation about the conformational change of the supercomplexes of the ETC for energy production. Composition and interplay of supercomplexes differ among tissues and could also reassemble according to metabolic status (Ramírez-Camacho et al., 2020). The substrate shift and change in complex preferences of the ETC of both tissues may indicate that the muscle tissue sought a conformational change toward CII+CIII+CIV after Cvs exposure, and the liver tissue toward CI+CIII+CIV. It would be of interest to determine the

tissue specific supercomplex composition after Cvs, as the results presented provide a sound basis to address such research question in the future.

The economy of mitochondria showed in muscle was increased complex II-driven thermodynamic coupling (q-value) with a value of q_p^{ec} , suggesting that CII attempts to achieve optimal economic efficiency while increasing thermodynamic efficiency of oxidative phosphorylation (η -opt) for CII after Cvs in muscle. These data suggest that muscle mitochondria maximize cellular energy status and cellular integrity to make mitochondrial ATP synthesis by FADH₂ (complex II)-associated OXPHOS more efficient after Cvs in muscle. In contrast, no changes in thermodynamic coupling (q-value) were evident in liver after Cvs, whereas the thermodynamic efficiency of oxidative phosphorylation (η -opt) was significantly increased for CI, i.e. the NADH-driven OXPHOS pathway. This indicates that the economic level of energy production was not altered in this current metabolic state (q-value), but the efficiency of substrate conversion to energy was greatly increased (η -opt) for CI in the liver.

This suggests that both tissues respond to the short-term stress response, which is directly influenced by environment on available substrates for OXPHOS supply, with an increase in complex-specific respiratory efficiency and respond with specific mitochondrial functionality immediately after Cvs intervention. These data suggest altered tissue-specific substrate availability, i.e., enhanced glycolysis in muscle resulted in higher supply of CII through its byproduct FADH₂, and in liver, enhanced β -oxidation resulted in higher supply of CI through its byproduct NADH after Cvs. Thus, this work adds novel knowledge that muscle mitochondria exhibited high thermodynamic efficiency for oxidative phosphorylation (η -opt) in complex II-linked respiration, whereas liver mitochondria exhibited high η -opt in complex I-linked respiration after Cvs.

Interestingly, only the latter was a prerequisite for the development of differential mtDNA methylation and loss of energetic phenotype after Cvs during a stress-free recovery period. This is consistent with previous studies that found a direct link between CI, but not CII, of the OXPHOS system and methylation regulation (Cui et al., 2022). A direct link of succinate (CI-supplier) and an altered DNA methylation pattern seems logical. However, there was no link that succinate alters DNA methylation pattern. So this work was in line with missing literature evidence that succinate alone is responsible for epigenetic changes. This reinforces the assumption that muscle alone copes with stress overcoming through its metabolic adaptation of mitochondria and its functionality.

Overall, muscle did not show extensive changes in transcriptome and methylome data that could have widespread effects on the whole organism. However, hypomethylation was detected in the nuclear-encoded mitochondrial tRNA synthase *Lars2*, which, in the context of the overall work, could also indicate altered mitochondrial function, as *Lars2* is involved in

mitochondrial genome stability and its activation leads to increased mitochondrial respiration in skeletal muscle (Feng et al., 2022).

It appears that muscle is better adapted to such short-term environmental changes because of its rapid response in everyday life, such as producing ATP quickly and abundantly during exercise, and its ability to respond to substrate availability with increased mitochondrial efficiency (Huertas et al., 2019). Muscle tissue is also known to have a higher density of mitochondria tailored for high phosphorylation capacity (Benard et al., 2006).

In contrast to muscle, the liver seems to have greater ability in adapting to metabolic changes but only manages to do so up to a certain point. Although the coupling experiments did not show any changes after Cvs, thermodynamic efficiency was seen to be significantly increased for CI. The increased β -oxidation by Cvs leads to a substrate excess that cannot be compensated in the long run, thus leading to the *circulum vitiosus* and, in retrospect, to the loss of metabolic flexibility.

The switch from CII to CI increased thermodynamic efficiency has a direct impact on epigenetics. In numerous scientific articles, a link has been established between CII and epigenetic regulation, in contrast to CI and epigenetics in muscle (Emmerzaal et al., 2020). The link between CII functionality, substrate feeding and epigenetic regulation was demonstrated and confirmed in this work for liver tissue.

From the data in this work, it appears that the changes at the epigenetic level after a recovery period are the result of a derailed metabolism producing specific metabolites to achieve the memory effect in the liver. The attempt of mitochondrial adaptation to metabolic conditions triggered a long-term effect, although the stress factor was removed. The increased CI thermodynamic efficiency had an impact at epigenetic and transcriptional levels, but most importantly, it was shown here that the derailed metabolism had a long-lasting effect on mtDNA after a recovery period of Cvs. However, in combination with the altered transcriptional pattern of mitochondria-associated transcripts and the loss of the energetic phenotype in hepatocytes at this stage, it can be concluded that Cvs also does not directly trigger epigenetic changes in the liver, but that metabolic adaptations initiated in the liver lead to altered mtDNA methylation. In analogy to this process known from the aging process (Amorim et al., 2022), Cvs can also lead to a premature decline in metabolic capacity. From this finding of the work, further research questions can be derived regarding the kinetics or the mechanism of altered methylation, being an active process involving regulation of mitochondrial methylases or an altered mitochondrial turnover.

This study showed that the muscle has a faster adaptability, which is probably due to the nature of the muscle, which is designed to produce a lot of energy in a short time. The liver seems to withstand the short stress period, but in the long-term analysis it was seen that the metabolic

derailment caused by Cvs had a much greater impact on the liver tissue, especially on the liver methylome, than on the muscle tissue.

A limitation of this study could be the use of a translational model to investigate the effects of chronic variable stress (Cvs) on metabolism has versus human studies. However, this type of analysis was chosen to ensure a uniform genetic background under standardized laboratory conditions and to consider the Cvs effect in isolation from exogenous confounders. Accordingly, the transferability of the data to humans needs to be verified and would require further investigation in the future to understand the metabolic adaptation effect at the cellular level to maintain energy balance at the human level.

5. CONCLUSION

In summary, a 15-day Cvs intervention resulted in altered metabolite flux with adaptation of the proteome of muscle and liver tissue, a significant increase in the thermodynamic efficiency of CII of muscle and CI of liver, and a sustained change in epigenetics as well as gene regulation. It is suggested that increased thermodynamic efficiency of energy conversion of muscle and liver mitochondria is responsible in response to a Cvs-induced metabolic derailment. Thus, mice may in turn maintain their mitochondrial energy function to a Cvs-induced hypermetabolic state by maximizing ATP production to maintain their cellular energy state, regardless of cost and substrate source. Along with increased FAO, a decrease in energy expenditure has resulted in a negative energy balance and consequent weight loss. The immediate metabolic reprogramming of hepatic metabolism by Cvs, persists in the form of epigenetic changes at the longitudinal level.

REFERENCES

- (2022). The Galaxy platform for accessible, reproducible and collaborative biomedical analyses: 2022 update. *Nucleic acids research* *50*, W345-w351.
- Adams, L.A., Anstee, Q.M., Tilg, H., and Targher, G. (2017). Non-alcoholic fatty liver disease and its relationship with cardiovascular disease and other extrahepatic diseases. *Gut* *66*, 1138-1153.
- Ahlqvist, E., Storm, P., Käräjämäki, A., Martinell, M., Dorkhan, M., Carlsson, A., Vikman, P., Prasad, R.B., Aly, D.M., Almgren, P., *et al.* (2018). Novel subgroups of adult-onset diabetes and their association with outcomes: a data-driven cluster analysis of six variables. *The lancet Diabetes & endocrinology* *6*, 361-369.
- Akalin, A., Kormaksson, M., Li, S., Garrett-Bakelman, F.E., Figueroa, M.E., Melnick, A., and Mason, C.E. (2012). methylKit: a comprehensive R package for the analysis of genome-wide DNA methylation profiles. *Genome biology* *13*, R87.
- Al-Mehdi, A.B., Pastukh, V.M., Swiger, B.M., Reed, D.J., Patel, M.R., Bardwell, G.C., Pastukh, V.V., Alexeyev, M.F., and Gillespie, M.N. (2012). Perinuclear mitochondrial clustering creates an oxidant-rich nuclear domain required for hypoxia-induced transcription. *Science signaling* *5*, ra47.
- Alberti, K.G., Johnston, D.G., Piniewska-Hulas, M., and Whittaker, J. (1981). Disturbances of metabolic homeostasis is liver disease. *Acta medica portuguesa*, 35-47.
- Amador, A., Campbell, S., Kazantzis, M., Lan, G., Burriss, T.P., and Solt, L.A. (2018). Distinct roles for REV-ERB α and REV-ERB β in oxidative capacity and mitochondrial biogenesis in skeletal muscle. *PLoS one* *13*, e0196787.
- Amorim, J.A., Coppotelli, G., Rolo, A.P., Palmeira, C.M., Ross, J.M., and Sinclair, D.A. (2022). Mitochondrial and metabolic dysfunction in ageing and age-related diseases. *Nature reviews Endocrinology* *18*, 243-258.
- Antonicka, H., Ogilvie, I., Taivassalo, T., Anitori, R.P., Haller, R.G., Vissing, J., Kennaway, N.G., and Shoubridge, E.A. (2003). Identification and characterization of a common set of complex I assembly intermediates in mitochondria from patients with complex I deficiency. *J Biol Chem* *278*, 43081-43088.
- Arlington (2000). American Psychiatric Association. Diagnostic and Statistical Manual of Mental Disorders-DSM-IV-TR[™]. Arlington: American Psychiatric Publishing *4th ed.* .
- Arner, P., and Kulyté, A. (2015). MicroRNA regulatory networks in human adipose tissue and obesity. *Nature reviews Endocrinology* *11*, 276-288.
- Ashcroft, S.P., Fletcher, G., Philp, A.M., Jenkinson, C., Das, S., Hansbro, P.M., Atherton, P.J., and Philp, A. (2021). Diet-induced vitamin D deficiency reduces skeletal muscle mitochondrial respiration. *J Endocrinol* *249*, 113-124.
- Barbot, M., Zilio, M., and Scaroni, C. (2020). Cushing's syndrome: Overview of clinical presentation, diagnostic tools and complications. *Best Pract Res Clin Endocrinol Metab* *34*, 101380.
- Barzilai, N., Guarente, L., Kirkwood, T.B., Partridge, L., Rando, T.A., and Slagboom, P.E. (2012). The place of genetics in ageing research. *Nature reviews Genetics* *13*, 589-594.
- Basolo, A., Magno, S., Santini, F., and Ceccarini, G. (2022). Ketogenic Diet and Weight Loss: Is There an Effect on Energy Expenditure? *Nutrients* *14*.
- Bassi, G., Sidhu, S.K., and Mishra, S. (2021). The Expanding Role of Mitochondria, Autophagy and Lipophagy in Steroidogenesis. *Cells* *10*.

- Baylin, S.B., and Jones, P.A. (2016). Epigenetic Determinants of Cancer. Cold Spring Harbor perspectives in biology 8.
- Beaupere, C., Liboz, A., Feve, B., Blondeau, B., and Guillemain, G. (2021). Molecular Mechanisms of Glucocorticoid-Induced Insulin Resistance. International journal of molecular sciences 22.
- Belsky, D.W., Caspi, A., Arseneault, L., Baccarelli, A., Corcoran, D.L., Gao, X., Hannon, E., Harrington, H.L., Rasmussen, L.J., Houts, R., *et al.* (2020). Quantification of the pace of biological aging in humans through a blood test, the DunedinPoAm DNA methylation algorithm. eLife 9.
- Benard, G., Faustin, B., Passerieux, E., Galinier, A., Rocher, C., Bellance, N., Delage, J.P., Casteilla, L., Letellier, T., and Rossignol, R. (2006). Physiological diversity of mitochondrial oxidative phosphorylation. American journal of physiology Cell physiology 291, C1172-1182.
- Berdanier, C.D. (1989). Role of glucocorticoids in the regulation of lipogenesis. FASEB journal : official publication of the Federation of American Societies for Experimental Biology 3, 2179-2183.
- Berglund, A., Putney, R.M., Hamaidi, I., and Kim, S. (2021). Epigenetic dysregulation of immune-related pathways in cancer: bioinformatics tools and visualization. Experimental & molecular medicine 53, 761-771.
- Bharadwaj, M.S., Tyrrell, D.J., Lyles, M.F., Demons, J.L., Rogers, G.W., and Molina, A.J. (2015). Preparation and respirometric assessment of mitochondria isolated from skeletal muscle tissue obtained by percutaneous needle biopsy. Journal of visualized experiments : JoVE.
- Bizerea-Moga, T.O., Pitulice, L., Pantea, C.L., Olah, O., Marginean, O., and Moga, T.V. (2022). Extreme Birth Weight and Metabolic Syndrome in Children. Nutrients 14.
- Black, P.R., Brooks, D.C., Bessey, P.Q., Wolfe, R.R., and Wilmore, D.W. (1982). Mechanisms of insulin resistance following injury. Annals of surgery 196, 420-435.
- Blessing, E.M., Reus, V., Mellon, S.H., Wolkowitz, O.M., Flory, J.D., Bierer, L., Lindqvist, D., Dhabhar, F., Li, M., Qian, M., *et al.* (2017). Biological predictors of insulin resistance associated with posttraumatic stress disorder in young military veterans. Psychoneuroendocrinology 82, 91-97.
- Bodine, S.C., and Furlow, J.D. (2015). Glucocorticoids and Skeletal Muscle. Adv Exp Med Biol 872, 145-176.
- Bouillon-Minois, J.B., and Dutheil, F. (2022). Biomarker of Stress, Metabolic Syndrome and Human Health. Nutrients 14.
- Brand, M.D. (2010). The sites and topology of mitochondrial superoxide production. Experimental gerontology 45, 466-472.
- Brown, Z.J., Fu, Q., Ma, C., Kruhlak, M., Zhang, H., Luo, J., Heinrich, B., Yu, S.J., Zhang, Q., Wilson, A., *et al.* (2018). Carnitine palmitoyltransferase gene upregulation by linoleic acid induces CD4(+) T cell apoptosis promoting HCC development. Cell death & disease 9, 620.
- Buzzetti, E., Pinzani, M., and Tsochatzis, E.A. (2016). The multiple-hit pathogenesis of non-alcoholic fatty liver disease (NAFLD). Metabolism 65, 1038-1048.
- Cabib, S., and Puglisi-Allegra, S. (2012). The mesoaccumbens dopamine in coping with stress. Neuroscience and biobehavioral reviews 36, 79-89.
- Cairns, C.B., Walther, J., Harken, A.H., and Banerjee, A. (1998). Mitochondrial oxidative phosphorylation thermodynamic efficiencies reflect physiological organ roles. Am J Physiol 274, R1376-1383.
- Castañeda, P., Muñoz, M., García-Rojo, G., Ulloa, J.L., Bravo, J.A., Márquez, R., García-Pérez, M.A., Arancibia, D., Araneda, K., Rojas, P.S., *et al.* (2015). Association of N-cadherin levels and downstream

- effectors of Rho GTPases with dendritic spine loss induced by chronic stress in rat hippocampal neurons. *Journal of neuroscience research* 93, 1476-1491.
- Castañeda, T.R., Nogueiras, R., Müller, T.D., Krishna, R., Grant, E., Jones, A., Ottaway, N., Ananthakrishnan, G., Pfluger, P.T., Chaudhary, N., *et al.* (2011). Decreased glucose tolerance and plasma adiponectin:resistin ratio in a mouse model of post-traumatic stress disorder. *Diabetologia* 54, 900-909.
- Chaaban, M.R., Illing, E., Riley, K.O., and Woodworth, B.A. (2014). Spontaneous cerebrospinal fluid leak repair: a five-year prospective evaluation. *The Laryngoscope* 124, 70-75.
- Challis, B.G., Coll, A.P., Yeo, G.S., Pinnock, S.B., Dickson, S.L., Thresher, R.R., Dixon, J., Zahn, D., Rochford, J.J., White, A., *et al.* (2004). Mice lacking pro-opiomelanocortin are sensitive to high-fat feeding but respond normally to the acute anorectic effects of peptide-YY(3-36). *Proc Natl Acad Sci U S A* 101, 4695-4700.
- Chance, B., and Williams, G.R. (1955a). Respiratory enzymes in oxidative phosphorylation. I. Kinetics of oxygen utilization. *J Biol Chem* 217, 383-393.
- Chance, B., and Williams, G.R. (1955b). Respiratory enzymes in oxidative phosphorylation. III. The steady state. *J Biol Chem* 217, 409-427.
- Chandel, N.S. (2015). Evolution of Mitochondria as Signaling Organelles. *Cell metabolism* 22, 204-206.
- Chen, H.C., Chen, Y.Z., Wang, C.H., and Lin, F.J. (2020). The nonalcoholic fatty liver disease-like phenotype and lowered serum VLDL are associated with decreased expression and DNA hypermethylation of hepatic ApoB in male offspring of ApoE deficient mothers fed a with Western diet. *The Journal of nutritional biochemistry* 77, 108319.
- Cheng, L., Wang, J., Dai, H., Duan, Y., An, Y., Shi, L., Lv, Y., Li, H., Wang, C., Ma, Q., *et al.* (2021). Brown and beige adipose tissue: a novel therapeutic strategy for obesity and type 2 diabetes mellitus. *Adipocyte* 10, 48-65.
- Chew, K., and Zhao, L. (2021). Interactions of Mitochondrial Transcription Factor A with DNA Damage: Mechanistic Insights and Functional Implications. *Genes* 12.
- Chiou, J., Geusz, R.J., Okino, M.L., Han, J.Y., Miller, M., Melton, R., Beebe, E., Benaglio, P., Huang, S., Korgaonkar, K., *et al.* (2021). Interpreting type 1 diabetes risk with genetics and single-cell epigenomics. *Nature* 594, 398-402.
- Chomyn, A., Cleeter, M.W., Ragan, C.I., Riley, M., Doolittle, R.F., and Attardi, G. (1986). URF6, last unidentified reading frame of human mtDNA, codes for an NADH dehydrogenase subunit. *Science* 234, 614-618.
- Chomyn, A., Mariottini, P., Cleeter, M.W., Ragan, C.I., Matsuno-Yagi, A., Hatefi, Y., Doolittle, R.F., and Attardi, G. (1985). Six unidentified reading frames of human mitochondrial DNA encode components of the respiratory-chain NADH dehydrogenase. *Nature* 314, 592-597.
- Christensen, B.C., and Marsit, C.J. (2011). Epigenomics in environmental health. *Frontiers in genetics* 2, 84.
- Chrousos, G.P. (2009). Stress and disorders of the stress system. *Nature reviews Endocrinology* 5, 374-381.
- Chrousos, G.P., and Gold, P.W. (1992). The concepts of stress and stress system disorders. Overview of physical and behavioral homeostasis. *Jama* 267, 1244-1252.
- Chuang, J.C., Cui, H., Mason, B.L., Mahgoub, M., Bookout, A.L., Yu, H.G., Perello, M., Elmquist, J.K., Repa, J.J., Zigman, J.M., *et al.* (2010). Chronic social defeat stress disrupts regulation of lipid synthesis. *Journal of lipid research* 51, 1344-1353.

- Clare, C.E., Brassington, A.H., Kwong, W.Y., and Sinclair, K.D. (2019). One-Carbon Metabolism: Linking Nutritional Biochemistry to Epigenetic Programming of Long-Term Development. *Annual review of animal biosciences* 7, 263-287.
- Corella, D., Coltell, O., Mattingley, G., Sorlí, J.V., and Ordovas, J.M. (2017). Utilizing nutritional genomics to tailor diets for the prevention of cardiovascular disease: a guide for upcoming studies and implementations. *Expert review of molecular diagnostics* 17, 495-513.
- Corominas-Faja, B., Quirantes-Piné, R., Oliveras-Ferraros, C., Vazquez-Martin, A., Cufí, S., Martin-Castillo, B., Micol, V., Joven, J., Segura-Carretero, A., and Menendez, J.A. (2012). Metabolomic fingerprint reveals that metformin impairs one-carbon metabolism in a manner similar to the antifolate class of chemotherapy drugs. *Aging* 4, 480-498.
- Crick, D.C.P., Halligan, S.L., Howe, L.D., Lacey, R.E., Khandaker, G.M., Burgner, D., Herbert, A., Suderman, M., Anderson, E.L., and Fraser, A. (2022). Associations between Adverse Childhood Experiences and the novel inflammatory marker glycoprotein acetyls in two generations of the Avon Longitudinal Study of Parents and Children birth cohort. *Brain, behavior, and immunity* 100, 112-120.
- Crofts, A.R. (2004). Proton-coupled electron transfer at the Qo-site of the bc1 complex controls the rate of ubiquinol oxidation. *Biochimica et biophysica acta* 1655, 77-92.
- Cui, W., Huang, Z., and Pfeifer, G.P. (2022). Lack of Major Genome-Wide DNA Methylation Changes in Succinate-Treated Human Epithelial Cells. *Int J Mol Sci* 23.
- Czogala, W., Czogala, M., Strojny, W., Wator, G., Wołkow, P., Wójcik, M., Bik Multanowski, M., Tomasik, P., Wędrychowicz, A., Kowalczyk, W., *et al.* (2021). Methylation and Expression of FTO and PLAG1 Genes in Childhood Obesity: Insight into Anthropometric Parameters and Glucose-Lipid Metabolism. *Nutrients* 13.
- D'Souza A, M., Beaudry, J.L., Szigiato, A.A., Trumble, S.J., Snook, L.A., Bonen, A., Giacca, A., and Riddell, M.C. (2012). Consumption of a high-fat diet rapidly exacerbates the development of fatty liver disease that occurs with chronically elevated glucocorticoids. *American journal of physiology Gastrointestinal and liver physiology* 302, G850-863.
- D'Urso, A., and Brickner, J.H. (2014). Mechanisms of epigenetic memory. *Trends in genetics : TIG* 30, 230-236.
- Dai, Y., Zhu, J., Meng, D., Yu, C., and Li, Y. (2016). Association of homocysteine level with biopsy-proven non-alcoholic fatty liver disease: a meta-analysis. *Journal of clinical biochemistry and nutrition* 58, 76-83.
- Dallman, M.F., Strack, A.M., Akana, S.F., Bradbury, M.J., Hanson, E.S., Scribner, K.A., and Smith, M. (1993). Feast and famine: critical role of glucocorticoids with insulin in daily energy flow. *Front Neuroendocrinol* 14, 303-347.
- Das, K.C. (2013). Hyperoxia decreases glycolytic capacity, glycolytic reserve and oxidative phosphorylation in MLE-12 cells and inhibits complex I and II function, but not complex IV in isolated mouse lung mitochondria. *PloS one* 8, e73358.
- DeFronzo, R.A. (1981). Glucose intolerance and aging. *Diabetes care* 4, 493-501.
- den Hoed, M., Westerterp-Plantenga, M.S., Bouwman, F.G., Mariman, E.C., and Westerterp, K.R. (2009). Postprandial responses in hunger and satiety are associated with the rs9939609 single nucleotide polymorphism in FTO. *The American journal of clinical nutrition* 90, 1426-1432.
- Dille, M., Nikolic, A., Wahlers, N., Fahlbusch, P., Jacob, S., Hartwig, S., Lehr, S., Kabra, D., Klymenko, O., Al-Hasani, H., *et al.* (2022). Long-term adjustment of hepatic lipid metabolism after chronic stress and the role of FGF21. *Biochimica et biophysica acta Molecular basis of disease* 1868, 166286.

- Ding, R.B., Bao, J., and Deng, C.X. (2017). Emerging roles of SIRT1 in fatty liver diseases. *International journal of biological sciences* 13, 852-867.
- Dubinina, M.V., Talanov, E.Y., Tenkov, K.S., Starinets, V.S., Belosludtseva, N.V., and Belosludtsev, K.N. (2020). The Effect of Deflazacort Treatment on the Functioning of Skeletal Muscle Mitochondria in Duchenne Muscular Dystrophy. *International journal of molecular sciences* 21.
- Ducker, G.S., and Rabinowitz, J.D. (2017). One-Carbon Metabolism in Health and Disease. *Cell metabolism* 25, 27-42.
- Emmerzaal, T.L., Preston, G., Geenen, B., Verweij, V., Wiesmann, M., Vasileiou, E., Grüter, F., de Groot, C., Schoorl, J., de Veer, R., *et al.* (2020). Impaired mitochondrial complex I function as a candidate driver in the biological stress response and a concomitant stress-induced brain metabolic reprogramming in male mice. *Translational psychiatry* 10, 176.
- Eslam, M., Valenti, L., and Romeo, S. (2018). Genetics and epigenetics of NAFLD and NASH: Clinical impact. *Journal of hepatology* 68, 268-279.
- Even, P.C., and Nadkarni, N.A. (2012). Indirect calorimetry in laboratory mice and rats: principles, practical considerations, interpretation and perspectives. *Am J Physiol Regul Integr Comp Physiol* 303, R459-476.
- Fahlbusch, P., Nikolic, A., Hartwig, S., Jacob, S., Kettel, U., Köllmer, C., Al-Hasani, H., Lehr, S., Müller-Wieland, D., Knebel, B., *et al.* (2022). Adaptation of Oxidative Phosphorylation Machinery Compensates for Hepatic Lipotoxicity in Early Stages of MAFLD. *International journal of molecular sciences* 23.
- Fan, Y., and Pedersen, O. (2021). Gut microbiota in human metabolic health and disease. *Nature reviews Microbiology* 19, 55-71.
- Fathi Dizaji, B. (2018). The investigations of genetic determinants of the metabolic syndrome. *Diabetes & metabolic syndrome* 12, 783-789.
- Faulenbach, M., Uthoff, H., Schwegler, K., Spinass, G.A., Schmid, C., and Wiesli, P. (2012). Effect of psychological stress on glucose control in patients with Type 2 diabetes. *Diabetic medicine : a journal of the British Diabetic Association* 29, 128-131.
- Feng, S., Wan, S., Liu, S., Wang, W., Tang, M., Bai, L., and Zhu, Y. (2022). LARS2 Regulates Apoptosis via ROS-Mediated Mitochondrial Dysfunction and Endoplasmic Reticulum Stress in Ovarian Granulosa Cells. *Oxid Med Cell Longev* 2022, 5501346.
- Feo, F., Canuto, R.A., and Garcea, R. (1973). Acceptor control ratio of mitochondria. Factors affecting it in Morris hepatoma 5123 and Yoshida hepatoma AH-130. *European journal of cancer* 9, 203-214.
- Fernandez-Twinn, D.S., and Ozanne, S.E. (2010). Early life nutrition and metabolic programming. *Ann N Y Acad Sci* 1212, 78-96.
- Ferrannini, E. (1988). The theoretical bases of indirect calorimetry: a review. *Metabolism* 37, 287-301.
- File, S.E., and Fernandes, C. (1994). Noise stress and the development of benzodiazepine dependence in the rat. *Anxiety* 1, 8-12.
- Fisher-Wellman, K.H., Lin, C.T., Ryan, T.E., Reese, L.R., Gilliam, L.A., Cathey, B.L., Lark, D.S., Smith, C.D., Muoio, D.M., and Neuffer, P.D. (2015). Pyruvate dehydrogenase complex and nicotinamide nucleotide transhydrogenase constitute an energy-consuming redox circuit. *The Biochemical journal* 467, 271-280.
- Fletcher, J.A., DeJa, S., Satapati, S., Fu, X., Burgess, S.C., and Browning, J.D. (2019). Impaired ketogenesis and increased acetyl-CoA oxidation promote hyperglycemia in human fatty liver. *JCI insight* 5.

- Fraga, M.F., Ballestar, E., Paz, M.F., Ropero, S., Setien, F., Ballestar, M.L., Heine-Suñer, D., Cigudosa, J.C., Urioste, M., Benitez, J., *et al.* (2005). Epigenetic differences arise during the lifetime of monozygotic twins. *Proc Natl Acad Sci U S A* *102*, 10604-10609.
- Frankenfield, D.C. (2010). On heat, respiration, and calorimetry. *Nutrition (Burbank, Los Angeles County, Calif)* *26*, 939-950.
- Franke, A., Baris, O.R., Bergschneider, E., von Toerne, C., Hauck, S.M., Aichler, M., Walch, A.K., Wurst, W., Wiesner, R.J., Johnston, I.C., *et al.* (2013). Efficient isolation of pure and functional mitochondria from mouse tissues using automated tissue disruption and enrichment with anti-TOM22 magnetic beads. *PLoS One* *8*, e82392.
- Frayling, T.M., Timpson, N.J., Weedon, M.N., Zeggini, E., Freathy, R.M., Lindgren, C.M., Perry, J.R., Elliott, K.S., Lango, H., Rayner, N.W., *et al.* (2007). A common variant in the FTO gene is associated with body mass index and predisposes to childhood and adult obesity. *Science* *316*, 889-894.
- Gao, J., Wen, S., Zhou, H., and Feng, S. (2015). De-methylation of displacement loop of mitochondrial DNA is associated with increased mitochondrial copy number and nicotinamide adenine dinucleotide subunit 2 expression in colorectal cancer. *Molecular medicine reports* *12*, 7033-7038.
- García-Martínez, L.F., and Appling, D.R. (1993). Characterization of the folate-dependent mitochondrial oxidation of carbon 3 of serine. *Biochemistry* *32*, 4671-4676.
- Gathercole, L.L., Morgan, S.A., Bujalska, I.J., Hauton, D., Stewart, P.M., and Tomlinson, J.W. (2011). Regulation of lipogenesis by glucocorticoids and insulin in human adipose tissue. *PloS one* *6*, e26223.
- Gavaldà-Navarro, A., Villarroya, J., Cereijo, R., Giralt, M., and Villarroya, F. (2022). The endocrine role of brown adipose tissue: An update on actors and actions. *Reviews in endocrine & metabolic disorders* *23*, 31-41.
- Gnaiger, E. (2009). Capacity of oxidative phosphorylation in human skeletal muscle: new perspectives of mitochondrial physiology. *Int J Biochem Cell Biol* *41*, 1837-1845.
- Goll, M.G., and Bestor, T.H. (2005). Eukaryotic cytosine methyltransferases. *Annual review of biochemistry* *74*, 481-514.
- Granata, C., Caruana, N.J., Botella, J., Jamnick, N.A., Huynh, K., Kuang, J., Janssen, H.A., Reljic, B., Mellett, N.A., Laskowski, A., *et al.* (2021). High-intensity training induces non-stoichiometric changes in the mitochondrial proteome of human skeletal muscle without reorganisation of respiratory chain content. *Nature communications* *12*, 7056.
- Greenberg, M.V.C., and Bourc'his, D. (2019). The diverse roles of DNA methylation in mammalian development and disease. *Nature reviews Molecular cell biology* *20*, 590-607.
- Griss, T., Vincent, E.E., Egnatchik, R., Chen, J., Ma, E.H., Faubert, B., Viollet, B., DeBerardinis, R.J., and Jones, R.G. (2015). Metformin Antagonizes Cancer Cell Proliferation by Suppressing Mitochondrial-Dependent Biosynthesis. *PLoS biology* *13*, e1002309.
- Groennebaek, T., Nielsen, J., Jespersen, N.R., Botker, H.E., de Paoli, F.V., Miller, B.F., and Vissing, K. (2020). Utilization of biomarkers as predictors of skeletal muscle mitochondrial content after physiological intervention and in clinical settings. *Am J Physiol Endocrinol Metab* *318*, E886-E889.
- Gunnar, M., and Quevedo, K. (2007). The neurobiology of stress and development. *Annual review of psychology* *58*, 145-173.
- Gut, P., and Verdin, E. (2013). The nexus of chromatin regulation and intermediary metabolism. *Nature* *502*, 489-498.
- Hackett, R.A., and Steptoe, A. (2016). Psychosocial Factors in Diabetes and Cardiovascular Risk. *Current cardiology reports* *18*, 95.

- Hao, N., and O'Shea, E.K. (2011). Signal-dependent dynamics of transcription factor translocation controls gene expression. *Nature structural & molecular biology* *19*, 31-39.
- Hatefi, Y. (1985). The mitochondrial electron transport and oxidative phosphorylation system. *Annual review of biochemistry* *54*, 1015-1069.
- Hatefi, Y., and Bearden, A.J. (1976). Electron paramagnetic resonance studies on the reduction of the components of complex I and transhydrogenase-inhibited complex I by NADH and NADPH. *Biochemical and biophysical research communications* *69*, 1032-1038.
- Hatefi, Y., Haavik, A.G., and Griffiths, D.E. (1962). Studies on the electron transfer system. XL. Preparation and properties of mitochondrial DPNH-coenzyme Q reductase. *J Biol Chem* *237*, 1676-1680.
- Hattersley, A.T., Greeley, S.A.W., Polak, M., Rubio-Cabezas, O., Njølstad, P.R., Mlynarski, W., Castano, L., Carlsson, A., Raile, K., Chi, D.V., *et al.* (2018). ISPAD Clinical Practice Consensus Guidelines 2018: The diagnosis and management of monogenic diabetes in children and adolescents. *Pediatric diabetes* *19 Suppl 27*, 47-63.
- Hazlehurst, J.M., and Tomlinson, J.W. (2013). Non-alcoholic fatty liver disease in common endocrine disorders. *Eur J Endocrinol* *169*, R27-37.
- Hazra, A., Kraft, P., Lazarus, R., Chen, C., Chanock, S.J., Jacques, P., Selhub, J., and Hunter, D.J. (2009). Genome-wide significant predictors of metabolites in the one-carbon metabolism pathway. *Human molecular genetics* *18*, 4677-4687.
- Herman, J.P., McKlveen, J.M., Ghosal, S., Kopp, B., Wulsin, A., Makinson, R., Scheimann, J., and Myers, B. (2016). Regulation of the Hypothalamic-Pituitary-Adrenocortical Stress Response. *Comprehensive Physiology* *6*, 603-621.
- Hirschenson, J., Melgar-Bermudez, E., and Mailloux, R.J. (2022). The Uncoupling Proteins: A Systematic Review on the Mechanism Used in the Prevention of Oxidative Stress. *Antioxidants (Basel)* *11*.
- Hirst, J., Carroll, J., Fearnley, I.M., Shannon, R.J., and Walker, J.E. (2003). The nuclear encoded subunits of complex I from bovine heart mitochondria. *Biochimica et biophysica acta* *1604*, 135-150.
- Hoffman, D.J., Powell, T.L., Barrett, E.S., and Hardy, D.B. (2021). Developmental origins of metabolic diseases. *Physiological reviews* *101*, 739-795.
- Hondares, E., Iglesias, R., Giralt, A., Gonzalez, F.J., Giralt, M., Mampel, T., and Villarroya, F. (2011). Thermogenic activation induces FGF21 expression and release in brown adipose tissue. *J Biol Chem* *286*, 12983-12990.
- Horváth, J., Czigler, I., Birkás, E., Winkler, I., and Gervai, J. (2009). Age-related differences in distraction and reorientation in an auditory task. *Neurobiology of aging* *30*, 1157-1172.
- Hue, L., and Taegtmeier, H. (2009). The Randle cycle revisited: a new head for an old hat. *Am J Physiol Endocrinol Metab* *297*, E578-591.
- Huertas, J.R., Casuso, R.A., Agustín, P.H., and Cogliati, S. (2019). Stay Fit, Stay Young: Mitochondria in Movement: The Role of Exercise in the New Mitochondrial Paradigm. *Oxid Med Cell Longev* *2019*, 7058350.
- Hussain, W., Campbell, M., Walia, H., and Morota, G. (2018). ShinyAIM: Shiny-based application of interactive Manhattan plots for longitudinal genome-wide association studies. *Plant direct* *2*, e00091.
- Huszar, D., Lynch, C.A., Fairchild-Huntress, V., Dunmore, J.H., Fang, Q., Berkemeier, L.R., Gu, W., Kesterson, R.A., Boston, B.A., Cone, R.D., *et al.* (1997). Targeted disruption of the melanocortin-4 receptor results in obesity in mice. *Cell* *88*, 131-141.

- Ikeda, R., Tsuchiya, Y., Koike, N., Umemura, Y., Inokawa, H., Ono, R., Inoue, M., Sasawaki, Y., Grieten, T., Okubo, N., *et al.* (2019). REV-ERB α and REV-ERB β function as key factors regulating Mammalian Circadian Output. *Scientific reports* *9*, 10171.
- Islam, T., Afonso, M.B., and Rodrigues, C.M.P. (2022). The role of RIPK3 in liver mitochondria bioenergetics and function. *European journal of clinical investigation* *52*, e13648.
- Iyegha, I.D., Chieh, A.Y., Bryant, B.M., and Li, L. (2019). Associations between poor sleep and glucose intolerance in prediabetes. *Psychoneuroendocrinology* *110*, 104444.
- Izumiya, Y., Bina, H.A., Ouchi, N., Akasaki, Y., Kharitonov, A., and Walsh, K. (2008). FGF21 is an Akt-regulated myokine. *FEBS Lett* *582*, 3805-3810.
- Jackson, R.S., Creemers, J.W., Ohagi, S., Raffin-Sanson, M.L., Sanders, L., Montague, C.T., Hutton, J.C., and O'Rahilly, S. (1997). Obesity and impaired prohormone processing associated with mutations in the human prohormone convertase 1 gene. *Nature genetics* *16*, 303-306.
- Jaggi, A.S., Bhatia, N., Kumar, N., Singh, N., Anand, P., and Dhawan, R. (2011). A review on animal models for screening potential anti-stress agents. *Neurological sciences : official journal of the Italian Neurological Society and of the Italian Society of Clinical Neurophysiology* *32*, 993-1005.
- Jelenik, T., Dille, M., Müller-Lühlhoff, S., Kabra, D.G., Zhou, Z., Binsch, C., Hartwig, S., Lehr, S., Chadt, A., Peters, E.M.J., *et al.* (2018). FGF21 regulates insulin sensitivity following long-term chronic stress. *Molecular metabolism* *16*, 126-138.
- Jezek, P., Engstová, H., Zácková, M., Vercesi, A.E., Costa, A.D., Arruda, P., and Garlid, K.D. (1998). Fatty acid cycling mechanism and mitochondrial uncoupling proteins. *Biochimica et biophysica acta* *1365*, 319-327.
- Jing, X.P., Wang, W.J., Degen, A.A., Guo, Y.M., Kang, J.P., Liu, P.P., Ding, L.M., Shang, Z.H., Zhou, J.W., and Long, R.J. (2021). Energy substrate metabolism in skeletal muscle and liver when consuming diets of different energy levels: comparison between Tibetan and Small-tailed Han sheep. *Animal : an international journal of animal bioscience* *15*, 100162.
- John, R.M., and Rougeulle, C. (2018). Developmental Epigenetics: Phenotype and the Flexible Epigenome. *Front Cell Dev Biol* *6*, 130.
- Jung, M., and Pfeifer, G.P. (2015). Aging and DNA methylation. *BMC biology* *13*, 7.
- Juvinao-Quintero, D.L., Marioni, R.E., Ochoa-Rosales, C., Russ, T.C., Deary, I.J., van Meurs, J.B.J., Voortman, T., Hivert, M.F., Sharp, G.C., Relton, C.L., *et al.* (2021). DNA methylation of blood cells is associated with prevalent type 2 diabetes in a meta-analysis of four European cohorts. *Clinical epigenetics* *13*, 40.
- Kadenbach, B., Jaraus, J., Hartmann, R., and Merle, P. (1983). Separation of mammalian cytochrome c oxidase into 13 polypeptides by a sodium dodecyl sulfate-gel electrophoretic procedure. *Analytical biochemistry* *129*, 517-521.
- Kahn, S.E., Cooper, M.E., and Del Prato, S. (2014). Pathophysiology and treatment of type 2 diabetes: perspectives on the past, present, and future. *Lancet (London, England)* *383*, 1068-1083.
- Kalantari, N., Keshavarz Mohammadi, N., Izadi, P., Doaei, S., Gholamalizadeh, M., Eini-Zinab, H., Salonurmi, T., Rafieifar, S., Janipoor, R., and Azizi Tabesh, G. (2018). A haplotype of three SNPs in FTO had a strong association with body composition and BMI in Iranian male adolescents. *PloS one* *13*, e0195589.
- Kang, D., Zhao, D., Ryu, S., Guallar, E., Cho, J., Lazo, M., Shin, H., Chang, Y., and Sung, E. (2020). Perceived stress and non-alcoholic fatty liver disease in apparently healthy men and women. *Scientific reports* *10*, 38.

- Kappler, L., Hoene, M., Hu, C., von Toerne, C., Li, J., Bleher, D., Hoffmann, C., Böhm, A., Kollipara, L., Zischka, H., *et al.* (2019). Linking bioenergetic function of mitochondria to tissue-specific molecular fingerprints. *Am J Physiol Endocrinol Metab* 317, E374-e387.
- Karatsoreos, I.N., and McEwen, B.S. (2011). Psychobiological allostasis: resistance, resilience and vulnerability. *Trends in cognitive sciences* 15, 576-584.
- Keilin, D. (1925). On cytochrome, a respiratory pigment, common to animals, yeast, and higher plants. *Proceedings of the Royal Society of London Series B, Containing Papers of a Biological Character* 98690.
- Keilin, D.E., F. Hartee; and E. F. Hartree (1939). Cytochrome and cytochrome oxidase. *Proceedings of the Royal Society of London Series B-Biological Sciences* 12784.
- Kita, K., Oya, H., Gennis, R.B., Ackrell, B.A., and Kasahara, M. (1990). Human complex II (succinate-ubiquinone oxidoreductase): cDNA cloning of iron sulfur (Ip) subunit of liver mitochondria. *Biochemical and biophysical research communications* 166, 101-108.
- Kivimäki, M., and Steptoe, A. (2018). Effects of stress on the development and progression of cardiovascular disease. *Nature reviews Cardiology* 15, 215-229.
- Klose, R.J., and Zhang, Y. (2007). Regulation of histone methylation by demethylation and demethylation. *Nature reviews Molecular cell biology* 8, 307-318.
- Knebel, B., Fahlbusch, P., Dille, M., Wahlers, N., Hartwig, S., Jacob, S., Kettel, U., Schiller, M., Herebian, D., Koellmer, C., *et al.* (2019). Fatty Liver Due to Increased de novo Lipogenesis: Alterations in the Hepatic Peroxisomal Proteome. *Front Cell Dev Biol* 7, 248.
- Kodama, K., Ichihara, A., Seki, Y., Ikarashi, Y., Sagawa, T., Kogiso, T., Taniai, M., and Tokushige, K. (2020). Characteristics of NAFLD Based on Hypopituitarism. *Canadian journal of gastroenterology & hepatology* 2020, 8814435.
- Kokkinopoulou, I., Diakoumi, A., and Moutsatsou, P. (2021). Glucocorticoid Receptor Signaling in Diabetes. *International journal of molecular sciences* 22.
- Kokkinopoulou, I., and Moutsatsou, P. (2021). Mitochondrial Glucocorticoid Receptors and Their Actions. *International journal of molecular sciences* 22.
- Koliwad, S.K., Kuo, T., Shipp, L.E., Gray, N.E., Backhed, F., So, A.Y., Farese, R.V., Jr., and Wang, J.C. (2009). Angiopoietin-like 4 (ANGPTL4, fasting-induced adipose factor) is a direct glucocorticoid receptor target and participates in glucocorticoid-regulated triglyceride metabolism. *J Biol Chem* 284, 25593-25601.
- Kong, X., Yao, T., Zhou, P., Kazak, L., Tenen, D., Lyubetskaya, A., Dawes, B.A., Tsai, L., Kahn, B.B., Spiegelman, B.M., *et al.* (2018). Brown Adipose Tissue Controls Skeletal Muscle Function via the Secretion of Myostatin. *Cell metabolism* 28, 631-643.e633.
- Koolhaas, J.M., Bartolomucci, A., Buwalda, B., de Boer, S.F., Flügge, G., Korte, S.M., Meerlo, P., Murison, R., Olivier, B., Palanza, P., *et al.* (2011). Stress revisited: a critical evaluation of the stress concept. *Neuroscience and biobehavioral reviews* 35, 1291-1301.
- Kovner, I., Taicher, G.Z., and Mitchell, A.D. (2010). Calibration and validation of EchoMRI™ whole body composition analysis based on chemical analysis of piglets, in comparison with the same for DXA. *International journal of body composition research* 8, 17-29.
- Krämer, A., Green, J., Pollard, J., Jr., and Tugendreich, S. (2014). Causal analysis approaches in Ingenuity Pathway Analysis. *Bioinformatics (Oxford, England)* 30, 523-530.
- Krause, C., Geißler, C., Tackenberg, H., El Gammal, A.T., Wolter, S., Spranger, J., Mann, O., Lehnert, H., and Kirchner, H. (2020). Multi-layered epigenetic regulation of IRS2 expression in the liver of obese individuals with type 2 diabetes. *Diabetologia* 63, 2182-2193.

- Krieg, L., Didt, K., Karkossa, I., Bernhart, S.H., Kehr, S., Subramanian, N., Lindhorst, A., Schaudinn, A., Tabei, S., Keller, M., *et al.* (2022). Multiomics reveal unique signatures of human epiploic adipose tissue related to systemic insulin resistance. *Gut* *71*, 2179-2193.
- Krude, H., Biebermann, H., Luck, W., Horn, R., Brabant, G., and Grüters, A. (1998). Severe early-onset obesity, adrenal insufficiency and red hair pigmentation caused by POMC mutations in humans. *Nature genetics* *19*, 155-157.
- Krueger, F., and Andrews, S.R. (2011). Bismark: a flexible aligner and methylation caller for Bisulfite-Seq applications. *Bioinformatics (Oxford, England)* *27*, 1571-1572.
- Krzywinski, M., Schein, J., Birol, I., Connors, J., Gascoyne, R., Horsman, D., Jones, S.J., and Marra, M.A. (2009). Circos: an information aesthetic for comparative genomics. *Genome research* *19*, 1639-1645.
- Lagace, D.C., Donovan, M.H., DeCarolis, N.A., Farnbauch, L.A., Malhotra, S., Berton, O., Nestler, E.J., Krishnan, V., and Eisch, A.J. (2010). Adult hippocampal neurogenesis is functionally important for stress-induced social avoidance. *Proc Natl Acad Sci U S A* *107*, 4436-4441.
- Lam, Y.Y., and Ravussin, E. (2016). Analysis of energy metabolism in humans: A review of methodologies. *Molecular metabolism* *5*, 1057-1071.
- Lapp, H.E., Bartlett, A.A., and Hunter, R.G. (2019). Stress and glucocorticoid receptor regulation of mitochondrial gene expression. *Journal of molecular endocrinology* *62*, R121-r128.
- Larsen, S., Nielsen, J., Hansen, C.N., Nielsen, L.B., Wibrand, F., Stride, N., Schroder, H.D., Boushel, R., Helge, J.W., Dela, F., *et al.* (2012). Biomarkers of mitochondrial content in skeletal muscle of healthy young human subjects. *The Journal of physiology* *590*, 3349-3360.
- Lea, P.J., and Hollenberg, M.J. (1989). Mitochondrial structure revealed by high-resolution scanning electron microscopy. *The American journal of anatomy* *184*, 245-257.
- Lee, E., Korf, H., and Vidal-Puig, A. (2023). An adipocentric perspective on the development and progression of non-alcoholic fatty liver disease. *Journal of hepatology* *78*, 1048-1062.
- Lewis, M.T., Levitsky, Y., Bazil, J.N., and Wiseman, R.W. (2022). Measuring Mitochondrial Function: From Organelle to Organism. *Methods Mol Biol* *2497*, 141-172.
- Li, E., Beard, C., and Jaenisch, R. (1993). Role for DNA methylation in genomic imprinting. *Nature* *366*, 362-365.
- Li, E., and Zhang, Y. (2014). DNA methylation in mammals. *Cold Spring Harbor perspectives in biology* *6*, a019133.
- Li, H., Handsaker, B., Wysoker, A., Fennell, T., Ruan, J., Homer, N., Marth, G., Abecasis, G., and Durbin, R. (2009). The Sequence Alignment/Map format and SAMtools. *Bioinformatics (Oxford, England)* *25*, 2078-2079.
- Li, S., Peng, Y., and Panchenko, A.R. (2022). DNA methylation: Precise modulation of chromatin structure and dynamics. *Current opinion in structural biology* *75*, 102430.
- Lienhard, M., Grimm, C., Morkel, M., Herwig, R., and Chavez, L. (2014). MEDIPS: genome-wide differential coverage analysis of sequencing data derived from DNA enrichment experiments. *Bioinformatics (Oxford, England)* *30*, 284-286.
- Liesa, M., Palacín, M., and Zorzano, A. (2009). Mitochondrial dynamics in mammalian health and disease. *Physiological reviews* *89*, 799-845.
- Lin, B., Morris, D.W., and Chou, J.Y. (1998). Hepatocyte nuclear factor 1alpha is an accessory factor required for activation of glucose-6-phosphatase gene transcription by glucocorticoids. *DNA and cell biology* *17*, 967-974.

- Lindqvist, D., Dhabhar, F.S., Mellon, S.H., Yehuda, R., Grenon, S.M., Flory, J.D., Bierer, L.M., Abu-Amara, D., Coy, M., Makotkine, I., *et al.* (2017). Increased pro-inflammatory milieu in combat related PTSD - A new cohort replication study. *Brain, behavior, and immunity* 59, 260-264.
- Ling, C., and Rönn, T. (2019). Epigenetics in Human Obesity and Type 2 Diabetes. *Cell metabolism* 29, 1028-1044.
- Liu, W., Acín-Peréz, R., Geghman, K.D., Manfredi, G., Lu, B., and Li, C. (2011). Pink1 regulates the oxidative phosphorylation machinery via mitochondrial fission. *Proc Natl Acad Sci U S A* 108, 12920-12924.
- Liu, Y.F., Zhu, J.J., Yu Tian, X., Liu, H., Zhang, T., Zhang, Y.P., Xie, S.A., Zheng, M., Kong, W., Yao, W.J., *et al.* (2020). Hypermethylation of mitochondrial DNA in vascular smooth muscle cells impairs cell contractility. *Cell death & disease* 11, 35.
- Loeffen, J.L., Smeitink, J.A., Trijbels, J.M., Janssen, A.J., Triepels, R.H., Sengers, R.C., and van den Heuvel, L.P. (2000). Isolated complex I deficiency in children: clinical, biochemical and genetic aspects. *Human mutation* 15, 123-134.
- Loos, R.J.F., and Yeo, G.S.H. (2022). The genetics of obesity: from discovery to biology. *Nature reviews Genetics* 23, 120-133.
- Losón, O.C., Song, Z., Chen, H., and Chan, D.C. (2013). Fis1, Mff, MiD49, and MiD51 mediate Drp1 recruitment in mitochondrial fission. *Molecular biology of the cell* 24, 659-667.
- Loud, A.V. (1968). A quantitative stereological description of the ultrastructure of normal rat liver parenchymal cells. *The Journal of cell biology* 37, 27-46.
- Lumey, L.H., Ravelli, A.C., Wiessing, L.G., Koppe, J.G., Treffers, P.E., and Stein, Z.A. (1993). The Dutch famine birth cohort study: design, validation of exposure, and selected characteristics of subjects after 43 years follow-up. *Paediatric and perinatal epidemiology* 7, 354-367.
- Mahajan, A., Taliun, D., Thurner, M., Robertson, N.R., Torres, J.M., Rayner, N.W., Payne, A.J., Steinthorsdottir, V., Scott, R.A., Grarup, N., *et al.* (2018). Fine-mapping type 2 diabetes loci to single-variant resolution using high-density imputation and islet-specific epigenome maps. *Nature genetics* 50, 1505-1513.
- Maiti, A., and Drohat, A.C. (2011). Thymine DNA glycosylase can rapidly excise 5-formylcytosine and 5-carboxylcytosine: potential implications for active demethylation of CpG sites. *J Biol Chem* 286, 35334-35338.
- Mannella, C.A., Marko, M., Penczek, P., Barnard, D., and Frank, J. (1994). The internal compartmentation of rat-liver mitochondria: tomographic study using the high-voltage transmission electron microscope. *Microscopy research and technique* 27, 278-283.
- Mansour, A.M., and Nass, S. (1970). In vivo cortisol action on RNA synthesis in rat liver nuclei and mitochondria. *Nature* 228, 665-667.
- Margulis, L. (1975). Symbiotic theory of the origin of eukaryotic organelles; criteria for proof. *Symposia of the Society for Experimental Biology*, 21-38.
- Margulis, L. (1981). *Symbiosis in cell evolution: Life and its environment on the early earth*. Book.
- Margulis, L., and Bermudes, D. (1985). Symbiosis as a mechanism of evolution: status of cell symbiosis theory. *Symbiosis (Philadelphia, Pa)* 1, 101-124.
- Martínez-Reyes, I., Diebold, L.P., Kong, H., Schieber, M., Huang, H., Hensley, C.T., Mehta, M.M., Wang, T., Santos, J.H., Woychik, R., *et al.* (2016). TCA Cycle and Mitochondrial Membrane Potential Are Necessary for Diverse Biological Functions. *Molecular cell* 61, 199-209.

- Martínez, J.A., Milagro, F.I., Claycombe, K.J., and Schalinske, K.L. (2014). Epigenetics in adipose tissue, obesity, weight loss, and diabetes. *Advances in nutrition (Bethesda, Md)* 5, 71-81.
- Mathers, J.C., Strathdee, G., and Relton, C.L. (2010). Induction of epigenetic alterations by dietary and other environmental factors. *Advances in genetics* 71, 3-39.
- Matilainen, O., Quirós, P.M., and Auwerx, J. (2017). Mitochondria and Epigenetics - Crosstalk in Homeostasis and Stress. *Trends in cell biology* 27, 453-463.
- Mazziotti, G., Gazzaruso, C., and Giustina, A. (2011). Diabetes in Cushing syndrome: basic and clinical aspects. *Trends Endocrinol Metab* 22, 499-506.
- McEwen, B.S. (1998). Stress, adaptation, and disease. Allostasis and allostatic load. *Ann N Y Acad Sci* 840, 33-44.
- McEwen, B.S. (2007). Physiology and neurobiology of stress and adaptation: central role of the brain. *Physiological reviews* 87, 873-904.
- McGarry, J.D., and Foster, D.W. (1980). Regulation of hepatic fatty acid oxidation and ketone body production. *Annual review of biochemistry* 49, 395-420.
- McLaughlin, K.L., Hagen, J.T., Coalson, H.S., Nelson, M.A.M., Kew, K.A., Wooten, A.R., and Fisher-Wellman, K.H. (2020). Novel approach to quantify mitochondrial content and intrinsic bioenergetic efficiency across organs. *Sci Rep* 10, 17599.
- Mellon, S.H., Bersani, F.S., Lindqvist, D., Hammamieh, R., Donohue, D., Dean, K., Jett, M., Yehuda, R., Flory, J., Reus, V.I., *et al.* (2019). Metabolomic analysis of male combat veterans with post traumatic stress disorder. *PLoS One* 14, e0213839.
- Mellon, S.H., Gautam, A., Hammamieh, R., Jett, M., and Wolkowitz, O.M. (2018). Metabolism, Metabolomics, and Inflammation in Posttraumatic Stress Disorder. *Biological psychiatry* 83, 866-875.
- Meng, S., Cao, J., Feng, Q., Peng, J., and Hu, Y. (2013). Roles of chlorogenic Acid on regulating glucose and lipids metabolism: a review. *Evidence-based complementary and alternative medicine : eCAM* 2013, 801457.
- Mi, H., Muruganujan, A., Huang, X., Ebert, D., Mills, C., Guo, X., and Thomas, P.D. (2019). Protocol Update for large-scale genome and gene function analysis with the PANTHER classification system (v.14.0). *Nature protocols* 14, 703-721.
- Mitchell, P. (1961). Coupling of phosphorylation to electron and hydrogen transfer by a chemi-osmotic type of mechanism. *Nature* 191, 144-148.
- Mitsui, T., Azuma, H., Nagasawa, M., Iuchi, T., Akaike, M., Odomi, M., and Matsumoto, T. (2002a). Chronic corticosteroid administration causes mitochondrial dysfunction in skeletal muscle. *J Neurol* 249, 1004-1009.
- Mitsui, T., Umaki, Y., Nagasawa, M., Akaike, M., Aki, K., Azuma, H., Ozaki, S., Odomi, M., and Matsumoto, T. (2002b). Mitochondrial damage in patients with long-term corticosteroid therapy: development of osculoskeletal symptoms similar to mitochondrial disease. *Acta Neuropathol* 104, 260-266.
- Mohandas, T., Sparkes, R.S., and Shapiro, L.J. (1981). Reactivation of an inactive human X chromosome: evidence for X inactivation by DNA methylation. *Science* 211, 393-396.
- Morris, E.M., Meers, G.M., Booth, F.W., Fritsche, K.L., Hardin, C.D., Thyfault, J.P., and Ibdah, J.A. (2012). PGC-1 α overexpression results in increased hepatic fatty acid oxidation with reduced triacylglycerol accumulation and secretion. *American journal of physiology Gastrointestinal and liver physiology* 303, G979-992.

- Muraca, M., and Cappariello, A. (2020). The Role of Extracellular Vesicles (EVs) in the Epigenetic Regulation of Bone Metabolism and Osteoporosis. *Int J Mol Sci* 21.
- Nandipati, K.C., Subramanian, S., and Agrawal, D.K. (2017). Protein kinases: mechanisms and downstream targets in inflammation-mediated obesity and insulin resistance. *Molecular and cellular biochemistry* 426, 27-45.
- NIH.gov (18.05.2022). Metabolic syndrome.
- Nikolic, A., Fahlbusch, P., Wahlers, N., Riffelmann, N.K., Jacob, S., Hartwig, S., Kettel, U., Dille, M., Al-Hasani, H., Kotzka, J., *et al.* (2023). Chronic stress targets mitochondrial respiratory efficiency in the skeletal muscle of C57BL/6 mice. *Cellular and molecular life sciences : CMLS* 80, 108.
- Ohnishi, T. (1998). Iron-sulfur clusters/semiquinones in complex I. *Biochimica et biophysica acta* 1364, 186-206.
- Okano, H. (2000). [Neural stem cells: the basic biology and prospects for brain repair]. *Nihon shinkei seishin yakurigaku zasshi = Japanese journal of psychopharmacology* 20, 21-26.
- Onodera, A., González-Avalos, E., Lio, C.J., Georges, R.O., Bellacosa, A., Nakayama, T., and Rao, A. (2021). Roles of TET and TDG in DNA demethylation in proliferating and non-proliferating immune cells. *Genome biology* 22, 186.
- Osellame, L.D., Blacker, T.S., and Duchon, M.R. (2012). Cellular and molecular mechanisms of mitochondrial function. *Best Pract Res Clin Endocrinol Metab* 26, 711-723.
- Oster, H., Challet, E., Ott, V., Arvat, E., de Kloet, E.R., Dijk, D.J., Lightman, S., Vgontzas, A., and Van Cauter, E. (2017). The Functional and Clinical Significance of the 24-Hour Rhythm of Circulating Glucocorticoids. *Endocrine reviews* 38, 3-45.
- Ouni, M., and Schürmann, A. (2020). Epigenetic contribution to obesity. *Mammalian genome : official journal of the International Mammalian Genome Society* 31, 134-145.
- Oyedotun, K.S., and Lemire, B.D. (2001). The Quinone-binding sites of the *Saccharomyces cerevisiae* succinate-ubiquinone oxidoreductase. *J Biol Chem* 276, 16936-16943.
- Packard, A.E., Ghosal, S., Herman, J.P., Woods, S.C., and Ulrich-Lai, Y.M. (2014). Chronic variable stress improves glucose tolerance in rats with sucrose-induced prediabetes. *Psychoneuroendocrinology* 47, 178-188.
- Padovan, C.M., and Guimarães, F.S. (2000). Restraint-induced hypoactivity in an elevated plus-maze. *Brazilian journal of medical and biological research = Revista brasileira de pesquisas medicas e biologicas* 33, 79-83.
- Pagoto, S.L., Schneider, K.L., Bodenlos, J.S., Appelhans, B.M., Whited, M.C., Ma, Y., and Lemon, S.C. (2012). Association of post-traumatic stress disorder and obesity in a nationally representative sample. *Obesity (Silver Spring)* 20, 200-205.
- Palmer, C.S., Osellame, L.D., Laine, D., Koutsopoulos, O.S., Frazier, A.E., and Ryan, M.T. (2011). MiD49 and MiD51, new components of the mitochondrial fission machinery. *EMBO reports* 12, 565-573.
- Pan, X., Wu, Y., Peng, H., Cai, X., Hu, Z., Lin, X., and Peng, X.E. (2022). Genome-wide DNA methylation profiling in nonalcoholic fatty liver reveals predictive aberrant methylation in PRKCE and SEC14L3 promoters. *Digestive and liver disease : official journal of the Italian Society of Gastroenterology and the Italian Association for the Study of the Liver* 54, 521-528.
- Pattaranit, R., and van den Berg, H.A. (2008). Mathematical models of energy homeostasis. *Journal of the Royal Society, Interface* 5, 1119-1135.
- Pearson, E.R. (2019). Type 2 diabetes: a multifaceted disease. *Diabetologia* 62, 1107-1112.

- Pekgor, S., Duran, C., Berberoglu, U., and Eryilmaz, M.A. (2019). The Role of Visceral Adiposity Index Levels in Predicting the Presence of Metabolic Syndrome and Insulin Resistance in Overweight and Obese Patients. *Metabolic syndrome and related disorders* 17, 296-302.
- Peng, L., Yuan, Z., Ling, H., Fukasawa, K., Robertson, K., Olashaw, N., Koomen, J., Chen, J., Lane, W.S., and Seto, E. (2011). SIRT1 deacetylates the DNA methyltransferase 1 (DNMT1) protein and alters its activities. *Mol Cell Biol* 31, 4720-4734.
- Péronnet, F., and Massicotte, D. (1991). Table of nonprotein respiratory quotient: an update. *Canadian journal of sport sciences = Journal canadien des sciences du sport* 16, 23-29.
- Piaggi, P., Vinales, K.L., Basolo, A., Santini, F., and Krakoff, J. (2018). Energy expenditure in the etiology of human obesity: spendthrift and thrifty metabolic phenotypes and energy-sensing mechanisms. *Journal of endocrinological investigation* 41, 83-89.
- Pibernik-Okanović, M., Roglič, G., Prasek, M., and Metelko, Z. (1993). War-induced prolonged stress and metabolic control in type 2 diabetic patients. *Psychological medicine* 23, 645-651.
- Picard, M., and McEwen, B.S. (2018a). Psychological Stress and Mitochondria: A Conceptual Framework. *Psychosomatic medicine* 80, 126-140.
- Picard, M., and McEwen, B.S. (2018b). Psychological Stress and Mitochondria: A Systematic Review. *Psychosomatic medicine* 80, 141-153.
- Picard, M., Vincent, A.E., and Turnbull, D.M. (2016). Expanding Our Understanding of mtDNA Deletions. *Cell metabolism* 24, 3-4.
- Pirola, C.J., Gianotti, T.F., Burgueño, A.L., Rey-Funes, M., Loidl, C.F., Mallardi, P., Martino, J.S., Castaño, G.O., and Sookoian, S. (2013). Epigenetic modification of liver mitochondrial DNA is associated with histological severity of nonalcoholic fatty liver disease. *Gut* 62, 1356-1363.
- Qing, H., Desrouleaux, R., Israni-Winger, K., Mineur, Y.S., Fogelman, N., Zhang, C., Rashed, S., Palm, N.W., Sinha, R., Picciotto, M.R., *et al.* (2020). Origin and Function of Stress-Induced IL-6 in Murine Models. *Cell* 182, 372-387.e314.
- Quiros, P.M., Goyal, A., Jha, P., and Auwerx, J. (2017). Analysis of mtDNA/nDNA Ratio in Mice. *Current protocols in mouse biology* 7, 47-54.
- Rabasa, C., Askevik, K., Schele, E., Hu, M., Vogel, H., and Dickson, S.L. (2019). Divergent Metabolic Effects of Acute Versus Chronic Repeated Forced Swim Stress in the Rat. *Obesity (Silver Spring)* 27, 427-433.
- Radhakutty, A., Mangelsdorf, B.L., Drake, S.M., Samocha-Bonet, D., Jenkins, A.B., Heilbronn, L.K., Smith, M.D., Thompson, C.H., and Burt, M.G. (2016). Effect of acute and chronic glucocorticoid therapy on insulin sensitivity and postprandial vascular function. *Clinical endocrinology* 84, 501-508.
- Rahimi, L., Rajpal, A., and Ismail-Beigi, F. (2020). Glucocorticoid-Induced Fatty Liver Disease. *Diabetes, metabolic syndrome and obesity : targets and therapy* 13, 1133-1145.
- Rai, D., Bhatia, G., Sen, T., and Palit, G. (2003). Comparative study of perturbations of peripheral markers in different stressors in rats. *Canadian journal of physiology and pharmacology* 81, 1139-1146.
- Ramírez-Camacho, I., García-Niño, W.R., Flores-García, M., Pedraza-Chaverri, J., and Zazueta, C. (2020). Alteration of mitochondrial supercomplexes assembly in metabolic diseases. *Biochimica et biophysica acta Molecular basis of disease* 1866, 165935.
- Ramos Figueira, E.R., Rocha Filho, J.A., Souto Nacif, L., Carneiro D'Albuquerque, L., and Linetzky Waitzberg, D. (2015). NUTRITIONAL SUPPORT FOR FULMINANT HEPATITIS. *Nutricion hospitalaria* 32, 2427-2432.

- Randle, P.J. (1998). Regulatory interactions between lipids and carbohydrates: the glucose fatty acid cycle after 35 years. *Diabetes/metabolism reviews* 14, 263-283.
- Rasche, H., and Hiltmann, S. (2020). Galactic Circos: User-friendly Circos plots within the Galaxy platform. *GigaScience* 9.
- Ravussin, Y., Xiao, C., Gavrilova, O., and Reitman, M.L. (2014). Effect of intermittent cold exposure on brown fat activation, obesity, and energy homeostasis in mice. *PLoS one* 9, e85876.
- Reichmann, H., Hoppeler, H., Mathieu-Costello, O., von Bergen, F., and Pette, D. (1985). Biochemical and ultrastructural changes of skeletal muscle mitochondria after chronic electrical stimulation in rabbits. *Pflügers Archiv : European journal of physiology* 404, 1-9.
- Reynolds, R.M., Labad, J., Strachan, M.W., Braun, A., Fowkes, F.G., Lee, A.J., Frier, B.M., Seckl, J.R., Walker, B.R., and Price, J.F. (2010). Elevated fasting plasma cortisol is associated with ischemic heart disease and its risk factors in people with type 2 diabetes: the Edinburgh type 2 diabetes study. *The Journal of clinical endocrinology and metabolism* 95, 1602-1608.
- Roca-Portoles, A., and Tait, S.W.G. (2021). Mitochondrial quality control: from molecule to organelle. *Cellular and molecular life sciences : CMLS* 78, 3853-3866.
- Rogers, G.W., Brand, M.D., Petrosyan, S., Ashok, D., Elorza, A.A., Ferrick, D.A., and Murphy, A.N. (2011). High throughput microplate respiratory measurements using minimal quantities of isolated mitochondria. *PLoS one* 6, e21746.
- Rogers, J.M. (2019). Smoking and pregnancy: Epigenetics and developmental origins of the metabolic syndrome. *Birth defects research* 111, 1259-1269.
- Rohde, K., Keller, M., la Cour Poulsen, L., Blüher, M., Kovacs, P., and Böttcher, Y. (2019). Genetics and epigenetics in obesity. *Metabolism* 92, 37-50.
- Rolfe, D.F., and Brown, G.C. (1997). Cellular energy utilization and molecular origin of standard metabolic rate in mammals. *Physiological reviews* 77, 731-758.
- Romanello, V., Guadagnin, E., Gomes, L., Roder, I., Sandri, C., Petersen, Y., Milan, G., Masiero, E., Del Piccolo, P., Foretz, M., *et al.* (2010). Mitochondrial fission and remodelling contributes to muscle atrophy. *EMBO J* 29, 1774-1785.
- Roussel, D., Dumas, J.F., Augeraud, A., Douay, O., Foussard, F., Malthiery, Y., Simard, G., and Ritz, P. (2003). Dexamethasone treatment specifically increases the basal proton conductance of rat liver mitochondria. *FEBS Lett* 541, 75-79.
- Rubner, M. ((1883)). Ueber den Einfluss der Körpergröße auf Stoff- und Kraftwechsel. *Zeitschrift für Biologie* 19, S. 535–562.
- Russell, G., and Lightman, S. (2019). The human stress response. *Nature reviews Endocrinology* 15, 525-534.
- Ryu, W.I., Shen, M., Lee, Y., Healy, R.A., Bormann, M.K., Cohen, B.M., and Sonntag, K.C. (2022). Nicotinamide riboside and caffeine partially restore diminished NAD availability but not altered energy metabolism in Alzheimer's disease. *Aging cell* 21, e13658.
- Saeed, S., Arslan, M., Manzoor, J., Din, S.M., Janjua, Q.M., Ayesha, H., Ain, Q.T., Inam, L., Lobbens, S., Vaillant, E., *et al.* (2020). Genetic Causes of Severe Childhood Obesity: A Remarkably High Prevalence in an Inbred Population of Pakistan. *Diabetes* 69, 1424-1438.
- Saeedi, P., Petersohn, I., Salpea, P., Malanda, B., Karuranga, S., Unwin, N., Colagiuri, S., Guariguata, L., Motala, A.A., Ogurtsova, K., *et al.* (2019). Global and regional diabetes prevalence estimates for 2019 and projections for 2030 and 2045: Results from the International Diabetes Federation Diabetes Atlas, 9(th) edition. *Diabetes research and clinical practice* 157, 107843.

- Sangwung, P., Petersen, K.F., Shulman, G.I., and Knowles, J.W. (2020). Mitochondrial Dysfunction, Insulin Resistance, and Potential Genetic Implications. *Endocrinology* *161*.
- Sasaki, K., Cripe, T.P., Koch, S.R., Andreone, T.L., Petersen, D.D., Beale, E.G., and Granner, D.K. (1984). Multihormonal regulation of phosphoenolpyruvate carboxykinase gene transcription. The dominant role of insulin. *J Biol Chem* *259*, 15242-15251.
- Sazanov, L.A., and Hinchliffe, P. (2006). Structure of the hydrophilic domain of respiratory complex I from *Thermus thermophilus*. *Science* *311*, 1430-1436.
- Schägger, H., and Pfeiffer, K. (2000). Supercomplexes in the respiratory chains of yeast and mammalian mitochondria. *Embo j* *19*, 1777-1783.
- Schmidt-Nielsen, B. (1984). August and Marie Krogh and respiratory physiology. *Journal of applied physiology: respiratory, environmental and exercise physiology* *57*, 293-303.
- Schneeweiss, B., Pammer, J., Ratheiser, K., Schneider, B., Madl, C., Kramer, L., Kranz, A., Ferenci, P., Druml, W., Grimm, G., *et al.* (1993). Energy metabolism in acute hepatic failure. *Gastroenterology* *105*, 1515-1521.
- Schrader, S., Perfilyev, A., Ahlqvist, E., Groop, L., Vaag, A., Martinell, M., García-Calzón, S., and Ling, C. (2022). Novel Subgroups of Type 2 Diabetes Display Different Epigenetic Patterns That Associate With Future Diabetic Complications. *Diabetes care* *45*, 1621-1630.
- Selye, H. (1980). Stress and holistic medicine. *Family & community health* *3*, 85-88.
- Shahsavari, A., D'Occhio, M.J., and Al Jassim, R. (2016). The role of rumen-protected choline in hepatic function and performance of transition dairy cows. *Br J Nutr* *116*, 35-44.
- Sharma, J., Kumari, R., Bhargava, A., Tiwari, R., and Mishra, P.K. (2021). Mitochondrial-induced Epigenetic Modifications: From Biology to Clinical Translation. *Curr Pharm Des* *27*, 159-176.
- Sharma, N., Pasala, M.S., and Prakash, A. (2019). Mitochondrial DNA: Epigenetics and environment. *Environmental and molecular mutagenesis* *60*, 668-682.
- Shields, B.M., Shepherd, M., Hudson, M., McDonald, T.J., Colclough, K., Peters, J., Knight, B., Hyde, C., Ellard, S., Pearson, E.R., *et al.* (2017). Population-Based Assessment of a Biomarker-Based Screening Pathway to Aid Diagnosis of Monogenic Diabetes in Young-Onset Patients. *Diabetes care* *40*, 1017-1025.
- Shulman, G.I., Rothman, D.L., Jue, T., Stein, P., DeFronzo, R.A., and Shulman, R.G. (1990). Quantitation of muscle glycogen synthesis in normal subjects and subjects with non-insulin-dependent diabetes by ¹³C nuclear magnetic resonance spectroscopy. *The New England journal of medicine* *322*, 223-228.
- Simonson, D.C., and DeFronzo, R.A. (1990). Indirect calorimetry: methodological and interpretative problems. *The American journal of physiology* *258*, E399-412.
- Skulachev, V.P. (1991). Fatty acid circuit as a physiological mechanism of uncoupling of oxidative phosphorylation. *FEBS Lett* *294*, 158-162.
- Skvortsova, K., Iovino, N., and Bogdanović, O. (2018). Functions and mechanisms of epigenetic inheritance in animals. *Nature reviews Molecular cell biology* *19*, 774-790.
- Soboll, S., and Stucki, J. (1985). Regulation of the degree of coupling of oxidative phosphorylation in intact rat liver. *Biochimica et biophysica acta* *807*, 245-254.
- Soeters, M.R., Soeters, P.B., Schooneman, M.G., Houten, S.M., and Romijn, J.A. (2012). Adaptive reciprocity of lipid and glucose metabolism in human short-term starvation. *Am J Physiol Endocrinol Metab* *303*, E1397-1407.

- Solís-Muñoz, P., de la Flor-Robledo, M., García-Ruiz, I., Fernández-García, C.E., González-Rodríguez, Á., Shah, N., Bataller, R., Heneghan, M., García-Monzón, C., and Solís-Herruzo, J.A. (2023). Mitochondrial respiratory chain activity is associated with severity, corticosteroid response and prognosis of alcoholic hepatitis. *Alimentary pharmacology & therapeutics* 57, 1131-1142.
- Stauch, K.L., Purnell, P.R., and Fox, H.S. (2014). Aging synaptic mitochondria exhibit dynamic proteomic changes while maintaining bioenergetic function. *Aging* 6, 320-334.
- Stelling, J., Sauer, U., Szallasi, Z., Doyle, F.J., 3rd, and Doyle, J. (2004). Robustness of cellular functions. *Cell* 118, 675-685.
- Stoccoro, A., Mosca, L., Carnicelli, V., Cavallari, U., Lunetta, C., Marocchi, A., Migliore, L., and Coppedè, F. (2018). Mitochondrial DNA copy number and D-loop region methylation in carriers of amyotrophic lateral sclerosis gene mutations. *Epigenomics* 10, 1431-1443.
- Stucki, J.W. (1980). The optimal efficiency and the economic degrees of coupling of oxidative phosphorylation. *Eur J Biochem* 109, 269-283.
- Stucki, J.W. (1991). Non-equilibrium thermodynamic sensitivity of oxidative phosphorylation. *Proc Biol Sci* 244, 197-202.
- Stumvoll, M., Goldstein, B.J., and van Haeften, T.W. (2005). Type 2 diabetes: principles of pathogenesis and therapy. *Lancet (London, England)* 365, 1333-1346.
- Swarup, S., Goyal, A., Grigorova, Y., and Zeltser, R. (2023). Metabolic Syndrome. In *StatPearls (Treasure Island (FL) ineligible companies. StatPearls Publishing Copyright © 2023, StatPearls Publishing LLC.)*.
- Talikka, M., Sierro, N., Ivanov, N.V., Chaudhary, N., Peck, M.J., Hoeng, J., Coggins, C.R., and Peitsch, M.C. (2012). Genomic impact of cigarette smoke, with application to three smoking-related diseases. *Critical reviews in toxicology* 42, 877-889.
- Tallima, H., and El Ridi, R. (2018). Arachidonic acid: Physiological roles and potential health benefits - A review. *Journal of advanced research* 11, 33-41.
- Thomas, P.D., Ebert, D., Muruganujan, A., Mushayahama, T., Albou, L.P., and Mi, H. (2022). PANTHER: Making genome-scale phylogenetics accessible to all. *Protein science : a publication of the Protein Society* 31, 8-22.
- Tilg, H., and Moschen, A.R. (2010). Evolution of inflammation in nonalcoholic fatty liver disease: the multiple parallel hits hypothesis. *Hepatology (Baltimore, Md)* 52, 1836-1846.
- Timper, K., and Brüning, J.C. (2017). Hypothalamic circuits regulating appetite and energy homeostasis: pathways to obesity. *Disease models & mechanisms* 10, 679-689.
- Tremblay, J., and Yergeau, E. (2019). Systematic processing of ribosomal RNA gene amplicon sequencing data. *GigaScience* 8.
- Tseng, Y.H., Cypess, A.M., and Kahn, C.R. (2010). Cellular bioenergetics as a target for obesity therapy. *Nature reviews Drug discovery* 9, 465-482.
- Uehara, M., Yamazaki, H., Yoshikawa, N., Kuribara-Souta, A., and Tanaka, H. (2020). Correlation among body composition and metabolic regulation in a male mouse model of Cushing's syndrome. *Endocr J* 67, 21-30.
- Ulrich-Lai, Y.M., and Herman, J.P. (2009). Neural regulation of endocrine and autonomic stress responses. *Nature reviews Neuroscience* 10, 397-409.
- Urban, L.A., Trinh, A., Pearlman, E., Siryaporn, A., and Downing, T.L. (2021). The impact of age-related hypomethylated DNA on immune signaling upon cellular demise. *Trends in immunology* 42, 464-468.

- Vaisse, C., Clement, K., Guy-Grand, B., and Froguel, P. (1998). A frameshift mutation in human MC4R is associated with a dominant form of obesity. *Nature genetics* *20*, 113-114.
- van Bodegom, M., Homberg, J.R., and Henckens, M. (2017). Modulation of the Hypothalamic-Pituitary-Adrenal Axis by Early Life Stress Exposure. *Front Cell Neurosci* *11*, 87.
- van den Berk-Clark, C., Secrest, S., Walls, J., Hallberg, E., Lustman, P.J., Schneider, F.D., and Scherrer, J.F. (2018). Association between posttraumatic stress disorder and lack of exercise, poor diet, obesity, and co-occurring smoking: A systematic review and meta-analysis. *Health Psychol* *37*, 407-416.
- van Otterdijk, S.D., Mathers, J.C., and Strathdee, G. (2013). Do age-related changes in DNA methylation play a role in the development of age-related diseases? *Biochem Soc Trans* *41*, 803-807.
- Vegiopoulos, A., and Herzig, S. (2007). Glucocorticoids, metabolism and metabolic diseases. *Molecular and cellular endocrinology* *275*, 43-61.
- Verkhovskaya, M., and Bloch, D.A. (2013). Energy-converting respiratory Complex I: on the way to the molecular mechanism of the proton pump. *Int J Biochem Cell Biol* *45*, 491-511.
- Vitali, A., Murano, I., Zingaretti, M.C., Frontini, A., Ricquier, D., and Cinti, S. (2012). The adipose organ of obesity-prone C57BL/6J mice is composed of mixed white and brown adipocytes. *Journal of lipid research* *53*, 619-629.
- Vomhof-Dekrey, E.E., and Picklo, M.J., Sr. (2012). The Nrf2-antioxidant response element pathway: a target for regulating energy metabolism. *The Journal of nutritional biochemistry* *23*, 1201-1206.
- Waddington, C.H. (1942). Canalization of development and the inheritance of acquired character. *Nature* *150*3811.
- Wang, D., Ji, D.C., Yu, C.Y., Wu, D.N., and Qi, L. (2023). Research progress on the mitochondrial mechanism of age-related non-alcoholic fatty liver. *World journal of gastroenterology* *29*, 1982-1993.
- Wang, Q., Xiong, F., Wu, G., Liu, W., Chen, J., Wang, B., and Chen, Y. (2022). Gene body methylation in cancer: molecular mechanisms and clinical applications. *Clinical epigenetics* *14*, 154.
- Wang, S., Song, J., Yang, Y., Zhang, Y., Wang, H., and Ma, J. (2015). HIF3A DNA Methylation Is Associated with Childhood Obesity and ALT. *PloS one* *10*, e0145944.
- Warburg, O. (1931). The oxygen-transferring ferment of respiration. *Nobel Lectures*.
- Weber, K., Brück, P., Mikes, Z., Küpper, J.H., Klingenspor, M., and Wiesner, R.J. (2002). Glucocorticoid hormone stimulates mitochondrial biogenesis specifically in skeletal muscle. *Endocrinology* *143*, 177-184.
- Weir, J.B. (1949). New methods for calculating metabolic rate with special reference to protein metabolism. *The Journal of physiology* *109*, 1-9.
- Wellen, K.E., Hatzivassiliou, G., Sachdeva, U.M., Bui, T.V., Cross, J.R., and Thompson, C.B. (2009). ATP-citrate lyase links cellular metabolism to histone acetylation. *Science* *324*, 1076-1080.
- WHO (2021a). World Health Organization Update Obesity.
- WHO (2021b). World Health Organization Update Report Diabetes.
- Wiedemann, N., and Pfanner, N. (2017). Mitochondrial Machineries for Protein Import and Assembly. *Annual review of biochemistry* *86*, 685-714.
- Wieser, M., Bonifer, R., Oster, W., Lindemann, A., Mertelsmann, R., and Herrmann, F. (1989). Interleukin-4 induces secretion of CSF for granulocytes and CSF for macrophages by peripheral blood monocytes. *Blood* *73*, 1105-1108.

- Wijnant, K., Klosowska, J., Braet, C., Verbeken, S., De Henauw, S., Vanhaecke, L., and Michels, N. (2021). Stress Responsiveness and Emotional Eating Depend on Youngsters' Chronic Stress Level and Overweight. *Nutrients* *13*.
- Wikström, M. (1984). Two protons are pumped from the mitochondrial matrix per electron transferred between NADH and ubiquinone. *FEBS Lett* *169*, 300-304.
- Wikström, M., Krab, K., and Sharma, V. (2018). Oxygen Activation and Energy Conservation by Cytochrome c Oxidase. *Chemical reviews* *118*, 2469-2490.
- Wikström, M., Sharma, V., Kaila, V.R., Hosler, J.P., and Hummer, G. (2015). New perspectives on proton pumping in cellular respiration. *Chemical reviews* *115*, 2196-2221.
- Wikstrom, M., and Springett, R. (2020). Thermodynamic efficiency, reversibility, and degree of coupling in energy conservation by the mitochondrial respiratory chain. *Commun Biol* *3*, 451.
- Williams, G.M., and Iatropoulos, M.J. (2002). Alteration of liver cell function and proliferation: differentiation between adaptation and toxicity. *Toxicologic pathology* *30*, 41-53.
- Willner, P. (1997). Validity, reliability and utility of the chronic mild stress model of depression: a 10-year review and evaluation. *Psychopharmacology* *134*, 319-329.
- Wilson, F.H., Hariri, A., Farhi, A., Zhao, H., Petersen, K.F., Toka, H.R., Nelson-Williams, C., Raja, K.M., Kashgarian, M., Shulman, G.I., *et al.* (2004). A cluster of metabolic defects caused by mutation in a mitochondrial tRNA. *Science* *306*, 1190-1194.
- Winning, A., Glymour, M.M., McCormick, M.C., Gilsanz, P., and Kubzansky, L.D. (2015). Psychological Distress Across the Life Course and Cardiometabolic Risk: Findings From the 1958 British Birth Cohort Study. *Journal of the American College of Cardiology* *66*, 1577-1586.
- Wolf, E.J., Maniates, H., Nugent, N., Maihofer, A.X., Armstrong, D., Ratanatharathorn, A., Ashley-Koch, A.E., Garrett, M., Kimbrel, N.A., Lori, A., *et al.* (2018). Traumatic stress and accelerated DNA methylation age: A meta-analysis. *Psychoneuroendocrinology* *92*, 123-134.
- Wright, M.M., Howe, A.G., and Zarembek, V. (2004). Cell membranes and apoptosis: role of cardiolipin, phosphatidylcholine, and anticancer lipid analogues. *Biochemistry and cell biology = Biochimie et biologie cellulaire* *82*, 18-26.
- Wu, Q.J., Zhang, T.N., Chen, H.H., Yu, X.F., Lv, J.L., Liu, Y.Y., Liu, Y.S., Zheng, G., Zhao, J.Q., Wei, Y.F., *et al.* (2022). The sirtuin family in health and disease. *Signal transduction and targeted therapy* *7*, 402.
- Wu, Y.L., Lin, Z.J., Li, C.C., Lin, X., Shan, S.K., Guo, B., Zheng, M.H., Li, F., Yuan, L.Q., and Li, Z.H. (2023). Epigenetic regulation in metabolic diseases: mechanisms and advances in clinical study. *Signal transduction and targeted therapy* *8*, 98.
- Yang, B.T., Dayeh, T.A., Kirkpatrick, C.L., Taneera, J., Kumar, R., Groop, L., Wollheim, C.B., Nitert, M.D., and Ling, C. (2011). Insulin promoter DNA methylation correlates negatively with insulin gene expression and positively with HbA(1c) levels in human pancreatic islets. *Diabetologia* *54*, 360-367.
- Yang, J., Zhou, R., and Ma, Z. (2019). Autophagy and Energy Metabolism. *Adv Exp Med Biol* *1206*, 329-357.
- Yang, L., Guo, Q., Leng, J., Wang, K., and Ding, Y. (2022). Late onset of type 2 diabetes is associated with mitochondrial tRNA(Trp) A5514G and tRNA(Ser(AGY)) C12237T mutations. *J Clin Lab Anal* *36*, e24102.
- Yankovskaya, V., Horsefield, R., Törnroth, S., Luna-Chavez, C., Miyoshi, H., Léger, C., Byrne, B., Cecchini, G., and Iwata, S. (2003). Architecture of succinate dehydrogenase and reactive oxygen species generation. *Science* *299*, 700-704.

- Yaribeygi, H., Maleki, M., Butler, A.E., Jamialahmadi, T., and Sahebkar, A. (2022). Molecular mechanisms linking stress and insulin resistance. *EXCLI J* 21, 317-334.
- Yi, C.X., Foppen, E., Abplanalp, W., Gao, Y., Alkemade, A., la Fleur, S.E., Serlie, M.J., Fliers, E., Buijs, R.M., Tschop, M.H., *et al.* (2012). Glucocorticoid signaling in the arcuate nucleus modulates hepatic insulin sensitivity. *Diabetes* 61, 339-345.
- Younossi, Z.M., Blissett, D., Blissett, R., Henry, L., Stepanova, M., Younossi, Y., Racila, A., Hunt, S., and Beckerman, R. (2016). The economic and clinical burden of nonalcoholic fatty liver disease in the United States and Europe. *Hepatology (Baltimore, Md)* 64, 1577-1586.
- Younossi, Z.M., Golabi, P., de Avila, L., Paik, J.M., Srishord, M., Fukui, N., Qiu, Y., Burns, L., Afendy, A., and Nader, F. (2019). The global epidemiology of NAFLD and NASH in patients with type 2 diabetes: A systematic review and meta-analysis. *Journal of hepatology* 71, 793-801.
- Younossi, Z.M., Stepanova, M., Younossi, Y., Golabi, P., Mishra, A., Rafiq, N., and Henry, L. (2020). Epidemiology of chronic liver diseases in the USA in the past three decades. *Gut* 69, 564-568.
- Yu, F.L., and Feigelson, P. (1970). A comparative study of RNA synthesis in rat hepatic nuclei and mitochondria under the influence of cortisone. *Biochimica et biophysica acta* 213, 134-141.
- Yu, G., Wang, L.G., and He, Q.Y. (2015). ChIPseeker: an R/Bioconductor package for ChIP peak annotation, comparison and visualization. *Bioinformatics (Oxford, England)* 31, 2382-2383.
- Zaharia, O.P., Strassburger, K., Strom, A., Bönhof, G.J., Karusheva, Y., Antoniou, S., Bódis, K., Markgraf, D.F., Burkart, V., Müssig, K., *et al.* (2019). Risk of diabetes-associated diseases in subgroups of patients with recent-onset diabetes: a 5-year follow-up study. *The lancet Diabetes & endocrinology* 7, 684-694.
- Zhang, N., Tian, X., Yan, T., Wang, H., Zhang, D., Lin, C., Liu, Q., and Jiang, S. (2023). Insights into the role of nucleotide methylation in metabolic-associated fatty liver disease. *Frontiers in immunology* 14, 1148722.
- Zhou, Q., Shen, L., Liu, C., Liu, C., Chen, H., and Liu, J. (2016). The Effects of Estradiol and Glucocorticoid on Human Osteosarcoma Cells: Similarities and Differences. *Anticancer Res* 36, 1683-1691.
- Zumbaugh, M.D., Johnson, S.E., Shi, T.H., and Gerrard, D.E. (2022). Molecular and biochemical regulation of skeletal muscle metabolism. *J Anim Sci* 100.
- Zurlo, F., Larson, K., Bogardus, C., and Ravussin, E. (1990). Skeletal muscle metabolism is a major determinant of resting energy expenditure. *The Journal of clinical investigation* 86, 1423-1427.

APPENDIX

Supplemental Table 1: Significant Regions deduced from differential methylated fragment enrichment based on mitochondrial chromosome.

Data were analysed using R-package MEDips (Lienhard et al., 2014) starting of annotated BAM files to determine variability in the data. Settings were as: extend: 300; paired: TrUE; shift 0; uniq: 0.001, window size: 100.

| Comparison acute Ctrl vs recovery Ctrl; acute Ctrl < recovery Ctrl | | | | | | | | | | | | |
|--|-------|-------|------------------|-----------|---------|------------|------------|----------------------|---------------|----------|--------------|-------------------------|
| chr | start | stop | annotation | geneStart | geneEnd | geneLength | geneStrand | transcriptId | distanceToTSS | geneName | edgeR.logFC | edgeR.adj.p.value |
| chrM | 7901 | 8000 | Promoter (<=1kb) | 7927 | 8607 | 681 | 1 | ENSMUST00000082408.1 | 0 | mt-Atp6 | -0,847724798 | 4,11E-07 |
| chrM | 9501 | 9600 | Promoter (<=1kb) | 9459 | 9806 | 348 | 1 | ENSMUST00000082411.1 | 43 | mt-Nd3 | -1,153549744 | 7,70E-11 |
| chrM | 11701 | 11900 | Promoter (<=1kb) | 11742 | 13565 | 1824 | 1 | ENSMUST00000082418.1 | 0 | mt-Nd5 | -0,695385117 | 1,63E-43 to 2,76E-45 |
| chrM | 13401 | 13500 | Promoter (<=1kb) | 13552 | 14070 | 519 | 2 | ENSMUST00000082419.1 | 570 | mt-Nd6 | -0,652342706 | 2,20E-10 |
| chrM | 13601 | 14000 | Promoter (<=1kb) | 13552 | 14070 | 519 | 2 | ENSMUST00000082419.1 | 70 | mt-Nd6 | -0,645846888 | 1,21E-27 to 7,07E-27 |
| chrM | 1601 | 1700 | Promoter (<=1kb) | 1094 | 2675 | 1582 | 1 | ENSMUST00000082390.1 | 508 | mt-Rnr2 | -0,644059342 | 1,96E-08 |
| chrM | 6201 | 6300 | Promoter (<=1kb) | 6870 | 6938 | 69 | 2 | ENSMUST00000082402.1 | 638 | mt-Ts1 | -1,099337086 | 4,32E-08 |
| chrM | 15001 | 15200 | Promoter (<=1kb) | 15289 | 15355 | 67 | 1 | ENSMUST00000082422.1 | -89 | mt-Tt | -0,840022931 | 2,72E-07 to 8,66E-09 |
| chrM | 4701 | 5000 | Promoter (<=1kb) | 4950 | 5016 | 67 | 1 | ENSMUST00000082397.1 | 0 | mt-Tw | -0,886126784 | 2,21E-21 |
| Comparison acute Cvs vs recovery Cvs; acute Cvs < recovery Cvs | | | | | | | | | | | | |
| chr | start | stop | annotation | geneStart | geneEnd | geneLength | geneStrand | transcriptId | distanceToTSS | geneName | edgeR.logFC | edgeR.adj.p.value |
| chrM | 701 | 1000 | Promoter (<=1kb) | 1025 | 1093 | 69 | 1 | ENSMUST00000082389.1 | -25 | mt-Tv | -1,114476271 | 1,62E-13 to 4,05E-14 |
| chrM | 1501 | 1800 | Promoter (<=1kb) | 1094 | 2675 | 1582 | 1 | ENSMUST00000082390.1 | 408 | mt-Rnr2 | -1,085117593 | 1,20E-07 to 2,3464E-12 |
| chrM | 1901 | 2000 | Promoter (<=1kb) | 2676 | 2750 | 75 | 1 | ENSMUST00000082391.1 | -676 | mt-Tl1 | -1,050930504 | 4,14E-07 |
| chrM | 2901 | 3000 | Promoter (<=1kb) | 2751 | 3707 | 957 | 1 | ENSMUST00000082392.1 | 151 | mt-Nd1 | -0,998787147 | 1,04E-07 |
| chrM | 3901 | 4200 | Promoter (<=1kb) | 3914 | 4951 | 1038 | 1 | ENSMUST00000082396.1 | 0 | mt-Nd2 | -1,531723629 | 1,13E-19 to 9,14E-08 |
| chrM | 4401 | 5000 | Promoter (<=1kb) | 4950 | 5016 | 67 | 1 | ENSMUST00000082397.1 | 0 | mt-Tw | -0,785421386 | 1,03E-27 to 4,561E-125 |
| chrM | 5801 | 5900 | Promoter (<=1kb) | 5328 | 6872 | 1545 | 1 | ENSMUST00000082402.1 | 474 | mt-Co1 | -1,118281736 | 1,26E-07 |
| chrM | 6101 | 6200 | Promoter (<=1kb) | 6870 | 6938 | 69 | 2 | ENSMUST00000082403.1 | 738 | mt-Ts1 | -1,161341164 | 3,57E-07 |
| chrM | 6301 | 6400 | Promoter (<=1kb) | 6870 | 6938 | 69 | 2 | ENSMUST00000082403.1 | 538 | mt-Ts1 | -1,188372159 | 3,03E-07 |
| chrM | 6601 | 6700 | Promoter (<=1kb) | 6870 | 6938 | 69 | 2 | ENSMUST00000082403.1 | 238 | mt-Ts1 | -1,174447219 | 1,385E-08 to 4,242E-07 |
| chrM | 6901 | 7000 | Promoter (<=1kb) | 6870 | 6938 | 69 | 2 | ENSMUST00000082403.1 | 0 | mt-Ts1 | -1,348647023 | 1,385E-08 |
| chrM | 7901 | 8000 | Promoter (<=1kb) | 7927 | 8607 | 681 | 1 | ENSMUST00000082408.1 | 0 | mt-Atp6 | -1,044229517 | 2,082E-07 |
| chrM | 9601 | 9700 | Promoter (<=1kb) | 9808 | 9875 | 68 | 1 | ENSMUST00000082412.1 | -108 | mt-Tr | -1,073811672 | 1,641E-07 |
| chrM | 10701 | 10800 | Promoter (<=1kb) | 10167 | 11544 | 1378 | 1 | ENSMUST00000082414.1 | 535 | mt-Nd4 | -1,223512937 | 7,84E-08 |
| chrM | 11001 | 11100 | Promoter (<=1kb) | 11546 | 11612 | 67 | 1 | ENSMUST00000082415.1 | -446 | mt-Th | -1,153017601 | 2,933E-08 |
| chrM | 11301 | 11500 | Promoter (<=1kb) | 11546 | 11612 | 67 | 1 | ENSMUST00000082415.1 | -46 | mt-Th | -1,054446148 | 3,404E-09 to 7,3936E-15 |
| chrM | 11701 | 11900 | Promoter (<=1kb) | 11742 | 13565 | 1824 | 1 | ENSMUST00000082418.1 | 0 | mt-Nd5 | -1,134995053 | 1,08E-110 to 2,642E-112 |
| chrM | 12101 | 12400 | Promoter (<=1kb) | 11742 | 13565 | 1824 | 1 | ENSMUST00000082418.1 | 360 | mt-Nd5 | -1,104605667 | 1,062E-07 to 3,7601E-11 |
| chrM | 12801 | 14100 | Promoter (<=1kb) | 13552 | 14070 | 519 | 2 | ENSMUST00000082419.1 | 0 | mt-Nd6 | -0,813265651 | 1,012E-07 to 8,8165E-08 |
| chrM | 14801 | 15200 | Promoter (<=1kb) | 15289 | 15355 | 67 | 1 | ENSMUST00000082422.1 | -89 | mt-Tt | -1,022917371 | 7,151E-08 |
| chrM | 15401 | 15600 | Promoter (<=1kb) | 15356 | 15422 | 67 | 2 | ENSMUST00000082423.1 | 0 | mt-Tp | -1,027912718 | 1,476E-08 to 4,2835E-08 |

Supplemental Table 2: Gene Ids with significant Regions in gene promoters (-3kb to TSS) deduced from differential methylated fragment enrichment.
 Enriched fragments were subjected to GO enrichment analyses using <http://www.pantherdb.org/> settings: GO biological function, reference list Mouse genome, FDR >0.05.

| Comparison acute Cvs vs recovery Cvs; acute Cvs < recovery Cvs | Analysis Type: | Annotation Version and Release Date: | Database DOI: ID:5383/ze nobo.6799722 Released 2022.07.01 | Client Text Box Input (Mus musculus) | Mus musculus (all genes in database) | FISHER | FDR | GO biological process complete | Mus musculus - REF LIST (21997) | Client Text Box Input (4) | Client Text Box Input (over/under) | Text Box Input (fold enrichment) | Text Box Input (raw P-value) | Client Text Box Input (FDR) |
|--|--|--------------------------------------|---|--------------------------------------|--------------------------------------|--------|------|--------------------------------|---------------------------------|---------------------------|------------------------------------|----------------------------------|------------------------------|-----------------------------|
| | ATP synthesis coupled electron transport (GO:0042773) | | | | 65 | 6 | 0.12 | 49.52 | 3.71E-09 | 6 | + | 49.52 | 3.71E-09 | 9.74E-06 |
| | mitochondrial ATP synthesis coupled electron transport (GO:0042775) | | | | 67 | 6 | 0.12 | 51.1 | 3.11E-09 | 6 | + | 51.1 | 3.11E-09 | 9.81E-06 |
| | proton motive force-driven ATP synthesis (GO:0015986) | | | | 67 | 6 | 0.12 | 48.05 | 4.39E-09 | 6 | + | 48.05 | 4.39E-09 | 9.89E-06 |
| | oxidative phosphorylation (GO:0006119) | | | | 105 | 7 | 0.2 | 35.77 | 1.41E-09 | 7 | + | 35.77 | 1.41E-09 | 1.11E-05 |
| | proton motive force-driven mitochondrial ATP synthesis (GO:0042774) | | | | 62 | 6 | 0.12 | 51.92 | 2.84E-09 | 6 | + | 51.92 | 2.84E-09 | 1.12E-05 |
| | mitochondrial electron transport, NADH to ubiquinone (GO:0006120) | | | | 26 | 5 | 0.05 | >100 | 2.84E-09 | 5 | + | >100 | 2.84E-09 | 1.48E-05 |
| | aerobic electron transport chain (GO:0019464) | | | | 54 | 6 | 0.1 | 59.61 | 1.32E-09 | 6 | + | 59.61 | 1.32E-09 | 2.07E-05 |
| | generation of precursor metabolites and energy (GO:0006091) | | | | 338 | 9 | 0.63 | 14.29 | 1.21E-08 | 9 | + | 14.29 | 1.21E-08 | 2.11E-05 |
| | aerobic respiration (GO:0009960) | | | | 144 | 7 | 0.27 | 26.8 | 1.14E-08 | 7 | + | 26.8 | 1.14E-08 | 2.25E-05 |
| | ATP biosynthetic process (GO:0006754) | | | | 83 | 6 | 0.15 | 38.78 | 1.47E-08 | 6 | + | 38.78 | 1.47E-08 | 2.31E-05 |
| | respiratory electron transport chain (GO:0022904) | | | | 87 | 6 | 0.16 | 37 | 1.91E-08 | 6 | + | 37 | 1.91E-08 | 2.51E-05 |
| | energy derivation by oxidation of organic compounds (GO:0015980) | | | | 245 | 8 | 0.46 | 17.52 | 1.86E-08 | 8 | + | 17.52 | 1.86E-08 | 2.67E-05 |
| | purine nucleoside triphosphate biosynthetic process (GO:0009145) | | | | 95 | 6 | 0.18 | 33.88 | 3.15E-08 | 6 | + | 33.88 | 3.15E-08 | 3.55E-05 |
| | purine nucleoside triphosphate biosynthetic process (GO:0009206) | | | | 94 | 6 | 0.18 | 34.25 | 2.97E-08 | 6 | + | 34.25 | 2.97E-08 | 3.60E-05 |
| | electron transport chain (GO:0022900) | | | | 98 | 6 | 0.18 | 32.85 | 3.75E-08 | 6 | + | 32.85 | 3.75E-08 | 3.70E-05 |
| | cellular respiration (GO:0045333) | | | | 176 | 7 | 0.33 | 21.94 | 4.30E-08 | 7 | + | 21.94 | 4.30E-08 | 3.76E-05 |
| | purine ribonucleotide biosynthetic process (GO:0009152) | | | | 172 | 7 | 0.32 | 21.83 | 3.69E-08 | 7 | + | 21.83 | 3.69E-08 | 3.88E-05 |
| | purine nucleotide biosynthetic process (GO:0006164) | | | | 181 | 7 | 0.34 | 20.75 | 5.17E-08 | 7 | + | 20.75 | 5.17E-08 | 4.29E-05 |
| | ribonucleotide biosynthetic process (GO:0009260) | | | | 184 | 7 | 0.34 | 20.41 | 5.77E-08 | 7 | + | 20.41 | 5.77E-08 | 4.94E-05 |
| | nucleoside triphosphate biosynthetic process (GO:0009142) | | | | 110 | 6 | 0.21 | 29.26 | 7.22E-08 | 6 | + | 29.26 | 7.22E-08 | 5.17E-05 |
| | purine-containing compound biosynthetic process (GO:007252) | | | | 189 | 7 | 0.35 | 19.87 | 6.88E-08 | 7 | + | 19.87 | 6.88E-08 | 5.17E-05 |
| | ribose phosphate biosynthetic process (GO:0046390) | | | | 193 | 7 | 0.36 | 19.46 | 7.90E-08 | 7 | + | 19.46 | 7.90E-08 | 5.4E-05 |
| | mitochondrial respiratory chain complex I assembly (GO:0082981) | | | | 57 | 5 | 0.11 | 47.06 | 1.04E-07 | 5 | + | 47.06 | 1.04E-07 | 6.53E-05 |
| | NADH dehydrogenase complex assembly (GO:0010257) | | | | 228 | 7 | 0.42 | 16.47 | 4.70E-07 | 7 | + | 16.47 | 4.70E-07 | 6.81E-05 |
| | nucleoside biosynthetic process (GO:0009165) | | | | 234 | 7 | 0.44 | 16.5 | 2.37E-07 | 7 | + | 16.5 | 2.37E-07 | 1.44E-04 |
| | nucleoside phosphate biosynthetic process (GO:1901298) | | | | 356 | 8 | 0.66 | 12.6 | 2.81E-07 | 8 | + | 12.6 | 2.81E-07 | 1.64E-04 |
| | purine ribonucleotide metabolic process (GO:0009150) | | | | 5 | 3 | 0.01 | >100 | 3.05E-07 | 3 | + | >100 | 3.05E-07 | 1.71E-04 |
| | energy coupled proton transmembrane transport, against electrochemical | | | | 5 | 3 | 0.01 | >100 | 3.33E-07 | 3 | + | >100 | 3.33E-07 | 1.75E-04 |
| | electron transport coupled proton transport (GO:0015990) | | | | 371 | 8 | 0.69 | 11.57 | 3.33E-07 | 8 | + | 11.57 | 3.33E-07 | 1.81E-04 |
| | purine nucleotide metabolic process (GO:0006168) | | | | 376 | 8 | 0.72 | 11.42 | 4.14E-07 | 8 | + | 11.42 | 4.14E-07 | 2.10E-04 |
| | ribonucleotide metabolic process (GO:0009259) | | | | 387 | 8 | 0.72 | 11.9 | 4.57E-07 | 8 | + | 11.9 | 4.57E-07 | 2.25E-04 |
| | ribose phosphate metabolic process (GO:0019693) | | | | 160 | 6 | 0.3 | 20.12 | 5.65E-07 | 6 | + | 20.12 | 5.65E-07 | 2.70E-04 |
| | ATP metabolic process (GO:0046034) | | | | 404 | 8 | 0.75 | 10.62 | 6.03E-07 | 8 | + | 10.62 | 6.03E-07 | 2.81E-04 |
| | purine-containing compound metabolic process (GO:0072521) | | | | 93 | 5 | 0.17 | 28.84 | 7.66E-07 | 5 | + | 28.84 | 7.66E-07 | 3.91E-04 |
| | mitochondrial respiratory chain complex assembly (GO:0033108) | | | | 387 | 6 | 0.35 | 17.21 | 1.04E-06 | 6 | + | 17.21 | 1.04E-06 | 4.55E-04 |
| | purine ribonucleoside triphosphate metabolic process (GO:0009205) | | | | 192 | 6 | 0.36 | 16.77 | 1.45E-06 | 6 | + | 16.77 | 1.45E-06 | 6.20E-04 |
| | ribonucleoside triphosphate metabolic process (GO:0009199) | | | | 193 | 6 | 0.36 | 16.68 | 1.69E-06 | 6 | + | 16.68 | 1.69E-06 | 7.01E-04 |
| | purine nucleoside triphosphate metabolic process (GO:0009144) | | | | 477 | 8 | 0.88 | 9 | 2.62E-06 | 8 | + | 9 | 2.62E-06 | 1.08E-03 |
| | nucleoside metabolic process (GO:0009117) | | | | 210 | 6 | 0.39 | 15.33 | 2.79E-06 | 6 | + | 15.33 | 2.79E-06 | 1.07E-03 |
| | nucleoside triphosphate metabolic process (GO:0009141) | | | | 484 | 8 | 0.9 | 8.95 | 2.91E-06 | 8 | + | 8.95 | 2.91E-06 | 1.09E-03 |
| | nucleoside phosphate metabolic process (GO:0006753) | | | | 860 | 9 | 1.6 | 7.99 | 6.19E-06 | 9 | + | 7.99 | 6.19E-06 | 2.27E-03 |
| | nucleoside-containing small molecule metabolic process (GO:0055086) | | | | 471 | 7 | 0.88 | 7.57 | 2.49E-05 | 7 | + | 7.57 | 2.49E-05 | 8.91E-03 |
| | organophosphate metabolic process (GO:0019637) | | | | 538 | 7 | 0.88 | 6.98 | 2.57E-05 | 7 | + | 6.98 | 2.57E-05 | 8.91E-03 |
| | organophosphate biosynthetic process (GO:0090407) | | | | 234 | 13 | 4.11 | 2.84 | 5.95E-05 | 13 | + | 2.84 | 5.95E-05 | 2.02E-02 |
| | carbohydrate derivative biosynthetic process (GO:1901137) | | | | 8 | 2 | 0.01 | >100 | 1.23E-04 | 2 | + | >100 | 1.23E-04 | 4.12E-02 |
| | cellular component assembly (GO:0022607) | | | | 8 | 2 | 0.01 | >100 | 1.51E-04 | 2 | + | >100 | 1.51E-04 | 4.94E-02 |

Supplemental Table 3: IPA canonical pathways analyses.

Data were analysed using the Core expression routine <https://www.qiagenbioinformatics.com/products/ingenuity-pathway-analysis>. Analysis settings: Cutoff before duplicate resolution, Cutoff for Expression fold change 0.05, Reference set used Ingenuity Knowledge Base (Genes Only), direct and indirect relationships were included.

| Comparison acute Cvs vs recovery Cvs | | | | |
|--|---------------|--------|--------|----|
| Ingenuity Canonical Pathways | -log(p-value) | zScore | Ratio | n |
| Superpathway of Cholesterol Biosynthesis | 14,4 | -3,742 | 0,483 | 14 |
| Cholesterol Biosynthesis I | 11,4 | -3,000 | 0,692 | 9 |
| Cholesterol Biosynthesis II (via 24,25-dihydrolanosterol) | 11,4 | -3,000 | 0,692 | 9 |
| Cholesterol Biosynthesis III (via Desmosterol) | 11,4 | -3,000 | 0,692 | 9 |
| Sirtuin Signaling Pathway | 10,9 | -1,633 | 0,109 | 32 |
| LPS/IL-1 Mediated Inhibition of RXR Function | 6,5 | 1,508 | 0,0906 | 23 |
| NRF2-mediated Oxidative Stress Response | 5,27 | 0,000 | 0,0844 | 20 |
| Zymosterol Biosynthesis | 5,16 | -2,000 | 0,667 | 4 |
| PXR/RXR Activation | 5,13 | -1,265 | 0,154 | 10 |
| Acute Phase Response Signaling | 5,05 | -0,333 | 0,0919 | 17 |
| LXR/RXR Activation | 4,64 | -0,816 | 0,106 | 13 |
| Complement System | 4,35 | 2,449 | 0,189 | 7 |
| Role of PKR in Interferon Induction and Antiviral Response | 4,18 | 2,121 | 0,0956 | 13 |
| BAG2 Signaling Pathway | 4,14 | -2,236 | 0,119 | 10 |
| Superpathway of Geranylgeranyldiphosphate Biosynthesis | 4,09 | -2,236 | 0,278 | 5 |
| Phagosome Maturation | 4,09 | | 0,0886 | 14 |
| Aryl Hydrocarbon Receptor Signaling | 4,06 | 2,000 | 0,0881 | 14 |
| Xenobiotic Metabolism AHR Signaling Pathway | 4,01 | -1,000 | 0,115 | 10 |
| Estrogen Biosynthesis | 3,79 | -1,134 | 0,156 | 7 |
| Oxidative Phosphorylation | 3,76 | 2,530 | 0,0991 | 11 |
| Xenobiotic Metabolism PXR Signaling Pathway | 3,73 | -0,775 | 0,0781 | 15 |
| Prostate Cancer Signaling | 3,66 | | 0,0965 | 11 |
| EIF2 Signaling | 3,43 | 1,265 | 0,0705 | 16 |
| Glutathione-mediated Detoxification | 3,42 | -2,236 | 0,162 | 6 |
| Mevalonate Pathway I | 3,41 | -2,000 | 0,286 | 4 |
| Glucocorticoid Receptor Signaling | 3,38 | | 0,0515 | 30 |
| Bupropion Degradation | 3,36 | -1,342 | 0,2 | 5 |
| HIF1 α Signaling | 3,35 | 2,840 | 0,0721 | 15 |
| Xenobiotic Metabolism CAR Signaling Pathway | 3,24 | -2,673 | 0,0733 | 14 |
| Huntington's Disease Signaling | 3,24 | 0,000 | 0,0636 | 18 |
| Aldosterone Signaling in Epithelial Cells | 3,17 | -0,447 | 0,0756 | 13 |
| Epoxycholesterol Biosynthesis | 3,16 | | 1 | 2 |
| Neutrophil Extracellular Trap Signaling Pathway | 3,16 | 2,711 | 0,0557 | 23 |
| Xenobiotic Metabolism Signaling | 3,1 | | 0,0619 | 18 |
| Mitochondrial Dysfunction | 3,03 | -2,065 | 0,058 | 20 |
| Estrogen Receptor Signaling | 2,86 | 1,604 | 0,0538 | 22 |
| Xenobiotic Metabolism General Signaling Pathway | 2,83 | -0,905 | 0,0769 | 11 |
| FXR/RXR Activation | 2,72 | | 0,0794 | 10 |
| PPAR α /RXR α Activation | 2,68 | 0,905 | 0,0667 | 13 |
| Nucleotide Excision Repair Pathway | 2,67 | | 0,143 | 5 |
| PPAR Signaling | 2,67 | 0,707 | 0,0841 | 9 |
| Ferroptosis Signaling Pathway | 2,57 | 0,333 | 0,0758 | 10 |
| Acute Myeloid Leukemia Signaling | 2,55 | -0,447 | 0,0879 | 8 |
| Necroptosis Signaling Pathway | 2,53 | 2,111 | 0,0705 | 11 |
| Role of Pattern Recognition Receptors in Recognition of Bacteria | 2,53 | 2,121 | 0,0705 | 11 |
| p70S6K Signaling | 2,46 | -1,134 | 0,0465 | 27 |
| Prolactin Signaling | 2,44 | -1,134 | 0,0842 | 8 |
| Hypoxia Signaling in the Cardiovascular System | 2,41 | 2,000 | 0,0921 | 7 |
| Neuregulin Signaling | 2,41 | -0,378 | 0,0769 | 9 |
| Nicotine Degradation III | 2,38 | -1,633 | 0,103 | 6 |
| Hepatic Cholestasis | 2,31 | | 0,0628 | 12 |
| Endometrial Cancer Signaling | 2,31 | 0,000 | 0,1 | 6 |
| Acetone Degradation I (to Methylglyoxal) | 2,28 | -1,342 | 0,116 | 5 |
| Melatonin Degradation I | 2,24 | -1,633 | 0,0968 | 6 |
| MIF Regulation of Innate Immunity | 2,23 | 2,000 | 0,114 | 5 |
| Trans, trans-farnesyl Diphosphate Biosynthesis | 2,18 | | 0,4 | 2 |
| NAD Signaling Pathway | 2,16 | 2,646 | 0,0662 | 10 |
| Macrophage Alternative Activation Signaling Pathway | 2,12 | 0,577 | 0,0594 | 12 |
| HER-2 Signaling in Breast Cancer | 2,12 | -0,277 | 0,0573 | 13 |
| Telomerase Signaling | 2,1 | -0,378 | 0,0741 | 8 |
| Nicotine Degradation II | 2,1 | -1,633 | 0,0909 | 6 |
| PI3K Signaling in B Lymphocytes | 2,09 | 2,000 | 0,044 | 26 |
| Superpathway of Melatonin Degradation | 2,07 | -1,633 | 0,0896 | 6 |
| Atherosclerosis Signaling | 2,05 | | 0,0677 | 9 |
| Assembly of RNA Polymerase II Complex | 2 | 2,236 | 0,1 | 5 |

Table 9: Overview of persons who contributed to experiments in publication Nikolic et al. 2023 (muscle).

List of figures and the respective experiments together with the person who realized these: AN: Aleksandra Nikolic, NW: Natalie Wahlers, SJ: Sylvia Jacob, Ulrike Kettel: UK, JK: Jörg Kotzka, PF: Pia Fahlbusch, BK: Birgit Knebel

| | Experiments | Performed by | Data analyzed by |
|----------------|--|---------------------|-------------------------|
| Fig. 8: | A-B) Weight change, body composition, and food uptake | NW | JK & AN |
| Fig. 9 | A-C) Physical activity, energy expenditure (EE), and substrate utilization | NW | JK & AN |
| Fig. 10 | A) Mitochondrial copy number | SJ | AN |
| | B-C) Citrate synthase activity and membrane integrity | AN | AN |
| Fig. 11 | A-C) Proteome analyses of ketolysis, glutaminolysis and BCAA | UK | JK |
| Fig. 12 | A-J) Proteome analyses of metabolic pathways | UK | JK |
| Fig. 13 | A-H) Mitochondrial proteome | UK | JK |
| Fig. 14 | A) UCP3 RNA level | AN | AN |
| | B) UCP 3 protein level | UK | AN |
| | C) Proteome analysis of ROS detoxification and TBARS activity assay | UK & AN | JK & AN |
| Fig. 15 | A-B) Mitochondrial electron flow and coupling analyses | AN | AN |
| Fig. 16 | A-B) Mitochondrial electron flow and coupling analyses in detail | AN | AN & PF |
| Fig. 17 | A-C) Respiratory control ratio, thermodynamic coupling and thermodynamic efficiency of oxidative phosphorylation | AN | AN |
| Fig. 18 | Differential methylated areas after Cvs | SJ & AN | BK |
| Fig. 19 | MTase and SIRT activity | AN | AN |
| Fig. 20 | Transcriptome analyses | SJ & AN | PF |

Table 10: Overview of persons who contributed to experiments in unpublished manuscript (liver).

List of figures and the respective experiments together with the person who realized these AN: Aleksandra Nikolic, NW: Natalie Wahlers, SJ: Sylvia Jacob, MS: Martina Schiller, Ulrike Kettel: UK, JK: Jörg Kotzka, PF: Pia Fahlbusch, BK: Birgit Knebel, MD: Matthias Dille

| | Experiments | Performed by | Data analyzed by |
|-----------------|---|---------------------|-------------------------|
| Fig. 21: | A-D) Weight change, body composition, and food intake | AN | AN & JK |
| | E), I), J) Plasma glucose, lactate and glutamate | AN | AN |
| | F), G), H) Plasma insulin, glucagon and leptin | MD | AN |
| | K-L) Plasma TAG and NEFA level | AN | AN |
| | M) Plasma NEFA composition | MS | JK |
| | N-O) Energy expenditure (EE) and respiratory exchange ratio (RER) | AN | AN |
| Fig. 22 | i.p. GTT | AN | AN |
| | i.p. PTT | NW | AN |
| Fig. 23 | A-H) Proteome abundances | UK | JK |
| | A), C), E), G) Ex vivo experiments in prim- hepatocytes | NW | JK & AN |
| | B), D), F) Ex vivo activity assays | AN | AN |
| Fig. 24 | A) Mitochondrial copy number, cytochrome c activity and citrate synthase activity | AN | AN |
| | B) Proteome analysis of ROS detoxification and TBARS activity assay | AN | JK & AN |
| Fig. 25 | A) Mitochondrial proteome | UK | JK |
| | B) Mitochondrial electron flow | AN | AN |
| Fig. 26 | A-J) Mitochondrial coupling experiment in detail | AN | AN & PF |
| Fig. 27 | A-D) Mitochondrial efficiency | AN | AN |
| | E-H) NAD ⁺ /NADH ratio, FAD, SIRT activity and MTase activity | AN | AN |
| | I) Mitochondrial energymap | MD | AN |
| Fig. 28 | A), C), D) Methylome analyses | SJ & AN | BK |
| | B) Transcriptome analyses | SJ & AN | PF |
| Fig. 29 | A-B) Methylome analyses | SJ & AN | BK |

DANKSAGUNG

Mein Dank gilt Prof. Dr. Hadi Al-Hasani, der mir ermöglicht hat, am Institut für Klinische Biochemie und Pathobiochemie zu promovieren und die Freiheit in der Gestaltung des Themas überlassen hat.

Weiterführend möchte ich mich auch bei Herrn Prof. Dr. Feldbrügge für die wissenschaftliche Betreuung als Zweitgutachter seitens der Heinrich-Heine-Universität bedanken.

Mein außerordentlicher Dank geht an Dr. Birgit Knebel und Dr. Jörg Kotzka für ihre immerwährende Unterstützung, die sehr gute Betreuung und die vielen förderlichen Ratschläge, sowie die stets geöffnete Tür. Beide haben mich nicht nur auf wissenschaftlicher, sondern auch auf persönlicher Ebene geprägt.

Ein besonderer Dank geht an Dr. Pia Fahlbusch, ohne deren Mithilfe ein solcher Arbeitsumfang nicht zu stemmen gewesen wäre. Danke für das offene Ohr und die fachliche sowie moralische Unterstützung.

Ein herzlicher Dank geht auch an Sylvia Jacob für die stetige Hilfe und unverdrossene Unterstützung bei der Überwindung diverser technischer Hindernisse. Ebenfalls gilt auch Dr. Matthias Dille, Nele-Kathrien Riffelmann und Natalie Wahlers ein besonderer Dank, welche mich tatkräftig im Labor unterstützt haben.

Außerdem bedanke ich mich bei aktuellen und ehemaligen Mitarbeitenden des Instituts für Klinische Biochemie und Pathobiochemie, die nach einer so intensiven Zeit großartige Freunde wurden. Besonderer Dank geht an Dr. Lena Espelage, Pia Marlene Förster und Anna Scheel.

Ein unermesslicher Dank gilt meiner Familie, insbesondere meinen Eltern, Snježana Nikolić und Dr. Slobodan Nikolić, meinem Bruder Bojan Nikolić und seiner Frau Christina Wendland. Ich danke ihnen für das Ermöglichen meines bisherigen Lebensweges, vor allem für ihre Ermutigung und unaufhörliche Unterstützung während dieser Zeit.

Beskrajno hvala što ste uvijek vjerovali u mene. Volim vas.

An letzter, doch eigentlich an erster Stelle danke ich meinem Freund Dr. Stefan Reinhold. Danke für unermüdliches und geduldiges Zuhören, Hilfe in Wort und Tat, für die Rücksichtnahme und uneingeschränkten Aufmunterungen sowie für jede einzelne Umarmung während dieser Promotion.

Ohne Eure Unterstützung, bedingungslose Geduld und den tiefen Glauben an mich, hätte ich diesen Weg nicht gehen können!

EIDESSTATTLICHE ERKLÄRUNG

Ich versichere an Eides Statt, dass die Dissertation von mir selbständig und ohne unzulässige fremde Hilfe unter Beachtung der „Grundsätze zur Sicherung guter wissenschaftlicher Praxis an der Heinrich-Heine-Universität Düsseldorf“ erstellt worden ist. Die Dissertation wurde in der vorgelegten oder in ähnlicher Form noch bei keiner anderen Institution eingereicht. Ich habe bisher keine erfolglosen Promotionsversuche unternommen.

Datum

Aleksandra Nikolić